

GYROKINETIC CONTINUUM SIMULATION OF TURBULENCE IN OPEN-FIELD-LINE PLASMAS

ERIC LEON SHI

A DISSERTATION
PRESENTED TO THE FACULTY
OF PRINCETON UNIVERSITY
IN CANDIDACY FOR THE DEGREE
OF DOCTOR OF PHILOSOPHY

RECOMMENDED FOR ACCEPTANCE
BY THE DEPARTMENT OF
ASTROPHYSICAL SCIENCES
PROGRAM IN PLASMA PHYSICS
ADVISER: GREGORY W. HAMMETT

SEPTEMBER 2017

© Copyright by Eric Leon Shi, 2017.
All rights reserved.

Abstract

The properties of the boundary plasma in a tokamak are now recognized to play a key role in determining the achievable fusion power and the lifetimes of plasma-facing components. Accurate quantitative modeling and improved qualitative understanding of the boundary plasma ultimately require five-dimensional gyrokinetic turbulence simulations, which have been successful in predicting turbulence and transport in the core. Gyrokinetic codes for the boundary plasma must be able to handle large-amplitude fluctuations, electromagnetic effects, open and closed magnetic field lines, magnetic X-points, and the dynamics of impurities and neutrals. The additional challenges of boundary-plasma simulation necessitate the development of new gyrokinetic codes or major modifications to existing core gyrokinetic codes.

In this thesis, we develop the first gyrokinetic continuum code capable of simulating plasma turbulence on open magnetic field lines, which is a key feature of a tokamak scrape-off layer. In contrast to prior attempts at this problem, we use an energy-conserving discontinuous Galerkin discretization in space. To model the interaction between the plasma and the wall, we design conducting-sheath boundary conditions that permit local currents into and out of the wall. We start by designing spatially one-dimensional kinetic models of parallel SOL dynamics and solve these systems using novel continuum algorithms. By generalizing these algorithms to higher dimensions and adding a model for collisions, we present results from the first gyrokinetic continuum simulations of turbulence on two types of open-field-line systems. The first simulation features uniform and straight field lines, such as found in some linear plasma devices. The second simulation is of a hypothetical model we developed of the NSTX scrape-off layer featuring helical field lines. In the context of discontinuous Galerkin methods, we also explore the use of exponentially weighted polynomials for a more efficient velocity-space discretization of the distribution function when compared to standard polynomials. We show that standard implementations do not conserve any moments of the distribution function, and we develop a modified algorithm that does. These developments comprise a major step towards a gyrokinetic continuum code for quantitative predictions of turbulence and transport in the boundary plasma of magnetic fusion devices.

Acknowledgements

Many fall in the face of chaos, but
not this one... not today.

Narrator, Darkest Dungeon

After more than six years at Princeton, I am finally ready to move on. Although I am eagerly anticipating what the future holds, I will also miss the tightly structured life that I have become accustomed to over the years. I would not have been able to complete my thesis without the direct support of many people.

Of course, I must thank Greg Hammett for being my adviser. Although I did not decide to come to Princeton to work with him (or anyone else) in particular, I realized later on in my graduate career how lucky I was to find an adviser who was an expert in both turbulence and numerical methods, had a code-development project written in a modern programming language, and had the patience to teach a student who knew so little. It is fitting that we both have a tendency to send e-mails well-past midnight. I will be happy if I can one day attain even a small fraction of his level of knowledge, creativity, and intuition.

I thank Tim Stoltzfus-Dueck for always making the time to share his incredible knowledge and powerful intuition about plasma physics with me. Tim has been a great mentor and teacher, often meeting with me several times a week, and I owe much of what I learned about SOL physics to him. Tim played an essential role in interpreting the physics of the simulations and suggesting systematic ways to test the code when the results appeared to be incorrect. Tim's commitment to do physics in an objective and transparent way has greatly influenced the way I conduct and present my own work. I hope that Tim will one day use his remarkable aptitude for teaching to train future generations of plasma physicists in edge and SOL physics.

I am very grateful to Ammar Hakim for creating the Gkeyll plasma-physics framework and for developing some of the additional capabilities required for my thesis. I owe a large part of the timely completion of my thesis (by Princeton standards, at least) to Ammar, who has designed the code with modern and sound software-engineering concepts. I would also like to thank Ammar for teaching me the basics about DG methods and for closely working with me for my second-year project.

I thank John Krommes for being an excellent teacher, academic adviser, and even boss. Although he must have been disappointed in how little I learned from his 'Irreversible Processes in Plasmas' class when I took it as a second-year student, I hope he recognized that I finally started learning something in the two semesters during which I worked as a grader for his class. As my academic adviser, John always listened intently to whatever dilemmas I brought to him and drew upon his experience to provide profoundly wise advice. I also credit John with instilling a strong belief in adhering to established rules and conventions for technical writing. Unfortunately, I will not return your \$31 if you catch five writing mistakes in my thesis.

I thank my thesis readers, Stewart Zweben and Matt Kunz, for carefully reading my thesis and providing valuable feedback. Greg Hammett and Tim Stoltzfus-Dueck

also provided valuable comments for my thesis. I would also like to thank Stewart Zweben (figures 1.2 and 1.3), the IAEA and Thomas Eich (figure 1.4), and Troy Carter and David Schaffner (figures 4.1, 4.2, and 4.14) for permission to use their figures in my thesis to illustrate important results.

I thank my other research collaborators for taking the time to learn about my research or code: Qingjiang Pan, Tess Bernard, and Jimmy Juno. I credit Noah Mandell with the formidable task of building the Gkeyll code on various systems. I also thank Dan Ruiz and Jeff Parker for enlisting my help on a side project about DW-ZF interactions.

I am very grateful to Curt Hillegas and Matt Kunz for their support for my use of the Perseus cluster at Princeton, which enormously sped up my time to graduate. I also thank Frank Jenko and Jason TenBarge for providing access to additional computational resources. I thank Troy Carter, Amitava Bhattacharjee, Paolo Ricci, Stewart Zweben, Frank Jenko, Bill Tang, Hantao Ji, and Bob Kaita for their encouragement and support. I also acknowledge useful discussions with John Krommes, Troy Carter, Paolo Ricci, Stewart Zweben, Denis St-Onge, Seung-Ho Ku, and Michael Churchill.

I thank Dan Ruiz for his consistent friendship over the year and being a great office mate. He probably would have graduated even sooner if he did not have me as an office mate to provide constant distractions. I am in awe of his personal integrity and ability to conjure original research ideas. I am also grateful to the friends I made at Princeton: Mike Hay, Jeff Parker, Seth Davidovits, Lee Ellison, Jake Nichols, Yao Zhou, Kenan Qu, Chang Liu, and Yuan Shi.

I thank Beth Leman, Barbara Sarfaty, and Jen Jones for shielding me from the host of complicated administrative details associated with being a graduate student at PPPL.

Lastly, I thank my family for their unconditional support. Rita, I would not have been so determined in my goals if I did not have an older sibling to show me what could be achieved. Mom and Dad, thank you for all the sacrifices you have made to help your children pursue their dreams. You have given me so much and have never asked for a single thing in return.

This work was funded by the U.S. Department of Energy under Contract No. DE-AC02-09CH11466, through the Max-Planck/Princeton Center for Plasma Physics and the Princeton Plasma Physics Laboratory. Some simulations in Chapters 4 and 5 were performed on the Perseus cluster at the TIGRESS high-performance computer center at Princeton University, which is jointly supported by the Princeton Institute for Computational Science and Engineering and the Princeton University Office of Information Technology's Research Computing department. Initial development on the simulations in Chapter 4 used the Edison system at the National Energy Research Scientific Computing Center, a DOE Office of Science User Facility supported by the Office of Science of the U.S. Department of Energy under Contract No. DE-AC02-05CH11231. The simulations in Chapters 4 and 5 also used the Extreme Science and Engineering Discovery Environment (XSEDE), which is supported by National Science Foundation grant number ACI-1548562.

To my parents.

Contents

Abstract	iii
Acknowledgements	iv
List of Tables	ix
List of Figures	x
1 Introduction	1
1.1 The Boundary Plasma	1
1.1.1 Basic Features of the SOL	3
1.1.2 Basic Plasma Physics Experiments	7
1.2 Boundary-Plasma Modeling	8
1.2.1 Fluid Modeling	10
1.2.2 Gyrokinetic Modeling	11
1.3 Thesis Overview	17
1.3.1 A Note on Color Maps	18
2 Models and Numerical Methods	21
2.1 Gyrokinetic Model	22
2.2 Discontinuous Galerkin Algorithms	24
2.2.1 DG for 1D Conservation Laws	26
2.2.2 DG for the Gyrokinetic System	30
2.3 Collision Operator	34
2.3.1 Second-Order Derivatives	36
2.3.2 Numerical Tests	40
2.4 Positivity of the Distribution Function	42
2.5 Sheath Boundary Conditions	45
2.5.1 Logical-Sheath Model	46
2.5.2 Conducting-Sheath Boundary Conditions	50
2.5.3 Future Considerations for Sheath Models	51
3 1D Scrape-Off-Layer Models	53
3.1 Introduction	53
3.2 Electrostatic 1D Gyrokinetic Model with Kinetic Electrons	55
3.2.1 Electrostatic Model with a Modified Ion Polarization Term	58
3.3 Numerical Implementation Details	61
3.4 Simulation Results	62
3.4.1 Initial Conditions	64

3.4.2	Divertor Heat Flux with Drift-Kinetic Electrons	66
3.4.3	Divertor Heat Flux with an Adiabatic-Electron Model	68
3.5	1D2V Model with Collisions	70
3.5.1	A Basic Recycling Model	73
3.6	Conclusions	75
4	Simulations of the Large Plasma Device	77
4.1	Simulation Parameters	79
4.2	Boundary Conditions and Energy Balance	82
4.3	Simulation Results	86
4.4	Limiter-Biasing Simulations	93
4.5	Conclusions	103
5	Simulations of a Helical Scrape-Off-Layer Model	107
5.1	Simulation Parameters	109
5.2	Simulation Results	115
5.3	Conclusions	128
6	Conservative Exponentially Weighted Basis Functions	131
6.1	The General Algorithm	133
6.2	1D Collision Operator Tests	137
6.3	A Classical-Heat-Transport Problem	140
6.4	Adjustment of the Exponential Weighting Factor	146
6.5	Conclusions	148
7	Summary and Future Directions	150
7.1	Summary	150
7.2	Future Directions	152
A	Plot Creation	156
B	Additional Comparisons Between ELM-Heat-Pulse Simulations	158
C	Numerical Energy Conservation in LAPD Simulations	162
D	Initial Conditions for Helical-SOL Simulations	165
E	Estimates of Interchange Instability	168
E.1	Basic Interchange Instability	168
E.2	Addition of Sheath Effects	170
Bibliography		174

List of Tables

3.1	Summary of parameters for the ELM-heat-pulse simulations.	63
3.2	Parameters for the phase-space grid used in 1D2V ELM heat-pulse simulations.	70
3.3	Summary of results from various simulations of the 1D ELM-heat-pulse problem.	73
3.4	Parameters for the phase-space grid used in 1D2V SOL recycling simulations.	74
4.1	Summary of input parameters used in LAPD simulations.	80
4.2	Parameters for the phase-space grid used in LAPD simulations. . . .	80
4.3	Some time and length scales of interest for characterizing the LAPD plasma.	81
5.1	Summary of simulation parameters for helical-SOL simulations. . .	111
5.2	Parameters for the phase-space grid used in helical-SOL simulations. .	112
5.3	Summary of helical-SOL simulation results with comparison to experimental values in the SOL.	129

List of Figures

1.1	Illustration of the core, edge, and SOL regions in a diverted tokamak.	2
1.2	Profiles of the steady-state D α light emission and corresponding fluctuation levels measured using gas puff imaging in the boundary of an H-mode NSTX plasma.	4
1.3	Sequence of GPI images from an H-mode NSTX plasma showing the ejection of a plasma blob across the LCFS into the SOL.	5
1.4	Outer-midplane SOL heat-flux width versus outer-midplane poloidal magnetic field for a multi-machine database of low-recycling H-mode discharges.	6
1.5	Comparison of electron-density snapshots from gyrokinetic simulations of LAPD using the rainbow color map and a perceptual color map.	20
2.1	Illustration of how a recovery polynomial that spans two neighboring cells is constructed using the DG solution from both cells.	38
2.2	Illustration of how 1D recovery polynomials are constructed for the evaluation of diffusion terms in 2D.	40
2.3	Initial and final distribution function for the collision operator benchmark with $T_{\text{tar}} = 3$ eV.	41
2.4	Time evolution of the relative error in number, momentum, and energy for a collision operator test.	41
2.5	Comparison of initial and final distribution function for the collision operator test with $T_{\text{tar}} = 1$ eV.	42
2.6	Negative regions in the distribution function after evolution to a steady state by the self-species collision operator.	43
2.7	Illustration of the potential structure near a plasma–material interface.	46
2.8	Application of sheath boundary conditions to an incident electron distribution function.	48
2.9	Illustration of how the sheath model boundary conditions use ghost cells to set the reflected distribution function.	49
3.1	Geometry used in the ELM heat-pulse test problem.	56
3.2	Spatial and temporal profiles of the source term used in the ELM heat-pulse test problem.	64
3.3	Parallel heat flux at the divertor plate versus time with drift-kinetic electrons in the ELM heat-pulse problem.	67

3.4	Comparison of the parallel heat flux at the divertor plate versus time obtained from a Gkeyll simulation and a GENE simulation.	69
3.5	Parallel heat flux at the divertor plate versus time from the adiabatic-electron model in the ELM heat-pulse problem.	70
3.6	Snapshots of the electron-density and electrostatic-potential profiles for a 1D2V ELM heat-pulse simulation with collisions.	71
3.7	Comparison of the total, electron, and ion parallel heat fluxes at the divertor plate versus time for 1D2V cases with and without collisions.	72
3.8	Comparison of the sheath-potential time history between 1D2V ELM heat-pulse simulations with and without same-species Lenard-Bernstein collisions.	72
3.9	Source profiles for the recycling simulations.	75
3.10	Steady-state profiles of the electron density, electron temperature, and ion temperature for different values of the recycling coefficient from 1D2V SOL simulations.	75
4.1	Diagram showing a side view of the LAPD device.	77
4.2	Normalized r.m.s. I_{sat} fluctuation level as a function of radius and I_{sat} fluctuation power spectral density as measured in an experiment on LAPD.	79
4.3	LAPD-simulation density source rate in the x - z plane.	83
4.4	LAPD-simulation density source rate and temperature of source electrons in the x - y plane.	83
4.5	Snapshots of the total electron density in the x - y plane from a 5D gyrokinetic simulation of an LAPD plasma at three times.	87
4.6	Snapshots in the x - y plane of the total electron density, electron temperature, and electrostatic potential from a 5D gyrokinetic simulation of an LAPD plasma.	88
4.7	Time-averaged radial profile of the ion-outflow Mach number across each parallel boundary and total outflow of electron and ion guiding centers across the parallel boundaries during a quasi-steady state.	88
4.8	Snapshots in the x - z plane of the total electron density, electron temperature, and electrostatic potential from a 5D gyrokinetic simulation of an LAPD plasma.	89
4.9	Average profiles of electron density, electron temperature, and electrostatic potential as a function of radius from a 5D gyrokinetic simulation of an LAPD plasma.	90
4.10	Profiles of the time-averaged radial particle flux due to electrostatic fluctuations and total outward parallel particle flux at end plates.	91
4.11	Normalized r.m.s. density fluctuation level as a function of radius and density-fluctuation power spectral density computed from a 5D gyrokinetic simulation of an LAPD plasma.	92
4.12	Density-fluctuation-amplitude PDF at three radial locations from a 5D gyrokinetic simulation of an LAPD plasma.	92

4.13	Radial profile of the r.m.s. current fluctuation amplitude at the sheath entrances.	93
4.14	Passive-imaging measurements of visible light from a LAPD discharge before and after limiter biasing is turned on.	94
4.15	The $\phi_w(x, y)$ fields used in the sheath-model boundary conditions to model limiters biased at three different voltages.	96
4.16	LAPD-simulation density source rate in the $x-z$ plane with additional annotations to indicate biasable-limiter locations.	97
4.17	Snapshots of the electrostatic potential in three LAPD simulations with different values of limiter biasing.	98
4.18	Snapshots of the electron density in the $x-y$ plane at for a simulation of an LAPD plasma with +15 V limiter biasing.	99
4.19	Comparison of the time-averaged radial particle fluxes due to $E \times B$ fluctuations and the time-averaged total outward parallel particle fluxes for simulations with different values of limiter biasing.	100
4.20	Comparison of the radial profiles of the background electrostatic potential, background electron density, and r.m.s. electron-density fluctuation levels for three LAPD simulations with different values of limiter biasing.	101
4.21	Comparison of the total radial-particle-flux integrands, cosine of cross phases, and coherence spectra for three LAPD simulations with different values of limiter biasing.	104
4.22	Comparison of the electric-field-fluctuation power spectral densities and the density-fluctuation power spectral densities for three LAPD simulations with different values of limiter biasing.	104
5.1	Illustration of the basic tokamak region approximated by the helical-SOL simulation domain.	108
5.2	Illustrations of 2D simulation flux surfaces for two cases with different magnetic-field-line incidence angles.	110
5.3	Helical-SOL-simulation density source rate and temperature of the electron and ion sources in the perpendicular $x-y$ plane.	113
5.4	Helical-SOL-simulation density source rate in the $x-z$ plane.	114
5.5	Snapshots of the electron density at various times near the beginning of a 5D gyrokinetic simulation of a helical SOL.	115
5.6	Average density of ions and electrons vs. time for three simulations with different magnetic-field-line pitches.	116
5.7	Snapshots of the electron density, electron temperature, and electrostatic potential from the quasi-steady state of a 5D gyrokinetic simulation of a helical SOL.	117
5.8	Comparison of an electron density snapshot between a simulation in a helical-magnetic-field-line geometry and a simulation in a straight-magnetic-field-line geometry.	118

5.9	Radial profiles of the background electron densities, normalized-electron-density fluctuation levels, and radial $E \times B$ particle fluxes for a helical SOL simulation and a straight-field-line simulation.	119
5.10	Comparison of electron-density profiles and fluctuation statistics for cases with varying electron mass.	120
5.11	Comparison of the steady-state parallel heat flux normal to the divertor plate for cases with different magnetic-field-line pitches.	121
5.12	Comparison of the radial $E \times B$ particle flux evaluated near the mid-plane for cases with different magnetic-field-line pitches.	122
5.13	Comparison of the electron-density fluctuation statistics and electrostatic-potential fluctuation statistics computed near the midplane for cases with different magnetic-field-line pitches.	123
5.14	Radial profiles of the steady-state ion and electron temperatures and ion-to-electron temperature ratios near the midplane for cases with different magnetic-field-line pitches.	124
5.15	Comparison of the parallel structure of the normalized r.m.s. electron-density fluctuation amplitude for cases with different magnetic-field-line pitches.	125
5.16	Comparison of the cross-coherence between $e\phi_{mid}/T_e$ and $e\phi_{sh}/T_e + \ln(n_{mid}/n_{sh})$ for cases with different magnetic-field-line pitches. . . .	126
5.17	Radial profiles of the autocorrelation times and correlation lengths for cases with different magnetic-field-line pitches.	127
5.18	Radial profiles of the steady-state parallel currents into the sheaths for cases with different magnetic-field-line pitches.	128
6.1	Comparison of standard polynomial basis functions (Legendre polynomials) with a set of exponentially weighted basis functions.	135
6.2	Comparison of the steady-state solutions to a collision operator test in μ using three DG methods.	139
6.3	Comparison of the number and energy-conservation properties of various DG methods using polynomial and exponentially weighted basis functions for collision-operator test in μ	140
6.4	Comparison of the steady-state solutions to a collision operator problem in $v_{ }$ using two DG methods.	141
6.5	Comparison of the number, momentum, and energy-conservation properties of conservative DG methods using quadratic-polynomial and exponentially weighted basis functions for a collision-operator test in $v_{ }$	141
6.6	Time evolution of the heat flux in simulations using polynomial and exponentially weighted polynomials at various grid resolutions.	144
6.7	Relative error in the steady-state heat flux versus effective cell size for various numerical methods.	145
6.8	Illustration of the normalized integrands for the calculation of a few moments of a Maxwellian distribution.	145
6.9	Calculation of an exponentially weighted approximation space from a specified initial condition.	147

A.1	Illustration of the image-creation procedure for a DG solution.	157
B.1	Comparison of the total parallel heat flux at the divertor plate versus time for 1D2V ELM-heat-pulse simulations with and without collisions.	158
B.2	Comparison of the total energy and electron and ion contributions between 1D2V ELM-heat-pulse simulations with and without same-species Lenard–Bernstein collisions.	161
C.1	Time traces of diagnostics tracking power sources and sinks in a LAPD simulation.	164
C.2	Time traces of power-error diagnostics in a LAPD simulation.	164

Chapter 1

Introduction

1.1 The Boundary Plasma

On a basic level, the plasma in a tokamak can be separated into core, edge, and scrape-off-layer (SOL) regions.¹ These regions are indicated in figure 1.1, which shows a poloidal cross section of a diverted tokamak plasma. The core is the hot, innermost region at the center of the plasma where fusion power is produced. Profile scale lengths in the core are on the order of the plasma minor radius, and a temperature ~ 10 keV is required to reach the break-even condition for D–T fusion (Kaw & Bandyopadhyay, 2012). The edge is a thin layer surrounding the core often characterized by steep pressure gradients (Stoltzfus-Dueck, 2009; Zweben *et al.*, 2007; Boedo *et al.*, 2009) and temperatures ~ 100 eV. In the high-confinement mode (H-mode), first discovered by Wagner *et al.* (1982), a strong sheared poloidal flow correlated with a reduction in edge turbulence levels is generically observed in the edge. The physics behind the generation of this sheared flow layer and the subsequent reduction of turbulent fluxes have received much attention over the years (Wagner, 2007; Connor & Wilson, 2000; Terry, 2000). In the core and edge, the magnetic field lines trace out nested, closed flux surfaces. Charged particles, which rapidly flow along the field lines, are therefore confined in these regions. Turbulence or collisions with other particles cause transport across these flux surfaces.

While a significant fraction of the tokamak plasma lies in the core and edge, there exists a region outside the edge called the SOL where the magnetic field lines no longer trace out closed flux surfaces and instead intersect material walls after winding around toroidally a number of times (in practice it is not possible to create a magnetic field with field lines that are perfectly tangential to the wall at every point (Strangeby, 2000; Ricci, 2015)). Charged particles in the SOL are therefore rapidly lost to material surfaces in contact with the magnetic field lines, where recombination occurs. On a basic level, the SOL properties are set through a balance between plasma outflow from the edge, cross-field turbulent transport, and strong parallel losses at

¹Note that authors sometimes collectively refer to the edge and SOL as indicated in figure 1.1 as the edge. For this thesis, it is important to distinguish between these two regions, so the term ‘boundary plasma’ is used to refer to the collective edge and SOL plasma.

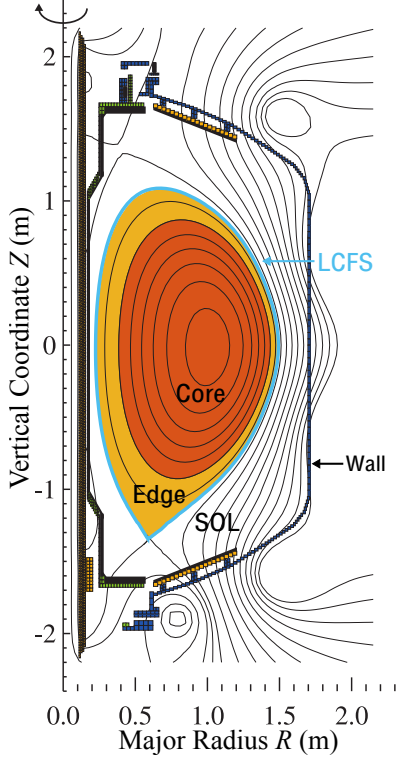


Figure 1.1: Illustration of the core, edge, and SOL regions in a diverted tokamak. The LCFS separating the edge and SOL is indicated by the blue line. The separation between the core and edge regions is less well defined. The black curves are magnetic flux surfaces from the EFIT magnetic reconstruction of an NSTX shot. The flux surfaces in the confined core and edge are closed, while the flux surfaces in the SOL are open. This figure was adapted with permission from [Stoltzfus-Dueck \(2009, figure 1.1\)](#).

the divertor or limiter plates ([Ricci et al., 2015; Mosetto, 2014](#)), where a Debye sheath layer forms to keep electron and ion particle fluxes to the wall approximately equal. Plasma–surface interactions (PSIs) such as recycling and impurity influx are also important in setting the particle and power balances in the SOL. Due to plasma–wall interactions, the SOL plasma is much colder ($T_e \sim 10\text{--}100$ eV ([Zweben et al., 2007; Stangeby, 2000; Stoltzfus-Dueck, 2009](#))) than the core and edge plasmas. The SOL and edge are separated by a boundary referred to as the *last-closed flux surface* (LCFS).

The properties of the boundary plasma constrain the performance and component lifetime of tokamak fusion reactor by affecting both the details of how heat is exhausted in the SOL as well as how much fusion power can be generated in the core, assuming that core profiles are stiff ([Kotschenreuther et al., 1995; Doyle et al., 2007; Kardaun et al., 2008](#),). A thorough understanding of the physics of boundary plasma is therefore key to improving the overall viability of the tokamak concept, but there are still many gaps in our present understanding that need to be filled in before ITER begins the very long-awaited D–T operations in ~ 2035 . Given the complexities

of edge and SOL turbulence, numerical simulations have become important in furthering our theoretical understanding of the boundary plasma. This thesis attempts to add to this line of research by developing gyrokinetic simulations of turbulence in open-field-line (as in the SOL) plasmas using a class of grid-based ('continuum' or 'Eulerian') numerical methods. In this introduction, we briefly review some basic features of the SOL and motivate the usefulness of gyrokinetic simulations as a tool to address important boundary-plasma physics questions in present-day and future tokamaks.

1.1.1 Basic Features of the SOL

The SOL plasma is defined as the plasma in the region extending from the LCFS to the material wall. Since the SOL plasma is in direct contact with solid surfaces, PSIs that lower plasma temperatures through radiative processes are inevitable (Stangeby, 2000). Just outside the LCFS, the SOL features steep exponential profiles and near-Gaussian probability distribution functions (PDFs). As one goes farther out radially in the SOL from the LCFS, the profiles become slowly decreasing or flat, and the PDFs become increasingly non-Gaussian (Zweben *et al.*, 2007). Relative electron density fluctuation levels in the SOL are also fairly large, increasing from $\sim 5\%$ near the LCFS to $\sim 100\%$ near the first wall (Zweben *et al.*, 2007). Figure 1.2 shows typical profiles of the D α light emission measured in the boundary plasma on NSTX using a gas puff imaging (GPI) diagnostic (Zweben *et al.*, 2017). The D α light emission is influenced by the neutral D₂ gas-puff density, the local electron density, and the local electron temperature (Zweben *et al.*, 2017), but the relative fluctuation levels should mostly be set by plasma fluctuations.

On the open magnetic field lines in the SOL, charged particles rapidly flow along the field lines towards solid surfaces (e.g., walls, limiters, divertors), where they recombine and are lost (Chen, 1984). Since electrons are much more mobile than ions, they initially are lost to the surfaces in contact with the magnetic field lines faster than the ions, leaving the plasma with a thin layer of net positive charge, which is confined to a layer at the plasma–material boundary a few Debye lengths wide due to Debye shielding. This layer is called the *electrostatic Debye sheath* (Stangeby, 2000; Chen, 1984) and its primary purpose is to establish a potential barrier that repels incident electrons and accelerates incident ions into the surface, keeping the particle fluxes of electrons and ions lost to the surfaces approximately equal. The plasma itself maintains quasineutrality. Only electrons with sufficient parallel velocity can surmount the sheath potential drop to reach the surface. The sheath plays an important role in governing both the properties of the SOL plasma and how particles and energy are lost to solid surfaces.

As charged particles in the SOL rapidly flow along field lines to solid surfaces through parallel motion, they also undergo a much slower but non-negligible motion across the magnetic field. As in the core, this cross-field transport is dominated by turbulence, but unlike the core, a significant fraction of the cross-field transport in the SOL (Boedo, 2009; Boedo *et al.*, 2003) is due to the radial convection of coherent structures called *blobs* or *filaments* (Zweben *et al.*, 2004; Terry *et al.*, 2007;

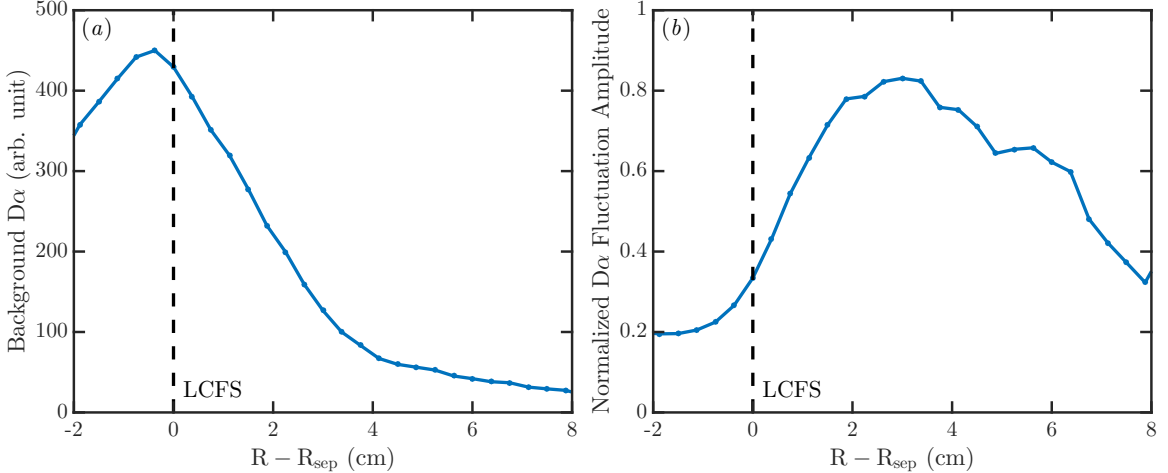


Figure 1.2: (a) Radial profile of the steady-state D α light emission measured in the outer midplane of an H-mode NSTX plasma (Discharge 138844). (b) Radial profile of the locally normalized root mean square D α -light-emission fluctuation amplitude showing large relative fluctuation levels in the edge and SOL. The LCFS inferred from the EFIT magnetic reconstruction is indicated by the dashed line. These profiles are obtained by averaging over a vertical band in the GPI images over a 10 ms period. The GPI camera records images at a rate of $\sim 4 \times 10^5$ frames/s. S. Zweben provided the data for these plots.

[Boedo et al., 2014](#); [Zweben, 1985](#); [Zweben & Gould, 1985](#)). Plasma blobs are highly elongated along the field line, with typical parallel scales $\sim 1\text{--}10$ m due to the rapid parallel motion of charged particles and much smaller cross-field scales $\sim 1\text{--}10$ cm ([Zweben et al., 2017](#)). Blobs have elevated densities and/or temperatures compared to the background plasma. Although the blob-formation mechanisms are not as well-understood as their transport mechanisms ([Krasheninnikov, 2016](#)), they are commonly observed to form in the edge, from where they are ejected across the LCFS into the SOL ([Boedo et al., 2003](#); [Terry et al., 2003](#); [Zweben et al., 2004](#)). Cross-field transport in the SOL is highly intermittent due to blob propagation ([Zweben et al., 2007](#)) and is consequently poorly described in terms of effective diffusion coefficients and convective velocities ([Naulin, 2007](#)).

Figure 1.3 shows raw camera images from a GPI diagnostic viewed along the local magnetic field direction near the outer midplane of the NSTX tokamak. These images show the 2D cross-field blob structure of a 3D plasma filament as it is ejected across the LCFS into the SOL. The standard picture of blob propagation involves the polarization of a blob by the curvature drift, which self-generates a vertical electric field across the blob that results in a radially outward $E \times B$ drift ([Krasheninnikov, 2001](#); [Krasheninnikov et al., 2008](#); [Grulke et al., 2006](#)). The efficient and fast convective radial transport of blobs towards the main chamber walls (instead of along the field lines to the divertor) can result in damage to first-wall components and the contamination of the core plasma by wall impurities ([Rudakov et al., 2005](#); [Terry et al., 2007](#)), which lowers the plasma temperature through radiative cooling. Both

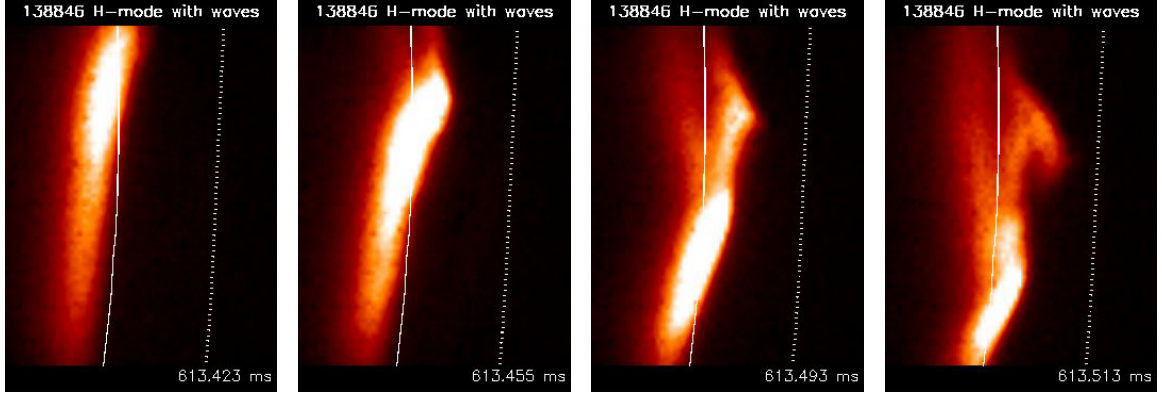


Figure 1.3: Sequence of GPI images from an H-mode NSTX plasma (Discharge 138846) showing the ejection of a plasma blob across the LCFS into the SOL. These images show the raw camera data taken near the outer midplane, covering a $24\text{ cm} \times 30\text{ cm}$ region. The LCFS is indicated by the solid line and is inferred from the EFIT magnetic reconstruction, while the dotted lines indicate the limiter shadow. The horizontal axis is the radially outward direction, and the vertical axis is the upward direction. These images are used with permission from S. Zweben (<http://w3.ppl.gov/~szweben/NSTX2013/NSTX2013.html>).

the generation of blobs in the edge and the structure and motion of blobs in the SOL (Zweben *et al.*, 2016, 2006) are ongoing research topics of practical interest.

Particle and Heat Loss in the SOL

The loss of particles and heat in the SOL to plasma-facing components (PFCs) is a major concern for future high-power devices like ITER (Lipschultz *et al.*, 2012) and Demo because a significant fraction ($\sim 20\%$) of the heat produced in the core is transported across the LCFS into the SOL by convection and conduction (Loarte *et al.*, 2007), where the heat must be exhausted somehow. The unmitigated steady-state parallel heat flux in the SOL is expected to be $\sim 1\text{ GW m}^{-2}$ for ITER (Loarte *et al.*, 2007) and $\sim 20\text{ GW m}^{-2}$ for Demo (Goldston, 2015), while material limitations set the maximum tolerable heat flux normal to the divertor plates at $\sim 10\text{ MW m}^{-2}$ for steady-state and $\sim 20\text{ MW m}^{-2}$ for transients (Loarte *et al.*, 2007), such as from disruptions and edge-localized modes. An often-quoted comparison in the fusion community is the transient heat flux of approximately 6 MW m^{-2} experienced by some components of a space vehicle during atmospheric reentry. The use of an extremely shallow incidence angle between the divertor plates and field lines ($\sim 2\text{--}5^\circ$) significantly reduces the heat flux normal to the divertor plates, but up to $\sim 95\%$ of the power (Goldston, 2015) may need to be dissipated in the SOL through various means before reaching the divertor plates to bring normal heat fluxes down to tolerable levels. Strategies to reduce the heat load on the divertor plates are still under development and include radiative divertor detachment (Soukhanovskii, 2017), advanced divertor geometries (Kotschenreuther *et al.*, 2016; Ryutov *et al.*, 2008; Valanju *et al.*,

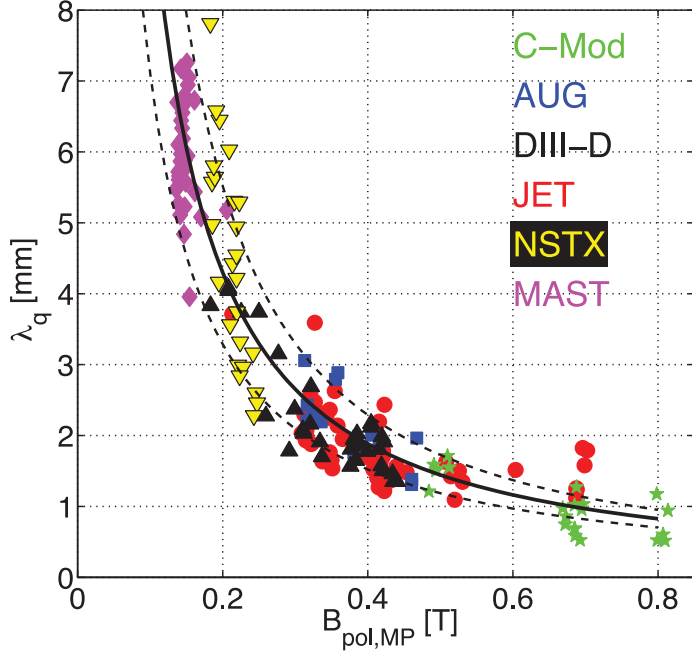


Figure 1.4: Outer-midplane SOL heat-flux width λ_q versus outer-midplane poloidal magnetic field B_{pol} for a multi-machine database of low-recycling H-mode discharges. The value of λ_q is inferred from infrared thermography measurements made at the outer divertor target. The regression $\lambda_q \text{ (mm)} = (0.63 \pm 0.08) \times B_{\text{pol}}^{-1.19 \pm 0.08}$ is indicated by the solid and dashed lines. Regression studies indicate that λ_q decreases approximately linearly with the value of B_{pol} and has much weaker dependencies on other machine parameters, including machine size. Figure reprinted from [Eich et al. \(2013, figure 3\)](#) with permission. Copyright © 2013 by the IAEA.

2009), and applied resonant magnetic perturbations ([Ahn et al., 2010; Evans et al., 2005; Jakubowski et al., 2009](#)).

The heat fluxes on the ITER divertor targets are believed to be enormous because experiments on present-day machines indicate that the heat exhausted into the SOL flows towards the divertor plates in an extremely narrow channel whose width at the outer midplane (quantified as an exponential decay length) is insensitive to the machine size ([Loarte et al., 2007; Makowski et al., 2012; Eich et al., 2013](#)). There exists major uncertainty about the validity of empirical extrapolations to ITER, however. The amount of power spreading along the ITER divertor legs is also not well understood (empirically or theoretically), and it is possible that power-spreading effects on ITER will be principal in setting the heat-flux width at the divertor plates, making such considerations of the midplane heat-flux width unimportant for predicting divertor-plate heat loads. Presumably, the location and strength of heat loads deposited on PFCs is set through a balance between confined plasma outflow across the LCFS, parallel losses at the sheaths, and cross-field turbulent or neoclassical transport in the SOL. Therefore, credible numerical investigations of the SOL heat-flux width require the use of sophisticated turbulence codes.

Figure 1.4 shows a plot from Eich *et al.* (2013) of the outer-midplane SOL heat-flux width λ_q versus the outer-midplane poloidal magnetic field B_{pol} computed from a multi-machine database of low-recycling H-mode tokamak discharges. In that study, the outer-midplane heat-flux width for each discharge was determined as a fit parameter to match infrared thermography measurements of the heat-flux profile at the outer divertor target (Eich *et al.*, 2011). Eich *et al.* (2013) found that “the strongest and essentially only dependence amongst the regression variables tested, at least for the conventional aspect ratio tokamaks, is an inverse scaling with plasma current (or equivalently [an inverse] dependence on outboard midplane poloidal magnetic field)”. Eich *et al.* (2013) and Makowski *et al.* (2012) also extrapolated the scaling to the ITER H-mode diverted plasma, finding an outer-midplane SOL heat-flux width of ≈ 1 mm, much smaller than the 5 mm value used in ITER design specifications and the 3.6 mm value from transport modeling (Kukushkin *et al.*, 2013). Goldston (2012) developed a heuristic drift-based (HD) model of the SOL heat-flux width that was consistent with the results of Eich *et al.* (2013) and Makowski *et al.* (2012). The HD model notably does not attempt to include turbulence, which could spoil its extrapolation to new parameter regimes (such as the ITER SOL).

It is important to study the heat-flux-width problem using turbulence simulations to provide a first-principles-based check of the empirical predictions and to investigate ways to broaden the heat-flux width, such as by increasing turbulent heat transport along the divertor legs. A recent electrostatic gyrokinetic simulation predicted the outer-midplane heat-flux width on ITER to be approximately 5.6 mm (Chang *et al.*, 2017), but no other gyrokinetic codes currently have the capability to cross-check this result. More research is required to understand the physics setting the SOL heat-flux width (at both the outer midplane and at the divertor plates), the validity of such empirical extrapolations to ITER, and the implications of such a narrow width on divertor-plate heat loads (Goldston, 2015).

1.1.2 Basic Plasma Physics Experiments

While experimental measurements of the SOL plasma in tokamaks have been highly successful in improving our understanding of SOL turbulence (Zweben *et al.*, 2007; Tynan *et al.*, 2009), the complicated physics situation in a tokamak can make detailed comparisons of analytical theories and numerical simulations with experimental data extremely challenging. Fortunately, there are a number of basic plasma physics experiments that produce highly reproducible, well-diagnosed plasmas in simple, open-magnetic-field-line configurations. Measurements of turbulence and transport in these laboratory plasma devices can shed light on topics of relevance to tokamak plasmas, such as sheared-flow suppression of turbulence (Carter & Maggs, 2009; Schaffner *et al.*, 2013; Gentle *et al.*, 2010), turbulence intermittency (Carter, 2006; Windisch *et al.*, 2011), and turbulence saturation. The plasmas are usually relatively cold ($T_e \sim 10$ eV) and low pressure ($\beta \sim 10^{-4}$), so electrostatic 3D fluid simulations are commonly used to study the turbulence in basic plasma physics experiments (Friedman *et al.*, 2013; Ricci & Rogers, 2009; Rogers & Ricci, 2010; Naulin *et al.*, 2008). Although the plasmas created in these devices are not in the same parameter regime

as fusion plasmas, the free energy sources, dissipation mechanisms, and nonlinear transfer processes identified in these devices may be generic and thus relevant to tokamaks ([Tynan *et al.*, 2009](#); [Fasoli *et al.*, 2006](#)).

Linear devices create a column of plasma in a uniform, axial background magnetic field. Some examples of linear devices include LAPD ([Gekelman *et al.*, 1991, 2016](#)), CSDX ([Burin *et al.*, 2005](#); [Thakur *et al.*, 2014](#)), VINETA ([Franck *et al.*, 2002](#)), Hel-Cat ([Gilmore *et al.*, 2015](#)), and Mirabelle ([Pierre *et al.*, 1987](#); [Brandt *et al.*, 2011](#)). Turbulence in linear devices is typically driven by temperature or density profile gradients (drift-wave instabilities). Toroidal basic plasma physics devices, called *simple magnetized tori* (SMTs), create a magnetic geometry composed of helical magnetic field lines (a superposition of vertical and toroidal magnetic fields) that intersect the vessel on each end. Compared to linear devices, the turbulence and transport in SMTs are more relevant to a tokamak SOL because they can also be driven by magnetic-field-line-curvature effects, which are important in the generation of blobs (as we will see in Chapter 5). Examples of SMTs include TORPEX ([Fasoli *et al.*, 2006](#)) and Helimak ([Gentle & He, 2008](#)).

The relative simplicity, availability of detailed diagnostics, and ease of parameter scans in basic plasma physics experiments also facilitates comparisons between simulations and experiments. The Global Braginskii Code (GBS) has been used to perform rigorous validation studies with data from TORPEX ([Ricci *et al.*, 2015, 2011, 2009](#)). In the development of complex numerical codes, comparisons with basic plasma physics experiments can be made relatively early on with a minimal set of features implemented in the code to benchmark and test the models and numerical algorithms in a physically relevant setting. We adopt this strategy in this thesis, where we first simulate turbulence in LAPD to test 5D gyrokinetic continuum simulations before adding additional levels of complexity.

1.2 Boundary-Plasma Modeling

Due to the complications of the edge and SOL, numerical simulations have become an important tool for elucidating the physics of the boundary plasma. The use of a particular simulation can be classified as interpretive, predictive, or generic ([Mitchell *et al.*, 2000](#)). Since these classifications are seldom explained in plasma-physics literature, and sometimes incorrectly applied, we first provide a brief description of the different types of modeling.

Interpretive modeling. To aid in experimental analysis and physical understanding, interpretive modeling uses simulations with data collected from an experiment as inputs to estimate other variables described by reduced models. These estimated variables are often difficult or impossible to measure in the actual experiment due to diagnostic limitations. Some interpretive models have several free parameters that can be tuned automatically so that a subset of the output data matches the corresponding experimentally measured data (e.g., density and temperature profiles), making it straightforward (but somewhat questionable) to run additional simulations in a predictive manner by using hypothetical initial conditions and

plasma parameters (Ricci, 2015). These tools have become standard in analyzing data from tokamak discharges to infer transport levels and energy confinement. Since interpretive simulations are limited by the fidelity of the underlying reduced models (which can be empirical rather than physics based) and by the availability and quality of experimental data, caution must be used when drawing physics conclusions based on interpretive simulations and when extrapolating the models to parameter regimes that are outside the range of demonstrated validity.

Predictive modeling. As their name suggests, the goal of predictive models is to make quantitative predictions about the physics given a collection of initial conditions and assumptions (e.g., plasma sources, boundary conditions, fluid vs. kinetic description). They are particularly valuable for testing and improving interpretive models and predicting the plasma behavior in situations that cannot be investigated by experiments (such as in future fusion reactors like ITER). The use of free parameters in predictive models should be minimized, and the insensitivity of results to specific values of the model free parameters must be verified. Ideally, predictive simulations should solve first-principles equations without *ad hoc* terms and empirical models (Barnes, 2008; Candy *et al.*, 2009; Görler *et al.*, 2014). However, such first-principles simulations for a given application (e.g., turbulence on transport time scales) can be computationally infeasible even on state-of-the-art high-performance computers, in which case reduced models must be used in some capacity (Kotschenreuther *et al.*, 1995; Staebler *et al.*, 2007; Kinsey *et al.*, 2011). A code that can make quantitatively accurate predictions of the boundary plasma is likely to require a high degree of sophistication, having models of the numerous PSIs that occur in the SOL. An example of a boundary-plasma predictive simulation is the use of the XGC1 gyrokinetic PIC code to calculate the SOL heat-flux width in ITER (Chang *et al.*, 2017), although this is a prediction that cannot be validated for many years. Predictive simulations for high-fusion-power ITER regimes are particularly valuable because mistakes in the design of ITER based on our understanding of existing experiments can result in irreparable damage to the machine and to the overall ITER project.

Generic modeling. Generic modeling concerns the modeling of hypothetical situations, often with a number of highly simplifying assumptions. This type of modeling is useful for helping assemble a theoretical picture to explain observed phenomena and for testing the theoretical models of others using first-principles simulations. Since the purpose is neither to analyze a particular experiment nor to make definite predictions, sophisticated physics models that are essential for accurate predictive modeling can be neglected, which reduces the computing requirements and code complexity. Some uses of generic modeling for the boundary plasma include understanding the low-to-high confinement-mode (L–H) transition in tokamaks (Connor & Wilson, 2000), which is a rapid bifurcation between two plasma states associated with the formation of an edge transport barrier. Many studies of the mechanisms driving turbulence in the edge and SOL also employ generic modeling (Scott, 2005a; Ribeiro & Scott, 2008; Halpern *et al.*, 2016). The simulations that are presented in this thesis also fall into this category.

1.2.1 Fluid Modeling

Fluid-based codes have been and still are commonly used to model the boundary plasma. One class of these codes solves simplified transport equations based on the Braginskii fluid equations in two dimensions assuming axisymmetry. Plasma turbulence is not captured in these models, so the use of *ad hoc* anomalous diffusion terms (Dekeyser *et al.*, 2011) or coupling to a turbulence code (Schneider *et al.*, 2006; Rognlien *et al.*, 2004) is required to model the turbulent transport across the magnetic field. Perhaps the most widely used of these fluid plasma transport codes is the SOLPS package (Schneider *et al.*, 1992; Rozhansky *et al.*, 2009), which contains a 2D boundary-plasma transport component coupled to a kinetic Monte Carlo model for neutral transport (Reiter *et al.*, 2005). SOLPS has become the standard tool used for ITER divertor and boundary-plasma modeling (Wiesen *et al.*, 2015). Some physics models implemented in SOLPS include impurities, charge-exchange, ionization, radiation, and sputtering. Other boundary-plasma transport codes which also solve similar equations include UEDGE (Rognlien *et al.*, 1999, 1994) and EDGE2D (Simonini *et al.*, 1994). Although interpretive transport codes have become packed with features over decades of development, incorporating many sophisticated models for physics believed to be relevant in the boundary plasma (Schneider & Runov, 2007), the basic fact that they often do not capture plasma turbulence self-consistently makes it questionable to use them in a predictive capacity, especially as a principal tool for quantitative modeling of the challenging SOL in ITER, a machine which costs \sim US\$20 billion just to construct (Kramer, 2016). Some shortcomings of fluid plasma transport codes for boundary-plasma modeling are discussed by Boedo *et al.* (2009).

Boundary-plasma turbulence codes solving drift-ordered fluid equations (Zeiler *et al.*, 1997; Simakov & Catto, 2003; Scott, 1997; Xu & Cohen, 1998) in two or three dimensions have also been developed (Ricci *et al.*, 2008; Dudson *et al.*, 2009; Naulin *et al.*, 2008; Xu *et al.*, 2000, 2008; Tamain *et al.*, 2010), although many codes employ approximations or omit physics that might have significant effects on the results, such as neglecting adiabatic coupling² by dropping electron pressure in the Ohm's law (Park *et al.*, 2015; Li *et al.*, 2016, 2017; Garcia *et al.*, 2006; Beyer *et al.*, 2011), neglecting geodesic coupling³ (Bisai *et al.*, 2005; Li *et al.*, 2016, 2017; Shurygin, 2001), or assuming cold ions ($T_i/T_e \approx 1-4$ is typically observed just outside the LCFS and increases with radius in the SOL (Kočan *et al.*, 2011)). Their underlying models are usually derived by applying a low-frequency approximation to the Braginskii equations in which the gyrofrequencies are ordered fast compared to the frequencies of interest (Scott, 2003; Zeiler *et al.*, 1997). Since plasma turbulence is captured in these codes, they avoid one of the major drawbacks of transport codes at the cost of increased computational expense.

² Adiabatic coupling refers to the coupling of density and pressure through the parallel current (Stoltzfus-Dueck, 2009). The importance of retaining the adiabatic response for capturing the correct qualitative character of boundary-plasma turbulence has been emphasized by Scott (2007a, 2006b, 2005a) and for L-H-transition physics by Stoltzfus-Dueck (2016)

³The importance of retaining the geodesic coupling effect for zonal-flow dynamics in a toroidal geometry has been emphasized by Scott (2005b).

There are also boundary-plasma turbulence codes that solve 3D electromagnetic gyrofluid equations (Ribeiro & Scott, 2005, 2008; Xu *et al.*, 2013; Kendl *et al.*, 2010), which are more robust than drift-ordered fluid equations and model finite-Larmor-radius and Landau-damping effects (Dorland & Hammett, 1993; Snyder *et al.*, 1997). Gyrofluid codes have models for the treatment of dynamics on the ion-gyroradius scale and smaller, a regime in which drift-ordered fluid equations break down (Scott, 2007b,a). Both fluid and gyrofluid turbulence codes have yielded many insights into edge and SOL turbulence, but attempts to make quantitative comparisons with experimental data from tokamaks are rare and have produced mixed results (Zweben *et al.*, 2009; Halpern *et al.*, 2017, 2015; Cohen *et al.*, 2013). These codes keep just a few moments and cannot fully capture potentially important kinetic effects, such as trapped particles (Lackner *et al.*, 2012), nonlinear wave-particle interactions, and suprathermal electrons, and their model assumptions can be violated in edge and SOL plasmas (Bativschchev *et al.*, 1997; Takizuka, 2017). While fluid and gyrofluid models have been useful in revealing the qualitative physics of the boundary plasma, satisfactory and reliable quantitative prediction of boundary-plasma properties are believed to require the use of kinetic simulations in some capacity (Cohen & Xu, 2008; Scott *et al.*, 2010; Scott, 2003), including the direct or indirect coupling of a fluid transport code to kinetic turbulence code (Schneider & Runov, 2007).

For these reasons, there are efforts to develop first-principles gyrokinetic codes for boundary-plasma turbulence simulation (Chang *et al.*, 2009; Shi *et al.*, 2017; Dorf *et al.*, 2016; Korpilo *et al.*, 2016). Unlike drift-reduced Braginskii-fluid approaches, gyrokinetic approaches use equations that are valid across a wide range of collisionality regimes, even if the collisional mean free path is not small compared to the parallel scale length or if the ion drift-orbit excursions are not small compared to radial gradient length scales (Cohen & Xu, 2008). Gyrokinetic simulations, however, are much more computationally expensive than fluid simulations, so fluid-based transport and turbulence codes for the boundary plasma will remain useful for modeling the boundary plasma. The results from gyrokinetic simulations are also expected to aid in improving the fidelity of boundary-plasma fluid simulations (Ricci, 2015).

1.2.2 Gyrokinetic Modeling

Full six-dimensional kinetic modeling of plasma turbulence in tokamaks on macroscopic time and length scales by solving the Vlasov–Maxwell or Vlasov–Poisson equations have memory and processing power requirements several orders beyond what is currently possible on present-day and near-term supercomputers. Fortunately, there is a way to reduce the often insurmountable full 6D problem to a tractable 5D one, given that certain assumptions are well satisfied. Gyrokinetic theory is a reduced five-dimensional description of low-frequency plasma dynamics constructed by systematically removing the details of the charged particles' rapid gyromotion due to a magnetic field and other high-frequency phenomena (Krommes, 2012; Tronko *et al.*, 2016; Krommes, 2010; Sugama, 2000; Brizard & Hahm, 2007; Brizard, 2000a). This time-scale separation is well justified for particles in a strong background magnetic field with weak spatial inhomogeneity, such as those present in tokamaks and stellara-

tors, in which case the frequencies of turbulent fluctuations are much smaller than the ion gyrofrequency. The gyrokinetic system, which describes the evolution of a gyrocenter (the gyro-averaged particle position) distribution function over a 5D phase space, is much easier to simulate when compared to 6D kinetic descriptions of particle distribution functions because of the reduced dimensionality and from relaxing the restriction on the time step from the plasma period to turbulence time scales and the restriction on the grid spacing from the Debye length to the gyroradius ([Garbet et al., 2010](#)).

While 5D gyrokinetic simulations require much more computational resources than comparable 3D fluid simulations due to the high dimensionality of the gyrokinetic system, their use to study turbulent transport in the tokamak core has now become routine ([Garbet et al., 2010](#)). A number of important verification studies and cross-code benchmarks on core gyrokinetic codes have been performed ([Dimits et al., 2000](#); [Tronko et al., 2017](#); [Lapillonne et al., 2010](#); [McMillan et al., 2010](#); [Rewoldt et al., 2007](#)). More recently, gyrokinetic models have also been used to study astrophysical turbulence ([Scheokochihin et al., 2009](#); [Numata et al., 2010](#)). For many of the same reasons why quantitative modeling in the boundary plasma is difficult to approach analytically, gyrokinetic codes for boundary-plasma simulation are much less mature than than their core counterparts.

Some complications that must be faced by boundary-plasma codes include the need to handle large-amplitude fluctuations (invalidating conventional δf approaches ([Hu & Krommes, 1994](#))), open and closed magnetic field lines with a LCFS and X-point (which can cause difficulties with coordinates), electromagnetic fluctuations ([Scott, 2007b](#); [Scott et al., 2010](#)), a wide range of space and time scales, a wide range of collisionality regimes, sheath boundary conditions, plasma-wall interactions, atomic physics, and the existence of a high-frequency electrostatic shear Alfvén (ω_H) mode in electrostatic simulations ([Lee, 1987](#); [Belli & Hammett, 2005](#)) or sheath-interaction modes that one does not want to artificially excite. Major extensions to existing core gyrokinetic codes or new codes are required to handle the additional challenges of the edge and SOL regions.

Numerical Implementations of the Gyrokinetic Equations

A variety of numerical methods have been developed for the computationally challenging solution to the gyrokinetic equations. The two main types of numerical methods for solving the gyrokinetic equations are *continuum* methods ([Jenko & Dorland, 2001](#)) and the *particle-in-cell* (PIC) method ([Lee, 1983](#); [Bottino & Sonnendrücker, 2015](#); [Birdsall & Langdon, 2004](#)). There is also a third approach called *semi-Lagrangian* methods, which are a hybrid between continuum and PIC methods, but they have been seldom-used for gyrokinetic simulation so far ([Grandgirard et al., 2006, 2007](#)). While gyrokinetic simulations have been useful in elucidating the physical mechanisms behind tokamak and stellarator microturbulence, the ultimate goal of gyrokinetic simulations is to produce quantitatively reliable predictions of core and boundary plasma properties. As the history of core gyrokinetic codes has demonstrated, it is important to explore both PIC and continuum (and semi-Lagrangian) approaches as independent

cross-checks against each other and to continuously shore up the specific weaknesses of each method.

Continuum methods are Eulerian approaches to solve a kinetic equation (e.g., the 5D gyrokinetic equation) by discretizing the equation on a fixed phase-space mesh. Standard numerical methods developed for the solution of partial differential equations are used, including finite-difference, finite-volume, spectral, pseudospectral, finite-element, and discontinuous Galerkin (DG) methods. The PIC method is a Lagrangian approach that solves the kinetic equation using a finite set of particles called markers. Since it is often computationally infeasible to use a number of markers on the same order as the number of physical particles in a real plasma, a much lower number of markers are used in practice (Tskhakaya *et al.*, 2007). Each marker in the simulation then represents a ‘macroparticle’ or ‘superparticle’ encapsulating many physical particles. Starting with a set of markers that sample the initial positions in phase space, the marker positions are advanced over a small time step according to the characteristics of the kinetic equation. The source terms for the 3D field equations are then computed on a fixed grid from the markers, and the resulting fields are interpolated back to the marker positions so that the markers can be advanced again for next time step. PIC methods can be considered as a kind of Monte Carlo method that uses a finite set of markers to approximate integrals involving the distribution function (Bottino & Sonnendrücker, 2015; Krommes, 2012). The 3D field equations in both continuum and PIC approaches are solved using standard grid-based algorithms.

Both classes of numerical methods are associated with a unique set of advantages, disadvantages, and challenges. PIC methods automatically maintain the positivity of the distribution function and are relatively straightforward to implement (Krommes, 2012). They are also not subject to the Courant–Friedrichs–Lewy (CFL) condition when explicit time stepping is used (Garbet *et al.*, 2010), which results in instability if violated in a continuum simulation.⁴ PIC methods have been used for plasma simulation for several decades, and the first gyrokinetic simulation used a PIC method (Lee, 1983). Computational plasma physicists can consequently draw upon a larger body of knowledge in the field when developing PIC codes, while the first continuum gyrokinetic code GS2 was developed much later (Dorland *et al.*, 2000).⁵ As a Monte Carlo sampling technique, PIC methods have statistical noise in moments of the distribution function, and this error scales with the number N of markers as $1/\sqrt{N}$. Although there are a variety of techniques to reduce sampling noise (Garbet *et al.*, 2010), the effect of noise in PIC simulations can be subtle (Krommes & Hu, 1994; Krommes, 2007) and can even dominate the results of a simulation, which has led to misunderstandings in the past (Nevins *et al.*, 2005; Bottino *et al.*, 2007). Wilkie & Dorland (2016) recently documented two time-discretization-independent numerical instabilities in the electrostatic δf -PIC algorithm, one of which is even converged on particle number. Statistical noise in PIC codes has also made electromagnetic simulations challenging (Hatzky *et al.*, 2007), which is a problem in the literature referred as

⁴Explicit time steps that violate the CFL condition in PIC simulations can result in inaccuracies such as numerical heating or numerical diffusion.

⁵The development of GS2 was motivated in part by the difficulties gyrokinetic PIC codes were having with handling electromagnetic fluctuations.

the *Ampère’s law cancellation problem*. This problem refers to the inaccuracy in the numerical cancellation of two large terms in Ampère’s law, which becomes severe at moderate to high plasma β (Chen & Parker, 2001; Mishchenko *et al.*, 2004) and small perpendicular wave numbers (Hatzky *et al.*, 2007). A variety of techniques for PIC simulations have been proposed over the years (Chen & Parker, 2003; Mishchenko *et al.*, 2014; Kleiber *et al.*, 2016; Hatzky *et al.*, 2007) to mitigate this problem, and recent developments have been promising.

Continuum methods are not Monte Carlo methods, so they avoid having to deal with the challenging statistical-noise issues that PIC methods face. These methods are however subject to a time-step size restriction from the CFL condition if explicit time stepping is used, which can be highly restrictive in electrostatic simulations (Lee, 1987; Belli & Hammett, 2005) and for the treatment of diffusive and hyperdiffusive terms. Therefore, the fastest dynamics of a system must always be resolved when explicit methods are used, even if they do not affect the results. Implicit or semi-implicit time stepping methods are required to avoid the CFL restriction, which can require computationally expensive global matrix-inversion operations and processor communication. Continuum methods usually do not automatically guarantee the positivity of the distribution function, which can be a particularly difficult issue to address for high-order schemes (Garbet *et al.*, 2010). Continuum methods often use upwind techniques that introduce some numerical dissipation that result in some smoothing of the particle distribution function at small scales, which can be beneficial in addressing the ‘entropy paradox’ (Krommes & Hu, 1994) and numerical-recurrence issues Garbet *et al.* (2010), which can affect the results if the grid is too coarse (Candy & Waltz, 2006). The inclusion of electromagnetic effects in continuum codes has been a long-solved issue⁶ (Kotschenreuther *et al.*, 1995; Dorland *et al.*, 2000; Jenko & Dorland, 2001; Candy & Waltz, 2003a,b; Dannert & Jenko, 2004), although electromagnetic simulations for certain types of problems can still be challenging for physics and not numerical reasons. High-order continuum methods, which perform more calculations per grid point than low-order methods, provide a path for faster convergence with solution size than PIC methods. Continuum methods for gyrokinetic and fully kinetic simulation still appear to be associated with misconceptions in the literature regarding larger memory requirements or worse computational efficiency (Takizuka, 2017; Doyle *et al.*, 2007; Kardaun *et al.*, 2008) when compared to PIC methods, despite attempts to show that they are similarly efficient for relevant problems (Jenko, 2000; Candy & Waltz, 2006). We note that comparisons between PIC and continuum codes may also be highly problem dependent. Nevertheless, it is essential to have independent PIC and continuum codes for the cross-verification of results, especially of those that cannot yet be experimentally verified.

Another difference between PIC and continuum codes is that PIC codes have increasingly good velocity space resolution for longer-wavelength modes, while continuum codes have a velocity-space resolution that is independent of spatial scale.

⁶A key realization was to compute all terms appearing in Ampère’s law numerically and in a consistent manner. This idea was first presented by G. Hammett and F. Jenko in presentations at the Plasma Microturbulence Project meeting at General Atomics on July 25, 2001 (see Chen & Parker, 2003, footnote 13).

The required velocity-space resolution is highly problem dependent, and the resonance broadening by nonlinear scattering (island overlap) and collisions should be accounted for. The effects described in [Su & Oberman \(1968\)](#) show that collisional diffusion sets a limit on velocity-space resolution requirements that scales as $\nu^{1/3}$, where ν is the collision frequency, so the moderate collisionality of the boundary plasma often means that the velocity-space resolution does not need to be very high (see also [Smith, 1997](#)).

Gyrokinetic Codes for the Boundary Plasma

Currently, the most sophisticated gyrokinetic code for the boundary plasma is the XGC1 gyrokinetic particle code ([Chang et al., 2009](#)), which presently uses a ‘hybrid-Lagrangian scheme’ ([Ku et al., 2016](#)) and includes a realistic diverted-plasma geometry, neutral particles, charge-exchange and ionization interactions, and radiation cooling ([Chang et al., 2017](#)). Recent electrostatic XGC1 simulations have predicted the midplane heat-flux width on an attached ITER plasma to be 5.6 mm, which can be compared to the 5 mm ITER design specification and the 1 mm empirical scaling based on present experiments ([Chang et al., 2017](#)). The authors were able to reproduce the measured midplane heat-flux widths in three major tokamaks to build confidence in their ‘gyrokinetic projection’ to ITER. The heat-flux width in XGC1 simulations of present-day tokamaks was found to be dominated by ion-drift-orbit excursions, while the heat-flux width in the ITER simulation was found to be dominated by turbulent electron-heat-flux spreading. It remains to be seen what challenges the inclusion of electromagnetic effects in XGC1 simulations with kinetic electrons will present and whether similar calculations can be obtained at much cheaper computational cost through other codes or models (the ITER simulation reported in [Chang et al. \(2017\)](#) used 300 billion markers and ran on 90% of the Titan computer for a few days). ELMFIRE ([Korpilo et al., 2016](#); [Heikkinen et al., 2008](#)) is another 5D gyrokinetic PIC code being extended to handle the boundary plasma, although it is still in an early stage of development.

On the other hand, the development of gyrokinetic continuum codes for the boundary plasma has lagged significantly behind gyrokinetic PIC codes, despite the promising review of three main efforts at the time by [Cohen & Xu \(2008\)](#). Unfortunately, negative results are seldom reported in science, and so it is unclear what issues have held up the development of these gyrokinetic continuum codes. Some hints are found in the literature, however. Recent papers reporting G5D simulations ([Kawai et al., 2017](#); [Idomura, 2014, 2012](#)) focus only on core turbulence and no longer have indications that the code is being extended to the boundary plasma. The FEFI code ([Scott et al., 2010](#); [Scott, 2006a](#)) tried to proceed directly to electromagnetic simulations in the SOL, but ran into difficulties arising from sheath-model stability and shear-Alfvén dynamics in low-density regions ([Zweben et al., 2009](#)). The development of TEMPEST ([Xu et al., 2007](#)) was apparently halted sometime after results from 4D gyrokinetic transport simulations were presented in [Xu et al. \(2010\)](#), perhaps due to issues stemming from the non-conservation properties of the underlying numerical scheme ([Cohen & Xu, 2008](#)). Some members of the TEMPEST team eventually began

the development of the COGENT code (Dorf *et al.*, 2012), which features a conservative fourth-order finite-volume discretization (Colella *et al.*, 2011). COGENT was recently used to perform axisymmetric 4D gyrokinetic transport simulations in a realistic geometry with an anomalous radial-diffusion term to model radial transport due to turbulence (Dorf *et al.*, 2016). A modified version of the GENE code (widely used for core turbulence simulation) has recently begun development for boundary-plasma applications (Pan *et al.*, 2016). A gyrokinetic continuum code with similar capabilities of XGC1 would be extremely valuable to the plasma physics field, since XGC1 is the only gyrokinetic code capable of performing ITER boundary-plasma simulations at present. Having the same prediction made by two (or several) independent gyrokinetic codes for the boundary plasma using different numerical approaches would be highly reassuring.

In continuum codes, spectral techniques are commonly used in some directions, which can have problems with Gibbs phenomena that result in negative overshoots. Most algorithms used in magnetic fusion research are designed for cases in which viscous or dissipative scales are fully resolved and do not use limiters, and thus can have problems with small negative oscillations. Negative densities may result in unphysical behavior in the solution (for example, a negative density in the tail of the electron distribution function can reverse the slope of the sheath current versus sheath potential relation), and inaccuracies in the sheath boundary conditions can also lead qualitatively incorrect results. Some finite-difference algorithms make it easier to calculate derivatives across the LCFS with field-aligned coordinates, but may have problems with particle conservation, and small imbalances in electron and ion gyrocenter densities may drive large errors in the electric field.

For these reasons, we were motivated to investigate discontinuous Galerkin methods for gyrokinetic continuum simulation in boundary plasmas. DG methods are a class of finite-element methods that use discontinuous basis functions (typically piecewise polynomials) to represent the solution in each cell. The most popular version of DG is the Runge–Kutta discontinuous Galerkin method (Cockburn & Shu, 1998b, 2001; Shu, 2009), which uses a high-order DG method for space discretization and explicit, strong stability-preserving (SSP) high-order Runge–Kutta methods (Gottlieb *et al.*, 2001) for time discretization. The RKDG method was originally developed for the solution of nonlinear, time-dependent hyperbolic systems and has found use in numerous applications (Cockburn *et al.*, 2000), especially for Euler and Navier–Stokes equations. Since continuity in the solution is not required across cell interfaces, DG methods gain a number of important benefits that are not available to traditional finite-element methods. The RKDG method is attractive because it is highly local, highly parallelizable, able to handle complex geometries, allows high-order accuracy, and enforces local conservation laws. For an introduction to DG methods, the reader is referred to Shu (2009); Durran (2010); Hesthaven & Warburton (2008).

1.3 Thesis Overview

This thesis focuses on efforts towards the development of a gyrokinetic continuum code for the simulation of boundary-plasma turbulence. Specifically, we investigate the application of discontinuous Galerkin algorithms to handle the difficulties in open-field-line plasmas, which is the situation found in the SOL. The algorithms that we use have been implemented in the Gkeyll code, which is a framework for kinetic and fluid plasma simulations using a variety of grid-based numerical algorithms. The Gkeyll code is primarily developed at the Princeton Plasma Physics Laboratory, with contributors from a variety of institutions around the United States. We note that we have not yet performed a ‘gyrokinetic continuum simulation of a tokamak SOL’. At a minimum, a tokamak SOL simulation needs to include a confined edge region where plasma is sourced and a realistic diverted geometry including a LCFS and X-point. Additionally, kinetic modeling of wall-recycled neutrals and models of radiative power losses, charge-exchange interactions, and ionization are required for quantitative prediction, since these processes play important energy-dissipation roles in the SOL. Nevertheless, major steps towards this goal have been completed in the course of this thesis.

In Chapter 2, we discuss the important models and algorithms used in other chapters of the thesis. We first describe the gyrokinetic model that has been implemented in Gkeyll, which at present employs a number of simplifications (electrostatics, long-wavelength, linear polarization) to make the problem tractable in the scope of a PhD thesis. Next, we discuss discontinuous Galerkin algorithms, starting from a 1D example before covering the specific energy-conserving version of DG that we use in our simulations. We also discuss important aspects of a simplified Lenard–Bernstein collision operator and how positivity issues in the distribution function are addressed. A key component of simulating plasma dynamics on open magnetic field lines is the sheath-model boundary condition applied at the material interfaces, and we describe two kinds of sheath models that can be used and note an important shortcoming of these models concerning the Bohm sheath criterion that is not usually acknowledged.

In Chapter 3, we present results from our initial efforts to investigate the feasibility of using DG methods for gyrokinetic continuum simulation in the boundary plasma in spatially 1D kinetic simulations. We describe the construction of a simplified 1D1V (one position dimension, one velocity dimension) gyrokinetic model that incorporates ion polarization effects through a specified perpendicular wavenumber in a modified gyrokinetic Poisson equation. Combined with logical-sheath boundary conditions, this model is then used to simulate the parallel propagation of an ELM heat pulse in the SOL, which is a problem that has been studied before using kinetic simulations that fully resolved the sheath and fluid simulations that used sheath boundary conditions. This model is then extended to 1D2V and some collisional effects are added through a Lenard–Bernstein collision operator. Despite not directly resolving the sheath, our 1D1V and 1D2V gyrokinetic simulations agree quantitatively well with comparable fully kinetic simulations that are much more computationally expensive due to restrictive spatial and temporal resolution requirements.

Chapter 4 presents the key accomplishment of the thesis, which are the first 5D gyrokinetic continuum simulations of turbulence in a straight-magnetic-field-line geometry. Specifically, we present simulations of the Large Plasma Device (LAPD), which is a basic plasma physics experiment at the University of California, Los Angeles. Compared to a realistic scrape-off layer, the LAPD plasma is at a much colder temperature and is not subject to magnetic-curvature effects. The LAPD plasma is very well diagnosed, so we compare turbulence characteristics from our simulations to previous LAPD measurements published elsewhere. We also describe a simple modification to the sheath-model boundary conditions that allows us to simulate a set of LAPD experiments to investigate sheared-flow-suppression of turbulence using bias-induced flows.

In Chapter 5, we add some additional complexity to the open-field-line simulations by adding magnetic-curvature effects to simulate turbulence on helical field lines. While the new magnetic geometry makes the simulations particularly suitable for simulating the plasma turbulence in SMTs, we design a test case for a helical SOL using parameters relevant for the NSTX SOL. The helical-SOL simulations are qualitatively different from the LAPD simulations, with the generation and radial propagation of blobs playing an important role in transporting plasma across the magnetic field lines. We also show how the magnetic-field-line incidence angle affects plasma profiles and turbulence characteristics in these simulations. In this simple model, we show that the heat-flux width is strongly affected by the strength of the vertical (poloidal) magnetic field.

In Chapter 6, we present a numerical method that uses exponentially weighted polynomials to represent the solution while maintaining important conservation properties. The use of non-polynomial basis functions is motivated by the need to use as few pieces of data to represent the solution as possible, and exponentially weighted polynomials appear to be a reasonable choice to represent the distribution function in problems in which collisions are strong. Previous work (Yuan & Shu, 2006) in using non-polynomial basis functions in standard DG methods does not conserve number, momentum, and energy. Using 1D numerical tests of collisional relaxation, we show how the new method conserves important quantities to machine precision. Results from a non-trivial calculation of the parallel heat flux in a simplified Spitzer–Härm test problem are then presented to compare the accuracy and efficiency of the new method with standard DG methods using polynomials. The generalization of this method to high dimensions and the implementation of this method in Gkeyll is left for future work.

In Chapter 7, we summarize the main results of this thesis and discuss what are high-priority directions for near-term future work.

1.3.1 A Note on Color Maps

Due to the continued popularity of the rainbow color map for representing interval data in plasma-physics papers, we briefly explain why authors should avoid using the rainbow color map for such purposes. We decided to place this discussion here in the introduction chapter instead of in the appendices to help spread general awareness of

this issue. In fact, even we are guilty of using a rainbow color map for the 2D plots in a recent publication ([Shi et al., 2017](#)) before this issue was brought to our attention.

As done by most authors, we present 2D data using pseudocoloring, in which data is displayed by mapping scalar data values to colors according to a *color map*. While many authors still use a color map that is ordered according to the visible light spectrum, known as the *rainbow color map*, data visualization experts have long recognized that the rainbow color map is confusing and misleading ([Eddins, 2014](#); [Borland & Taylor II, 2007](#); [Ware, 1988](#); [Rogowitz & Treinish, 1998](#)). Many of these issues arise from the lack of *perceptual ordering* and *perceptual uniformity* in the rainbow color map. Perceptual ordering refers to a color map that uses a sequence of colors with a consistent, inherent ordering: Given a set of distinct colors, will most people order the color in the same sequence based on their color perception (and not a mnemonic)? Many issues in the rainbow color map come from our perception of yellow as the brightest color, while the rainbow color map assigns the largest data values to red. Perceptual uniformity refers how the same difference between two data values corresponds to the same perceived difference in color on the entire color scale. The perceived difference between the colors representing the values 1 and 2 should also be the same between the colors representing the values 9 and 10.

The color map used for 2D data visualization in this thesis is the ‘inferno’ color map ([Smith & van der Walt, 2016](#)), which is available Matlab, Matplotlib, and R. The inferno color map is perceptually uniform and perceptually ordered. Figure 1.5 shows a comparison of electron-density snapshots from a gyrokinetic simulation of LAPD (discussed in Chapter 4) using the rainbow color map (called the *jet* color map in Matlab) and the inferno color map. By comparing the two sets of plots, several visual artifacts can be identified in the plots with the rainbow color map. Additionally, the detail in green and cyan regions is wiped out due to the perceptual similarity of these two colors.

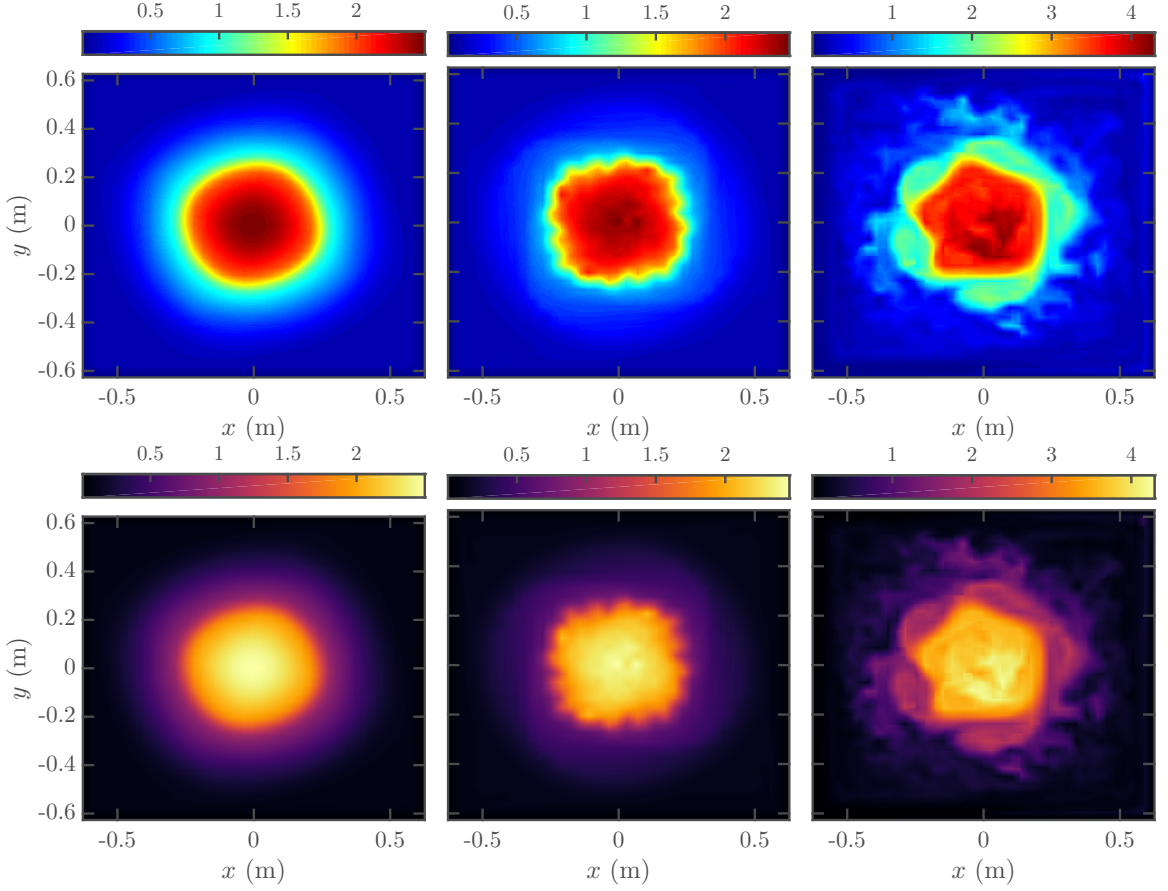


Figure 1.5: Comparison of electron-density snapshots (in 10^{18} m^{-3}) from gyrokinetic simulations of LAPD using (top row) the rainbow color map and (bottom row) a perceptual color map. Several visual artifacts appear in the plots using the rainbow color map but not in the corresponding set of plots using a perceptual color map. In the upper set of plots, yellow edges and cyan ‘halos’ are prominent, and large-scale dark-blue artifacts are visible in the outer regions in all three plots. The yellow outlines imply distinct, sharp-gradient regions in the data that are not actually present. Since green and cyan are extremely similar in hue, green and cyan regions tend to blend together and smear out fine structures, while such details are not obscured in the corresponding perceptual plots. Before the reader consults the color key, the dark-red features near the center of each upper plot also falsely suggest a depression in the data, since it resembles a shadow.

Chapter 2

Models and Numerical Methods

In this chapter, we discuss some of the common models and numerical algorithms used elsewhere in this thesis. Although it is well known that scientific results must be reproducible, authors sometimes do not describe their simulations in published papers in enough detail for other researchers to replicate their results. One should strive to publicly document the model equations, initial conditions, boundary conditions, grid resolution, and any special techniques that were necessary to obtain stable simulations. We hope to facilitate any future attempts to reproduce our results and to break away from the tendency to be vague about the ‘ugly parts’ of a simulation by providing a clear description of our approach for the open-field-line simulations discussed in Chapters 4 and 5, including the difficulties we encountered and what was done to address them.

In Section 2.1, we describe the gyrokinetic model we solve in Chapters 4 and 5. We then provide an overview of discontinuous Galerkin (DG) methods and discuss how we apply an energy-conserving DG method (Liu & Shu, 2000) to solve the gyrokinetic system in Section 2.2. We provide details about the numerical implementation of the Lenard–Bernstein collision operator in Section 2.3, which also motivates the need for a positivity-adjustment procedure described in Section 2.4. Lastly, we specify the sheath-model boundary conditions that are used in our simulations in Section 2.5.

These models and algorithms are implemented in the Gkeyll code, which is a framework for kinetic and fluid plasma-physics problems. Recently, Gkeyll has been used for fluid studies of magnetic reconnection (Wang *et al.*, 2015; Ng *et al.*, 2015), kinetic simulations of the Vlasov–Maxwell system (Juno *et al.*, 2017), and kinetic and multi-fluid sheath modeling (Cagas *et al.*, 2017). Gkeyll is composed of a core component written in C++ and problem-specific configuration components written in the Lua scripting language (Ierusalimschy *et al.*, 1996).

Gkeyll was originally designed and developed at the Princeton Plasma Physics Laboratory (PPPL) by A. Hakim, who created the core framework components (e.g., Lua integration, data structures, and grid classes) used in the various applications. For the simulations presented in this thesis, A. Hakim added additional domain-decomposition capabilities, developed the gyrokinetic-Poisson-equation solver, and contributed to the extension of the energy-conserving Liu & Shu algorithm (Liu & Shu, 2000) to generic Hamiltonian systems (Section 2.2.2). There are currently sev-

eral code contributors from various academic institutions across the United States. At the time of writing, the Gkeyll repository is stored on Bitbucket and access must be requested.¹

The core C++ component contains implementations of the basic self-contained classes, such as data structures to store solutions, rectangular finite-element meshes, and solvers, which generically perform operations on input data to produce output data. Currently, Gkeyll has classes that implement discontinuous Galerkin, finite-element, finite-volume, and finite-difference algorithms. Most of the work in this thesis required the addition of new capabilities to the Gkeyll code in the form of solvers.

The configuration component uses Lua for problem-specific applications of the Gkeyll code. The core Gkeyll code only needs to be compiled by the user once, while a Lua script is provided as an input argument to the executable and is automatically compiled at run time. Lua is used for much more than supplying parameter values for a simulation. In a Lua script, a user defines which objects (implemented in the core code) are to be created for a simulation and how these objects interact with each other. To elaborate, there is no implementation of an ‘open-field-line simulation’ in the core C++ code. There are several classes relevant to this problem, such as implementations of sheath boundary conditions, basis functions, a Poisson-equation solver, a kinetic-equation solver, and more, but a Lua script is required to connect all these pieces together and determine the sequence in which various tasks are performed. Lua scripts for the 5D gyrokinetic continuum simulations have approximately 3000 lines of code.

2.1 Gyrokinetic Model

The gyrokinetic model discussed in this section is used in simulations of the Large Plasma Device (LAPD) (Chapter 4) and a helical scrape-off-layer (SOL) model (Chapter 5). Several versions of full- f gyrokinetic equations have been derived with various formulations, ordering assumptions, and levels of accuracy (Brizard & Hahm, 2007; Sugama, 2000; Hahm *et al.*, 2009; Parra & Calvo, 2011; Parra *et al.*, 2014; Dimits, 2012; McMillan & Sharma, 2016), and can generically be written in the form of an evolution equation for the gyrocenter distribution function, with a Poisson bracket for the phase-space velocities and expressions for the Lagrangian/Hamiltonian, coupled to field equations to determine the potentials. Here, we solve a long-wavelength (drift-kinetic) limit of electrostatic full- f gyrokinetic equations with a linearized polarization term for simplicity, as summarized by Idomura *et al.* (2009). As the code is further developed, it can be extended to more accurate and more general equations, though the equations will still have this generic structure.

The fundamental assumption of standard gyrokinetics is that there is a coordinate system in which things change slowly compared to the gyrofrequency. In some

¹The author is well aware of the irony in discussing the need for transparency in the plasma-simulation literature while working on a closed-source code. Access to the code is available upon request, however, and there are currently plans to make Gkeyll publically available.

gyrokinetic derivations, the ordering assumptions are written in a more restrictive form requiring that the fluctuation amplitudes must be small. But as discussed in various places (such as Hahm *et al.*, 2009; Dimits, 2012; McMillan & Sharma, 2016), more general derivations that are appropriate for the edge region of fusion devices are possible, such as using a small vorticity ordering (McMillan & Sharma, 2016), which allows large flows and large-amplitude fluctuations at long wavelengths.

We solve a full- f gyrokinetic equation written in the conservative form (Brizard & Hahm, 2007; Sugama, 2000; Idomura *et al.*, 2009)

$$\frac{\partial \mathcal{J}f_s}{\partial t} + \nabla_{\mathbf{R}} \cdot (\mathcal{J}\dot{\mathbf{R}}f_s) + \frac{\partial}{\partial v_{\parallel}}(\mathcal{J}\dot{v}_{\parallel}f_s) = \mathcal{J}C[f_s] + \mathcal{J}S_s, \quad (2.1)$$

where $f_s = f_s(\mathbf{R}, v_{\parallel}, \mu, t)$ is the gyrocenter distribution function for species s , $\mathcal{J} = B_{\parallel}^*$ is the Jacobian of the gyrocenter coordinates, $B_{\parallel}^* = \mathbf{b} \cdot \mathbf{B}^*$, $\mathbf{B}^* = \mathbf{B} + (Bv_{\parallel}/\Omega_s)\nabla \times \mathbf{b}$, $C[f_s]$ represents the effects of collisions, $\Omega_s = q_s B/m_s$, and $S_s = S_s(\mathbf{R}, v_{\parallel}, \mu, t)$ represents plasma sources (e.g., neutral ionization or core plasma outflow). In a straight-field-line geometry, B_{\parallel}^* simplifies to B . The phase-space advection velocities are defined as $\dot{\mathbf{R}} = \{\mathbf{R}, H\}$ and $\dot{v}_{\parallel} = \{v_{\parallel}, H\}$, where the gyrokinetic Poisson bracket is

$$\{F, G\} = \frac{\mathbf{B}^*}{m_s B_{\parallel}^*} \cdot \left(\nabla_{\mathbf{R}} F \frac{\partial G}{\partial v_{\parallel}} - \frac{\partial F}{\partial v_{\parallel}} \nabla_{\mathbf{R}} G \right) - \frac{1}{q_s B_{\parallel}^*} \mathbf{b} \cdot \nabla_{\mathbf{R}} F \times \nabla_{\mathbf{R}} G. \quad (2.2)$$

The gyrocenter Hamiltonian is

$$H_s = \frac{1}{2} m_s v_{\parallel}^2 + \mu B + q_s \langle \phi \rangle_{\alpha}, \quad (2.3)$$

where $\langle \phi \rangle_{\alpha}$ is the gyro-averaged potential (with the gyro-angle denoted by α). In the simulations discussed in Chapters 4 and 5, we consider a long-wavelength limit of the gyrokinetic system and neglect gyroaveraging in the Hamiltonian to take $\langle \phi \rangle_{\alpha} = \phi$. This system has similarities to some versions of drift kinetics (and is sometimes referred to as the drift-kinetic limit of gyrokinetics (Dorf *et al.*, 2016, 2013; Cohen & Xu, 2008)), but is unlike versions that include the polarization drift in the kinetic equation or determine the potential from some other equation. In a straight-magnetic-field geometry, (2.1)–(2.3) reduce to the description of parallel streaming, an $E \times B$ drift, and acceleration along the field line due to E_{\parallel} (see (4.5), which is solved in our LAPD simulations).

The potential is solved for using the long-wavelength gyrokinetic Poisson equation with a linearized ion polarization density

$$-\nabla_{\perp} \cdot \left(\frac{n_{i0}^g q_i^2 \rho_{s0}^2}{T_{e0}} \nabla_{\perp} \phi \right) = \sigma_g = q_i n_i^g(\mathbf{R}) - e n_e(\mathbf{R}), \quad (2.4)$$

where $\rho_{s0} = c_{s0}/\Omega_i$, $c_{s0} = \sqrt{T_{e0}/m_i}$, and n_{i0}^g is the background ion gyrocenter density that we will take to be a constant in space and in time. Gyroaveraging in the gyrocenter densities is neglected in this long-wavelength limit. The replacement of

$n_i^g(\mathbf{R})$ by n_{i0}^g on the left-hand side of (2.4) is analogous to the Boussinesq approximation employed in some Braginskii fluid codes (Dudson *et al.*, 2015; Halpern *et al.*, 2016; Angus & Umansky, 2014). We note that the use of a linearized ion polarization charge density is formally valid when ion density fluctuations are small.

Note that (2.4) is a statement of quasineutrality, where the right-hand side is the gyrocenter component of the charge density σ_g , and the left-hand side is the negative of the ion polarization charge density, $-\sigma_{\text{pol}}$ (due to the plasma response to a cross-field electric field), so this equation is equivalent to $0 = \sigma = \sigma_g + \sigma_{\text{pol}}$. The simulations are done in a Cartesian geometry with x and y being used as coordinates perpendicular to the magnetic field, which lies solely in the z direction. Therefore, $\nabla_{\perp} = \hat{\mathbf{x}}\partial_x + \hat{\mathbf{y}}\partial_y$.

2.2 Discontinuous Galerkin Algorithms

Consider a numerical method to solve the following time-dependent partial differential equation over a domain Ω :

$$\frac{\partial f}{\partial t} + G(f) = 0, \quad (2.5)$$

where G is an operator that involves spatial derivatives in x and an initial condition and boundary conditions are prescribed. One class of numerical methods, called series-expansion methods, solves (2.5) by approximating $f(x, t)$ as a linear combination of a finite number of predetermined basis functions:

$$f \approx f_h = \sum_{k=1}^N f_k(t) \psi_k(x). \quad (2.6)$$

In almost all practical cases of interest, it is not possible to find a solution that satisfies (2.5) by this expansion because the ψ_k 's are generally not eigenfunctions of G (Durran, 2010), so the \approx sign is used to relate f to the numerical solution f_h . Therefore, we settle for finding the degrees of freedom $f_1(t), \dots, f_N(t)$ that minimize some kind of error that quantifies the degree to which the numerical solution fails to satisfy (2.5). For this purpose, it is convenient to define the residual $R(f_h)$

$$R(f_h) = \frac{\partial f_h}{\partial t} + G(f_h) \quad (2.7)$$

and try to minimize a function involving the residual in an integral sense over Ω or at a set of N points in Ω .

In Galerkin methods, a system of equations for the time evolution of the degrees of freedom, $\partial f_1/\partial t, \dots, \partial f_N/\partial t$, is obtained by requiring that the residual be orthogonal to each basis function:

$$\int_{\Omega} dx R(f_h) \psi_k(x) = 0, \quad 1 \leq k \leq N. \quad (2.8)$$

The solution to (2.8) determines the time evolution of the degrees of freedom such that the squared- L^2 -norm error

$$(\|R(f_h)\|_2)^2 = \int_{\Omega} dx R(f_h)^2 = \int_{\Omega} dx \left(\frac{\partial f_h}{\partial t} + G(f_h) \right)^2 \quad (2.9)$$

is minimized. To see this, we substitute the expansion (2.6) into (2.9), take a derivative with respect to $\dot{f}_j = df_j/dt$, and look for critical points:

$$0 = \frac{\partial}{\partial \dot{f}_j} \int_{\Omega} dx \left[\left(\sum_{k=1}^N \dot{f}_k \psi_k \right) + G \left(\sum_{k=1}^N f_k \psi_k \right)^2 \right]^2 \quad (2.10)$$

$$= 2 \int_{\Omega} dx \left[\left(\sum_{k=1}^N \dot{f}_k \psi_k \right) + G \left(\sum_{k=1}^N f_k \psi_k \right)^2 \right] \psi_j \quad (2.11)$$

$$= 2 \int_{\Omega} dx R(f_h) \psi_j(x). \quad (2.12)$$

This choice of \dot{f}_j minimizes the squared- L^2 -norm error because the second derivative of with respect to \dot{f}_j is positive:

$$\frac{\partial^2}{\partial \dot{f}_j^2} \int_{\Omega} dx R(f_h)^2 = 2 \int_{\Omega} dx \psi_j(x)^2. \quad (2.13)$$

The Galerkin approximation (2.8) is used in many series-expansion methods, including the spectral method, some finite-element methods, and the discontinuous Galerkin method. The Runge–Kutta discontinuous Galerkin (RKDG) method (Cockburn & Shu, 1998b, 2001; Shu, 2009) is a semi-discrete numerical method that uses a discontinuous Galerkin discretization for the spatial variables and explicit high-order-accurate Runge–Kutta methods (made of convex combinations of first-order Euler steps) for time discretization. The method is particularly well-suited for the solution of nonlinear, time-dependent hyperbolic conservation laws and has found use in numerous applications (Cockburn *et al.*, 2000). As its name implies, the discontinuous Galerkin method is a Galerkin method that uses discontinuous basis functions. In contrast to other Galerkin methods, the condition (2.8) is enforced element-by-element instead of globally over the entire domain.

The use of discontinuous basis functions that are smoothly varying within a cell but zero everywhere outside of it enables several benefits for DG methods. Computations are highly localized in the sense that data only needs to be shared with immediate neighbors regardless of the basis function degree,² which is a desirable property for scalability and parallel efficiency on massively parallel architectures. For other high-resolution methods, a wider stencil needs to be used to achieve high-order

²This statement comes with some exceptions. In the energy-conserving algorithm we use for the gyrokinetic system, a non-local solve is required for the electrostatic potential.

accuracy (Cockburn & Shu, 2001). The locality of the DG algorithm also makes it well-suited for adaptive h (element size) and p (basis function degree) refinement and coarsening (Remacle *et al.*, 2003). We also note that a DG method that expands a scalar solution as only a constant in each cell is a finite-volume, monotone scheme, so DG methods can be considered as a higher-order generalization of finite-volume methods (Cockburn & Shu, 1998b, 2001).

2.2.1 DG for 1D Conservation Laws

We review the RKDG method for a 1D nonlinear conservation law

$$\frac{\partial f}{\partial t} + \frac{\partial g(f)}{\partial x} = 0. \quad (2.14)$$

As in finite-element methods, we first partition the domain Ω into a number of cells $I_j = [x_{j-\frac{1}{2}}, x_{j+\frac{1}{2}}]$, for $1 \leq j \leq N$ and define an approximation space for the discrete solution f_h

$$V_h = \{v : v|_{I_j} \in V(I_j); 1 \leq j \leq N\}, \quad (2.15)$$

where the local space $V(I_j)$ is usually taken to be $P^k(I_j)$, the space of polynomials up to degree k for $x \in I_j$. Local basis functions that span $V(I_j)$ are required for numerical implementation, and the solution in I_j is expressed as

$$f_h(x) = \sum_{l=1}^k f_j^l \psi_j^l, \quad x \in I_j, \quad (2.16)$$

so the RKDG method prescribes a way to solve for the evolution of the degrees of freedom

$$\mathbf{f}_j = \begin{pmatrix} f_j^1 \\ \vdots \\ f_j^k \end{pmatrix}, \quad 1 \leq j \leq N. \quad (2.17)$$

Legendre and Lagrange polynomials are typically used as basis functions in modal and nodal DG representations, respectively. We have also implemented Serendipity basis functions (Arnold & Awanou, 2011), which are an attractive alternative to Lagrange polynomials. The Serendipity finite-element space has fewer basis functions (smaller dimension) than the Lagrange finite-element space, while achieving the same convergence rate. The Serendipity finite-element space can also represent solutions that are continuous across elements. The disparity between the size of these two finite element spaces grows with the degree of the finite element space and the space dimension. For example, $k = (2+1)^5 = 243$ degrees of freedom are required to represent the solution in 5D for a second-degree Lagrange finite element, while only $k = 112$ degrees of freedom are needed for a second-degree Serendipity finite element, and one could expect a factor of five speedup when using Serendipity finite elements in this case due to prevalence of matrix operations of size $k \times k$ in DG methods. We have not yet explored the use of higher-order Serendipity elements for

5D gyrokinetic simulations and use first-order elements (where the two finite-element spaces are identical) in those simulations for simplicity. DG methods also allow for the use of non-polynomial basis functions (Yuan & Shu, 2006), which can also result in significant savings over polynomial basis functions. These ideas are explored in Chapter 6.

Recalling that Galerkin methods minimize the squared- L^2 -norm error by requiring that the residual be orthogonal to the basis functions (2.8), we multiply (2.14) by an arbitrary test function $v(x)$ and integrate over a cell I_j

$$\int_{I_j} dx v(x) \frac{\partial f(x, t)}{\partial t} = \int_{I_j} dx \frac{\partial v}{\partial x} g(f(x, t)) - g\left(f\left(x_{j+\frac{1}{2}}, t\right)\right) v\left(x_{j+\frac{1}{2}}\right) + g\left(f\left(x_{j-\frac{1}{2}}, t\right)\right) v\left(x_{j-\frac{1}{2}}\right), \quad (2.18)$$

where an integration by parts was performed to move the spatial derivative on g onto the test function v . Next, the exact solution f is replaced by the numerical solution f_h , the flux $g(f(x, t))$ evaluated at the element interfaces is replaced by the numerical flux $\hat{g}(f_h(x, t))$, and the test function v is replaced by $v_h \in V(I_j)$:

$$\int_{I_j} dx v_h(x) \frac{\partial f_h(x, t)}{\partial t} = \int_{I_j} dx \frac{\partial v_h}{\partial x} g(f_h(x, t)) - \hat{g}\left(f_h\left(x_{j+\frac{1}{2}}, t\right)\right) v_h(x_{j+\frac{1}{2}}^-) + \hat{g}\left(f_h\left(x_{j-\frac{1}{2}}, t\right)\right) v_h(x_{j-\frac{1}{2}}^+). \quad (2.19)$$

The $-$ and $+$ superscripts indicate that a discontinuous function is evaluated at the interface using the left and right limits of the discontinuous numerical solution, respectively. In (2.19), the test functions are evaluated inside I_j .

The numerical flux \hat{g} is an approximation to the exact flux g and depends on the value of f_h on each side of a boundary:

$$\hat{g}\left(f_h\left(x_{j+\frac{1}{2}}, t\right)\right) = \hat{g}\left(f_h\left(x_{j+\frac{1}{2}}^-, t\right), f_h\left(x_{j+\frac{1}{2}}^+, t\right)\right). \quad (2.20)$$

The single-valued numerical flux is only defined at cell interfaces, where f_h is discontinuous. The numerical flux does not appear in the volume integrals because there is no ambiguity in the value of f_h to use in the interior of a cell. The choice of numerical flux must be consistent with the physical flux $g(a)$ that it approximates: $\hat{g}(a, a) = g(a)$. The numerical flux must also be a non-decreasing function of its first argument and a non-increasing function of its second argument, which are required for the numerical scheme to reduce to a monotone finite-volume scheme when the solution is approximated by a constant in each cell (Cockburn & Shu, 2001). A standard choice for the numerical flux is to use the *upwind numerical flux*. If $g(f) = cf$, then the upwind flux is

$$\hat{g}(a, b) = \begin{cases} ca & \text{if } c \geq 0, \\ cb & \text{if } c < 0. \end{cases} \quad (2.21)$$

It is important to use a numerical flux suitable for the problem at hand because the choice affects the approximation quality (Cockburn & Shu, 2001).

We can now obtain a system of k coupled equations that can be solved for the k unknowns $\partial f_j^l / \partial t$ in each cell I_j by substituting the basis function expansion for f (2.16) and taking $v_h = \psi_j^m$ for $1 \leq m \leq k$ in (2.19):

$$\sum_{l=1}^k \mathbb{M}(m, l) \frac{\partial f_j^l}{\partial t} = \int_{I_j} dx \frac{\partial \psi_j^m}{\partial x} g(f_h(x, t)) - \hat{g}\left(f_h\left(x_{j+\frac{1}{2}}, t\right)\right) \psi_j^m\left(x_{j+\frac{1}{2}}^-\right) + \hat{g}\left(f_h\left(x_{j-\frac{1}{2}}, t\right)\right) \psi_j^m\left(x_{j-\frac{1}{2}}^+\right), \quad (2.22)$$

where $\mathbb{M}(m, l) = \int_{I_j} dx \psi_j^m(x) \psi_j^l(x)$ are the components of the $k \times k$ mass matrix for I_j . Equation (2.22) can be written as a matrix equation $\mathbb{M} \dot{\mathbf{f}}_j = \mathbf{c}$, where the element c_m of the vector \mathbf{c} is the right hand side of (2.22) evaluated for $1 \leq m \leq k$. In this example, \mathbb{M} is independent of time and is the same for all I_j , and so it is advantageous to compute \mathbb{M} once and store its inverse \mathbb{M}^{-1} at the beginning of a simulation.

Integrals are numerically evaluated using Gaussian quadrature methods. In the Gkeyll code, Gauss–Legendre quadrature is typically used to approximate the definite integral of a function $f(x)$ from $x = a$ to $x = b$ by taking a weighted sum of the evaluation of the function to be integrated at a set of N_q points:

$$\int_a^b dx f(x) \approx \sum_{j=1}^{N_q} w_j f(x_j), \quad (2.23)$$

where the approximation is exact when $f(x)$ is a polynomial of degree $2N_q - 1$ or less. On the interval $[-1, 1]$, the Gauss–Legendre quadrature nodes x_j are the zeros of $P_{N_q}(x)$, the N_q th Legendre polynomial for $x \in [-1, 1]$, and the associated weights w_j are computed as (Press *et al.*, 2007)

$$w_j = \frac{2}{(1 - x_j)^2 [P'_{N_q}(x_j)]^2}. \quad (2.24)$$

The quadrature rule on the interval $[-1, 1]$ can be scaled to an arbitrary interval $[a, b]$ using the relation

$$\int_a^b dx f(x) = \frac{b-a}{2} \int_{-1}^1 dx f\left(\frac{b-a}{2}x + \frac{a+b}{2}\right), \quad (2.25)$$

so the quadrature rule becomes (Press *et al.*, 2007)

$$\int_a^b dx f(x) \approx \frac{b-a}{2} \sum_{j=1}^{N_q} w_j f\left(\frac{b-a}{2}x_j + \frac{a+b}{2}\right). \quad (2.26)$$

We note that other quadrature rules with different weights and nodes can be constructed for general integrals of the form $\int_a^b dx W(x) f(x)$, where $W(x)$ is an arbitrary (possibly non-polynomial) weight function (for an investigation of several choices, see [Landreman & Ernst, 2013](#)). Gaussian quadrature rules for integrals involving multiple directions are simply computed by taking tensor products of the 1D quadrature rule.

In order to apply Gaussian quadrature methods to evaluate integrals as they appear in (2.22), auxiliary matrices³ are needed to compute the set of function evaluations at quadrature nodes $\{f(x_1), \dots, f(x_{N_q})\}$ from the vector \mathbf{f}_j . For this reason, it is necessary to compute and store the $N_q \times k$ quadrature matrix

$$\mathbb{Q} = \begin{pmatrix} \psi_j^1(x_1) & \psi_j^2(x_1) & \cdots & \psi_j^k(x_1) \\ \psi_j^1(x_2) & \psi_j^2(x_2) & \cdots & \psi_j^k(x_2) \\ \vdots & \vdots & \ddots & \vdots \\ \psi_j^1(x_{N_q}) & \psi_j^2(x_{N_q}) & \cdots & \psi_j^k(x_{N_q}) \end{pmatrix} \quad (2.27)$$

from the basis functions whose analytical form is known.

We also compute and store a matrix that calculates $\partial f_h / \partial x$ in terms of the same basis functions used to represent the spatial dependence of f_h , which is used when the evaluation of spatial derivatives is required (such as in the volume integral on the right-hand side of (2.22)). That is, we seek the weights $f_{x,j}^l$ in element I_j such that

$$\frac{\partial f_h}{\partial x} = \sum_{l=1}^k f_{x,j}^l \psi_j^l, \quad x \in I_j. \quad (2.28)$$

We multiply (2.28) by each basis function ψ_j^m , substitute the basis function expansion for f_h , and integrate over I_j to get the system of equations that can be solved for the $f_{x,j}^i$:

$$\int_{I_j} dx \psi_j^m \sum_{l=1}^k f_j^l \frac{\partial \psi_j^l}{\partial x} = \int_{I_j} dx \psi_j^m \sum_{l=1}^k f_{x,j}^l \psi_j^l, \quad 1 \leq m \leq k. \quad (2.29)$$

By defining an additional auxiliary $k \times k$ matrix \mathbb{S}_x whose elements are

$$\mathbb{S}_x(m, n) = \int_{I_j} dx \frac{\partial \psi_j^m}{\partial x} \psi_j^n, \quad (2.30)$$

we see that $\mathbf{f}_{x,j} = \mathbb{M}^{-1} \mathbb{S}_x \mathbf{f}_j$.

Finally, once (2.22) has been solved for the weights $\partial f_j^l / \partial t$, we use an explicit high-order strong-stability-preserving (SSP) time stepping method to advance the solution in time. These methods achieve high-order accuracy by taking convex combinations of first-order forward Euler steps. Specifically, the three-stage, third-order SSP Runge-

³When DG is applied to systems with multiple spatial dimensions, separate quadrature rules are needed for the evaluation of integrals on each surface of the element in addition to the quadrature rule for volume integrals.

Kutta method ([Gottlieb *et al.*, 2001](#)) is used in the simulations discussed in this thesis and is the most popular choice ([Shu, 2009](#)) for solving equations of the form

$$\frac{\partial f}{\partial t} = L(f), \quad (2.31)$$

where $L(f)$ is the space discretization of the $-\partial g(f)/\partial x$ operator in (2.14). If the first-order Euler time discretization of (2.31) is stable under a certain norm for a sufficiently small time step (e.g., satisfying the Courant–Friedrichs–Levy condition), high-order SSP methods are designed to automatically maintain the strong stability property for certain higher-order time discretizations ([Gottlieb *et al.*, 2001](#)) under a possibly more restrictive time step. To advance $f(x, t^n) \equiv f^n$ to $f(x, t^n + \Delta t) \equiv f^{n+1}$, the third-order SSP Runge–Kutta method is

$$f^{(1)} = f^n + \Delta t L(f^n), \quad (2.32)$$

$$f^{(2)} = \frac{3}{4} f^n + \frac{1}{4} [f^{(1)} + \Delta t L(f^{(1)})], \quad (2.33)$$

$$f^{n+1} = \frac{1}{3} f^n + \frac{2}{3} [f^{(2)} + \Delta t L(f^{(2)})]. \quad (2.34)$$

In this method, the time step restriction is the same as the time step needed for the forward-Euler method to be strongly stable. One downside to this method is the considerable storage requirement. At any given instant of the algorithm, three versions of f need to be stored. For two plasma species (electrons and one ion species), the storage requirement is doubled. It might be useful to consider the use of the low-storage, third-order SSP Runge–Kutta method, which only needs to store two versions of f , but requires a 3.125 times smaller time step ([Gottlieb *et al.*, 2001](#)).

2.2.2 DG for the Gyrokinetic System

An energy-conserving (in the continuous-time limit) discontinuous Galerkin algorithm ([Liu & Shu, 2000](#)) is used to discretize the equations in space. Although [Liu & Shu \(2000\)](#) presented their algorithm for the 2D incompressible Euler and Navier–Stokes equations, G. Hammett recognized the general applicability of their algorithm for Hamiltonian systems, and A. Hakim contributed to the generalization. Upwind interface fluxes (2.21) are used in the discretization of the gyrokinetic equation (2.1). This algorithm requires that the Hamiltonian be represented on a continuous subset of the basis set used to represent the distribution function. Therefore, the distribution function is represented using discontinuous (C^{-1}) polynomials, while the electrostatic potential is represented using continuous (C^0) polynomials (equivalent to continuous finite elements). In addition to contributing to the formulation of the generalized algorithm, A. Hakim also implemented and performed a number of two-dimensional tests (e.g. incompressible Euler equations, 1D1V Vlasov–Poisson system) to benchmark the convergence and conservation properties of this algorithm. Additional details regarding the generalization of the [Liu & Shu \(2000\)](#) algorithm will be provided in future paper by A. Hakim et al.

[Liu & Shu \(2000\)](#) presented their algorithm for 2D incompressible Euler equations in a vorticity–stream function formulation: $\partial\rho(x, y, t)/\partial t + \nabla \cdot (\mathbf{u}\rho) = 0$, with the stream function ψ given by $\nabla^2\psi = \rho$, and the velocity $\mathbf{u} = \nabla^\perp\psi = (-\partial_y\psi, \partial_x\psi)$. They showed analytically that the DG space discretization of these equations conserves energy if the basis functions for ψ are in a continuous subspace of the basis functions used for the vorticity ρ .⁴ This problem can also be written in a Hamiltonian form $\partial\rho/\partial t = -\{\psi, \rho\}$, where ψ is the Hamiltonian and the Poisson bracket in this case is $\{\psi, \rho\} = \partial_x\psi\partial_y\rho - \partial_y\psi\partial_x\rho$.

Here, we consider how the algorithm of [Liu & Shu \(2000\)](#) is applied to the gyrokinetic equation system (2.1)–(2.4), although we will neglect the collisions and source terms in the gyrokinetic equation (2.1) to focus on the Hamiltonian part of the system. First, we discretize the N -dimensional phase-space domain Ω by dividing it into a number of elements I_j . We also define the configuration-space domain Ω_x and its respective partition \mathcal{T}^x .

Next, we define the approximation spaces (following the notation of [Liu & Shu, 2000](#))

$$V^k = \{v : v|_{I_j} \in Q^k(I_j), \forall I_j \in \mathcal{T}\}, \quad (2.35)$$

$$W_0^k = V^k \cap C_0(\Omega), \quad (2.36)$$

where $Q^k(I_j)$ is the space of polynomials in N variables with each variable degree at most k for $z \in I_j$.

We note that the gyrokinetic equation (2.1) can be written in the general form

$$\frac{\partial}{\partial t}(\mathcal{J}f) + \frac{\partial}{\partial z^j}(\mathcal{J}\dot{z}^j f) = 0, \quad (2.37)$$

where the coordinates $\mathbf{z} = (z^1, z^2, z^3, z^4, z^5) = (x, y, z, v_\parallel, \mu)$ and $\dot{z}^i = dz^i/dt = \{z^i, H\}$, The Poisson bracket can be written as

$$\{f, g\} = \frac{\partial f}{\partial z^i} \Pi^{ij} \frac{\partial g}{\partial z^j}, \quad (2.38)$$

so $\dot{z}^i = \Pi^{ij}\partial H/\partial z^j$. The Poisson matrix Π is assumed to be antisymmetric. As a consequence of this antisymmetry, the component of the characteristic velocities normal to a surface is continuous on that surface. This means that $\mathbf{n} \cdot \dot{\mathbf{z}}$ evaluated at an interface between two cells has the same value when approached from either side of the interface. Equivalently, this means that $\mathbf{n} \cdot \dot{\mathbf{z}}$ evaluated on the interface between two cells can be correctly evaluated using the solution from only one of the cells. To see this, we compute

$$\mathbf{n} \cdot \dot{\mathbf{z}} = n_i \Pi^{ij} \partial H / \partial z^j = \tau^i \partial H / \partial z^j = \boldsymbol{\tau} \cdot \nabla H, \quad (2.39)$$

⁴The numerical tests of [Liu & Shu \(2000\)](#) did not actually use basis sets that satisfied these properties.

which is a term that will appear in surface integrals when we perform an integration by parts on the weak form of the advection equation. We also see that $\boldsymbol{\tau}$ is orthogonal to \mathbf{n} :

$$\boldsymbol{\tau} \cdot \mathbf{n} = n_i \Pi^{ij} n_j = \{\mathbf{n}, \mathbf{n}\} = 0. \quad (2.40)$$

Since we have required that the Hamiltonian be continuous, we see from (2.39) and (2.40) that $\mathbf{n} \cdot \dot{\mathbf{z}}$ is continuous on cell surfaces. While $\mathbf{n} \cdot \nabla H$ can be discontinuous at cell surfaces because H is only required to be C^0 continuous, $\boldsymbol{\tau} \cdot \nabla H$ will be continuous on a surface if H is also continuous on that surface.

As in standard DG methods, we multiply the gyrokinetic equation (2.1) by a test function v and integrate over each cell I_j :

$$\int_{I_j} d\Lambda v \frac{\partial}{\partial t} (\mathcal{J}f) + \oint_{\partial I_j} dS v \mathcal{J} \mathbf{n} \cdot \dot{\mathbf{z}} \hat{f} - \int_{I_j} d\Lambda \mathcal{J} \nabla v \cdot \dot{\mathbf{z}} f = 0. \quad (2.41)$$

By taking $v = 1$ and summing over all cells, we see that particle number is conserved by the discrete scheme (assuming that the constant 1 is in the approximation space):

$$\begin{aligned} \sum_{I_j} \int_{I_j} d\Lambda \frac{\partial}{\partial t} (\mathcal{J}f) + \oint_{\partial I_j} dS \mathcal{J} \mathbf{n} \cdot \dot{\mathbf{z}} \hat{f} &= 0 \\ \frac{\partial}{\partial t} \left(\sum_{I_j} \int_{I_j} d\Lambda \mathcal{J}f \right) &= 0. \end{aligned} \quad (2.42)$$

For the 5D gyrokinetic system, $\mathcal{J}\boldsymbol{\Pi}$ has the following form (see (2.2)):

$$\mathcal{J}\boldsymbol{\Pi} = \begin{pmatrix} 0 & -b_z/q_s & b_y/q_s & B_x^*/m_s & 0 \\ b_z/q_s & 0 & -b_x/q_s & B_y^*/m_s & 0 \\ -b_y/q_s & b_x/q_s & 0 & B_z^*/m_s & 0 \\ -B_x^*/m_s & -B_y^*/m_s & -B_z^*/m_s & 0 & 0 \\ 0 & 0 & 0 & 0 & 0 \end{pmatrix}. \quad (2.43)$$

Following a standard finite-element approach, in order to satisfy continuity constraints on the potential, we project the gyrokinetic Poisson equation onto the space of basis functions for the potential, yielding a single non-local 3D solve to find the potential. Multiplying (2.4) by a test function w and integrating over the entire configuration-space domain Ω_x (not just over an individual cell, since the basis functions for ϕ couple the cells together):

$$-\int_{\Omega_x} d^3x w \nabla_{\perp} (\epsilon \nabla_{\perp} \phi) = \int_{\Omega_x} d^3x w \sigma_g, \quad (2.44)$$

where $\epsilon = n_{i0}^g q_i^2 \rho_{s0}^2 / T_{e0}$. There are ways to solve (2.44) by performing a set of independent 2D solves, followed by a local self-adjoint smoothing/interpolation operation, but we have not yet implemented this potentially more efficient approach. Although

a non-local solve in three dimensions is required for the potential, the 5D gyrokinetic equation itself can be solved in a highly local manner.

We can see that there will be a conserved energy by taking v to be the discrete Hamiltonian:

$$\int_{I_j} d\Lambda H \frac{\partial}{\partial t} (\mathcal{J}f) + \oint_{\partial I_j} dS H \mathcal{J} \mathbf{n} \cdot \dot{\mathbf{z}} \hat{f} - \int_{I_j} d\Lambda \mathcal{J} \nabla H \cdot \dot{\mathbf{z}} f = 0. \quad (2.45)$$

The third term is zero because $\nabla H \cdot \dot{\mathbf{z}} = \{H, H\} = 0$. By summing (2.45) over all elements, the second term vanishes because the surface integrals not on the domain boundaries appear in equal and opposite pairs due to the C^0 continuity of H , while the surface integrals on the domain boundaries are zero by boundary conditions (e.g., zero flux or $\phi = 0$). Therefore, we have

$$\sum_{I_j} \int_{I_j} d\Lambda H \frac{\partial}{\partial t} (\mathcal{J}f) = 0. \quad (2.46)$$

To identify the conserved energy for the gyrokinetic system, we insert the discrete Hamiltonian into (2.46) and sum over all species:

$$\sum_s \sum_{I_j} \int_{I_j} d\Lambda \left(\frac{1}{2} m_s v_{\parallel}^2 + \mu B + q_s \phi \right) \frac{\partial}{\partial t} (\mathcal{J}f_s) = 0. \quad (2.47)$$

Carrying out the velocity-space integrals and identifying the first two terms as a thermal energy, we have

$$\frac{\partial W_k}{\partial t} + \sum_{I_j} \int_{I_j} d^3x \phi \frac{\partial \sigma}{\partial t} = 0, \quad (2.48)$$

where $W_k = \sum_s \sum_{I_j} \int_{I_j} d\Lambda (m_s v_{\parallel}^2 / 2 + \mu B) \mathcal{J}f_s$ and the species summation on the last term was carried out to write it in terms of the gyrocenter charge density σ . Next, we take a time derivative of (2.44) and set $w = \phi$ to get

$$\begin{aligned} \int_{\Omega} d^3x \phi \frac{\partial \sigma_g}{\partial t} &= - \int_{\Omega} d^3x \phi \nabla_{\perp} \left(\epsilon \nabla_{\perp} \frac{\partial \phi}{\partial t} \right) \\ &= \int_{\Omega} d^3x \epsilon \nabla_{\perp} \phi \frac{\partial \nabla_{\perp} \phi}{\partial t} \\ &= \frac{\partial}{\partial t} \int_{\Omega} d^3x \frac{\epsilon}{2} (\nabla_{\perp} \phi)^2, \end{aligned} \quad (2.49)$$

where the surface terms are zero from the boundary conditions (e.g., periodic or $\phi = 0$ on the side walls). Therefore, we have the energy conservation law for the discrete

system

$$\frac{\partial}{\partial t} (W_k + W_\phi) = 0, \quad (2.50)$$

where the $E \times B$ energy $W_\phi = \int_{\Omega} d^3x \epsilon (\nabla_{\perp} \phi)^2 / 2$.

For simplicity, we use nodal, linear basis functions to approximate the solution in each element for the 5D gyrokinetic simulations in Chapters 4 and 5. This choice leads to 32 degrees of freedom per cell in the 5D phase-space mesh (8 degrees of freedom in the 3D configuration-space mesh). With the 32 degrees of freedom specified in a cell, f can be evaluated anywhere within the cell without additional approximation. With knowledge of the basis functions, we can generate data for plotting without having to rely on approximate interpolation methods. This means that the data we show in various plots in this thesis have not been filtered or smoothed in post processing to make a more visually attractive image. Some more details about the plotting procedures used to create figures for this thesis are provided in Appendix A.

The choice of a linear-polynomial basis set means that v_{\parallel}^2 , which appears in the Hamiltonian (2.3), cannot be exactly represented. We therefore approximate v_{\parallel}^2 in the linear basis set by requiring that the piecewise-linear approximation equal v_{\parallel}^2 at the DG nodes. These nodes are located on the vertices of uniform rectangular cells, so the nodes of cell j either have $v_{\parallel} = v_{c,j} - \Delta v_{\parallel}/2$ or $v_{\parallel} = v_{c,j} + \Delta v_{\parallel}/2$, where $v_{c,j}$ is the v_{\parallel} coordinate of the center of cell j . By approximating v_{\parallel}^2 in such a manner, v_{\parallel}^2 will vary linearly in cell j from $(v_{c,j} - \Delta v_{\parallel}/2)^2$ to $(v_{c,j} + \Delta v_{\parallel}/2)^2$. Note that the approximated v_{\parallel}^2 is continuous across elements, as required for numerical energy conservation, and its first derivative is discontinuous across elements, i.e. $\partial_{v_{\parallel}} H = v_{c,j}$. We use rectangular meshes with uniform cell spacing, but we note that most of the DG algorithms discussed in this thesis are trivially generalizable to non-uniform and non-rectangular meshes.

2.3 Collision Operator

Electron-electron and ion-ion collisions are implemented using a Lenard-Bernstein model collision operator (Lenard & Bernstein, 1958)

$$\begin{aligned} C_{ss}[f_s] &= \nu_{ss} \frac{\partial}{\partial \mathbf{v}} \cdot \left[(\mathbf{v} - \mathbf{u}_s) f_s + v_{t,ss}^2 \frac{\partial f_s}{\partial \mathbf{v}} \right] \\ &= \nu_{ss} \frac{\partial}{\partial v_{\parallel}} \left[(v_{\parallel} - u_{\parallel,s}) f_s + v_{t,ss}^2 \frac{\partial f_s}{\partial v_{\parallel}} \right] + \nu_{ss} \frac{\partial}{\partial \mu} \left[2\mu f_s + 2 \frac{m_s v_{t,ss}^2}{B} \mu \frac{\partial f_s}{\partial \mu} \right], \end{aligned} \quad (2.51)$$

where standard expressions are used for collision frequency ν_{ss} (Huba, 2013, p. 37), $n_s v_{t,ss}^2 = \int d^3v (\mathbf{v} - \mathbf{u}_s)^2 f_s / 3$, and $n_s u_{\parallel,s} = \int d^3v v_{\parallel} f_s$. The exact expressions used

in our simulations for ν_{ee} and ν_{ii} are (Fitzpatrick, 2011)

$$\nu_{ee} = \frac{n_e(\mathbf{R}, t)e^4 \ln \Lambda}{6\sqrt{2}\pi^{3/2}\epsilon_0^2\sqrt{m_e}T_e(\mathbf{R}, t)^{3/2}}, \quad (2.52)$$

$$\nu_{ii} = \frac{n_i(\mathbf{R}, t)e^4 \ln \Lambda}{12\pi^{3/2}\epsilon_0^2\sqrt{m_i}T_i(\mathbf{R}, t)^{3/2}}, \quad (2.53)$$

where $\ln \Lambda = 6.6 - 0.5 \ln(n_0/10^{20}) + 1.5 \ln T_{e0}$ is Coulomb logarithm for n_0 expressed in m^{-3} and T_e expressed in eV. As implied by these expressions, the variation of densities and temperatures in time and in space is taken into account for the collision frequencies used in the code, except in the Coulomb logarithm.

This collision operator relaxes to a local Maxwellian, contains pitch-angle scattering, and analytically conserves number, momentum, and energy. Note that the collision frequency is independent of velocity; the v^{-3} dependence of the collision frequency expected for Coulomb collisions is neglected. This collision operator is long wavelength and ignores finite-gyroradius corrections, which lead to classical cross-field diffusion. This model operator represents many of the key features of the full Landau operator, including velocity-space diffusion that preferentially damps small velocity-space scales, but is much simpler to implement in the code. Collisions with neutrals are neglected at present.

For simplicity, electron–ion collisions are also modeled using Lenard–Bernstein collision operator rather than an operator that only causes pitch-angle scattering:

$$C_{ei}[f_e] = \nu_{ei} \frac{\partial}{\partial v_{\parallel}} \left[(v_{\parallel} - u_{\parallel,i}) f_e + v_{t,ei}^2 \frac{\partial f_e}{\partial v_{\parallel}} \right] + \nu_{ei} \frac{\partial}{\partial \mu} \left[2\mu f_e + 2 \frac{m_e v_{t,ei}^2}{B} \mu \frac{\partial f_e}{\partial \mu} \right], \quad (2.54)$$

where $\nu_{ei} = \nu_{ee}/1.96$ is used in the simulations and $n_e v_{t,ei}^2 = \int d^3v (\mathbf{v} - \mathbf{u}_i)^2 f_e / 3$. The coefficients are chosen so that the electrons relax to become isotropic in the frame of the mean ion velocity, and conserves energy while losing mean momentum to the ions. Because electron–electron collisions cause both pitch-angle scattering and energy diffusion, we set ν_{ei} to a smaller value than ν_{ee} . The corresponding small change in the ion velocity is neglected, leading to a small $\mathcal{O}(m_e/m_i)$ violation of momentum conservation. The very slow energy exchange due to the C_{ie} operator is also neglected.

The collision operators that we have implemented are constructed to numerically conserve number and energy, but do not conserve momentum. Analytical expressions for the forms of $u_{\parallel,s'}$ and $v_{t,ss'}^2$ necessary for exact numerical conservation momentum and energy are difficult to derive due to the complicated nature of the calculation of diffusion terms (see the following section). Number conservation comes from the fact that the DG method solves the collision operators in a weak form and the polynomial space spanned by the basis functions includes the constant 1. Energy conservation is achieved by choosing the numerical value of $v_{t,ss'}^2$ by first calculating the power of the

drag and diffusion terms, e.g.,

$$P_{\text{drag}} = \nu_{ss'} \int d\Lambda H \left(\frac{\partial}{\partial v_{\parallel}} [(v_{\parallel} - u_{\parallel,ss'}) f_s] + \frac{\partial}{\partial \mu} (2\mu f_s) \right) \quad (2.55)$$

$$P_{\text{diff}} = \nu_{ss'} \int d\Lambda H \left[v_{t,ss'}^2 \frac{\partial^2 f_s}{\partial v_{\parallel}^2} + \frac{\partial}{\partial \mu} \left(2 \frac{m_s v_{t,ss'}^2}{B} \mu \frac{\partial f_s}{\partial \mu} \right) \right], \quad (2.56)$$

and then multiplying the diffusion terms in (2.51) or (2.54) by a near-unity constant such that energy is exactly conserved by the collision operator:

$$\begin{aligned} C_{ss'}[f_s] &= \nu_{ss'} \frac{\partial}{\partial v_{\parallel}} \left[(v_{\parallel} - u_{\parallel,ss'}) f_s + c_E v_{t,ss'}^2 \frac{\partial f_s}{\partial v_{\parallel}} \right] \\ &\quad + \nu_{ss'} \frac{\partial}{\partial \mu} \left[2\mu f_s + 2c_E \frac{m_s v_{t,ss'}^2}{B} \mu \frac{\partial f_s}{\partial \mu} \right], \end{aligned} \quad (2.57)$$

where $c_E = -P_{\text{drag}}/P_{\text{diff}} \approx 1$. This choice to conserve energy is not unique. In principle, a similar procedure can be used to construct a same-species collision operator that also numerically conserves momentum, but we have not yet done this.

2.3.1 Second-Order Derivatives

Second-order derivatives in the collision operator are calculated using the recovery-based DG method (van Leer & Nomura, 2005), which has the desirable property of producing symmetric solutions. Originally, we used the popular local discontinuous Galerkin method (Cockburn & Shu, 1998a) for the second-order derivatives, but the asymmetries inherent to the use of alternating fluxes combined with the positivity-adjustment procedure described in Section 2.4 led to large, unphysical asymmetries (such as in the flow) in our LAPD simulations. We note that we do not need to follow the approach of van Leer *et al.* (2007) for 2D diffusion problems because the grids we used are composed of quadrilaterals.

Before we discuss how we apply the recovery-based DG method in our 5D simulations, we will first review how this method is used to solve diffusion equations in 1D. Consider the diffusion equation

$$\frac{\partial f}{\partial t} = D \frac{\partial^2 f}{\partial v^2}, \quad (2.58)$$

where D is a positive diffusion coefficient. To enforce the Galerkin condition (2.8) element by element, we multiply (2.58) by each basis function ψ_k and then integrate by parts:

$$\int_{I_j} dv \psi_k \frac{\partial f}{\partial t} = D \psi_k \frac{\partial f}{\partial v} \Big|_{v_{j-\frac{1}{2}}}^{v_{j+\frac{1}{2}}} - D \int_{I_j} dv \frac{\partial \psi_k}{\partial v} \frac{\partial f}{\partial v}. \quad (2.59)$$

In the recovery-based DG method, one more integration by parts is performed, and we have

$$\int_{I_j} dv \psi_k \frac{\partial f}{\partial t} = D \left(\psi_k \frac{\partial f_r}{\partial v} - \frac{\partial \psi_k}{\partial v} f_r \right) \Big|_{v_{j-\frac{1}{2}}}^{v_{j+\frac{1}{2}}} + D \int_{I_j} dv \frac{\partial^2 \psi_k}{\partial v^2} f \quad (2.60)$$

after replacing f and $\partial_v f$ in the interface terms by a recovered smooth polynomial f_r and its first derivative. The basis function and its derivative evaluated at the interfaces is evaluated from inside I_j . The volume-integral term in (2.60) is zero unless basis functions of degree $p \geq 2$ are used. The recovery polynomial f_r is constructed using the DG solution in two cells sharing a common boundary for the evaluation of f_r and $\partial_v f_r$ on the shared boundary. The recovery polynomial f_r is chosen to be identical in a weak sense to the DG solution f , so it satisfies the following system of equations (see [van Leer & Nomura, 2005](#), p. 13):

$$\left. \begin{aligned} \int_{I_j} dv f_r \psi_k &= \int_{I_j} dv f \psi_k \\ \int_{I_{j+1}} dv f_r \psi_k &= \int_{I_{j+1}} dv f \psi_k \end{aligned} \right\}, \quad k = 0, \dots, p. \quad (2.61)$$

Since there are $2p+2$ pieces of data ($p+1$ pieces of data from each cell) available for the reconstruction, f_r is determined as a polynomial of degree $2p+1$ on $v \in [v_{j-\frac{1}{2}}, v_{j+\frac{3}{2}}]$:

$$f_r(\xi) = f_0 + \xi f'_0 + \frac{1}{2} \xi^2 f''_0 + \dots + \frac{1}{(2p+1)!} \xi^{2p+1} f_0^{(2p+1)}, \quad (2.62)$$

where $\xi = v - v_{j+\frac{1}{2}}$. [van Leer & Nomura \(2005\)](#) notes that the 1D recovery scheme for the diffusion operator using a piecewise-linear basis is fourth-order accurate. Figure 2.1 illustrates the recovery procedure for a case in which the DG solution is represented using piecewise-linear polynomials (two degrees of freedom per cell). In this figure, a 3rd-order recovery polynomial that spans cells j and $j+1$ is constructed for the evaluation of f_r and $\partial_v f_r$ at $v_{j+\frac{1}{2}}$, which appear in the boundary-flux terms in (2.60).

Commenting on the code implementation of this procedure, we note that we do not need to directly solve (2.61) for f_r . The following discussion is not made in [van Leer & Nomura \(2005\)](#). Instead, f_r can be constructed as a Lagrange interpolation polynomial ([Archer & Weisstein, 2005](#)), requiring that f_r be equivalent to f at a set of $2p+2$ points. From the requirement that f and f_r be identical in the weak sense (2.60), we see that points must be chosen to be the Gauss–Legendre quadrature nodes in each cell for a $p+1$ -point quadrature rule:

$$f_r(\xi) = \sum_{l=0}^{2p+1} f(\xi_l) L_l(\xi), \quad (2.63)$$

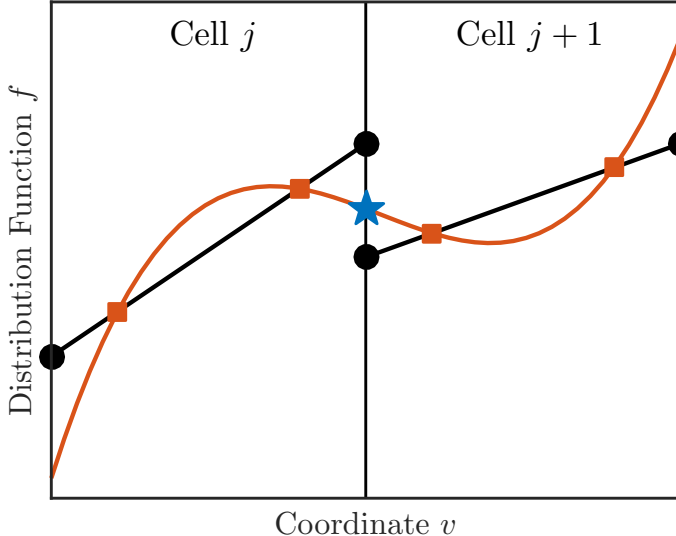


Figure 2.1: Illustration of how a recovery polynomial (red) that spans two neighboring cells is constructed using the DG solution from both cells (black). The recovery polynomial is identical to the DG solution in the weak sense, and it is equivalent to the Lagrange interpolation polynomial that passes through f at the $p + 1$ Gauss–Legendre quadrature points in each cell (red squares). The locally recovered smooth solution and its derivatives are used in the evaluation of fluxes on the shared boundary (blue).

where the ξ_l and ξ_k are the Gauss–Legendre quadrature nodes and

$$L_l(\xi) = \prod_{\substack{k=0 \\ k \neq l}}^{2p+1} \frac{\xi - \xi_k}{\xi_l - \xi_k}. \quad (2.64)$$

We emphasize that the equivalence of the two approaches to obtain f_r only holds when nodes for the $p + 1$ point Gauss–Legendre quadrature rule are used in the Lagrange interpolation polynomial. Almost always, we use a Gauss–Legendre quadrature rule with more points everywhere else in the code,⁵ and so it is important not to mix up the use of these different quadrature rules in the code.

For completeness, we also note that

$$\frac{\partial L_l}{\partial \xi} = L_l(\xi) \sum_{\substack{k=0 \\ k \neq l}}^{2p+1} \frac{1}{\xi - \xi_k}, \quad (2.65)$$

which is useful for computing f'_r . Therefore, we can easily pre-compute matrices that calculate the vector $[f_r(\xi = 0), f'_r(\xi = 0)]$ when multiplied by a vector containing the degrees of freedom in two neighboring elements.

⁵ The reason for using a quadrature rule with more than $p + 1$ points is so that certain integrals can be evaluated exactly.

Now, we discuss the extension of the 1D recovery procedure to higher dimensions, specifically 2D. In the simulations presented in this thesis, diffusion terms appear in the collision operators like (2.51), so an implementation of diffusion in (v_{\parallel}, μ) space is required. At present, the (v_{\parallel}, μ) grid is composed of rectangular elements, which greatly simplifies the implementation of the recovery-based DG method. Let us consider the following diffusion equation on the (v_{\parallel}, μ) grid:

$$\frac{\partial f}{\partial t} = D \frac{\partial}{\partial \mu} \left(\mu \frac{\partial f}{\partial \mu} \right). \quad (2.66)$$

As before, we multiply this equation by each basis function ψ_k and integrate over all space, performing two integration by parts:

$$\begin{aligned} \iint_{I_j} dv_{\parallel} d\mu \psi_k \frac{\partial f}{\partial t} &= D \int_{\partial I_j} dv_{\parallel} \left[\psi_k \mu \frac{\partial f_r}{\partial \mu} - \frac{\partial \psi_k}{\partial \mu} \mu f_r \right] \Big|_{\mu_{j-\frac{1}{2}}, R}^{\mu_{j+\frac{1}{2}}, L} \\ &\quad + D \iint_{I_j} dv_{\parallel} d\mu \left(\frac{\partial^2 \psi_k}{\partial \mu^2} \mu + \frac{\partial \psi_k}{\partial \mu} \right) f. \end{aligned} \quad (2.67)$$

The boundary fluxes are now computed as surface integrals in v_{\parallel} involving f_r and $\partial_{\mu} f_r$, and f_r is a function of both v_{\parallel} and μ . Specifically, f_r is degree p in v_{\parallel} and degree $2p+1$ in μ , which results in polynomial expansion involving $2(p+1)^2$ monomials and matches the total available degrees of freedom from the two neighboring cells. The recovery polynomial satisfies

$$\left. \begin{aligned} \iint_{I_j} dv d\mu f_r \psi_k &= \iint_{I_j} dv d\mu f \psi_k \\ \iint_{I_{j+1}} dv d\mu f_r \psi_k &= \iint_{I_{j+1}} dv d\mu f \psi_k \end{aligned} \right\}, \quad k = 0, \dots, p. \quad (2.68)$$

As before, we do not need to directly solve (2.68) for the $2(p+1)^2$ monomial coefficients of f_r , although this approach is certainly a valid one. Instead, we can directly compute what we ultimately need from the recovery-based DG method, i.e. the values of f_r and $\partial_{\mu} f_r$ evaluated at the surface quadrature points. To do this, we recover a 1D polynomial in μ that spans both cells at *at every surface quadrature node*. The linear variation in v_{\parallel} of f_r is automatically contained in the basis functions ψ_k , and the results of performing a separate 1D recovery calculation at every surface quadrature node are equivalent to those obtained from solving (2.68) for f_r and interpolating f_r to the surface quadrature nodes for evaluation of the boundary fluxes.

The 2D recovery-based DG method currently implemented in the code is illustrated in figure 2.2, where a 3-point quadrature rule is used for the numerical evaluation of the $\int dv_{\parallel}$ surface integral as an example of a case in which a higher-order quadrature rule is needed to evaluate integrals exactly. At each surface quadrature node, a 1D recovery procedure is performed to calculate the value of f_r and $\partial_{\mu} f_r$ there. Therefore, f needs to be evaluated at certain points in the cell (the red squares in

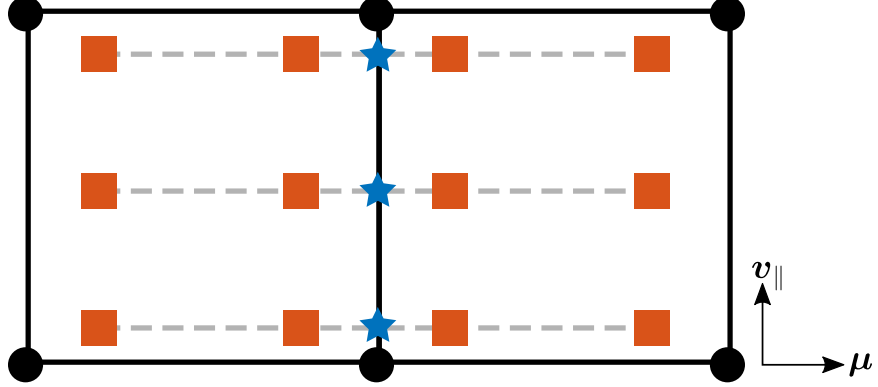


Figure 2.2: Illustration of how 1D recovery polynomials are constructed for the evaluation of diffusion terms in 2D. Two neighboring elements are shown here ($p = 1$), with the solution nodes located at the black circles. At each surface quadrature point (blue stars), a high-order, 1D Lagrange polynomial of degree $2p + 1$ that passes through the solution at a set of $2p + 2$ points (red squares) is constructed, which is the locally recovered smooth solution. The recovered polynomial that passes through each surface quadrature point is then used to compute the local value of f_r and $\partial_\mu f_r$.

figure 2.2) to facilitate these calculations. Since the collision operator also contains a term for diffusion in v_{\parallel} , an analogous procedure is performed on the shared cell boundaries in v_{\parallel} .

2.3.2 Numerical Tests

Here, we present a benchmark of the self-species collision operator (2.51) by solving the equation $\partial_t f_e = C_{ee}[f_e]$ from $t = 0$ to $t = 10 \mu\text{s}$. For this test, the 5D distribution function for electrons is initialized to a top-hat distribution with temperature T_{tar} :

$$f(v_{\parallel}, \mu) = \begin{cases} c_n & \mu \leq \mu_0 \text{ and } u_0 - v_0 \leq v_{\parallel} \leq u_0 + v_0, \\ 0 & \text{otherwise,} \end{cases} \quad (2.69)$$

where c_n is chosen so that the density of discretized distribution function is exactly $2 \times 10^{18} \text{ m}^{-3}$, u_0 is arbitrarily set to $\sqrt{T_{\text{tar}}/m_e}$, $v_0 = \sqrt{3T_{\text{tar}}/m_e}$, $\mu_0 = 2T_{\text{tar}}/B_0$, and $B_0 = 0.0398 \text{ T}$. The distribution function is initialized according to (2.69) at nodes, i.e. (2.69) is evaluated at each of the 32 nodes in a 5D element to set the value of f for the initial condition.

The velocity-space grid covers $v_{\parallel} \in [-4\sqrt{T_{e,\text{grid}}/m_s}, 4\sqrt{T_{e,\text{grid}}/m_s}]$, where $T_{e,\text{grid}} = 3 \text{ eV}$, and $\mu \in [0, 0.75m_e v_{\parallel,\text{max}}^2 / (2B_0)]$. Ten cells are used in v_{\parallel} , and five cells are used in μ . A single cell is used in the position-space dimensions for this 5D test, which allows this test to be executed on a single processor. A realistic (not reduced) collision frequency is used and no positivity-correction procedures (discussed in Section 2.4) are applied. Figure 2.3 shows the initial and final states of the distribution function for this test with $T_{\text{tar}} = 3 \text{ eV}$. The distribution function

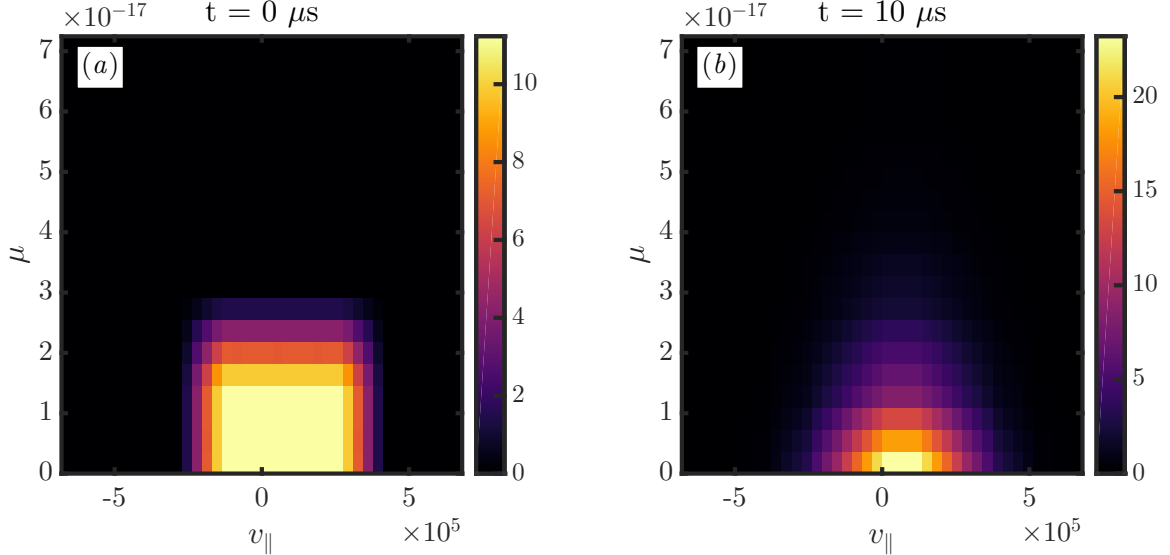


Figure 2.3: Comparison of (a) initial and (b) final distribution function for the collision operator benchmark with $T_{\text{tar}} = 3 \text{ eV}$.

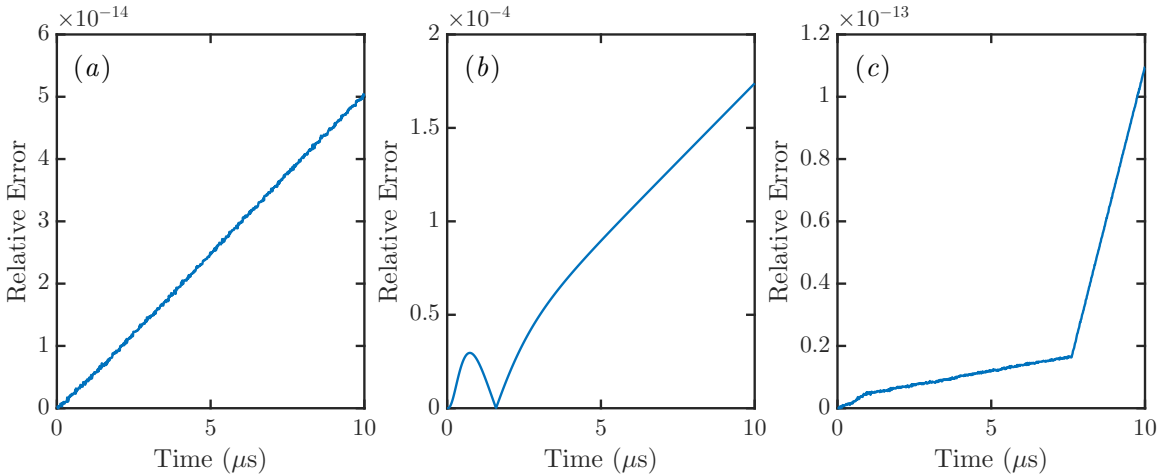


Figure 2.4: Time evolution of the relative error in (a) number, (b) momentum, and (c) energy for a collision operator test.

visually appears to relax to a Maxwellian distribution function, as expected. Figure 2.4 shows the number, momentum, and energy-conservation properties of the collision operator, as measured in this benchmark. The use of a CFL number of 0.1 results in time steps of size $\Delta t = 1.29552 \times 10^{-8} \text{ s}$, so 772 RK3 time steps are taken to advance the distribution function from $t = 0$ to $t = 10 \mu\text{s}$ ⁶.

To motivate the discussion in the next section about positivity issues, we run the same collision-operator benchmark, but initialize the distribution function with a much colder temperature. The grid is still based on $T_{e,\text{grid}} = 3 \text{ eV}$, but the distribution

⁶A final time step of size $\Delta t = 1.15754 \times 10^{-8} \text{ s}$ is taken so that the end time is exactly 10 μs .

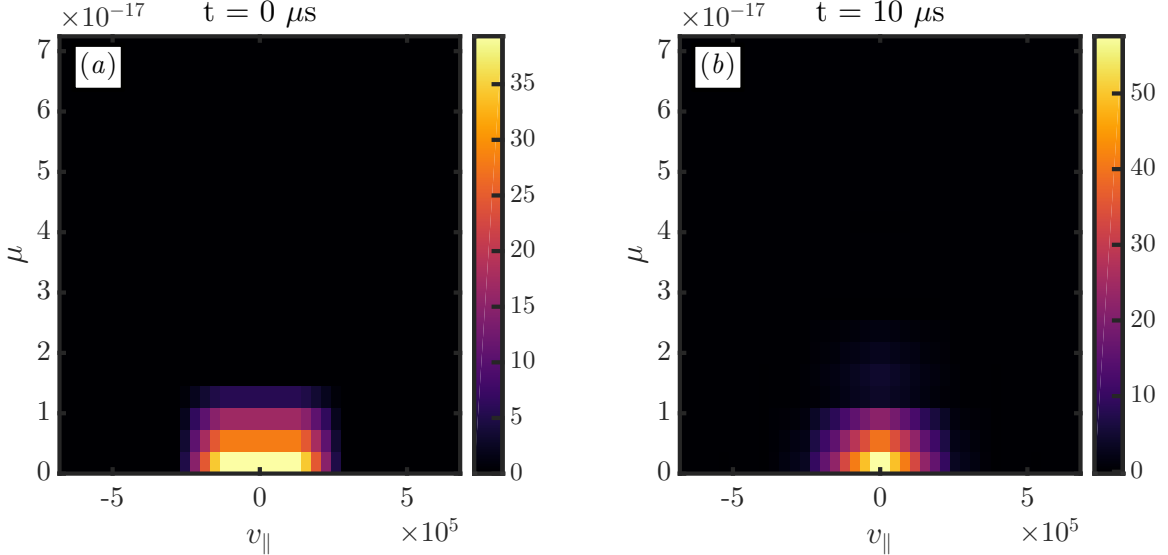


Figure 2.5: Comparison of (a) initial and (b) final distribution function for the collision operator test with $T_{\text{tar}} = 1 \text{ eV}$.

function has temperature $T_{\text{tar}} = 1 \text{ eV}$, which is below the minimum T_{\perp} that can be represented on the grid. By initializing the distribution function in a nodal manner, the initial numerical value of T_{\perp} for the distribution function will be the minimum T_{\perp} and not 1 eV. Figure 2.5 shows the initial and final states of the distribution function for this test, which still appear reasonable. Upon closer inspection of the distribution function, however, we see that negative regions now appear at large v_{\parallel} and large μ . Figure 2.6 shows plots that focus on the negative regions in the same distribution function from figure 2.5. These negative regions of the distribution function are unphysical and can lead to issues with code stability. For example, these negative regions can grow over time and eventually cause the calculation of the density or temperature at a location \mathbf{R} to be negative.

2.4 Positivity of the Distribution Function

One challenge with continuum methods is making sure that the distribution function does not go negative. Particle-in-cell methods do not have to deal with this issue. We found it necessary to adjust the distribution function of each species at every time step so that $f_s \geq 0$ at every node to avoid stability issues. After much investigation, the main source of negativity in the distribution function in our LAPD simulations (Chapter 4) appears to be the collision operator at locations where the perpendicular temperature of the distribution function is close to the lowest perpendicular temperature that can be represented on the grid.

If one considers a velocity-space grid composed of uniform cells with widths Δv_{\parallel} and $\Delta \mu$ in the parallel and perpendicular coordinates, the minimum temperatures for a realizable distribution are computed by assuming that the distribution function

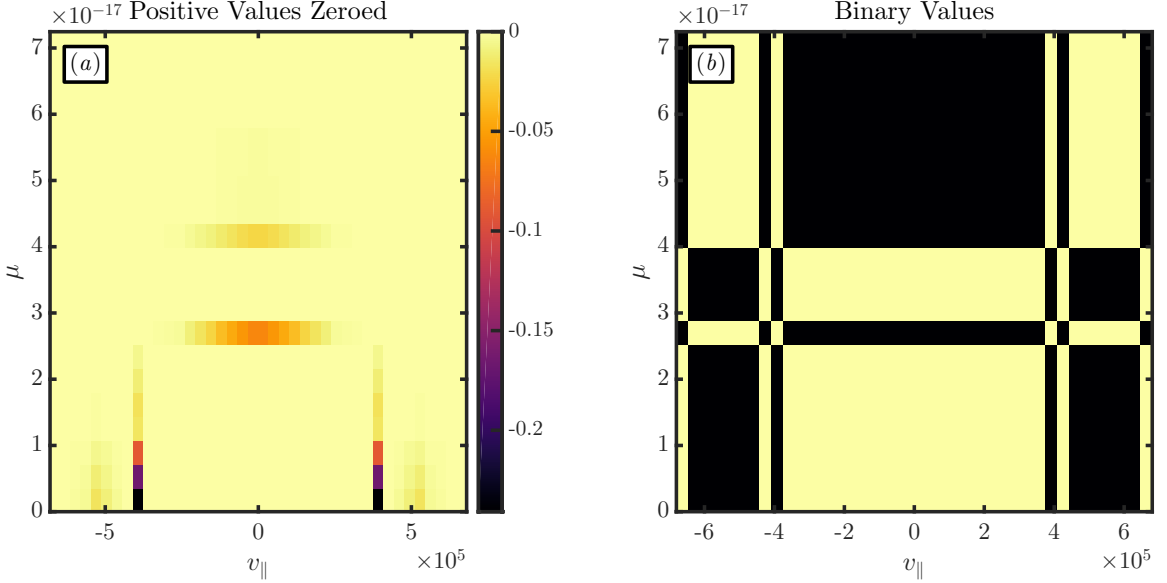


Figure 2.6: Identification of negative regions in the distribution function after evolution to a steady state by the self-species collision operator, showing (a) the distribution function with all positive values set to 0, leaving the negative values unmodified and (b) the negative regions of the distribution function in black and the positive regions in yellow.

is non-zero at the node located at $(v_{\parallel} = 0, \mu = 0)$ and 0 at all other nodes. Using piecewise-linear basis functions,

$$T_{\parallel,\min} = \frac{m}{6} (\Delta v_{\parallel})^2, \quad (2.70)$$

$$T_{\perp,\min} = \frac{B}{3} \Delta \mu, \quad (2.71)$$

$$T_{\min} = \frac{1}{3} (T_{\parallel,\min} + 2T_{\perp,\min}). \quad (2.72)$$

Typical values of Δv_{\parallel} and $\Delta \mu$ for a uniformly spaced grid that contains a few $v_t = \sqrt{T/m}$ usually result in $T_{\parallel,\min} < T_{\perp,\min}$. A situation can occur in which the collision operator will try to relax the T_{\perp} of the distribution function at a location \mathbf{R} to a value below $T_{\perp,\min}$, resulting in negative regions appearing in the distribution function.

This positivity issue might be avoided by choosing a velocity-space grid that has $T_{\parallel,\min} = T_{\perp,\min} = T_{\min}$, either by increasing the resolution in μ relative to the resolution in v_{\parallel} , using non-polynomial basis functions (Yuan & Shu, 2006) that guarantee the positivity of the distribution function, or using $\sqrt{\mu}$ as a coordinate instead of μ . Initial investigation in the use of a non-uniformly spaced grid in μ showed that the positivity issues resulting from the collision operator were nearly eliminated, but more severe positivity issues arose in the kinetic-equation solver. A possible explanation for why the positivity issues in the kinetic-equation solver are not an issue in the case with a uniformly spaced grid in μ is because a much lower $T_{\perp,\min}$ also allows regions

with much lower T_{\parallel} to exist in the simulation (since collisions keep $T_{\perp} \approx T_{\parallel}$, and the LAPD case is highly collisional), and the advection of a distribution function with T_{\parallel} close to $T_{\parallel,\min}$ might result in positivity issues for the kinetic-equation solver.

For now, we use a simpler correction procedure described in this section, which has a philosophy similar to the correction operator used by [Taitano et al. \(2015\)](#). The magnitude of the correction operator scales with the truncation error of the method, and so it vanishes as the grid is refined and does not affect the order of accuracy of the algorithm while making the simulation more robust on coarse grids by preserving key conservation laws. Our relatively simple positivity-adjustment procedure is to eliminate the negative nodes of the distribution functions while keeping the number density and thermal energy unchanged. This procedure is conceptually similar to ‘filling algorithms’, which attempt to remove negative regions in the solution by moving mass in from nearby positive regions ([Durran, 2010](#); [Rood, 1987](#)). First, the number density, parallel energy, perpendicular energy, and parallel momentum for each species are computed. Next, all negative nodes of the distribution functions are set to zero, resulting in changes to the thermal energy and density at locations where the distribution functions have been modified. To compensate for the increased density, the distribution function is scaled uniformly in velocity space at each configuration-space node to restore the original density. In cases which the original density at a location \mathbf{R} is negative to begin with, a Maxwellian distribution with zero flow velocity and a temperature profile identical to the initial condition is added to both species such that the density of both species at that location is above some floor value (we used $n_{\text{floor}} = 10^{-5} n_0$ in our tests in Chapter 4) and the charge density σ_g is unchanged.

The remaining task is to modify the distribution function so that no additional energy is added through the positivity-adjustment procedure. To remove parallel thermal energy $\int d^3v m_s v_{\parallel}^2 f_s / 2$ added through the positivity-adjustment procedure, we use a numerical drag term of the form

$$\frac{\partial f}{\partial t} = \frac{\partial}{\partial v_{\parallel}} \left[\alpha_{\text{corr},v_{\parallel}} (v_{\parallel} - u_{\parallel}) f \right], \quad (2.73)$$

where $\alpha_{\text{corr},v_{\parallel}}$ is a small numerical correction drag rate that is chosen each time step to remove the extra parallel energy added. To guarantee that the numerical drag term will not cause any nodes to go negative, this operator is implemented in a finite-volume sense, adjusting the mean values:

$$\frac{\bar{f}_j^{n+1} - \bar{f}_j^n}{\Delta t} = \frac{\alpha_{\text{corr},v_{\parallel}}}{\Delta v_{\parallel}} \left((v_{\parallel} - u_{\parallel})_{j+1/2} \hat{f}_{j+1/2}^n - (v_{\parallel} - u_{\parallel})_{j-1/2} \hat{f}_{j-1/2}^n \right), \quad (2.74)$$

where the interface flux $\hat{f}_{j+1/2}^n = g(\bar{f}_j^n, \bar{f}_{j+1}^n)$ is chosen in an upwind sense according to the sign of $v_{\parallel} - u_{\parallel}$ and \bar{f}_j denotes the cell-averaged value of f_j . To ensure that the parallel drag term does not modify the perpendicular energy $\int d^3v \frac{1}{2} m_s v_{\perp}^2 f_s$, this operator is applied at fixed (\mathbf{R}, μ) . In our tests, we found that $\alpha_{\text{corr},v_{\parallel}}$ cannot be generally chosen to restore the parallel thermal energy at every position-space node, since there is a limit on how large $\alpha_{\text{corr},v_{\parallel}}$ can be while keeping $\bar{f}_j \geq 0$ in every cell.

Instead, we choose $\alpha_{\text{corr},v_{\parallel}}$ to restore the cell-averaged parallel energy

$$\bar{W}_{\parallel,j} = \int_{x_j-\Delta x/2}^{x_j+\Delta x/2} dx \int_{y_j-\Delta y/2}^{y_j+\Delta y/2} dy \int_{z_j-\Delta z/2}^{z_j+\Delta z/2} dz \int d^3v \frac{1}{2} m_s v_{\parallel}^2 f_s, \quad (2.75)$$

which results in some position-space diffusion of energy.

We employ a similar procedure to remove the unphysical perpendicular energy added through positivity:

$$\frac{\partial f}{\partial t} = \frac{\partial}{\partial \mu} (2\alpha_{\text{corr},\mu} \mu f). \quad (2.76)$$

Here, the factor $\alpha_{\text{corr},\mu}$ is chosen to restore the cell-averaged perpendicular energy. Similarly, this operation modifies the perpendicular energy without changing the parallel energy. Generally speaking, all of the parallel energy added through positivity can usually be removed through the numerical drag operator while a small amount (< 10%) of perpendicular energy added through positivity remains even after applying the numerical drag operator, a consequence from the choice of a uniformly spaced grid in μ (energy is typically added in the distribution function tails, so a uniformly spaced energy grid will be more constrained than a quadratically spaced energy grid in removing positivity-added energy using a numerical drag operator). We observe that much of the extra energy added through the positivity-adjustment procedure are in cells located in the outer region $r > 0.4$ m and near the boundaries in the parallel direction where much of it may be quickly lost in the outflows through the sheaths, so we think the extra energy added will not have a significant impact on the turbulence characteristics in the main part of the simulation. (Our present model for the physical source in the LAPD simulations is uniform in z , but there may be a localized source from recycling near the real end plates, which may offset the need for the numerical positivity source there.) Ultimately, we hope to develop a more satisfactory solution to deal with these positivity issues.

2.5 Sheath Boundary Conditions

A layer of net positive charge called the *electrostatic Debye sheath* forms at the plasma–material interface, such as where open magnetic field lines intersect a grounded conducting divertor or limiter in a tokamak. As shown in figure 2.7, the sheath sets up a potential drop that accelerates ions into the wall and repels low-energy electrons, keeping the particle flux of electrons and ions into the wall in approximate balance. Accurate modeling of sheath effects is important for the calculation of particle and heat fluxes to plasma-facing components and plasma–surface interactions. The sheath is a few electron-Debye-lengths wide and forms on a time scale of order the electron plasma period, which are both very disparate scales compared to the turbulence scales of interest in gyrokinetics, so it is natural and desirable to treat the sheath through model boundary conditions to avoid the need to directly resolve it. The implementation of sheath-boundary conditions

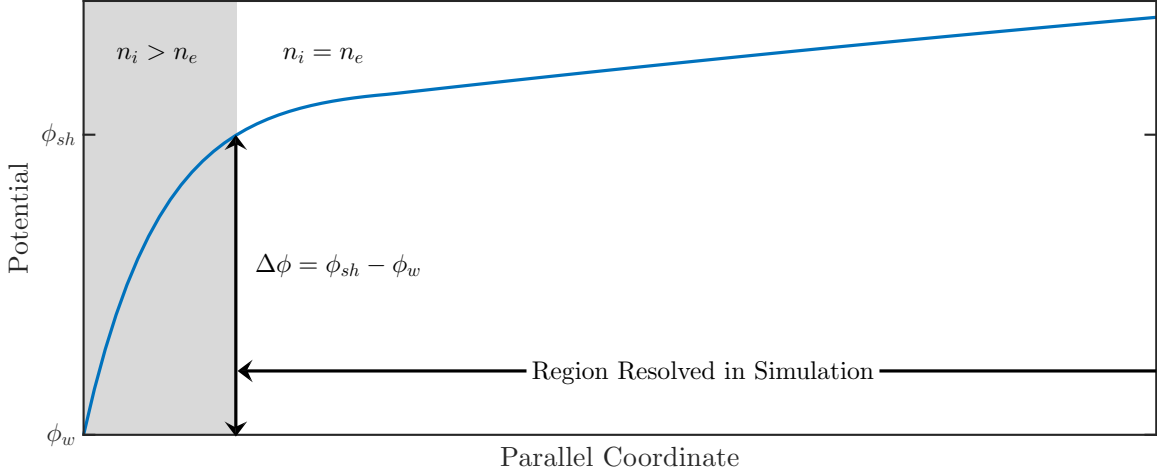


Figure 2.7: Illustration of the potential structure near a plasma–material interface. The shaded region is the Debye sheath, which is a region of net positive charge that is a few electron-Debye-lengths wide. In gyrokinetic simulations, the sheath cannot be resolved since the plasma is assumed to be quasineutral ($\sum_i Z_i n_i = n_e$) and its effects must be modeled using boundary conditions. Additionally, spatial and temporal resolution of the sheath in turbulence simulations is computationally impractical.

should be considered a distinguishing feature of a gyrokinetic code for open-field-line simulations.

The electron Debye length in LAPD is ($\lambda_{De} \sim 10^{-6}$ m), which is very small compared to the ion gyroradius ($\sim 10^{-2}$ m) and even smaller compared to the parallel scales of the turbulence (~ 10 m). The electron plasma frequency is $\omega_{pe} \sim 10^9$ s $^{-1}$, which is much larger compared to the ion gyrofrequency ($\sim 10^6$ s $^{-1}$), and even larger than the turbulence frequencies of interest ($\omega_* \sim 10^4$ s $^{-1}$ at $k_\theta \rho_{s0} \sim 0.3$). Since the quasineutrality and low-frequency assumptions of gyrokinetics break down in the sheath, gyrokinetic models cannot directly handle sheaths. There is also a transition region between the collisional upstream region and the collisionless sheath, with a width of order the mean free path. This region is not resolved in the simulations we have performed. We also note that the end walls (divertor plates) in tokamaks and in basic plasma physics experiments are typically grounded, so sheath-model boundary conditions should be reflective of this situation.

2.5.1 Logical-Sheath Model

The 1D gyrokinetic model with kinetic electrons described in Chapter 3 uses logical-sheath boundary conditions, which were originally developed for fully kinetic 1D2V PIC simulations by Parker *et al.* (1993) to address inaccuracies in sheath effects that were observed when using a direct implicit PIC method with $\Delta t \omega_{pe} > 1$. In that work, the authors needed to use a coarser spatial resolution Δz as the time-step size Δt was increased in order to avoid numerical heating and cooling, so the sheath became increasingly poorly resolved in the implicit limit $\Delta t \omega_{pe} > 1$. Logical-sheath boundary

conditions were developed to model the essential sheath effects in simulations with coarse spatial resolution of the sheath.

Logical-sheath boundary conditions impose the steady state behavior $j_{\parallel} = 0$ to the wall at each instant, and they are sometimes referred to as insulting-wall boundary conditions in fluid models (in contrast to conducting-wall boundary conditions). For a normal, positively charged sheath, all incident ions flow into the wall because they are accelerated by the sheath potential drop, while incident electrons are partially reflected. Only electrons with a high enough parallel velocity can surpass the sheath potential drop and reach the wall, and the rest are reflected back into the plasma. In a logical sheath, the sheath potential is determined from the $j_{\parallel} = 0$ condition, so the lowest-parallel-velocity electrons are reflected to satisfy $j_{\parallel} = 0$, and then the sheath potential is calculated using the v_{\parallel} of the slowest electrons that have enough parallel energy to overcome the sheath potential drop and flow into the wall. No boundaries conditions are applied to the ions in the logical-sheath model.

If logical-sheath boundary conditions are applied at $z = z_R$, the typical $j_{\parallel} = 0$ condition for a 1D1V (one) problem is expressed as

$$\int_0^{\infty} dv_{\parallel} v_{\parallel} f_i(z_R, v_{\parallel}, t) = \int_{v_{\text{cut}}}^{\infty} dv_{\parallel} v_{\parallel} f_e(z_R, v_{\parallel}, t). \quad (2.77)$$

The cutoff velocity $v_{\text{cut}} > 0$ is found numerically by first finding the velocity-space cell in which the cutoff velocity lies ($v_{c,j} - \Delta v_{\parallel}/2 \leq v_{\parallel} \leq v_{c,j} + \Delta v_{\parallel}/2$, where $v_{c,j}$ is the v_{\parallel} in the center of cell j) and then using a bisection method such that (2.77) is satisfied to a desired tolerance level. The sheath potential ϕ_{sh} is then determined using the relation $e\Delta\phi = e(\phi_{sh} - \phi_w) = m_e v_{\text{cut}}^2/2$, where the wall potential ϕ_w is usually taken to be 0 V for a grounded wall. Figure 2.8 illustrates how the incident electrons are partially reflected by the sheath-model boundary conditions.

In order to reflect all electrons incident on the sheath with parallel outgoing velocity in the range $0 < v_{\parallel} < v_{\text{cut}}$, the electron distribution function in this interval is copied into ghost cells according to

$$f_e(z_R, -v_{\parallel}, t) = f_e(z_R, v_{\parallel}, t), \quad 0 < v_{\parallel} < v_{\text{cut}}, \quad (2.78)$$

and $f_e(z_R, -v_{\parallel}, t) = 0$ for $v_{\parallel} > v_{\text{cut}}$. This condition can also be written as $f_e(z_R, -v_{\parallel}, t) = f_e(z_R, v_{\parallel}, t)H(v_{\text{cut}} - v_{\parallel})$ for $v_{\parallel} > 0$. This condition results in the reflection of electrons with velocity in the range $0 < v_{\parallel} < v_{\text{cut}}$ back into the domain with the opposite velocity, while the electrons with energy sufficient to overcome the sheath potential will flow out of the system to the divertor plates.

To summarize, our implementation of the logical sheath in 1D kinetic continuum models with a single ion species has the following steps:

1. Calculate the outward ion and electron fluxes at the sheath entrance, $\Gamma_i = \int_0^{\infty} dv_{\parallel} v_{\parallel} f_i$ and $\Gamma_e = \int_0^{\infty} dv_{\parallel} v_{\parallel} f_e$ respectively.
2. Compare Γ_i to Γ_e to identify the reflected species.
 - $\Gamma_e > \Gamma_i$ (Typical Case): Reflect slowest outgoing *electrons* in next step.

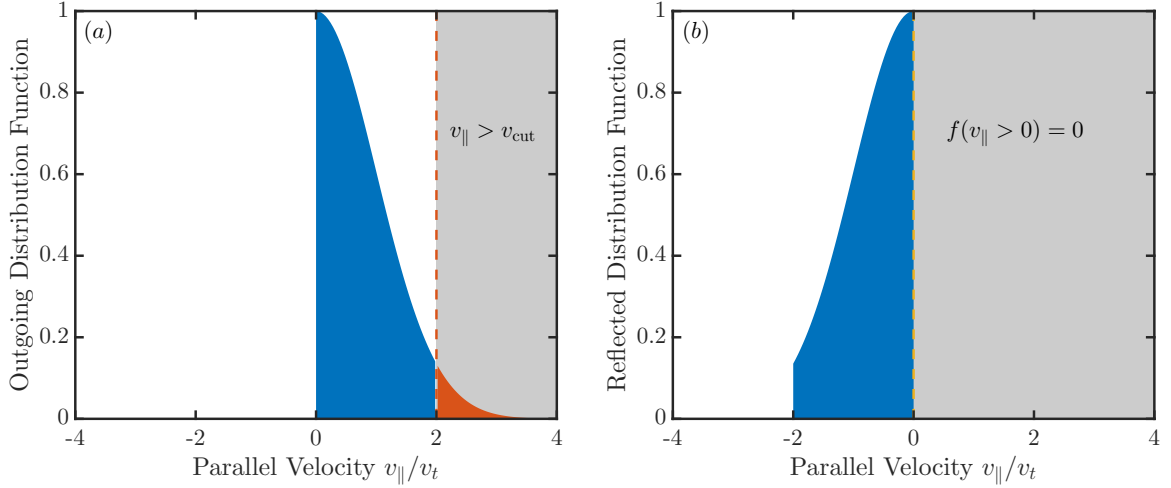


Figure 2.8: Application of sheath boundary conditions to an incident electron distribution function. (a) The distribution function incident to the sheath. The cutoff velocity, determined by the $j_{\parallel} = 0$ condition in the logical-sheath model or by the gyrokinetic Poisson equation in the conducting-sheath model, is indicated by the dashed red line. Electrons with $v_{\parallel} > v_{\text{cut}}$ are in red and have enough energy to surpass the sheath potential, while incident electrons with $v_{\parallel} \leq v_{\text{cut}}$ are reflected back into the plasma. (b) The reflected distribution function is the portion of the incident distribution function that does not have sufficient parallel velocity to overcome the sheath potential, reflected about the $v_{\parallel} = 0$ axis. These particles come back into the plasma.

- $\Gamma_e > \Gamma_i$ (Rare Case): Reflect slowest outgoing *ions* in next step.
- 3. For the reflected species, find v_{cut} , the v_{\parallel} above which particles can overcome the sheath potential drop $\Delta\phi$ and leave the system, such that $\int_{v_{\text{cut}}}^{\infty} dv_{\parallel} v_{\parallel} f_e = \Gamma_i$ if electrons are reflected or $\int_{v_{\text{cut}}}^{\infty} dv_{\parallel} v_{\parallel} f_i = \Gamma_e$ if ions are reflected. Numerically, the cutoff velocity is found using the bisection method.
- 4. For the reflected species, reflect the outgoing distribution function in the interval $0 \leq v_{\parallel} \leq v_{\text{cut}}$ about the $v_{\parallel} = 0$ axis, and copy the result to the boundaries of the appropriate ghost cells.
- 5. Determine the sheath potential ϕ_{sh} from the cutoff velocity as $e\Delta\phi = e(\phi_{sh} - \phi_w) = m_e v_{\text{cut}}^2 / 2$, which will be used as boundary conditions for the gyrokinetic Poisson equation solve.

The implementation of logical-sheath boundary conditions needs a slight modification for use in a continuum code. Typically, the cutoff velocity will fall within a cell and not exactly on a cell edge. A direct projection of the discontinuous reflected distribution onto the basis functions used in a cell could lead to negative values of the distribution function at some velocities in the cell. Future work could consider methods of doing higher-order projections that incorporate positivity constraints, but for now we have used a simple scaling method, in which the entire distribution function

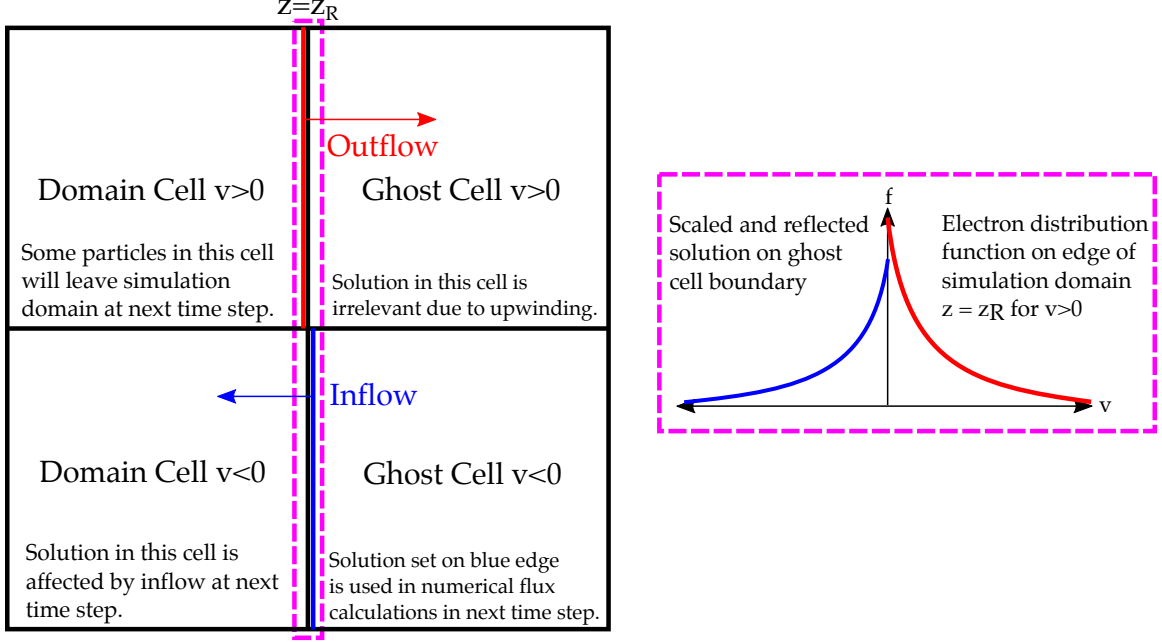


Figure 2.9: An illustration of how the sheath model boundary conditions use ghost cells to set the reflected distribution function. Left: sheath boundary conditions are applied to the distribution function at $z = z_R$, which results in the determination of the reflected distribution function (blue edge) in the ghost cell based on the outgoing distribution function (red edge) in the domain cell. Right: the distribution function on the $z = z_R$ boundary after application of sheath boundary conditions, which corresponds to the dashed-box region on the left diagram.

inside the ‘cutoff cell’ is copied into the ghost cell and then scaled by the fraction required to ensure that the electron flux at the domain edge equals the ion flux. For scaling the reflected distribution function in the cutoff cell on the right boundary, this fraction is

$$c = \frac{\int_{v_{c,j}-\Delta v_{||}/2}^{v_{\text{cut}}} dv_{||} v_{||} f_e(z_R, v_{||}, t)}{\int_{v_{c,j}-\Delta v_{||}/2}^{v_{c,j}+\Delta v_{||}/2} dv_{||} v_{||} f_e(z_R, v_{||}, t)}, \quad (2.79)$$

where $\Delta v_{||}$ is the cell width in $v_{||}$ (assumed to be uniform), and $v_{c,j}$ denotes the $v_{||}$ coordinate of the center of the cutoff cell.

For cells whose parallel velocity extents do not bound v_{cut} , the reflection procedure is straightforward: find the corresponding ghost cell j' with $v_{c,j'} = -v_{c,j}$ and copy the solution after reflection about the $v_{||}$ axis. Figure 2.9 illustrates how ghost cells are used to provide inflow characteristics in sheath-model boundary conditions. In 5D gyrokinetic simulations, this reflection procedure is applied at each position-space node on the upper and lower surfaces in z at the end of the simulation domain, which are assumed to be end plates. Sheath boundary conditions are not applied on the x and y boundaries.

2.5.2 Conducting-Sheath Boundary Conditions

For 5D gyrokinetic simulations, we use conducting-sheath boundary conditions instead of logical-sheath boundary conditions. Based on our success with the logical-sheath boundary conditions in 1D models (Chapter 3), we originally implemented logical-sheath boundary conditions for LAPD simulations, but we encountered stability issues. We found better robustness by implementing a set of sheath boundary conditions motivated by how some fluid (or gyrofluid) codes determine ϕ everywhere (including the sheath potential) from the fluid vorticity equation (or polarization equation) and then use the sheath potential to set the boundary condition on the parallel electron velocity (Xu & Cohen, 1998; Rogers & Ricci, 2010; Friedman *et al.*, 2013; Ribeiro & Scott, 2005).

In conducting-sheath boundary conditions, we use the gyrokinetic Poisson equation (2.4) to solve for the potential $\phi(x, y, z)$ everywhere in the simulation domain. The sheath potential $\phi_{sh}(x, y)$ on each boundary in z (where the field lines intersect the wall) is obtained by simply evaluating ϕ on that boundary, so at the upper boundary in z , $\phi_{sh}(x, y) = \phi(x, y, L_z/2)$. The wall is taken to be just outside the simulation domain and the wall potential ϕ_w is 0 for a grounded wall. Outgoing particles with $\frac{1}{2}m_s v_\parallel^2 < -q_s(\phi_{sh} - \phi_w)$ are reflected (e.g., when $\phi_{sh} - \phi_w$ is positive, some electrons will be reflected), while the rest of the outgoing particles leave the simulation domain.

In the conducting-sheath approach, the sheath potential is determined by other effects (the gyrokinetic Poisson equation or the related fluid vorticity equation in fluid simulations) and is used to determine what fraction of electrons are reflected and thus the resulting currents to the wall. In contrast to the logical-sheath model, the conducting-sheath model allows parallel current fluctuations into the wall, since the $\Gamma_i = \Gamma_e$ condition is never directly imposed, with steady-state current paths closing through the walls. As we show in Chapters 4 and 5, we observe large local current fluctuations and local steady-state currents in some simulations, so qualitative differences might be expected between logical-sheath or conducting-sheath boundary conditions. If one starts with an initial condition where $\sigma_g = 0$ in (2.4) so $\phi = 0$, then electrons will rapidly leave the plasma, causing the gyrocenter charge σ_g to rise to be positive, and thus the sheath potential will quickly rise to reflect most of the electrons, and bring the sheath currents down to a much smaller level, while allowing the sheath currents to self-consistently fluctuate in interactions with the turbulence.

The boundary condition we use for ions is the same as the one used in the logical-sheath model (Parker *et al.*, 1993) (a variant of which are used in the XGCa and XGC1 gyrokinetic PIC codes (Churchill *et al.*, 2016)): the ions just pass out freely at whatever velocity they have been accelerated to by the potential drop from the upstream source region to the sheath entrance. The only boundary condition that the sheath model imposes on the ions is that there are no incoming ions, i.e. at the incoming lower sheath boundary we have the boundary condition that $f_i(x, y, z = -L_z/2, v_\parallel, \mu) = 0$ for all $v_\parallel \geq 0$. While this leads to a well-posed set of boundary conditions and appears to give physically reasonable results for the simulations carried out in this thesis, it might need improvements in some parameter regimes.

2.5.3 Future Considerations for Sheath Models

Sheaths have long been studied in plasma physics, including kinetic effects and angled magnetic fields, and there is a vast literature on them. The standard treatments look at steady-state results in one dimension, in which the potential is determined by solving the Poisson equation along a field line (for the case here in which the magnetic field is perpendicular to the surface), but for gyrokinetic turbulence, we need to consider time-varying fluctuations in which the sheath region needs to couple to an upstream gyrokinetic region where the potential is determined in 2D planes perpendicular to the magnetic field by solving the gyrokinetic quasineutrality equation (2.4). The details of how this matching or coupling is carried out may depend on the particular numerical algorithm used and how it represents electric fields near a boundary.

There are a range of possible sheath models of different levels of complexity and accuracy that could be considered in future work. The present model does not guarantee that the Bohm sheath criterion is met, which requires that the ion outflow velocity exceed the sound speed, $u_{\parallel i} \geq c_s$, for a steady-state sheath and in the sheath-entrance region. However, the present simulations of LAPD start at a low density and ramp up the density to an approximate steady state over a period of a few sound transit times, and during this phase, the pressure and potential drop from the central source region to the edges is large enough to accelerate ions to near-sonic velocities. We show in Chapter 4 that the steady-state outflow velocities are very close to or slightly exceed the sound speed in our LAPD simulations.

There could be other cases where the acceleration of ions in the upstream region is not strong enough to enforce the Bohm sheath criterion for a steady-state result. In such a case, some kind of rarefaction fan may propagate from near the sheath, accelerating ions back up to a sonic level. This situation is very similar to the Riemann problem for the expansion of a gas into a vacuum (Munz, 1994) or into a perfectly absorbing surface, which leads to a rarefaction wave that always maintains $u_{\parallel i} \geq c_s$ at the boundary (but also modifies the density and temperature at the outflow boundary because of the rarefaction in the expanding flow). A Riemann solver has been implemented in the two-fluid version of Gkeyll for 1D simulations that resolve the sheath (Cagas *et al.*, 2017), and the results were compared with a fully kinetic solver. Exact and approximate Riemann solvers are often used in computational fluid dynamics to determine upwind fluxes at an interface (LeVeque, 2002; Durrant, 2010). It could be useful to work out a kinetic analogue of this process, or a kinetic model based on the approximate fluid result, but those are beyond the scope of this thesis.

There is ongoing research to develop improved sheath models for fluid codes. In some past fluid simulations of LAPD, the parallel ion dynamics were neglected and modeled by sink terms to maintain a desired steady state on average (Popovich *et al.*, 2010b; Friedman *et al.*, 2012, 2013). Rogers & Ricci (2010) included parallel ion dynamics in their fluid simulations and imposed the boundary condition $u_{\parallel i} = c_s$, thus avoiding the problem of $u_{\parallel i} < c_s$. This boundary condition could be generalized to allow $u_{\parallel i} > c_s$ at the sheath entrance to handle cases in which turbulent fluctuations or other effects give more upstream acceleration (Togo *et al.*, 2016; Dudson & Leddy,

2017). Loizu *et al.* (2012) carried out a kinetic study to develop improved sheath model boundary conditions for fluid codes that include various effects (including the magnetic pre-sheath (Chodura, 1982) in an oblique magnetic field and the breakdown of the ion drift approximation) that have been incorporated into later versions of the GBS code (Halpern *et al.*, 2016).

Chapter 3

1D Scrape-Off-Layer Models

The development of a complex gyrokinetic code begins with the investigation of tests in a spatially one-dimensional geometry. In this chapter, some simple 1D kinetic models of parallel propagation in an open-field-line region are explored. We apply an electrostatic, gyrokinetic-based model to simulate the parallel plasma transport of an edge-localized-mode (ELM) heat pulse in the scrape-off layer (SOL) to a divertor plate. We focus on a test problem that has been studied previously, using parameters chosen to model a heat pulse driven by an ELM in JET. Previous work used direct particle-in-cell (PIC) equations with full dynamics and collisions, or Vlasov or fluid equations with only parallel dynamics. With the use of the gyrokinetic quasineutrality equation and logical-sheath boundary conditions in our model, spatial and temporal resolution requirements are no longer set by the electron Debye length λ_{De} and plasma period ω_{pe}^{-1} , respectively. This test problem also helps illustrate some of the physics contained in the Hamiltonian form of the gyrokinetic equations and some of the numerical challenges in developing a gyrokinetic code for the boundary plasma. The discussion in this chapter on 1D1V models is based on [Shi et al. \(2015\)](#), while the results from 1D2V simulations have not been published before. We note that the work presented here was later used as a test case for a version of the GENE gyrokinetic code that was being extended to handle the SOL using finite-volume methods ([Pan et al., 2016](#)).

3.1 Introduction

One of the major issues for the operation of ITER and subsequent higher-power tokamaks in the high-confinement mode (H-mode) is the power load on plasma-facing components (PFCs) from periodic bursts of energy expelled into the scrape-off layer by Type I ELMs. ELMs are an MHD instability triggered by a steep pressure gradient in the edge plasma (e.g., the H-mode pedestal) that is followed by a loss of plasma stored energy and profile relaxation ([Leonard, 2014](#)). Excessive total and peak power loads from ELM heat pulses can cause melting or ablation of solid surfaces, such as the divertor targets and the main chamber wall ([Pitts et al., 2005](#)). In a single ITER discharge, several hundred ELMs are expected ([Loarte et al., 2007](#)). The ability

to suppress ELMs or at least mitigate the damage they cause to PFCs is crucial for the viability of reactor-scale tokamaks. An accurate prediction of how heat is transported in the plasma boundary in future devices is important for the development of mitigation concepts.

Numerical simulations of ELM heat-pulse propagation are valuable in understanding the time-dependence of power loads on divertor targets due to different sizes of ELMs. Such simulations can also be used to predict the peak divertor surface temperature due to an ELM, which is important for material-erosion considerations. Pitts *et al.* (2007) studied the parallel propagation of an ELM heat pulse in the SOL to a divertor plate using 1D3V PIC simulations, including the effects of collisions. The authors recognized the inadequacy of fluid codes for this task, since they usually employ approximate flux limiters on parallel heat fluxes and assume constant sheath heat-transmission coefficients. The authors simulated ELM crashes with different energies, temperatures, densities, and durations.

Some quantities of interest in the simulations of Pitts *et al.* (2007) included the time variation of sheath heat-transmission factors, how much of the energy deposited on the divertor plate is from electrons, and how much of ELM energy is deposited before the peak heat flux at the divertor plate, which affects the peak surface temperature (Loarte *et al.*, 2007; Leonard, 2014). These simulations were able to reproduce the characteristic heat-flux rise time on the order of the fast-ion (at the pedestal temperature) sound-transit time seen on several machines. The authors found that the fraction of energy deposited before the peak heat flux to be in the range 0.25–0.35, which was consistent with experimental measurements on JET. This agreement with experimental data for low ELM energies provided some confidence in their simulation results for a hypothetical 2.46 MJ ELM (approximating a small Type I ELM on ITER).

Manfredi *et al.* (2011) later developed a Vlasov-Poisson code to study this problem. Havlíčková *et al.* (2012) carried out a benchmark of fluid, Vlasov, and PIC approaches to this problem. An implementation of this test case in BOUT++ was used to compare non-local and diffusive heat-flux models for SOL modeling (Omotani & Dudson, 2013). With the exception of initial conditions, the parameters we have adopted for these simulations are described in Havlíčková *et al.* (2012). This test case involves just one spatial dimension (along the field line), treating an ELM as an intense source near the midplane without trying to directly calculate the magnetohydrodynamic instability and reconnection processes that drive the ELM. Nevertheless, this test problem is useful for testing codes and understanding some of the physics involved in parallel propagation and divertor heat fluxes.

Unlike previous approaches, we have developed and studied gyrokinetic-based models with logical-sheath boundary conditions (Parker *et al.*, 1993) using kinetic electrons or by assuming an adiabatic response for the electrons. As is often done in gyrokinetics, a gyrokinetic quasineutrality equation (which includes a polarization-shielding term) is used, so the Debye length does not need to be resolved. To handle the sheath, logical-sheath boundary conditions (Parker *et al.*, 1993) are used, which maintain zero local net current to the wall at each time step. Logical-sheath boundary conditions are described in detail in Section 2.5.1. Although our simulations are one-

dimensional, perpendicular effects can be incorporated by assuming axisymmetry. In an axisymmetric system, poloidal gradients have components that are both parallel and perpendicular to the magnetic field. The perpendicular ion polarization dynamics then enter the field equation by accounting for the finite pitch of the magnetic field.

A major advantage of the models we have developed is their low computational cost. Earlier kinetic models with explicit time stepping have been described as computationally intensive ([Pitts et al., 2007](#)) due to restrictions in the time step to $\sim\omega_{pe}^{-1}$ and in the spatial resolution to $\sim\lambda_{De}$. A 1D Vlasov model using an asymptotic-preserving implicit numerical scheme described in [Manfredi et al. \(2011\)](#) was only able to relax these restrictions somewhat for this problem, using $\Delta x \sim 2\lambda_{De}$ and $\Delta t \sim 4/\omega_{pe}$ because their simulation still included the sheath directly. By using a gyrokinetic-based model with logical-sheath boundary conditions, we verify that our simulations can use grid sizes and time steps that are several orders of magnitude larger than this and still accurately model the sheath potential drop and the consequent outflow of particles and heat from the SOL. We find that the divertor-plate heat fluxes (electron, ion, and total) obtained in our gyrokinetic simulation are within $\sim 5\%$ of those from a Vlasov–Poisson simulation (see [Havlíčková et al., 2012](#), figure 2). For simplicity, the simulations are fully explicit at present. While fluid models require much fewer computational resources when compared to kinetic models, they miss some kinetic effects, including the effect of hot tail electrons on the heat flux on the divertor plate and the subsequent rise of sheath potential.

In this chapter, we focus on simulations in one spatial dimension using the parameters of for a 0.4 MJ ELM on JET (see [Pitts et al., 2007](#), table 1). Section 3.2 describes an electrostatic 1D gyrokinetic-based model with a modification to the ion polarization term to set a minimum value for the wavenumber. Numerical implementation details and initial conditions are described in Section 3.3. Results from 1D1V numerical simulations are presented in Section 3.4. We later extended our simulations to 1D2V and added a model for self-species collisions. These results, which result in improved agreement with PIC simulations, are presented in Section 3.5. We summarize the main results of this chapter in Section 3.6.

3.2 Electrostatic 1D Gyrokinetic Model with Kinetic Electrons

In this chapter, we focus on the long-wavelength, drift-kinetic limit of gyrokinetics and ignore finite-Larmor-radius effects for simplicity. Polarization effects are kept in the gyrokinetic Poisson equation, and the model has the general form of gyrokinetics.

The geometry used in the ELM heat-pulse test problem is illustrated in figure 3.1. The Vlasov and fluid codes used by [Havlíčková et al. \(2012\)](#) consider only the parallel dynamics, while the 1D3V PIC code used by [Havlíčková et al. \(2012\)](#) includes full-orbit (not gyro-averaged) particle dynamics in an axisymmetric system and so

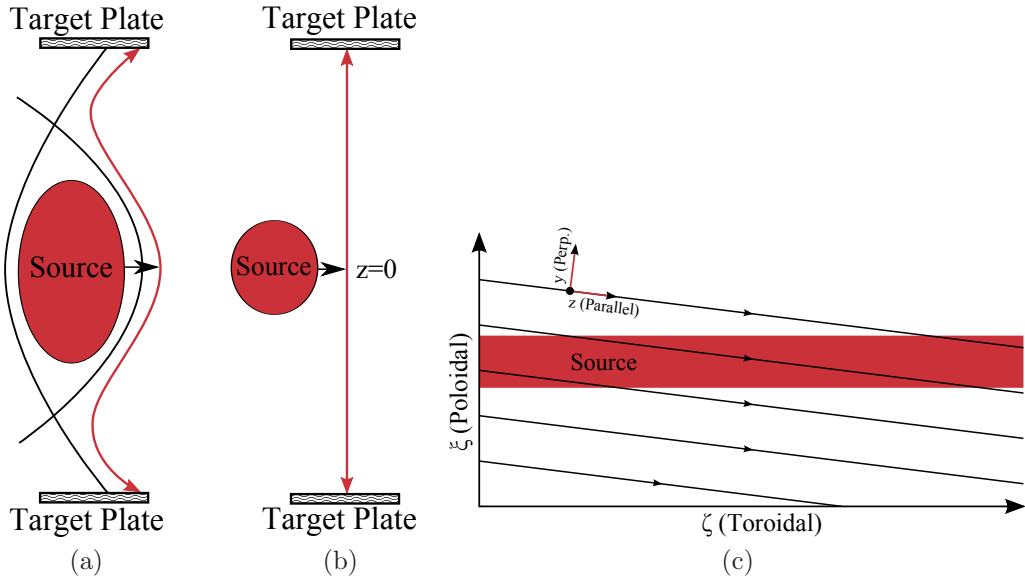


Figure 3.1: Illustration of the geometry used in the ELM heat-pulse test problem. The scrape-off layer region in the poloidal cross section (a) is treated as straight (b) in this test, with the ELM represented by an intense source near the midplane region. The time history of the resulting heat flux to the target plate is calculated in the simulation. The side view (c) illustrates that although there is no toroidal variation in this axisymmetric problem, poloidal variations lead to both parallel and perpendicular gradient components.

would automatically include polarization effects on time scales longer than an ion gyroperiod.

The gyrokinetic equation can be written as a Hamiltonian evolution equation for species s of a plasma

$$\frac{\partial f_s}{\partial t} = \{H_s, f_s\}, \quad (3.1)$$

where $H_s = p_{\parallel}^2/2m_s + q_s\phi - m_sV_E^2/2$ is the Hamiltonian for the 1D electrostatic case considered here, $p_{\parallel} = m_s v_{\parallel}$ is the parallel momentum, and $\{f, g\} = (\partial f / \partial z)(\partial g / \partial p_{\parallel}) - (\partial f / \partial p_{\parallel})(\partial g / \partial z)$ is the Poisson bracket operator for any two functions f and g . The potential is determined by a gyrokinetic Poisson equation (in the long-wavelength quasineutral limit):

$$-\partial_{\perp}(\epsilon_{\perp}\partial_{\perp}\phi) = \frac{\sigma_g}{\epsilon_0} = \frac{1}{\epsilon_0} \sum_s q_s \int dv_{\parallel} f_s. \quad (3.2)$$

Here, σ_g is the *guiding-center* charge density, while the left-hand side is the negative of the polarization contribution to the density, where the plasma perpendicular

dielectric is

$$\epsilon_{\perp} = \frac{c^2}{v_A^2} = \sum_s \frac{n_s m_s}{\epsilon_0 B^2}. \quad (3.3)$$

The ion polarization dominates this term, but a sum over all species has been included for generality.

In the Hamiltonian, $V_E = -(1/B)\partial_{\perp}\phi$ is the $E \times B$ drift in the radial direction (out of the plane in figure 3.1(c)). Since there is no variation in the radial direction, there is no explicit $\mathbf{V}_E \cdot \nabla$ term, and V_E only enters through the second-order contribution to the Hamiltonian, $-mV_E^2/2$. Krommes (2013, 2012) provides some physical interpretations of this term, and Krommes (2013) gives a derivation of it in the cold-ion limit.

The conserved energy is given by

$$\begin{aligned} W_{\text{tot}} &= \int dz \sum_s \int dv_{\parallel} f_s H_s \\ &= W_K + \int dz \sigma_g \phi - \frac{1}{2} \int dz \rho V_E^2, \end{aligned} \quad (3.4)$$

where $W_K = \int dz \sum_s \int dv_{\parallel} f_s m_s v_{\parallel}^2 / 2$ is the kinetic energy, and ρ is the total mass density. Using the gyrokinetic Poisson equation (3.2) to substitute for σ_g in this equation and doing an integration by parts, one finds that the total conserved energy can be written as

$$\begin{aligned} W_{\text{tot}} &= \frac{1}{2} \int dz \sum_s \int dv_{\parallel} f_s (m_s v_{\parallel}^2 + m_s V_E^2) \\ &= W_K + \frac{1}{2} \int dz \rho V_E^2, \end{aligned} \quad (3.5)$$

where the global neutrality condition $\int dz \sigma_g = 0$ was used to eliminate boundary terms.

To verify energy conservation, first note that $\int dz \int dv_{\parallel} H_s \partial f_s / \partial t = 0$ by multiplying the gyrokinetic equation (3.1) by the Hamiltonian and integrating over all of phase-space. Here, periodic boundary conditions are used for simplicity; there are losses to the wall in a bounded system. The rate of change of the total conserved energy is then written as

$$\begin{aligned} \frac{dW_{\text{tot}}}{dt} &= \int dz \sum_s \int dv_{\parallel} f_s \left(q_s \frac{\partial \phi}{\partial t} - \frac{m_s}{2} \frac{\partial V_E^2}{\partial t} \right) \\ &= \int dz \left(\sigma_g \frac{\partial \phi}{\partial t} - \frac{1}{2} \sum_s n_s m_s \frac{\partial V_E^2}{\partial t} \right). \end{aligned} \quad (3.6)$$

Using the gyrokinetic Poisson equation (3.2) to substitute for σ_g and integrating by parts, one finds that these two terms cancel, so $dW_{\text{tot}}/dt = 0$. Note that the small

second-order Hamiltonian term $H_2 = -(m/2)V_E^2$ was needed to get exact energy conservation. In many circumstances, the $E \times B$ energy mV_E^2 is only a very small correction to the parallel kinetic energy $mv_{\parallel}^2/2$, but it is still assuring to know that exact energy conservation is possible. This automatically occurs in the Lagrangian field theory approach to full- f gyrokinetics (Sugama, 2000; Brizard, 2000b; Krommes, 2012), in which the gyrokinetic Poisson equation results from a functional derivative of the action with respect to the potential ϕ , so a term that is linear in ϕ in the gyrokinetic Poisson equation comes from a term that is quadratic in ϕ in the Hamiltonian.

3.2.1 Electrostatic Model with a Modified Ion Polarization Term

One can obtain a wave dispersion relation by linearizing (3.1) and (3.2) and Fourier transforming in time and space. With the additional assumption that $q_e = -q_i$ and neglecting ion perturbations (except for the ion polarization density), one has

$$k_{\perp}^2 \rho_s^2 + [1 + \xi Z(\xi)] = 0. \quad (3.7)$$

Here, $\rho_s^2 = T_e/(m_i \Omega_{ci}^2)$, $\xi = \omega/(\sqrt{2}k_{\parallel}v_{te})$, $v_{te} = \sqrt{T_e/m_e}$, and the plasma dispersion function is $Z(\xi) = \pi^{-1/2} \int dt \exp(-t^2)/(t - \xi)$ (or the analytic continuation of this for $\text{Im}(\xi) \leq 0$). In the limit $\xi \gg 1$, the solution to the dispersion relation is a wave with frequency

$$\omega_H = \frac{k_{\parallel}v_{te}}{|k_{\perp}| \rho_s}. \quad (3.8)$$

For $k_{\perp} \rho_s \ll 1$, this is a high-frequency wave that must be handled carefully to remain numerically stable. Note that this wave does not affect parallel transport in the SOL because the main heat pulse propagates at the ion sound speed, and this wave is even faster than the electrons for $k_{\perp} \rho_s \ll 1$.

This wave is the electrostatic limit of the shear Alfvén wave (Lee, 1987; Belli & Hammett, 2005), which lies in the regime of inertial Alfvén waves (Lysak & Lotko, 1996; Vincena *et al.*, 2004). The difficulties introduced by such a wave could be eased by including magnetic perturbations from A_{\parallel} , in which case the dispersion relation (in the fluid electron regime $\xi \gg 1$) becomes $\omega^2 = k_{\parallel}^2 v_{te}^2 / (\hat{\beta}_e + k_{\perp}^2 \rho_s^2)$, where $\hat{\beta}_e = (\beta_e/2)(m_i/m_e)$ and $\beta_e = 2\mu_0 n_e T_e / B^2$ (Belli & Hammett, 2005). In the electrostatic limit $\hat{\beta}_e = 0$, we recover (3.8), but retaining a finite $\hat{\beta}_e$ would set a maximum frequency at low k_{\perp} of $\omega = k_{\parallel}v_{te}/\hat{\beta}_e^{1/2} = k_{\parallel}v_A$, where v_A is the Alfvén velocity, avoiding the $k_{\perp} \rho_s \rightarrow 0$ singularity of the electrostatic case.

For electrostatic simulations, a modified ion polarization term can be introduced to effectively set a minimum value for the perpendicular wave number k_{\perp} . This modification can be used to slow down the electrostatic shear Alfvén wave to make it more numerically tractable. Even when magnetic fluctuations are included, one still

might want to consider an option of introducing a long-wavelength modification for numerical convenience or efficiency.

When choosing how to select the minimum value for $k_{\perp}\rho_s$, it is useful to consider the set of k_{\perp} 's represented on the grid for particular simulation parameters. Consider an axisymmetric system (as in figure 3.1(c)) with constant B/B_{ξ} , where B is the total magnetic field, and B_{ξ} and B_{ζ} are the components of \mathbf{B} in the poloidal and toroidal directions. It follows that $\partial_{\perp} = (B_{\zeta}/B_{\xi})\partial_{\parallel}$, so

$$k_{\perp,\max} = \frac{B_{\zeta}}{B_{\xi}} k_{\parallel,\max}. \quad (3.9)$$

The maximum parallel wavenumber can be estimated as $k_{\parallel,\max}\Delta z \sim \pi N_{nc}$, where Δz is the width of a single cell in position space, and N_{nc} is the total degrees of freedom per cell used in the DG representation of the position coordinate.

Therefore, one has

$$k_{\perp,\max} = \frac{B_{\zeta}}{B_{\xi}} \frac{\pi N_{nc}}{\Delta z}. \quad (3.10)$$

In our simulations, $N_{nc} = 3$ and $\Delta z = 10$ m using 8 cells in the spatial direction to represent an 80 m parallel length. Assuming that $B_{\xi}/B = \sin(6^\circ)$, one estimates that $k_{\perp,\max}\rho_s \approx 2.5 \times 10^{-2}$ for 1.5 keV deuterium ions with $B = 2$ T. Thus, the perpendicular wave wavenumbers represented by a typical grid are fairly small.

The general modified gyrokinetic Poisson equation we consider is of the form

$$-\partial_{\perp}(C_{\epsilon}\epsilon_{\perp}\partial_{\perp}\phi) + s_{\perp}(z,t)(\phi - \langle\phi\rangle) = \frac{\sigma_g(z)}{\epsilon_0}, \quad (3.11)$$

where $s_{\perp}(z,t) = k_{\min}^2(z)\epsilon_{\perp}(z,t)$ is a shielding factor (we allow k_{\min} to depend on position but not on time in order to preserve energy conservation, as described later in this section) and $\langle\phi\rangle$ is a dielectric-weighted, flux-surface-averaged potential defined as

$$\langle\phi\rangle = \frac{\int dz s_{\perp}\phi}{\int dz s_{\perp}}. \quad (3.12)$$

The fixed coefficient C_{ϵ} is for generality, making it easier to consider various limits later.

The sound gyroradius is chosen to be defined by $\rho_s^2(z,t) = c_s^2(z,t)/\Omega_{ci}^2 = T_e(z,t)/(m_i\Omega_{ci}^2)$, using the mass and cyclotron frequency of a main ion species. A time-independent sound gyroradius (using a typical or initial value for the electron temperature T_{e0}) is defined by $\rho_{s0}^2(z) = c_{s0}^2(z)/\Omega_{ci}^2 = T_{e0}(z)/(m_i\Omega_{ci}^2)$. Note that the shielding factor can also be written as $s_{\perp}(z,t) = [k_{\min}(z)\rho_{s0}(z)]^2\epsilon_{\perp}(z,t)/\rho_{s0}^2(z)$.

For simplicity, $k_{\min}\rho_{s0}$ is chosen to be a constant independent of position. Its value should be small enough that the wave in (3.8) is high enough in frequency that it does not interact with other dynamics of interest, but not so high in frequency that it forces the explicit time step to be excessively small. For some of our simulations,

we use $k_{\min}\rho_s = 0.2$, which leads to only a 2% correction to the ion acoustic wave frequency $\omega = k_{\parallel}c_s/\sqrt{1+k_{\perp}^2\rho_s^2}$ at long wavelengths. Convergence can be checked by taking the limit $k_{\min}\rho_{s0} \rightarrow 0$.

As a simple limit, one can even set $C_{\epsilon} = 0$ and keep just the s_{\perp} term, which replaces the usual differential gyrokinetic Poisson equation with a simpler algebraic model. This approach should work fairly well for low frequency dynamics. The basic idea is that for long-wavelength ion-acoustic dynamics, the left-hand side of (3.11) is small, so the potential is primarily determined by the requirement that it adjust to keep the electron density on the right-hand side almost equal to the ion guiding center density. At low frequencies, the electrons are near-adiabatic (in parallel force balance), so the density depends in part on the potential. In future work, one could consider using an implicit method, perhaps using the method here as a preconditioner. Alternatively, electromagnetic effects will slow down the high-frequency wave so that explicit methods may be sufficient.

The flux-surface-averaged potential $\langle\phi\rangle$ is subtracted off in (3.11) so that the model polarization term is gauge invariant like the usual polarization term. This choice is also related to our form of the logical-sheath boundary condition (Section 2.5.1), which enforces zero current to the wall. Since the electron and ion guiding-center fluxes to the wall are the equal, the net guiding center charge vanishes, $\int dz \sigma_g = 0$. Just as the net guiding-center charge vanishes, our model polarization charge density, $s_{\perp}(\phi - \langle\phi\rangle)$, also averages to zero. This approach neglects ion polarization losses to the wall, which is consistent in this model because integrating (3.2) over all space then gives $\partial_{\perp}\phi = 0$ at the plasma edge. One could consider future modifications to account for polarization drift losses to the wall, but the present model is found to agree fairly well with full-orbit PIC results.

With this approach, it is also necessary to modify the Hamiltonian in order to preserve energy consistency with this modified gyrokinetic Poisson equation. The modified Hamiltonian is written in the form

$$H_s = \frac{1}{2}m_s v_{\parallel}^2 + q_s(\phi - \langle\phi\rangle) - \frac{1}{2}m_s \hat{V}_E^2, \quad (3.13)$$

where \hat{V}_E^2 is a modified $E \times B$ velocity that is chosen to conserve energy. The constant $\langle\phi\rangle$ term in H_s has no effect on the gyrokinetic equation because only gradients of ϕ matter, but it simplifies the energy conservation calculation. The total energy is still $W_{\text{tot}} = \int dz \sum_s \int dv_{\parallel} f_s H_s$, and its time derivative (neglecting boundary terms that are straightforward to evaluate) can be written as

$$\begin{aligned} \frac{dW_{\text{tot}}}{dt} &= \int dz \sum_s \int dv_{\parallel} f_s \frac{\partial H}{\partial t} \\ &= \int dz \left(\sigma_g \frac{\partial}{\partial t} (\phi - \langle\phi\rangle) - \sum_s \frac{1}{2} n_s m_s \frac{\partial}{\partial t} \hat{V}_E^2 \right). \end{aligned} \quad (3.14)$$

Using the modified gyrokinetic Poisson equation (3.11) and integrating the first term by parts gives

$$\frac{dW_{\text{tot}}}{dt} = \int dz \left(\sum_s \frac{1}{2} n_s m_s C_\epsilon \frac{\partial}{\partial t} V_E^2 + \frac{\epsilon_0}{2} s_\perp \frac{\partial}{\partial t} (\phi - \langle \phi \rangle)^2 - \sum_s \frac{1}{2} n_s m_s \frac{\partial}{\partial t} \hat{V}_E^2 \right), \quad (3.15)$$

so energy is conserved if one chooses

$$\hat{V}_E^2 = C_\epsilon V_E^2 + \frac{\epsilon_0 s_\perp}{\sum_s n_s m_s} (\phi - \langle \phi \rangle)^2 \quad (3.16)$$

and require that the coefficient $\epsilon_0 s_\perp / (\sum_s n_s m_s)$ be independent of time so that it comes outside of a time derivative. Using (3.3) and the definition of s_\perp after (3.11), one sees that $\epsilon_0 s_\perp / (\sum_s n_s m_s) = k_{\min}^2(z) / B^2$, which is indeed independent of time because k_{\min} was chosen not to have any time dependence.

In the limit that one uses only the algebraic model polarization term with $C_\epsilon = 0$, one finds that

$$\hat{V}_E^2 = (k_{\min} \rho_{s0})^2 \left(\frac{e \delta \phi}{T_{e0}} \right)^2 c_{s0}^2, \quad (3.17)$$

where $\delta \phi = \phi - \langle \phi \rangle$. For $k_{\min} \rho_{s0} = 0.2$ and $e \delta \phi / T_{e0} \sim 1$, this $E \times B$ energy could be order 4% of the total energy. We use the $C_\epsilon = 0$ limit of this model for the simulations discussed in the next section.

3.3 Numerical Implementation Details

One detail of solving the modified gyrokinetic Poisson equation (3.11) is how to determine the flux-surface-averaged component, which is related to the boundary conditions. Consider the case in which $\epsilon_\perp = 0$, and expand $\phi = \langle \phi \rangle + \delta \phi$. Then $\delta \phi$ is determined by the algebraic equation

$$s_\perp(z) \delta \phi(z) = \frac{\sigma_g(z)}{\epsilon_0}. \quad (3.18)$$

Imposing the boundary condition that the value of ϕ at the plasma edge be equal to the sheath potential gives $\phi(z_R) = \phi_{sh} = \langle \phi \rangle + \delta \phi(z_R)$ (the left and right boundaries have been assumed to be symmetric here), which gives an additional equation to determine $\langle \phi \rangle$. The final expression is

$$\phi(z) = \delta \phi(z) - \delta \phi(z_R) + \phi_{sh}. \quad (3.19)$$

In order to maintain energy conservation, it is important that the algorithm preserve the numerical equivalent of certain steps in the analytic derivation. In our algorithm, based on Liu and Shu's (Liu & Shu, 2000) algorithm for the incompress-

ible Euler equation, ϕ must be obtained using continuous finite elements, although the charge density σ_g is discontinuous in our Poisson equation.

To preserve the integrations involved in energy conservation, it is important to ensure that one can multiply (3.18) by the fluctuating potential, integrate over all space, and preserve

$$\int dz \delta\phi s_{\perp} \delta\phi = \frac{1}{\epsilon_0} \int dz \delta\phi \sigma_g. \quad (3.20)$$

This requirement ensures that a potential part of the energy on the right-hand side is exactly related to a field-like-energy on the left-hand side. This quantity will be preserved if one projects the modified Poisson equation onto all of the continuous basis functions ψ_j that are used for ϕ (i.e., $\phi(z) = \sum_j \phi_j \psi_j(z)$) to ensure that

$$\langle \psi_j s_{\perp} \phi \rangle = \langle \psi_j \sigma_g \rangle. \quad (3.21)$$

For piecewise-linear basis functions, this leads to a tridiagonal equation for ϕ_j that has to be inverted to determine ϕ . Because $s_{\perp} \propto n(z, t)$ varies in time, this will take a little bit of work, but as one goes to higher dimensions in velocity space, the Poisson solve (which is only in the lower-dimensional configuration space) will be a negligible fraction of the computational time.

3.4 Simulation Results

The main parameters used for our simulations were described in [Havlíčková et al. \(2012\)](#); [Pitts et al. \(2007\)](#) and were chosen to model an ELM on the JET tokamak for a case in which the density and temperature at the top of the pedestal were $n_{\text{ped}} = 5 \times 10^{19} \text{ m}^{-3}$ and $T_{\text{ped}} = 1.5 \text{ keV}$. The ELM is modeled as an intense particle and heat source in the SOL that lasts for $200 \mu\text{s}$, spread over a poloidal extent $L_{\text{pol}} = 2.6 \text{ m}$ around the midplane and a radial width $\Delta R = 10 \text{ cm}$. The model SOL has a major radius $R = 3 \text{ m}$, and this source corresponds to a total ELM energy of about 0.4 MJ . Note that R and ΔR are simply volume-scaling parameters and do not affect the simulation results. The simulation domain has a length along field lines $2L_{\parallel} = 80 \text{ m}$, which models a magnetic field line on JET with an incidence angle θ of 6° .

The kinetic equation with the source term on the right-hand side is

$$\frac{\partial f}{\partial t} - \{H, f\} = g(t) S(z) F_M(v_{\parallel}, T_S(t)), \quad (3.22)$$

where $F_M(v_{\parallel}, T_S(t))$ is a unit Gaussian in variable v_{\parallel} with a time-dependent temperature $T_S(t)$. The function $S(z)$ is the same for both particle species, and is represented

Table 3.1: Summary of parameters for the ELM-heat-pulse simulations. These parameters are based on a simulation for a 0.4 MJ ELM released into the JET SOL, originally described in [Pitts et al. \(2007\)](#). This case was later used as a benchmark problem in [Havlíčková et al. \(2012\)](#).

Symbol	Value	Description
t_{ELM}	$200 \mu\text{s}$	ELM pulse duration
n_{ped}	$5 \times 10^{19} \text{ m}^{-3}$	Pedestal density
T_{ped}	1.5 keV	Temperature of ELM-pulse ions and electrons
W_{ELM}	0.4 MJ	Total ELM energy
L_s	25 m	Parallel length of source region
$2L_{\parallel}$	80 m	Parallel length of simulation domain
τ_e	$2.5 \mu\text{s}$	Electron transit time ($L_{\parallel}/v_{te,\text{ped}}$)
τ_i	$149 \mu\text{s}$	Ion transit time ($L_{\parallel}/c_{s,\text{ped}}$)
$k_{\perp}\rho_{s0}$	0.2	Perpendicular wavenumber
S_0	$9.07 \times 10^{23} \text{ m}^{-3} \text{ s}^{-1}$	Density source rate
θ	6°	Magnetic-field-line incidence angle

as

$$S(z) = \begin{cases} S_0 \cos\left(\frac{\pi z}{L_s}\right) & |z| < \frac{L_s}{2}, \\ 0 & \text{else,} \end{cases} \quad (3.23)$$

where $L_s = 25$ m is the length of the source along the magnetic field line. The value of S_0 was computed using the scaling ([Havlíčková et al., 2012](#))

$$S_0 = A n_{\text{ped}} c_{s,\text{ped}} / L_s, \quad (3.24)$$

where the constant of proportionality A was chosen to be $1.2\sqrt{2} \approx 1.7$ for comparison with [Havlíčková et al. \(2012\)](#). In our simulations, $S_0 \approx 9.07 \times 10^{23} \text{ m}^{-3} \text{ s}^{-1}$.

The function $g(t)$ in (3.22) is used to model the time-dependence of the particle source:

$$g(t) = \begin{cases} 1 & 0 < t < 200 \mu\text{s}, \\ 1/9 & t > 200 \mu\text{s}. \end{cases} \quad (3.25)$$

The post-ELM source also has reduced electron and ion temperature, represented by the $T_S(t)$ parameter in the Maxwellian term F_M in (3.22), which has the value 1.5 keV from $0 < t < 200 \mu\text{s}$ for both ions and electrons. The electron temperature for $t > 200 \mu\text{s}$ is 210 eV, and the ion temperature is reduced to 260 eV. The end time for the simulation is $t = 350 \mu\text{s}$. The functions $g(t)$ and $S(z)$ are shown in figure 3.2.

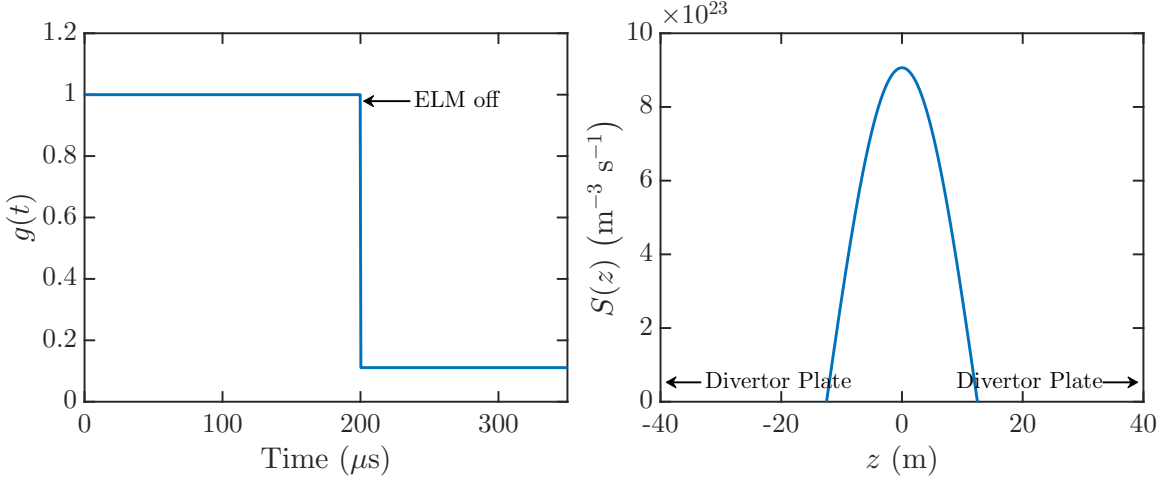


Figure 3.2: Spatial and temporal profiles of the source term used in the ELM heat-pulse test problem. After the intense-ELM source is turned off at $t = 200 \mu\text{s}$, the particle sources are reduced to 1/9th their original value, and the electron and ion source temperatures are also reduced from 1.5 keV to 210 eV and 260 eV, respectively.

We performed our simulations using second-order Serendipity basis functions (Arnold & Awanou, 2011) on a grid with eight cells in the spatial direction and 32 cells in the velocity direction. In one dimension, second-order basis functions correspond to piecewise-quadratic basis functions, or three degrees of freedom within each cell. The case with kinetic electrons and kinetic ions takes about three minutes to run on a personal computer.

3.4.1 Initial Conditions

In previous papers that looked at this problem, the codes were typically run for a while with the same weak source that would be used in the post-ELM phase to reach a quasi-steady state before the intense ELM source was turned on. The authors found that the final results were not very sensitive to the duration of the pre-ELM phase or the initial conditions used for it. However, there is formally no normal steady state for this problem in the collisionless limit (low-energy particles build up over time without collisions). To remove a possible source of ambiguity for future benchmarking, here we specify more precise initial conditions chosen to approximately match initial conditions at the beginning of the ELM phase used in previous work.

We model the initial electron distribution function as

$$f_{e0}(z, v_{\parallel}) = n_{e0}(z) F_M(v_{\parallel}, T_{e0}), \quad (3.26)$$

with $T_{e0} = 75 \text{ eV}$. The electron density profile (in 10^{19} m^{-3}) is chosen to be

$$n_{e0}(z) = 0.7 + 0.3 \left(1 - \left| \frac{z}{L_{\parallel}} \right| \right) + 0.5 \cos \left(\frac{\pi z}{L_s} \right) H \left(\frac{L_s}{2} - |z| \right). \quad (3.27)$$

The initial ion distribution function is modeled as

$$f_{i0}(z, v_{\parallel}) = \begin{cases} F_L & z < -\frac{L_s}{2}, \\ \left(\frac{1}{2} - \frac{z}{L_s}\right) F_L + \left(\frac{1}{2} + \frac{z}{L_s}\right) F_R & -\frac{L_s}{2} < z < \frac{L_s}{2}, \\ F_R & z > \frac{L_s}{2}. \end{cases} \quad (3.28)$$

Here, F_L and F_R are left and right half-Maxwellians defined as

$$F_R(z, v_{\parallel}; T_{i0}) = \hat{n}(z) F_M(v_{\parallel}, T_{i0}) H(v_{\parallel}), \quad (3.29)$$

$$F_L(z, v_{\parallel}; T_{i0}) = \hat{n}(z) F_M(v_{\parallel}, T_{i0}) H(-v_{\parallel}), \quad (3.30)$$

where $\hat{n}(z) = 2n_{i0}(z)$, H is the Heaviside step function, and the initial ion temperature profile (in eV) is defined as

$$T_{i0}(z) = 100 + 45 \left(1 - \left|\frac{z}{L_{\parallel}}\right|\right) + 30 \cos\left(\frac{\pi z}{L_s}\right) H\left(\frac{L_s}{2} - |z|\right). \quad (3.31)$$

The expressions for the n_{e0} and T_{i0} profiles were chosen to approximate those described in private communication with the author of [Havlíčková et al. \(2012\)](#), which were originally obtained from simulations that had run for a while with a weaker source to achieve a quasi-steady state before the strong ELM source was turned on, as described at the beginning of this subsection.

Given an initial electron density profile, we then calculate an initial ion-guiding-center-density profile to minimize the excitation of high-frequency shear Alfvén waves. We do this by choosing the initial ion-guiding-center-density $n_i(z)$ so that it gives a potential $\phi(z)$ that results in the electron density's being consistent with a Boltzmann equilibrium, i.e., the electrons are initially in parallel force balance (adiabatic) and do not excite high-frequency shear Alfvén waves. An adiabatic-electron response is

$$n_e(z) = C \exp\left(\frac{e\phi(z)}{T_e}\right). \quad (3.32)$$

Taking the log of the above equation and then an n_e -weighted average, one has

$$\langle \log n_e \rangle_{n_e} = \log C + \frac{e\langle \phi \rangle_{n_e}}{T_{e0}}, \quad (3.33)$$

where T_e has been assumed to be a constant T_{e0} .

Note that one is free to add an arbitrary constant to ϕ since only gradients of ϕ affect the dynamics. Choosing the additional constraint that $\langle \phi \rangle_{n_e} = 0$, one can express the constant C in terms of n_e . This convention for $\langle \phi \rangle_{n_e}$ is only for convenience, as any constant can be added to ϕ in the plasma interior without affecting the results. After the first time step, the sheath boundary condition will be imposed, which will give a non-zero value for the average potential.

One then has the following equation for ϕ :

$$\frac{e\phi}{T_{e0}} = \log n_e - \langle \log n_e \rangle_{n_e}. \quad (3.34)$$

This ϕ can be used with the gyrokinetic Poisson equation to solve for $n_i(z)$ by iteration. With a small m_e/m_i ratio, the gyrokinetic Poisson equation can be written as

$$n_i(z) \left(1 - k_\perp^2 \rho_{s0}^2 \frac{e(\phi - \langle \phi \rangle_{n_i})}{T_{e0}} \right) = n_e(z), \quad (3.35)$$

where with the small m_e/m_i ratio approximation, the dielectric-weighted average is equivalent to an ion density-weighted average. The left-hand side of this equation is a nonlinear function of n_i (because it appears as a leading coefficient and in the density-weighted average $\langle \phi \rangle_{n_i}$), which is solved for by using iteration:

$$n_i^{j+1}(z) = \frac{n_e(z)}{1 - k_\perp^2 \rho_{s0}^2 \frac{e}{T_{e0}} \left(\phi - \langle \phi \rangle_{n_i^j} \right)}. \quad (3.36)$$

Note that the averaged ϕ on the right-hand side is weighted by n_i^j , the previous iteration's ion density. Convergence can be improved by adding a constant to $n_i(z)$ each iteration to enforce global neutrality $\langle n_i \rangle = \langle n_e \rangle$. In our tests, the initial ion density profile was calculated to 10^{-15} relative error in five iterations.

3.4.2 Divertor Heat Flux with Drift-Kinetic Electrons

Figure 3.3 shows the parallel heat flux on the target plate versus time using the 1D electrostatic model with a fixed $k_\perp \rho_{s0} = 0.2$. A rapid response in the electron heat flux is observed at early times, on the order of the electron transit timescale $\tau_e \sim L_\parallel/v_{te,\text{ped}} \approx 2.5 \mu\text{s}$. This response is due to fast electrons reaching the target plate, which initially cause a modest rise in the electron heat flux from $t \sim 1 \mu\text{s}$ to $t \approx 1.5 \mu\text{s}$. This build-up of fast electrons results in a rise in the sheath potential at $t \approx 1.5 \mu\text{s}$, which causes a modest rise in the ion heat flux and a modest drop in the electron heat flux until the arrival of the bulk ion heat flux at a later time. We did a scan in $k_\perp^2 \rho_{s0}^2$ over a factor of 25 (0.02–0.5) and found only a few percent variation in the resulting plot of heat flux versus time, verifying that the results are not sensitive to the exact value of this parameter (as long as it is small).

The sheath is seen to play an essential role in mediating the power loads to the divertor. As discussed by [Leonard \(2014\)](#), one of the original motivations for these calculations was to address concerns that ELM energy deposition on time scales short compared to the ion-sound-transit time could lead to melting of the divertor due to excessive surface temperatures ([Pitts et al., 2007; Leonard, 2014; Loarte et al., 2007](#)). Our results confirm the previous 1D3V PIC calculations of [Pitts et al. \(2007\)](#) that found that the bulk of the ELM energy arrives at the target plate only on the slower ion-sound-transit time scale $\tau_i \sim L_\parallel/c_{s,\text{ped}} \approx 149 \mu\text{s}$, although there is a modest rise in

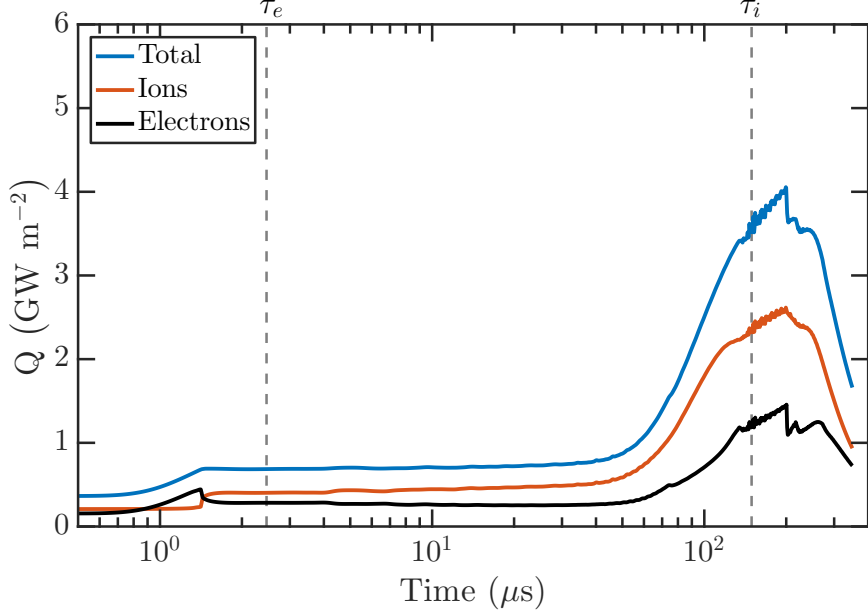


Figure 3.3: Parallel heat flux at the divertor plate versus time with drift-kinetic electrons. The electron and ion transit times τ_e and τ_i are indicated by the vertical dashed lines. The sharp drop in the electron heat flux occurs in the microseconds after the intense upstream source is turned off (see (3.25) and nearby discussion).

the heat flux on $\sim\tau_e$. This observation is consistent with measurements from several machines ([Loarte et al., 2007](#)).

The bulk of the ELM energy is carried by the ions, which arrive at the target plate on the order of the ion-sound transit time τ_i . Note that although the source power is equally divided between electrons and ions, the electric field transfers some thermal energy from electrons to the ions as the ions flow to the divertor plates. The reduction of source strength and temperature after $200 \mu\text{s}$ results in the abrupt drop seen in the heat fluxes. The parallel heat flux (parallel to the magnetic field) on the right target plate for each species is calculated as

$$Q_s = \frac{1}{2}m_s \int_{v_{c,s}}^{\infty} dv_{\parallel} f_s v_{\parallel}^3 + (T_{\perp} + q_s \phi_{sh}) \int_{v_{c,s}}^{\infty} dv_{\parallel} f_s v_{\parallel}, \quad (3.37)$$

where $v_{c,s} = \sqrt{\max(-2q_s \phi_{sh}/m_s, 0)}$ accounts for the reflection of electrons by the sheath. The $q_s \phi_{sh}$ term in the second integral models the acceleration of ions and deceleration of electrons as they pass through the sheath to the divertor plate, a region that is not resolved in our models. We have assumed that each species has a constant perpendicular temperature $T_{\perp} = T_{\text{ped}}$ for comparison with the 1D Vlasov results in [Havlíčková et al. \(2012\)](#). Note that the incidence angle of the magnetic field ($\theta \approx 6^\circ$) is not factored into this measure of heat flux on the target plate. The heat flux normal to the target plate is $Q_{s,n} = Q_s \sin(\theta)$, where θ is the (usually very small) angle between the magnetic field and the target-plate surface.

Figure 3.3 indicates good quantitative agreement with the collisionless 1D1V Vlasov results in Havlíčková *et al.* (2012, figure 2), supporting the accuracy of the logical-sheath boundary conditions and the gyrokinetic-based model used here. Specifically, our model quantitatively reproduces the peak total heat flux of $\approx 4 \text{ GW m}^{-2}$, the individual contributions to the total heat flux by electrons and ions within $\sim 5\%$, and the features on the electron and ion transit scales found in the 1D1V Vlasov simulation. As with the Vlasov simulation of Havlíčková *et al.* (2012), we obtain a lower peak total heat flux and lower fraction of energy carried by ions in our model compared to the PIC simulation of Havlíčková *et al.* (2012), which obtained peak heat fluxes of $\approx 1.1 \text{ GW m}^{-2}$ for electrons and $\approx 3.9 \text{ GW m}^{-2}$ for ions.

Small differences between our 1D1V results and the Vlasov results could be attributed to the use of different initial conditions, while discrepancies with the PIC simulation can be attributed to the lack of collisions, as discussed in Havlíčková *et al.* (2012). An extension to our model with self-species collisions is discussed in Section 3.5, where we confirm that the inclusion of collisions eliminates the major discrepancies in the heat fluxes.

In a previous study with a 1D1V PIC code (Pitts *et al.*, 2007), the fraction of total energy deposited on the divertor plate by each species was also of interest. We find that $\approx 35\%$ of the energy load on the divertor target is deposited by the electrons in the time interval $0 < t < 350 \mu\text{s}$ and that $\approx 51\%$ of the energy in the same time interval arrives before the peak in the heat flux at $t \approx 200 \mu\text{s}$. Both of these fractions appear to be larger than what was reported in the PIC simulation, which found that $\approx 23\%$ of the total energy load is deposited by the electrons and that $\approx 27\%$ of the total ELM energy arrives before the peak in the heat flux.

Our gyrokinetic 1D1V test problem (originally reported in Shi *et al.*, 2015) was later implemented in a finite-volume version of the GENE code (Pan *et al.*, 2016). A comparison of the Gkeyll and GENE results is shown in figure 3.4. Even with different numerical implementations, excellent quantitative agreement is obtained between the two codes, although the small oscillations in the heat fluxes on the ion-transit-time scale are absent in the GENE simulation.

3.4.3 Divertor Heat Flux with an Adiabatic-Electron Model

We have also investigated a model that includes the effect of kinetic ions but assumes an adiabatic response for the electrons. Specifically, the electron density takes the form

$$n_e(z) = n_e(z_R) \exp\left(\frac{e(\phi - \phi_{sh})}{T_e}\right), \quad (3.38)$$

where $n_e(z_R)$ is the electron density evaluated at the domain edge. This expression can be inverted to give another algebraic equation to determine the potential, similar to the electrostatic gyrokinetic model with a fixed $k_\perp \rho_{s0}$. Since the time step is set by the ions, these simulations have an execution time a factor of $\sim \sqrt{m_i/m_e}$ faster

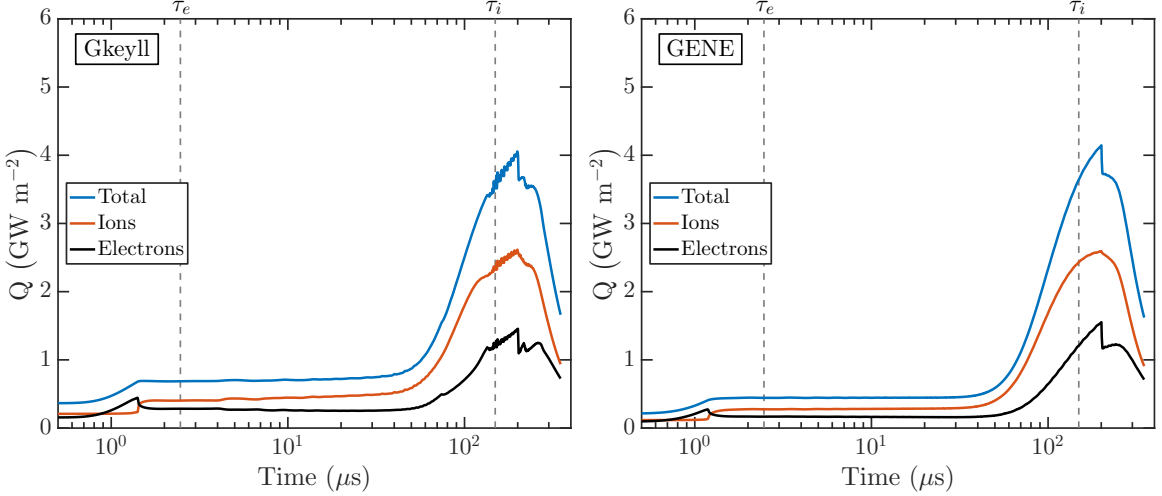


Figure 3.4: Comparison of the parallel heat flux at the divertor plate versus time with drift-kinetic electrons obtained from a Gkeyll simulation and a GENE simulation. The electron and ion transit times τ_e and τ_i are indicated by the vertical dashed lines. Data from the GENE simulation was provided by and used with permission from Q. Pan.

than the gyrokinetic simulation. This property makes the adiabatic-electron model useful as a test case for code development and debugging.

The sheath potential ϕ_{sh} can be determined by assuming that f_e at the target plate is a Maxwellian with temperature T_e . By using logical-sheath boundary conditions and quasineutrality, one finds

$$\phi_{sh} = -\frac{T_e}{e} \log \left(\frac{\sqrt{2\pi}\Gamma_i}{n_i v_{te}} \right), \quad (3.39)$$

where Γ_i is the outward ion flux, and all quantities are evaluated at the domain edge. For simplicity, we selected T_e in our simulations to be the field-line-averaged value of the ion temperature $T_i(z)$, but more accurate models for T_e could be used.

Figure 3.5 shows the parallel heat flux on the target plate versus time using adiabatic electrons. As expected, kinetic-electron effects seen in figure 3.3 are not resolved by this model. When compared to a simulation using kinetic electrons, the main heat flux at $t \approx 100\text{--}200 \mu\text{s}$ is overestimated but still predicted fairly well. The peak total heat flux is $\approx 4.77 \text{ GW m}^{-2}$ instead of $\approx 4.06 \text{ GW m}^{-2}$ from the simulation with kinetic electrons.

In this model, the electron parallel heat flux on the target plate is calculated as

$$\begin{aligned} Q_e &= \frac{1}{2} m_e \int_{v_c}^{\infty} dv_{\parallel} f_e v_{\parallel}^3 + (T_{\perp} - e\phi_{sh}) \int_{v_c}^{\infty} dv_{\parallel} f_e v_{\parallel} \\ &= (T_e + T_{\perp}) \int_0^{\infty} dv_{\parallel} f_i v_{\parallel}. \end{aligned} \quad (3.40)$$

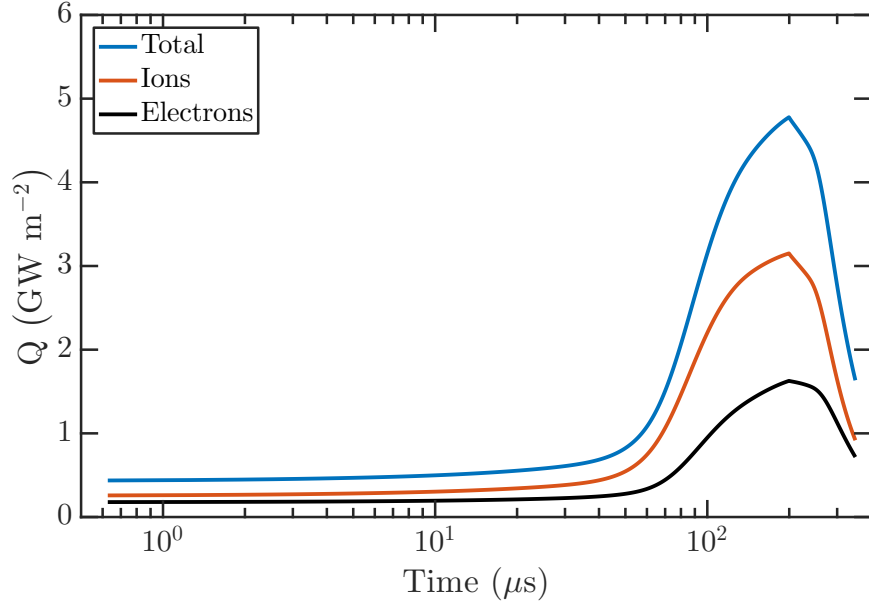


Figure 3.5: Parallel heat flux at the divertor plate versus time from the adiabatic-electron model in the ELM heat-pulse problem.

Table 3.2: Parameters for the phase-space grid used in 1D2V ELM heat-pulse simulations. Piecewise-quadratic basis functions are used, resulting in 20 degrees of freedom per cell.

Coordinate	Number of Cells	Minimum	Maximum
z	8	$-L_{\parallel}$	L_{\parallel}
v_{\parallel}	16	$-4\sqrt{T_{\text{ped}}/m_s}$	$4\sqrt{T_{\text{ped}}/m_s}$
μ	8	0	$4T_{\text{ped}}/B$

3.5 1D2V Model with Collisions

So far, we have focused on 1D1V (z, v_{\parallel}) models in the SOL. We added a third coordinate μ , the magnetic moment, and implemented Lenard–Bernstein same-species collisions (2.51) for electrons and ions to the ELM heat-pulse problem for better comparison with the 1D3V PIC results of Havlíčková *et al.* (2012) and to gain experience with simulations using two velocity coordinates. Unlike in the LAPD simulations of Chapter 4, a model for electron–ion collisions was not implemented for these 1D2V simulations. The grid parameters for the 1D2V ELM heat-pulse simulations are shown in table 3.2. Snapshots of the electron density and electrostatic potential profiles for a 1D2V ELM heat-pulse simulation with collisions are shown in figure 3.6.

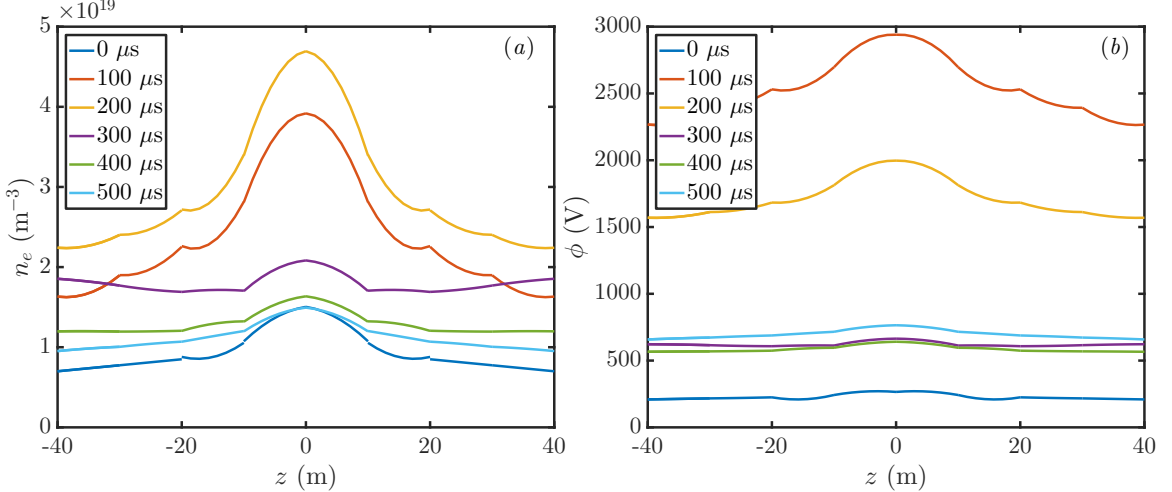


Figure 3.6: Snapshots of the (a) electron-density and (b) electrostatic-potential profiles in $100 \mu\text{s}$ intervals between $t = 0 \mu\text{s}$ and $t = 500 \mu\text{s}$ for a 1D2V ELM heat-pulse simulation with same-species Lenard–Bernstein collisions.

Since T_{\perp} is no longer a parameter of the model and can evolve through the collision operator, we modify the calculation of the parallel heat flux to

$$Q_s = \int_{v_{c,s}}^{\infty} dv_{\parallel} f_s v_{\parallel} \left(\frac{1}{2} m_s v_{\parallel}^2 + \mu B \right) + q_s \phi_{sh} \int_{v_{c,s}}^{\infty} dv_{\parallel} f_s v_{\parallel}. \quad (3.41)$$

The parallel temperature of the source plasma is still as described in the previous section, and the perpendicular temperature of the source is fixed at T_{ped} even after $t = 200 \mu\text{s}$. Figure (3.7) shows a comparison of the parallel heat flux at the divertor plate in a 1D2V case without collisions and a 1D2V case with same-species Lenard–Bernstein collisions. Notable differences between the two cases include an $\sim 20\%$ larger peak total heat flux ($Q \approx 5.23 \text{ GW m}^{-2}$) and a slightly reduced electron heat flux.

Overall, the heat flux profiles for the case with collisions is in better agreement with the PIC results of Havlíčková *et al.* (2012) and Pitts *et al.* (2007). In the 1D2V case with collisions, $\approx 44\%$ of the total energy deposited between $0 < t < 350 \mu\text{s}$ is deposited before the peak in the total heat flux (compared to $\approx 51\%$ in the 1D2V collisionless simulation). We also find that $\approx 19\%$ of the total energy deposited in the same time interval is from electrons (compared to $\approx 34\%$ in the 1D2V collisionless simulations), which is much closer to the $\approx 22\%$ reported by Pitts *et al.* (2007). A summary of various quantities measured in the 1D1V and 1D2V ELM-heat-pulse simulations is given in table 3.3.

In comparing the 1D2V simulations with and without collisions, we noticed that the time-integrated total heat flux over long times was not the same for the two cases, with the simulation with collisions having an $\approx 9.9\%$ larger energy deposited on the divertor plates. This discrepancy is explored in more detail in Appendix B, which

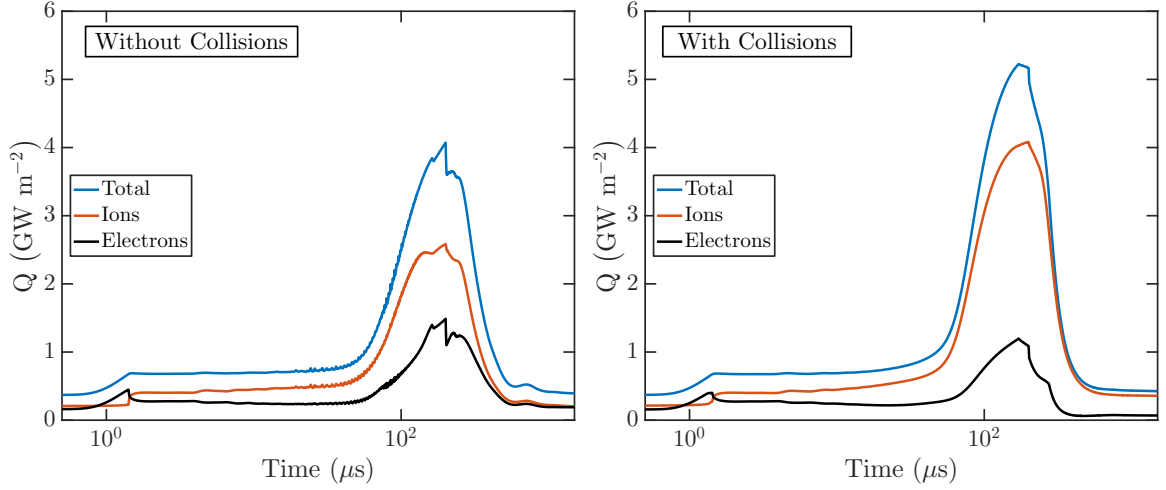


Figure 3.7: Comparison of the total, electron, and ion parallel heat fluxes at the divertor plate versus time for 1D2V cases with and without same-species Lenard–Bernstein collisions.

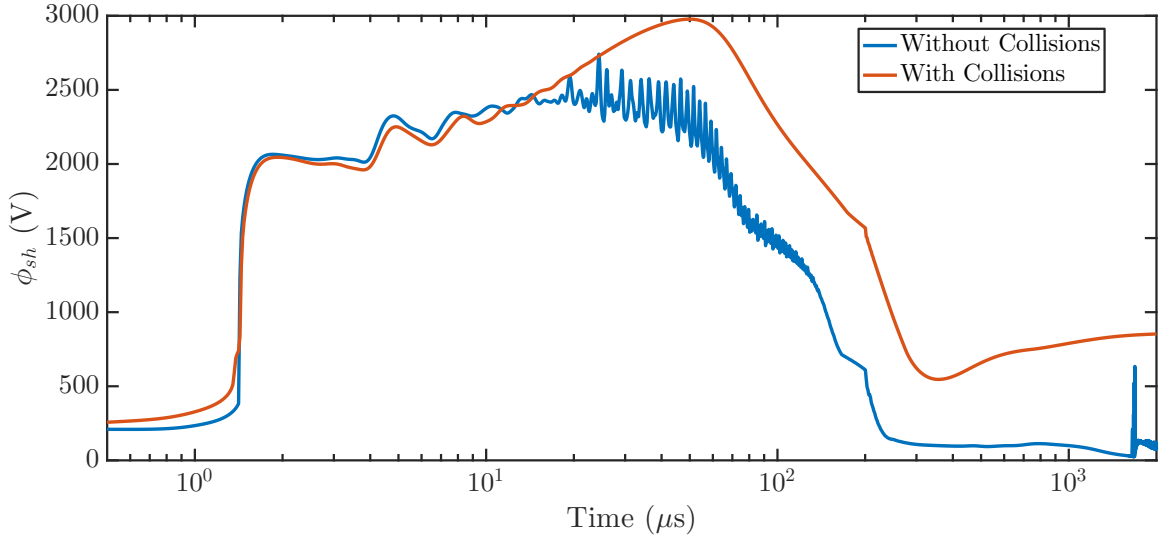


Figure 3.8: Comparison of the sheath-potential time history between 1D2V ELM heat-pulse simulations with and without same-species Lenard–Bernstein collisions. High-frequency oscillations in the sheath potential are not seen in the simulation with collisions.

reveals that the difference in energies deposited on the divertor plate is consistent with the collisionless simulations having more system energy at any given instant.

Some differences in the distribution of heat flux between electron and ions in the two cases can be understood by examining the sheath potential. As seen in figure 3.8, the sheath potential in the case with collisions does not exhibit high-frequency oscillations and is generally several hundred volts larger than the sheath potential in the case without collisions. These trends are believed to be connected to how collisions are able to replenish high- $v_{||}$ electrons throughout the simulation

Table 3.3: Summary of results from various simulations of the 1D ELM-heat-pulse problem. The simulations included in this table are 1D1V with drift-kinetic electrons ('1D1V'), 1D1V with adiabatic electrons ('1D1V (A)'), 1D2V without collisions ('1D2V (NC)'), 1D2V with collisions ('1D2V (NC)'), and 1D3V PIC with collisions ('PIC'). The values in the PIC column are from simulations of a 0.4 MJ 200 μ s-duration ELM reported in [Pitts et al. \(2007\)](#) and [Havlíčková et al. \(2012\)](#). 'Electron fraction of total energy' refers to the fraction of the total energy deposited on the divertor plate between $0 < t < 350 \mu\text{s}$, and 'Energy fraction before peak Q ' refers to the fraction of the energy that is deposited on the divertor plate before the peak in the total heat flux at the divertor plate ($t \approx 200 \mu\text{s}$).

Quantity	1D1V	1D1V (A)	1D2V (NC)	1D2V	PIC
Peak Q (GW m $^{-2}$)	4.05	4.78	4.07	5.23	5.21
Electron fraction of peak Q	0.35	0.34	0.37	0.23	0.24
Electron fraction of total energy	0.35	0.35	0.34	0.19	0.23
Energy fraction before peak Q	0.51	0.52	0.52	0.44	0.27

through pitch-angle scattering. From figure 3.8, it appears that the inclusion of collisions results in a stabilizing effect on the sheath-potential oscillations.

3.5.1 A Basic Recycling Model

When ions impact the divertor plate, some of the incident ions can reenter plasma as cold neutrals after some interactions with the solid surface (e.g., backscattering or desorption) and re-ionized, which is a process called *recycling* ([Li et al., 2012](#)). As long most recycled neutrals are re-ionized within the SOL and not in the core, favorable SOL regimes with large parallel temperature gradients and low temperatures near the targets can be achieved ([Strangeby, 2000](#)). While recycling near the divertor plates (far from the last closed flux surface) is desirable to help reduce heat loads on the divertor plates, recycling from the main chamber wall can harm fusion performance. The shorter distance to the last closed flux surface from the main chamber wall when compared to the divertor makes it easier for the recycled neutrals to penetrate into the core plasma before being ionized, which leads to radiative cooling and contamination of the core plasma. Experiments on Alcator C-Mod have observed significant amounts of recycling from the main chamber wall ([Umansky et al., 1998](#); [Terry et al., 2007](#)). Here, we discuss an extension to the 1D2V SOL simulations to model particle recycling only near divertor plates.

The recycling model provides a time-dependent source of particles near the divertor plate whose amplitude depends on the particle fluxes to the wall $\Gamma_i = \Gamma_e$ and the recycling coefficient R , which is between 0 and 1 and controls the level of recycling. The R parameter in this model is an input parameter, so it is not modeled using an empirical scaling law, atomic-physics models, or Monte Carlo calculations.

Table 3.4: Parameters for the phase-space grid used in 1D2V SOL recycling simulations. Piecewise-quadratic basis functions are used, resulting in 20 degrees of freedom per cell.

Coordinate	Number of Cells	Minimum	Maximum
z	12	$-L_{\parallel}$	L_{\parallel}
v_{\parallel}	16	$-4\sqrt{T_S/m_s}$	$4\sqrt{T_S/m_s}$
μ	8	0	$4T_S/B$

For $R = 0$, we have a situation similar to the previous ELM heat-pulse simulations in which there is no particle recycling, although we modify the midplane source for use in a steady-state calculation so that it has no time dependence. For $R = 1$, all particles that flow to the divertor plate come back into the system, and so there is no steady-state solution in this case. In these simulations, we use a midplane source that is constant in time ($g(t) = 1$) at with a reduced amplitude $S_0 = 0.075A n_{\text{pred}} c_{s,\text{ped}} / L_s$ when compared to the midplane source used in the ELM heat-pulse simulations. The midplane source is treated as an isotropic Maxwellian with temperature $T_S = 200$ eV. The parameters for these 1D2V SOL recycling simulations are summarized in table 3.4.

In diverted plasmas, the recycled neutrals are believed to be ionized near the divertor plates (Stangeby, 2000). The recycling source for electrons and ions has the following form:

$$S_R(z, \mathbf{v}, t) = R\Gamma_{\text{tot}}(t) \frac{1}{2L_R} \frac{e^{-(L_{\parallel}-|z|)/L_R}}{1 - e^{-L_{\parallel}/L_R}} F_M(\mathbf{v}, T_R), \quad (3.42)$$

where Γ_{tot} is the total outward flux (lower and upper surfaces in z), which is the same for both electrons and ions since logical-sheath boundary conditions are used. The function S_R is normalized such that it contributes a source of electrons and ions of amplitude $R\Gamma_{\text{tot}}(t)$ into the simulation domain. We choose the recycling-source scale length $L_R = 4$ m and the temperature of the recycled particles $T_R = 30$ eV. Here, $F_M(\mathbf{v}, T_R)$ represents an isotropic, normalized Maxwellian with temperature T_R . Figure 3.9 shows the profiles of the recycling and midplane plasma sources in the system.

Figure 3.10 shows the steady-state profiles calculated from running a set of 1D2V simulations with different values of the recycling coefficient. The slowest simulations are run to $t = 8$ ms to reach a steady state, while the fastest simulation only took 2.8 ms to reach a steady state. We see that as the recycling coefficient is increased, the electron density becomes increasingly peaked near the divertor plates (and eventually the density in front of the divertor plates becomes twice the density of the midplane), and the electron and ion temperatures in the SOL are reduced. Due to the rapid adiabatic-electron response, the ion temperature profile becomes much more peaked

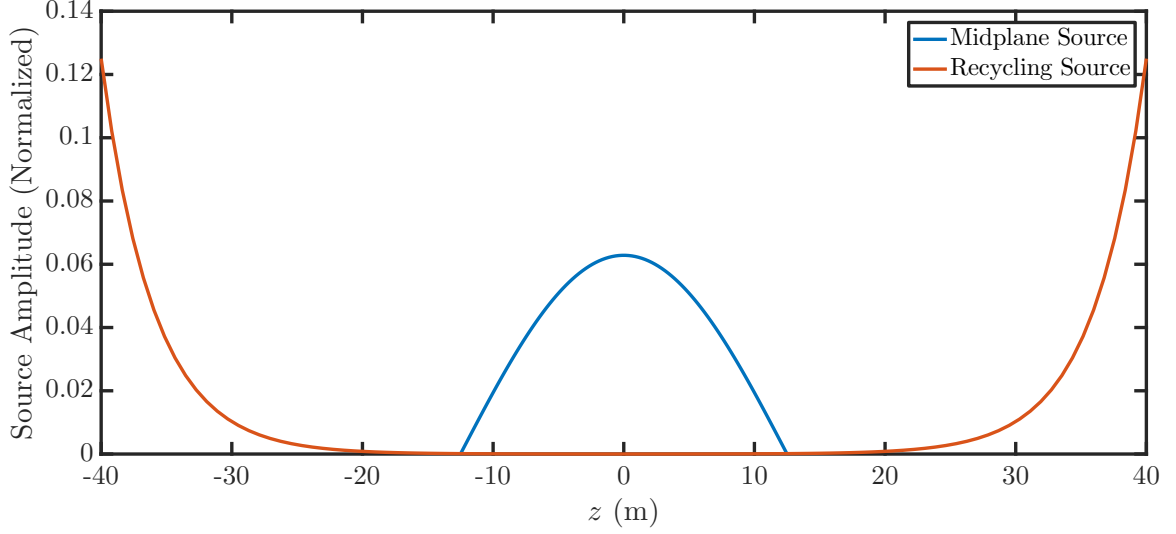


Figure 3.9: Source profiles for the recycling simulations. The recycling and midplane plasma sources are both normalized to a domain-integrated area of 1. For recycling coefficients $0 \leq R < 1$, a steady-state solution exists in which the sources are in balance with the plasma outflow to the divertor plates.

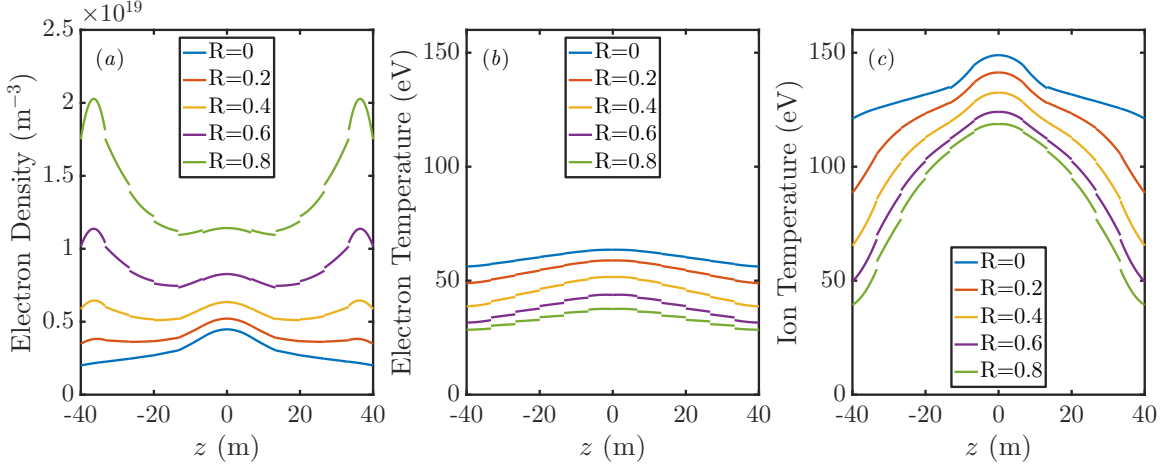


Figure 3.10: Steady-state profiles of the (a) electron density, (b) electron temperature, and (c) ion temperature for different values of the recycling coefficient R from 1D2V SOL simulations.

compared to the electron temperature profile, which remains relatively flat even for large values of R .

3.6 Conclusions

We have used a gyrokinetic-based model to simulate the propagation of an ELM heat pulse along a scrape-off layer to a divertor target plate. We have described a

modification to the ion polarization term to slow down the electrostatic shear Alfven wave.

Our main results include the demonstration that this gyrokinetic-based model with logical-sheath boundary conditions is able to agree well with Vlasov and full-orbit (non-gyrokinetic) PIC simulations, without needing to resolve the Debye length or plasma frequency. This simplification allows the spatial resolution to be several orders of magnitude coarser than the electron Debye length (and the time step several orders of magnitude larger than the plasma period) and thus leads to a much faster calculation. Our results also confirm previous work that the electrostatic potential in this problem varies to confine most of the electrons on the same time scale as the ions, so the main ELM heat deposition occurs on the slower ion-transit time scale.

Additionally, we have described a model using adiabatic electrons that is useful for code development and debugging. This model does not include kinetic-electron effects but runs much faster than simulations with kinetic electrons. Later, the original 1D1V model with drift-kinetic electrons was extended to 1D2V, and Lenard–Bernstein collision operators for self-species collisions were added. The 1D2V simulation with collisions obtained better quantitative agreement with the original 1D3V PIC simulation of Pitts *et al.* (2007), which also had collisions. Some initial work was then performed on including recycling effects in the model though source terms localized near the divertor plates with a strength proportional to a user-specified recycling coefficient and the particle fluxes to the divertor plates.

Since we have assumed only a single k_{\perp} mode in these simulations to limit the high frequency of the electrostatic shear Alfven wave, future work can allow for a spectrum of k_{\perp} modes. For 1D electromagnetic simulations, this modification requires inverting the ∇_{\perp}^2 operators that appear in the gyrokinetic Poisson equation and Ampere’s law. The inclusion of magnetic fluctuations will be important when a spectrum of very low k_{\perp} modes is kept in order to limit the frequency of the shear Alfven wave at low k_{\perp} . These models could eventually include more detailed effects such as secondary electron emission, charge exchange, and radiation, and could be used to study different types of divertor configurations.

Chapter 4

Simulations of the Large Plasma Device

In this chapter, we present results from gyrokinetic continuum simulations of electrostatic plasma turbulence in the Large Plasma Device (LAPD) at UCLA ([Gekelman et al., 1991, 2016](#)) using kinetic electrons with a reduced mass ratio and a single kinetic ion species. The LAPD is a linear device that creates a plasma column in a straight, open-field-line configuration. Figure 4.1 shows a diagram of the LAPD device. Despite its relatively low plasma temperature, the LAPD contains some of the basic elements of a SOL in a simplified (no X-point geometry, straight magnetic field lines, etc.), well-diagnosed setting, making this device a useful benchmark of gyrokinetic algorithms for boundary-plasma simulation. The LAPD plasma's relatively high collisionality also facilitates comparisons with Braginskii fluid codes, and good agreement between the two approaches is expected. The results presented here for the unbiased LAPD plasma were first published in [Shi et al. \(2017\)](#).

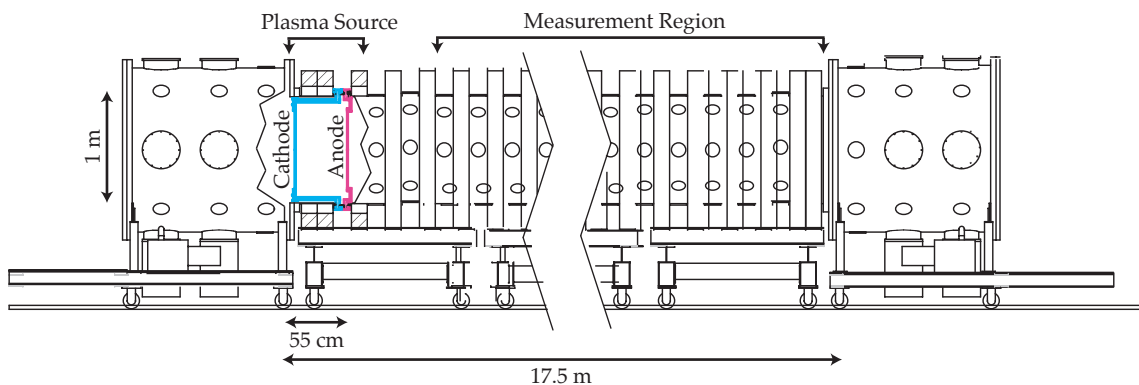


Figure 4.1: Diagram showing a side view of the LAPD device. The barium oxide (BaO) cathode at one end of the device is indicated in blue, which creates a plasma column that is 18 m in length and 60 cm in radius ([Gekelman et al., 2016](#)). This figure is used with permission from T. Carter.

We found that a major challenge in these simulations was the severe constraint on the explicit time-step size due to the high collision frequencies. To somewhat alleviate this time-step restriction, we used a reduced the electron–electron and electron–ion collision frequencies by a factor of 10, although the simulations were still costly. Additionally, we believe that the high collisionality of LAPD accentuated positivity issues caused by the numerical implementation of the collision operators. Nevertheless, the work presented in this chapter is an important demonstration of the feasibility of our discontinuous Galerkin (DG) approach and helps build confidence in the results before we discuss the more hypothetical helical SOL model in Chapter 5.

Our work is a gyrokinetic extension of prior fluid simulations of LAPD (Rogers & Ricci, 2010; Popovich *et al.*, 2010a), and in particular we follow much of the same simulation set-up as in Rogers & Ricci (2010). Originally, we had hoped to make direct quantitative comparisons with the fluid simulations of Rogers & Ricci (2010), but we eventually realized that the omission of a term in their momentum equation resulted in the questionable modeling of the neutrals as having a wind velocity that is the same as the ion flow velocity. These simulations are the first 5D gyrokinetic continuum simulations on open field lines including interactions with sheath losses and are also the first 5D gyrokinetic simulations including a sheath model of a basic laboratory plasma experiment. LAPD experiments relevant to the simulations in this chapter are reported in Carter & Maggs (2009); Carter (2006); Schaffner *et al.* (2013); Schaffner (2013). Relevant experimental data from LAPD are also plotted in some figures of papers presenting fluid simulations of LAPD (Popovich *et al.*, 2010b; Fisher *et al.*, 2015; Fisher & Rogers, 2017; Friedman *et al.*, 2012).

In considering these results, the reader should keep in mind that the main purpose of these simulations is a proof-of-principle demonstration of gyrokinetic continuum simulations with sheath-model boundary conditions. The simulation parameters of Rogers & Ricci (2010) do not appear to correspond to any particular set of experiments performed on LAPD and result in a core $T_e \approx 3$ eV, while most LAPD experiments report $T_e \approx 6$ eV. A faithful set of axial boundary conditions for quantitative modeling of LAPD also requires more investigation, as a portion of the innermost field lines terminate on the hot cathode at one end of the device instead of on the anode mesh (near ground) (Leneman *et al.*, 2006), and the plasma may be detached at the other end (Friedman *et al.*, 2013). Neutral effects such as ion–neutral collisions can also be important to capture some qualitative behaviors (Krasheninnikov & Smolyakov, 2003; Maggs *et al.*, 2007; Carter & Maggs, 2009). Careful quantitative comparisons with LAPD experiments is deferred for future work. Nevertheless, to satisfy the reader’s curiosity, we comment on how our simulations compare to the experiments in a qualitative sense. With additional levels of sophistication, the gyrokinetic capability we have developed may eventually find use in the quantitative design and prediction of LAPD experiments.

Figure 4.2 shows ion-saturation-current (I_{sat}) data measured with a triple Langmuir probe on LAPD between $r = 8$ cm and $r = 37.5$ cm in 0.5 cm increments. Figure 4.2(a) shows the profile of the root mean square (r.m.s.) I_{sat} fluctuation level, normalized globally to the peak value of the background I_{sat} profile. This global normalization for profiles of fluctuation levels is often done in papers that include

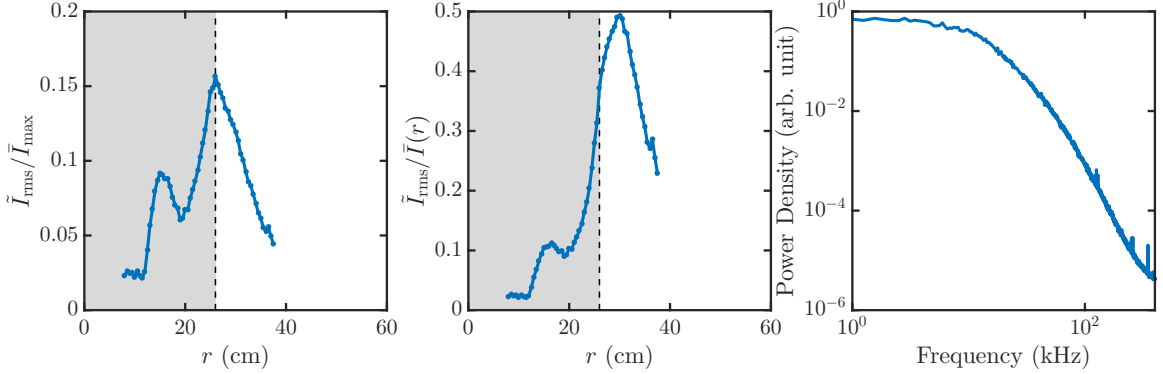


Figure 4.2: Ion-saturation-current fluctuation statistics as measured in an experiment on LAPD (magnetic field strength of 0.05 T). (a) The r.m.s. ion-saturation-current (I_{sat}) fluctuation level as a function of radius, normalized globally to the peak value of the background I_{sat} profile. (b) The r.m.s. I_{sat} fluctuation level as a function of radius, normalized locally to the background ion saturation current $\bar{I}_{\text{sat}}(r)$. (c) The I_{sat} -fluctuation power spectral density. The shaded regions in (a) and (b) illustrate the core region (inside the limiter edge at $r = 26$ cm). The radial plot range has been extended from $r = 0$ cm to $r = 60$ cm to aid in comparisons with figure 4.11, which shows similar plots made using simulation data. These plots were made using triple-Langmuir-probe data provided by T. Carter and D. Schaffner.

LAPD data. Another useful normalization of the fluctuation levels is employed in figure 4.2(b), which also shows the I_{sat} fluctuation level, but normalized locally to the background I_{sat} profile. Figure 4.2(c) shows the I_{sat} -fluctuation power spectral density, which is characteristic of the broadband turbulence that is observed in unbiased LAPD plasmas. Most of the I_{sat} -fluctuation power is seen to be concentrated at low frequencies ($\lesssim 5$ kHz).

4.1 Simulation Parameters

We selected the parameters for our simulations of an LAPD-like helium plasma based on those used by Rogers & Ricci (2010) in a previous Braginskii-fluid-based study, with some modifications for use in a kinetic model. These parameters are summarized in table 4.1. As done by Rogers & Ricci (2010), we have also used a reduced mass ratio of $m_e/m_i = 1/400$, which allows for larger time steps to be taken, but weakens the adiabatic electron response. These parameters are for a fairly collisional case, and the assumption that the collision frequency is small compared to the gyrofrequency is sometimes marginal. We have reduced the electron-electron and electron-ion collision frequencies by a factor of 10 for these simulations, which increases the minimum stable explicit time step size while keeping the collisional mean free path small compared to the parallel length of the simulation box. The rectangular simulation box (an approximation to the cylindrical LAPD plasma) has perpendicular lengths $L_{\perp} = L_x = L_y = 100\rho_{s0} \approx 1.25$ m and parallel length $L_z = 1440\rho_{s0} \approx 18$ m, where $\rho_{s0} = c_{s0}/\Omega_i$

Table 4.1: Summary of input parameters used in LAPD simulations. The normalizations (used for the simulation domain size and source terms) are based on the simulations of [Rogers & Ricci \(2010\)](#) and are used to set the box size and source terms for the simulation. The ion mass is expressed in terms of the proton mass m_p . Note that these normalization values do not necessarily reflect the values observed in the simulations.

Symbol	Value	Description
T_{e0}	6 eV	Electron temperature normalization
T_{i0}	1 eV	Ion temperature normalization
m_i	$3.973m_p$	Mass of ion species
B	0.0398 T	Background axial magnetic field strength
n_0	$2 \times 10^{18} \text{ m}^{-3}$	Density normalization
c_{s0}	$\approx 1.2 \times 10^4 \text{ m/s}$	Ion sound speed normalization
ρ_{s0}	$\approx 1.25 \text{ cm}$	Ion sound radius normalization
Ω_i	$\approx 9.6 \times 10^5 \text{ rad/sec}$	Ion gyrofrequency normalization
L_\perp	$\approx 1.25 \text{ m}$	Width of simulation domain in x and y
L_z	$\approx 18 \text{ m}$	Length of simulation domain in z

Table 4.2: Parameters for the phase-space grid used in the LAPD simulations. The temperatures appearing in the velocity-space extents are $T_{i,\text{grid}} = 1 \text{ eV}$ and $T_{e,\text{grid}} = 3 \text{ eV}$. Piecewise-linear basis functions are used, resulting in 32 degrees of freedom per cell

Coordinate	Number of Cells	Minimum	Maximum
x	36	$-50\rho_{s0}$	$50\rho_{s0}$
y	36	$-50\rho_{s0}$	$50\rho_{s0}$
z	10	$-L_z/2$	$L_z/2$
v_{\parallel}	10	$-4\sqrt{T_{s,\text{grid}}/m_s}$	$4\sqrt{T_{s,\text{grid}}/m_s}$
μ	5	0	$0.75m_s v_{\parallel,\text{max}}^2/(2B_0)$

and $c_{s0} = \sqrt{T_{e0}/m_i}$. The grid parameters are summarized in table 4.2, and 32 degrees of freedom are stored in each 5D cell. With these parameters, $T_{e,\text{min}} \approx 0.91 \text{ eV}$, $T_{\parallel e,\text{min}} = 0.32 \text{ eV}$, and $T_{\perp e,\text{min}} = 1.2 \text{ eV}$. For time stepping, the Courant number is set to 0.1. Some typical time and length scales of interest for the LAPD plasma we simulate are provided in table 4.3.

These simulations were run with 648 CPU cores, taking several wall-clock days to reach a quasi-steady state. This case is highly collisional ($\lambda_{ee}/(L_z/2) \approx 0.004$) compared to tokamak boundary plasmas (see [Umansky et al., 2011](#), table 1), and the time step is limited by the present explicit algorithm for collisions. An implicit

Table 4.3: Some time and length scales of interest for characterizing the LAPD plasma, assuming $T_i \approx 1$ eV and $T_e \approx 3$ eV. The electron quantities shown in this table are computed using the real electron mass. With a reduced electron mass $m_e/m_i = 1/400$, $\tau_{ee} \approx 0.2 \mu\text{s}$ (but λ_{ee} remains unchanged since it has no mass dependence). The electron–electron and electron–ion collision frequencies are further reduced by a factor of 10 in the simulations.

Symbol	Value	Description
τ_{ee}	$0.05 \mu\text{s}$	Typical electron–electron collision time
λ_{ee}	3.3 cm	Typical mean free path for electron–electron collisions
τ_{ii}	$1.1 \mu\text{s}$	Typical ion–ion collision time
λ_{ii}	0.5 cm	Typical mean free path for ion–ion collisions
ρ_i	0.5 cm	Typical ion gyroradius
ρ_e	0.01 cm	Typical electron gyroradius
ρ_s	0.9 cm	Typical ion sound gyroradius

algorithm for collisions is expected to reduce the cost of these simulations by a large factor. The underlying kinetic solver parallelizes well in multiple dimensions and the execution time is approximately linear in the number of cells.

By assuming that the magnetic field is a constant $\mathbf{B} = B\hat{z}$, the 5D gyrokinetic system we solve (see (2.1) and (2.43)) has the following simplified form for $\mathcal{J}\Pi$:

$$\mathcal{J}\Pi = \begin{pmatrix} 0 & -1/q_s & 0 & 0 & 0 \\ 1/q_s & 0 & 0 & 0 & 0 \\ 0 & 0 & 0 & B/m_s & 0 \\ 0 & 0 & -B/m_s & 0 & 0 \\ 0 & 0 & 0 & 0 & 0 \end{pmatrix}. \quad (4.1)$$

The initial density profile for both ions and electrons is chosen to be $n_0 A(r; c_{\text{edge}} = 1/20)$, where $r = \sqrt{x^2 + y^2}$ and $A(r; c_{\text{edge}})$ is a function that falls from the peak value of 1 at $r = 0$ to a constant value c_{edge} for $r > L_\perp/2$:

$$A(r; c_{\text{edge}}) = \begin{cases} (1 - c_{\text{edge}}) \left(1 - \frac{r^2}{(L_\perp/2)^2}\right)^3 + c_{\text{edge}} & r < L_\perp/2, \\ c_{\text{edge}} & \text{else.} \end{cases} \quad (4.2)$$

The initial electron temperature profile has the form $5.7A(r; c_{\text{edge}} = 1/5)$ eV, while the initial ion temperature profile is a uniform 1 eV. Both electrons and ions are initialized as non-drifting Maxwellians, although future runs could be initialized with a specified non-zero mean velocity as a function of the parallel coordinate computed from simplified 1D models (Shi *et al.*, 2015) to reach a quasi-steady state more quickly. This idea is used to initialize the distribution functions in the simulations for the helical-SOL simulations discussed in Chapter 5 (see Appendix D for the calculation).

Although we expect the quasi-steady state of the system to be insensitive to the choice of initial conditions, we found that it was important to start the simulation with a non-uniform density profile to avoid exciting large transient potential oscillations that resulted in extremely small restrictions being imposed on the time step (for stability, the time step is automatically adjusted based on the maximum gyrocenter characteristic velocities). Because the boundary conditions force ϕ to a constant on the side walls (see Section 4.2), electrons near the domain boundaries in x and y are quickly lost at thermal speeds from the simulation box. We believe that this large momentary imbalance in the electron and ion densities is the source of this stability issue.

The electron and ion sources have the form

$$S_s = 1.08 \frac{n_0 c_{s0}}{L_z} \left\{ 0.01 + 0.99 \left[\frac{1}{2} - \frac{1}{2} \tanh \left(\frac{r - r_s}{L_s} \right) \right] \right\} F_{M,s}(v_{||}, \mu; T_s), \quad (4.3)$$

where $r_s = 20\rho_{s0} = 0.25$ m, $L_s = 0.5\rho_{s0} = 0.625$ cm, and $F_{M,s}(v_{||}, \mu; T_s)$ is a normalized non-drifting Maxwellian distribution for species s with temperature T_s . Figure 4.3 shows the simulation geometry and density source rate in the x - z plane at $y = 0$ m, and figure 4.4 shows the density source rate and temperature in the x - y plane. The ion source has a uniform temperature of 1 eV, while the electron source has a temperature profile given by $6.8A(r; c_{\text{edge}} = 1/2.5)$ eV. In the actual LAPD experiment, the radius of the plasma column is controlled using a floating-plate limiter with a variable aperture size that is situated near the source end of the device (Carter, 2006). For clarity, we will refer to the region of the simulation domain with $r < r_s$ as the *core region*, since most of the electrons and ions are sourced there, the $r = r_s$ location as the *limiter edge*, and the region with $r > r_s$ as the *edge region*.

Unlike the sources used by Rogers & Ricci (2010), the sources we use model the neutrals as being ionized at zero mean velocity. In the fluid equations of Rogers & Ricci (2010), a zero-velocity plasma source would give rise to an additional term $-S_n V_{||i}/n$ on the right-hand side of the $\partial_t V_{||i}$ equation, which is kept in the more general equations of Wersal & Ricci (2015). In our simulations, electrons and ions are also sourced in the $r > r_s$ region at 1/100th the amplitude of the central source rate to avoid potential issues arising from zero-density regions. While there are no high-energy electrons emitted from the cathode source in the $r > r_s$ region in the actual LAPD device, Carter & Maggs (2009) have discussed the possibility of ionization in this region by electrons in the main plasma in some experiments with elevated edge electron temperatures. Note that (4.3) does not represent the only source of energy in the system, as the positivity-adjustment procedure also results in some energy being added to the particles at large r and near the sheath entrances, as discussed in Section 2.4.

4.2 Boundary Conditions and Energy Balance

Dirichlet boundary conditions $\phi = 0$ are used on the x and y boundaries for the potential solve (taking the side walls to be grounded to the $\phi_w = 0$ end plates), while

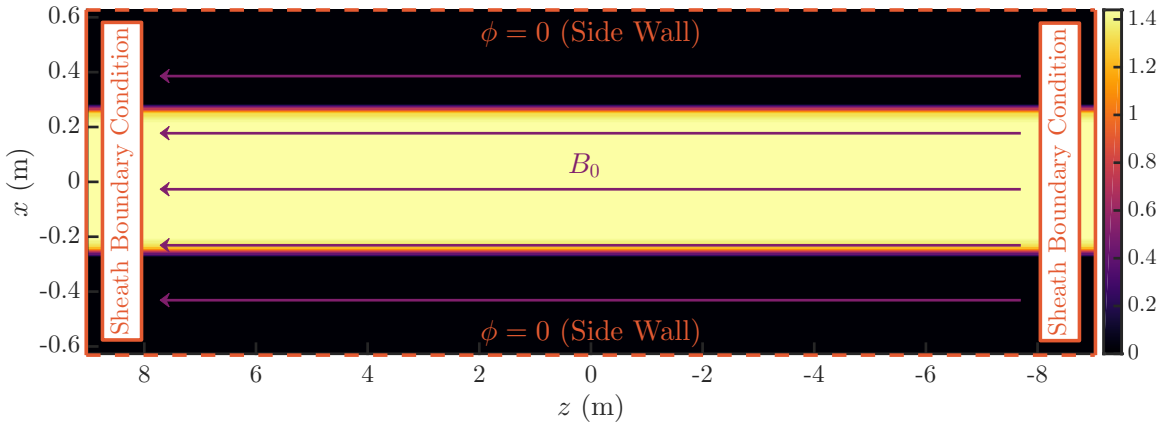


Figure 4.3: LAPD-simulation density source rate (in $10^{21} \text{ m}^{-3} \text{ s}^{-1}$) in the x - z plane at $y = 0$ m. The solid orange lines on the left and right edges of the plot indicate the locations at which sheath-model boundary conditions are applied. The dashed orange lines on the top and bottom edges indicate the locations of the side walls, which we take to be grounded.

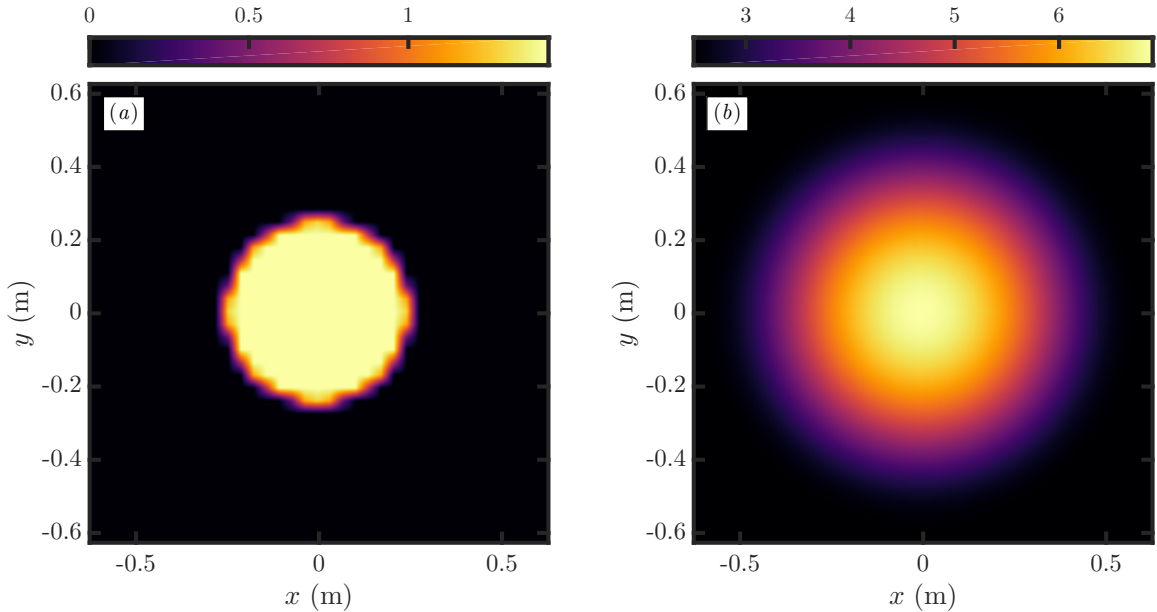


Figure 4.4: LAPD-simulation (a) source density rate (in $10^{21} \text{ m}^{-3} \text{ s}^{-1}$) and (b) temperature of source electrons (in eV) in the x - y plane. In this view, the side walls are located on all four sides of the square boundary. Note that the actual LAPD device has a circular cross section instead of the square cross section used in the simulation.

no boundary condition on ϕ is required in z because (2.4) contains no z derivatives. The distribution function uses zero-flux boundary conditions in x , y , v_{\parallel} , and μ , which amounts to zeroing out the interface flux evaluated on a boundary where zero-flux boundary conditions are to be applied. This ensures that particles are not lost through the domain boundaries in x , y , v_{\parallel} , and μ . It should be noted that zero-flux boundary conditions on the x and y boundaries are a result of the choice of a constant ϕ on the side-wall boundaries, so the $E \times B$ velocity at these boundaries is parallel to the wall. Sheath-model boundary conditions, discussed in the previous section, are applied to the distribution functions on the upper and lower boundaries in the z direction.

To demonstrate how the choice of $\phi = 0$ affects the energy balance in our long-wavelength gyrokinetic system with a linearized polarization term in the gyrokinetic Poisson equation, we define the plasma thermal energy as

$$W_K = \int d^3x \sum_s \int d^3v f_s H_0, \quad (4.4)$$

where $H_0 = \frac{1}{2}mv_{\parallel}^2 + \mu B$. Neglecting sources and collisions for simplicity, the gyrokinetic equation in a straight, constant magnetic field can be written as

$$\frac{\partial f_s}{\partial t} + \frac{\partial}{\partial z} (v_{\parallel} f_s) + \nabla \cdot (\mathbf{v}_E f_s) + \frac{\partial}{\partial v_{\parallel}} \left(\frac{q_s}{m_s} E_{\parallel} f_s \right) = 0, \quad (4.5)$$

where $E_{\parallel} = -\mathbf{b} \cdot \nabla \langle \phi \rangle$ and $\mathbf{v}_E = \mathbf{b} \times \nabla \langle \phi \rangle / B$.

Multiplying (4.5) by H_0 and integrating over phase space,

$$\begin{aligned} \frac{\partial W_K}{\partial t} &= - \int dx dy \sum_s \int d^3v H_0 v_{\parallel} f_s \Big|_{z_{\text{lower}}}^{z_{\text{upper}}} + \int d^3x \sum_s \int d^3v v_{\parallel} f_s q_s E_{\parallel} \\ &= - \int dx dy \sum_s \int d^3v H_0 v_{\parallel} f_s \Big|_{z_{\text{lower}}}^{z_{\text{upper}}} + \int d^3x j_{\parallel} E_{\parallel}, \end{aligned} \quad (4.6)$$

where we have used the fact that the normal component of \mathbf{v}_E vanishes on the side walls (since ϕ is a constant on the side walls) and zero-flux boundary conditions on f_s in v_{\parallel} . The first term on the right-hand side is the parallel heat flux out to the sheaths and the second term is the parallel acceleration by the electric field, which mediates the transfer of energy between thermal and field energies in this model (this term appears with the opposite sign in the equation for the evolution of $E \times B$ energy).

To calculate the field energy evolution, we take the time derivative of the gyrokinetic Poisson equation (2.4),

$$\begin{aligned} -\nabla_{\perp} \cdot \left(\epsilon \nabla_{\perp} \frac{\partial \phi}{\partial t} \right) &= \sum_s q_s \int d^3 v \frac{\partial f_s}{\partial t} \\ &= -\sum_s q_s \int d^3 v \left[\frac{\partial}{\partial z} (v_{\parallel} f_s) + \nabla \cdot (\mathbf{v}_E f_s) \right] \\ &= -\frac{\partial j_{\parallel}}{\partial z} - \nabla \cdot (\mathbf{v}_E \sigma_g), \end{aligned} \quad (4.7)$$

where $\epsilon = n_{i0}^g e^2 \rho_{s0}^2 / T_{e0}$. Next, we multiply (4.7) by ϕ and integrate over space:

$$\begin{aligned} -\int d^3 x \phi \nabla_{\perp} \cdot \left(\epsilon \nabla_{\perp} \frac{\partial \phi}{\partial t} \right) &= -\int d^3 x \phi \left[\frac{\partial j_{\parallel}}{\partial z} + \nabla \cdot (\mathbf{v}_E \sigma_g) \right] \\ -\int d\mathbf{S}_{\perp} \cdot \phi \epsilon \nabla_{\perp} \frac{\partial \phi}{\partial t} + \frac{1}{2} \int d^3 x \epsilon \frac{\partial (\nabla_{\perp} \phi)^2}{\partial t} &= -\int dx dy \phi j_{\parallel} \Big|_{z_{\text{lower}}}^{z_{\text{upper}}} + \int d^3 x \frac{\partial \phi}{\partial z} j_{\parallel} \\ &\quad - \int d\mathbf{S}_{\perp} \cdot \phi \mathbf{v}_E \sigma_g + \int d^3 x \nabla \phi \cdot \mathbf{v}_E \sigma_g. \end{aligned} \quad (4.8)$$

The integral involving $\int d\mathbf{S}_{\perp}$ on the right-hand side is zero because \mathbf{v}_E has no normal component on the side walls. By assuming that $\phi = 0$ on the side walls, the term on the left-hand side involving $\int d\mathbf{S}_{\perp} \phi$ is also zero and we have

$$\frac{\partial W_{\phi}}{\partial t} = \frac{\partial}{\partial t} \left(\frac{1}{2} \int d^3 x \epsilon (\nabla_{\perp} \phi)^2 \right) = -\int dx dy \phi j_{\parallel} \Big|_{z_{\text{lower}}}^{z_{\text{upper}}} - \int d^3 x j_{\parallel} E_{\parallel}. \quad (4.9)$$

If the wall is biased instead of grounded, as done in a set of experiments by Carter & Maggs (2009), one must retain the first term on the left-hand side of (4.8) in energy-balance considerations. The second term on the right-hand side of (4.9) is equal and opposite to the second term on the right-hand side of (4.6), and so cancels when the two equations are added together. The total energy is the sum of the kinetic energy W_k and the field energy W_{ϕ} . Substituting the definition of ϵ , this field energy can be written as $W_{\phi} = \int d^3 x n_{i0}^g m_i v_E^2 / 2$, indicating that it can be interpreted as the kinetic energy associated with the $E \times B$ motion. (The n_{i0}^g factor can be generalized to the full density $n_i^g(\mathbf{R}, t)$ as described in Section 2.1, with an additional contribution to the Hamiltonian.) The first term on the right-hand side of (4.9) corresponds to work done on particles as they are accelerated through the sheath. The ϕ in this boundary term is the potential at the z boundaries of the simulation domain, where the sheath entrances are. When $j_{\parallel} = 0$ at the sheath entrance, then the energy lost by electrons as they drop through the sheath is exactly offset by the energy gained by ions as they drop through the sheath. If more electrons than ions are leaving through the sheath, then the net energy lost in the unresolved sheath region contributes to an increase in the field energy.

There is also room for improvements in the side-wall boundary conditions. Identifying the left-hand side of (4.7) as $-\partial\sigma_{\text{pol}}/\partial t = \nabla \cdot \mathbf{j}_{\text{pol}}$, and integrating over all space,

$$\begin{aligned} \int d^3x \nabla \cdot \mathbf{j}_{\text{pol}} &= \int d\mathbf{S} \cdot \mathbf{j}_{\text{pol}} \\ &= \int d\mathbf{S}_\perp \cdot \epsilon \frac{\partial \mathbf{E}_\perp}{\partial t}, \end{aligned} \quad (4.10)$$

so we see that there is an ion polarization current into the side wall when the electric field pointing into the side wall is increasing in time, which is physically reasonable. However, if the sign of the electric-field time derivative reverses, it is not possible to pull ions out of the side wall (where they are trapped by quantum effects, or return as neutrals), and a boundary layer might form near the side walls. In fusion devices, it is rare for the magnetic field to be exactly parallel to the wall, so it could be appropriate to use a model of the Chodura magnetic pre-sheath (Chodura, 1982). Geraldini *et al.* (2017) also recently studied a gyrokinetic approach to the magnetic pre-sheath.

The inclusion of charge-neutral source terms and number-conserving collision operators to the above analysis does not result in additional sources of $E \times B$ energy, since they lead to the addition of terms to the right-hand side of (4.9) of the form

$$-\int d^3x \phi \sum_s q_s \int d^3v S_s(\mathbf{R}, \mathbf{v}, t) = 0. \quad (4.11)$$

4.3 Simulation Results

In this section we present results from our gyrokinetic simulation. Our goal here is not to argue that our simulations are a faithful model of the LAPD plasma, but instead to demonstrate the ability to carry out gyrokinetic continuum simulations of open-field-line plasmas in a numerically stable way and to demonstrate a reasonable level of qualitative agreement by making contact with turbulence measurements from the real LAPD device and previous Braginskii fluid simulations (Ricci & Rogers, 2010; Fisher *et al.*, 2015; Friedman *et al.*, 2012), since we have used similar plasma parameters and geometry. Starting from the initial conditions described in Section 4.1, the electron and ion distributions evolve for a few ion sound transit times ($\tau_s \sim (L_z/2)/c_s \approx 1.1$ ms using $T_e = 3$ eV) until a quasi-steady state is reached, during which the total number of particles of each species remains approximately constant. We have found that the time discretization results in relative errors in the energy conservation of $\sim 10^{-4}$. A discussion about the energy-conservation properties of these simulations is presented in Appendix C. Some snapshots of the total electron density in the transient stage are shown in figure 4.5.

As seen in LAPD experiments (Schaffner *et al.*, 2012, 2013), we observe a weak spontaneous rotation in the ion-diamagnetic-drift direction. Figure 4.6 shows snapshots in the perpendicular plane of the total electron density, electron temperature, and electrostatic potential after a few ion transit times, which are qualitatively simi-

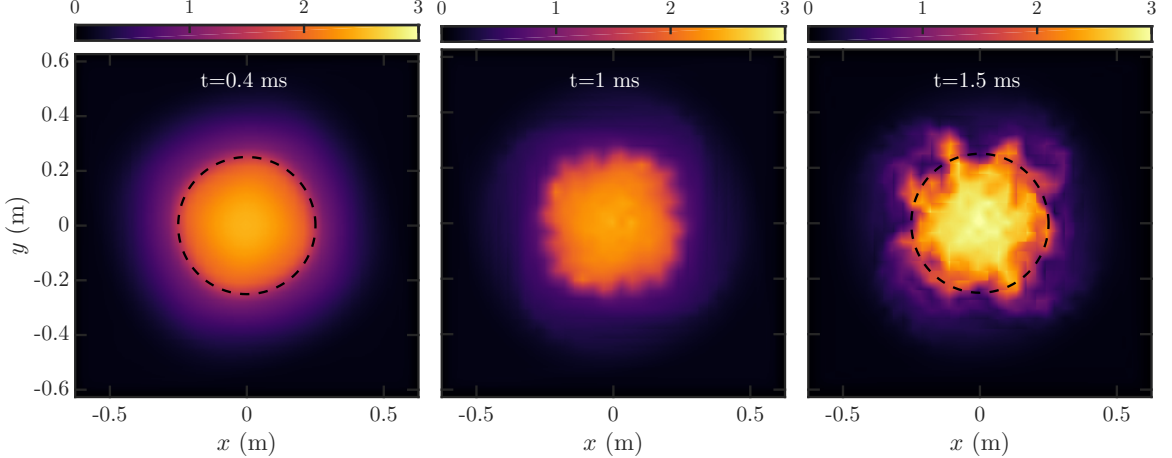


Figure 4.5: Snapshots of the total electron density (in 10^{18} m^{-3}) in the x - y plane from a 5D gyrokinetic simulation of an LAPD plasma at $t = 0.4$ ms, $t = 1$ ms, and $t = 1.5$ ms. The sources are concentrated inside the dashed line indicated (not shown on the $t = 1$ ms plot), which is located at $r = r_s = 20\rho_{s0}$. Starting from the initial condition, the source steepens the plasma profiles until short-wavelength structures begin to grow. At longer times, larger-wavelength structures develop and remain for the rest of the simulation. For additional details about how this plot and ones like it were created, see Appendix A.

lar to the snapshots presented from Braginskii fluid simulations of LAPD (Rogers & Ricci, 2010; Fisher *et al.*, 2015). Figure 4.7(a) shows the time-averaged radial profile of the ion-outflow Mach number across each parallel boundary, where we define the Mach number as u_\parallel/c_s . Since the electron mean free path is smaller than the effective parallel grid spacing, we do not resolve the collisionless transition layer in front of the sheath in which the outflow at the collisional sound speed ($\gamma = 5/3$) transitions to an outflow at the collisionless sound speed ($\gamma = 3$). Therefore, we expect the sound speed at the sheath to be $c_s = \sqrt{(T_e + \gamma T_i)/m_i}$ with $\gamma = 5/3$. Despite the fact that our sheath-model boundary conditions do not enforce outflows at the sound speed, we see that the Mach number is very close to 1 at the sheath entrance. Figure 4.7(b) shows the total loss rate of electron and ion guiding centers across the parallel boundaries over a period of several microseconds. We confirm that the particle loss rate is in an approximate balance with the particle source rate in this quasi-steady state. We note that in addition to the particle source of approximately $5.5 \times 10^{21} \text{ s}^{-1}$, there is a time-varying particle source of approximately 10^{21} s^{-1} that comes from adding electrons and ions to the system in order to keep the density above a floor of $2 \times 10^{12} \text{ m}^{-3}$ everywhere (see Section 2.4).

Figure 4.6(c) shows that a boundary layer with a width of order the sound gyroradius forms in the potential near the side walls, where the potential drops to match the boundary conditions $\phi = 0$ on the side walls. This means that a normal sheath at the ends in z with $\phi_s \sim 3T_e$ cannot occur very close to the side walls. However, one can still eventually get a quasi-steady state with the electron flux, $\sim n_e v_{te} \exp(-e\phi_s/T_e)$,

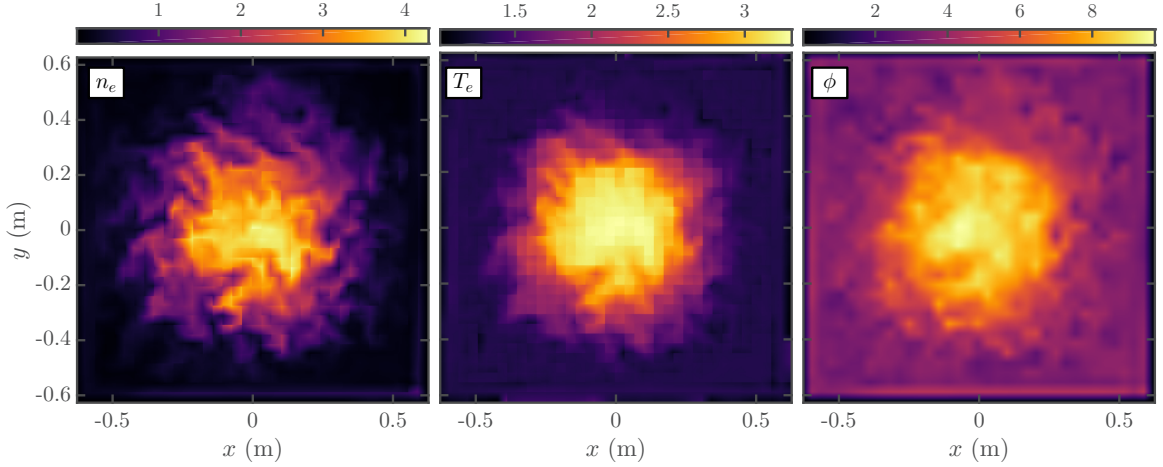


Figure 4.6: Snapshots of the total electron density n_e (in 10^{18} m^{-3}), electron temperature T_e (in eV), and electrostatic potential ϕ (in V) from a 5D gyrokinetic simulation of an LAPD plasma. The plots are made in center of the box at $z = 0$ m. In this simulation, a continuous source of plasma concentrated inside $r_s = 0.25$ m is transported radially outward by the turbulence as it flows at near-sonic speeds along the magnetic field lines to the end plates, where losses are mediated by sheath-model boundary conditions. The plots are made in the x - y plane perpendicular to the magnetic field in the middle of the device after a few ion transit times.

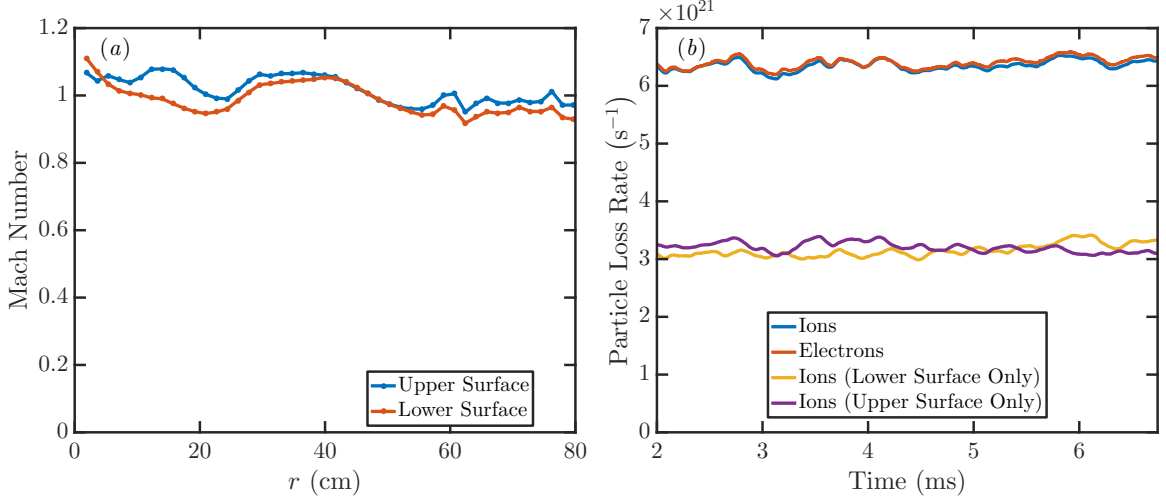


Figure 4.7: (a) Time-averaged radial profile of the ion-outflow Mach number across each parallel boundary, denoted as upper and lower surfaces. The Mach number is defined as u_{\parallel}/c_s , where $c_s = \sqrt{(T_e + \gamma T_i)/m_i}$ and $\gamma = 5/3$. (b) Total outflow of electron and ion guiding centers across the parallel boundaries during a quasi-steady state (in s^{-1}). Also indicated is the outflow for ions across each surface individually.

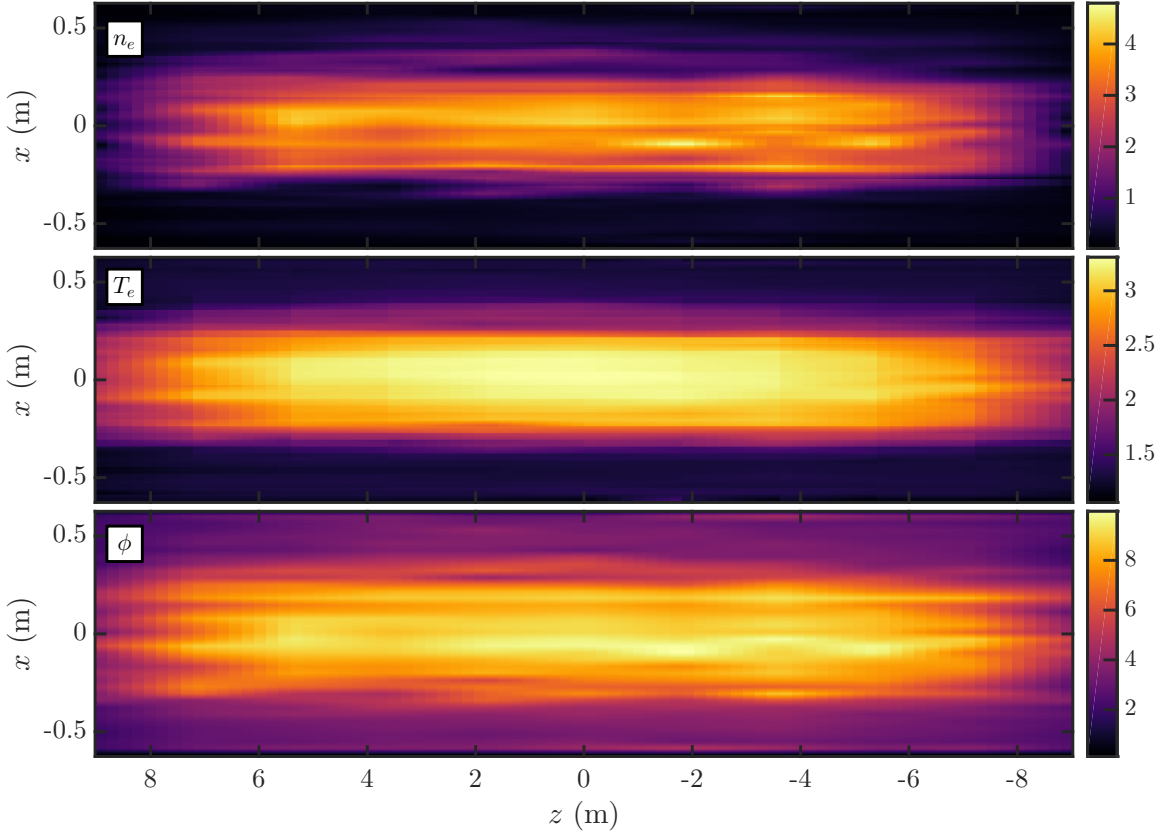


Figure 4.8: Snapshots of the total electron density n_e (in 10^{18} m^{-3}), electron temperature T_e (in eV), and electrostatic potential ϕ (in V) from a 5D gyrokinetic simulation of an LAPD plasma. The plots are made in the x - z plane at $y = 0$ m after a few ion transit times.

of order the ion flux because the electron density becomes very small near the side walls and the electrons become colder there. Figure 4.8 shows the same fields as in figure 4.6, but the plots are made in the $y = 0$ plane to show the parallel structure.

Figure 4.9 shows the time-averaged radial profile of n_e , T_e , and ϕ computed by averaging the data in the region $-4 \text{ m} < z < 4 \text{ m}$. We focus on this region since it is similar to the region in which probe measurements are taken in the LAPD, and there is little parallel variation in this region. Particle transport in the radial direction is especially evident in figure 4.9 from the broadening in the n_e profile. In figure 4.9, the electron temperature drops off at mid-radii but is rather flat at large r . To understand this, note that there is a ≈ 2.7 eV residual electron source at large r (see (4.3)), and that the observed temperature is close to the limit of the coldest temperature that can be represented on the grid when collisions dominate and the distribution function is isotropic, so $T_{e,\min} \approx T_{\perp e,\min} = 1.2$ eV. Our choice of velocity-space grid is a compromise between resolving low energies and the need to go up to significantly higher energies than the temperature of the source (which has a maximum temperature of 6.7 eV) to represent the tail. This will be improved in future work using a non-uniformly spaced velocity grid or exponential basis functions,

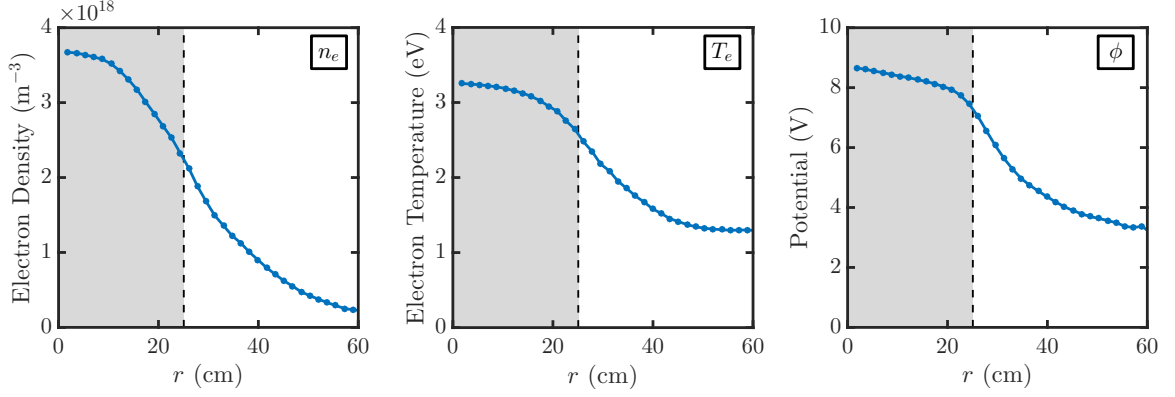


Figure 4.9: Average profiles of the electron density n_e , electron temperature T_e , and electrostatic potential ϕ as a function of radius. The fields in the region $-4 \text{ m} < z < 4 \text{ m}$ are time averaged over several ion transit times after the simulation has reached a quasi-steady state, evaluated at eight equally spaced points in each cell, and then binned by radius. The shaded region illustrates the core region inside the limiter edge at $r = r_s$.

which can represent a range of electron energies much more efficiently. We do not expect the non-vanishing T_e at large r to affect the results significantly because both n_e and the n_e fluctuation level are small at large r .

Figure 4.10(a) shows the time-averaged radial $E \times B$ particle flux due to electrostatic fluctuations, which we define as

$$\Gamma_{n,r} = n_e \mathbf{v}_E \cdot \hat{\mathbf{r}}. \quad (4.12)$$

The profile of $\Gamma_{n,r}$ is a measure of the turbulent radial particle transport in the plasma. To get a sense of how much the turbulence broadens the profiles radially, we can compare $\Gamma_{n,r}$ to the outward parallel particle flux $\Gamma_{n,z}$, which is shown in figure 4.10(b). We see that the total particle outflow in the core-plasma region is $\int_0^{r_s} dr 2\pi r \Gamma_{n,z} \approx 2.8 \times 10^{21} \text{ s}^{-1}$. From figure 4.10(a), we also see that the radial transport out of the core region is $2\pi r_s L_z \Gamma_{n,r}(r = r_s) \approx 2.3 \times 10^{21} \text{ s}^{-1}$. We conclude that rates at which particles leave the core region through turbulent radial transport and through parallel losses at the end plates are comparable. Note that the cross-field turbulent particle transport in linear devices is often negligible compared to the parallel particle transport. The large length and radius of the LAPD plasma column enable the turbulence to have a noticeable effect on the plasma profiles.

Electron-density-fluctuation profiles have also been measured in LAPD (Carter & Maggs, 2009; Popovich *et al.*, 2010b; Friedman *et al.*, 2012; Fisher *et al.*, 2015; Carter, 2006). We define the density fluctuation as $\tilde{n}_e(x, y, z, t) = n_e(x, y, z, t) - \bar{n}_e(x, y, z)$, where $\bar{n}(x, y, z)$ is computed by averaging the electron density using a $1 \mu\text{s}$ sampling interval over a period of 1 ms. The density fluctuation level is normalized both to the peak amplitude of \bar{n}_e at $r = 0$ (as done in Friedman *et al.*, 2012) and to the local value of $\bar{n}_e(x, y, z)$ and then binned by radius to calculate profiles of the r.m.s. density fluctuation level, which are shown in figures 4.11(a) and 4.11(b). Similar to

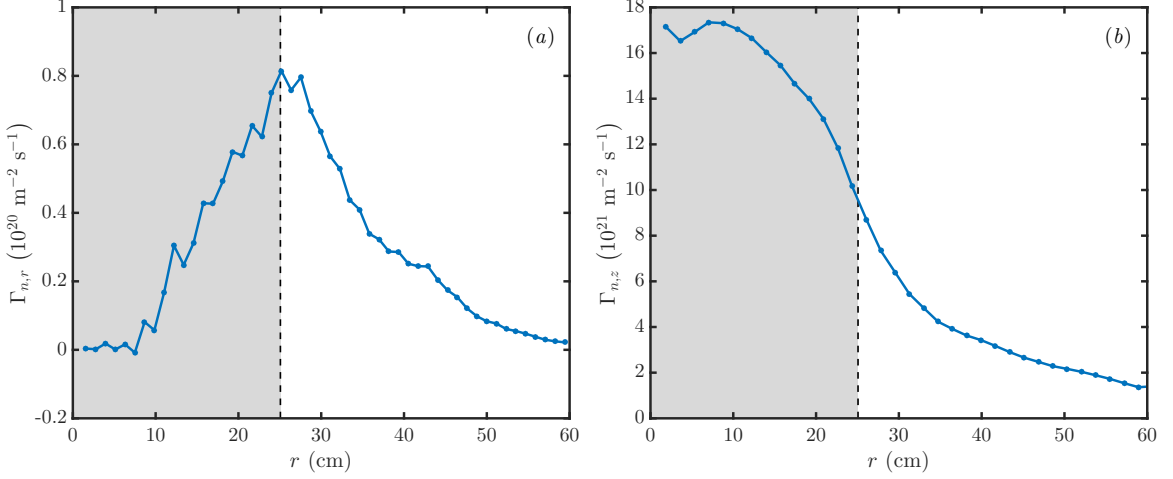


Figure 4.10: Profiles of the (a) time-averaged radial particle flux $\Gamma_{n,r}$ due to electrostatic fluctuations and (b) time-averaged total outward parallel particle flux $\Gamma_{n,z}$, which includes contributions from both end plates. The shaded region illustrates the core region inside the limiter edge at $r = r_s$. These profiles indicate that the parallel particle loss rate in the core is approximately $2.8 \times 10^{21} \text{ s}^{-1}$, while radial transport into the edge region due to turbulence is approximately $2.3 \times 10^{21} \text{ s}^{-1}$, so radial turbulent particle transport is comparable to parallel particle transport in these simulations (owing to the large ≈ 18 m length of the LAPD plasma column).

measurements reported in LAPD, we find that the maximum in the density fluctuation level (normalized to \bar{n}_{\max}) occurs at the limiter edge and at the $\sim 10\%$ level. The decay of the density fluctuation level (normalized to \bar{n}_{\max}) both radially inward and outward from the peak location is also commonly observed in LAPD. Figure 4.11(c) shows the power spectral density of electron-density fluctuations, which is computed by averaging the power spectra at each node in the region $25 \text{ cm} < r < 30 \text{ cm}$ and $-4 \text{ m} < z < 4 \text{ m}$. Similar to measurements reported in LAPD, we find that the turbulence has a broadband spectrum that drops by approximately six orders of magnitude from $\sim 10^3$ Hz to $\sim 10^5$ Hz.

The probability density function (PDF) of density fluctuations in LAPD has also been of interest. Carter (2006) focused on the intermittency of the density-fluctuation PDF measured at various radial locations. Figure 4.12 shows the simulation PDF at three radial locations (using $\Delta r = 0.5$ cm wide radial intervals) in the region $-4 \text{ m} < z < 4 \text{ m}$. We find symmetric and near-Gaussian PDFs in the core region at $r = 21$ cm, which is 4 cm from the limiter edge, and at $r = 24$ cm, which is 1 cm from the limiter edge. A few centimeters outside the core region at $r = 31$ cm, we find a positively skewed and non-Maxwellian PDF. Here, we see that there is a particularly strong enhancement of large-amplitude positive-density-fluctuation events. Compared to the experimental results of Carter (2006), the PDFs we observe at the inner-two radial locations are much closer to a Gaussian, and we do not observe a negatively skewed PDF at the innermost radial location.

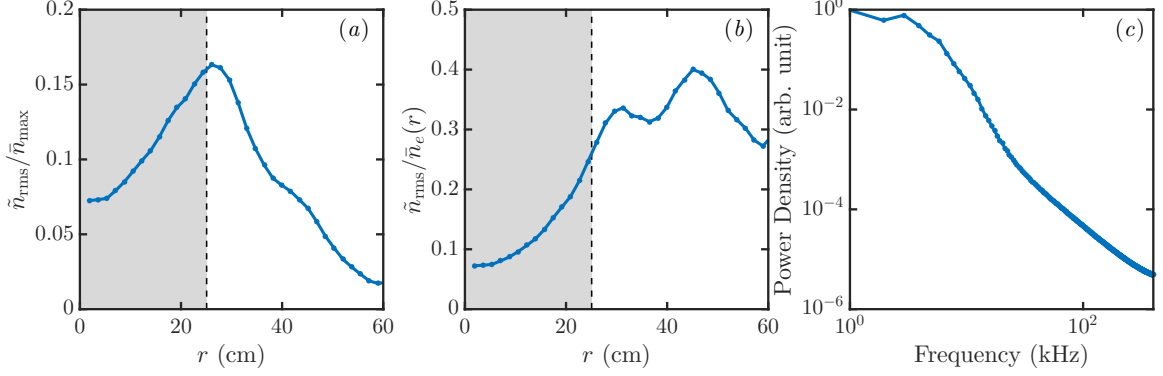


Figure 4.11: Density fluctuation statistics computed from a 5D gyrokinetic simulation of an LAPD plasma. (a) The r.m.s. density fluctuation level as a function of radius, normalized globally to the peak background electron density $\bar{n}_{\text{max}} \approx 3.68 \times 10^{18} \text{ m}^{-3}$. (b) The r.m.s. density fluctuation level as a function of radius, normalized locally to the background electron density $\bar{n}_e(r)$. (c) The density fluctuation power spectral density. These plots are in good qualitative agreement with LAPD measurements (Carter & Maggs, 2009; Popovich *et al.*, 2010b; Friedman *et al.*, 2012; Fisher *et al.*, 2015; Carter, 2006), reproducing features such as the maximum in the density fluctuation level (normalized to \bar{n}_{max}) occurring at the limiter edge and at the $\sim 10\%$ level, the decay of normalized density fluctuation level both radially inward and outward from the peak location, and the broadband fluctuation spectrum that drops by approximately six orders of magnitude from $\sim 10^3$ Hz to $\sim 10^5$ Hz. The shaded regions in (a) and (b) illustrate the core region inside the limiter edge at $r = r_s$.

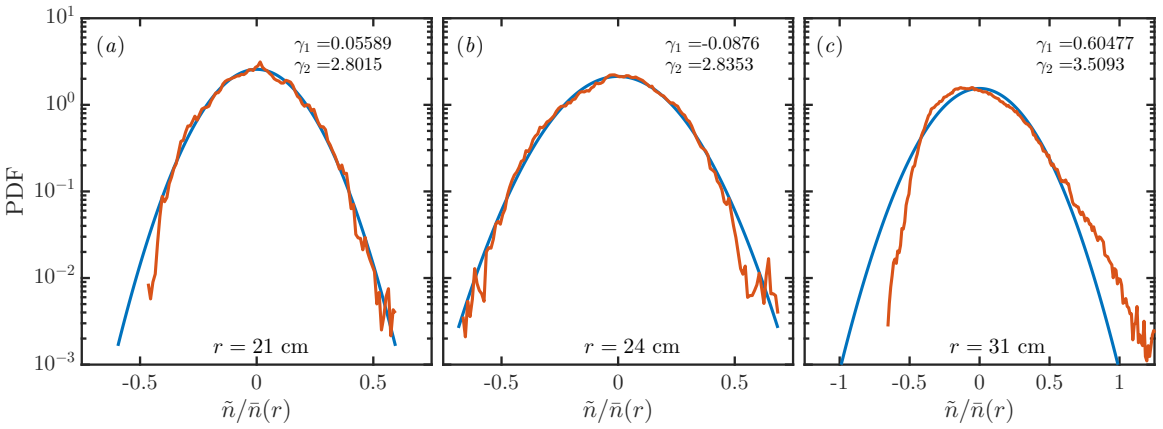


Figure 4.12: Density-fluctuation-amplitude PDF (in red and normalized local value of the background electron density) at three radial locations in the region $-4 \text{ m} < z < 4 \text{ m}$: (a) 4 cm from the limiter edge at $r = 21$ cm, (b) 1 cm from the limiter edge at $r = 24$ cm, and (c) a few centimeters outside the core region at $r = 31$ cm. Gaussian PDFs are shown in blue for comparison. Also indicated on each plot is the skewness $\gamma_1 = E[\tilde{n}_e^3]/\sigma^3$ and the kurtosis $\gamma_2 = E[\tilde{n}_e^4]/\sigma^4$, where σ is the standard deviation of \tilde{n}_e and $E[\dots]$ denotes the expected value.

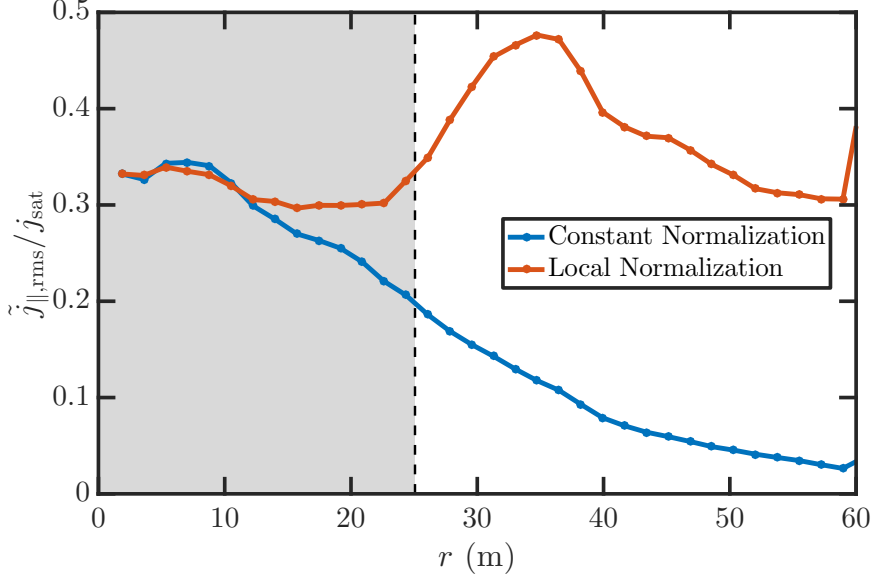


Figure 4.13: Radial profile of the r.m.s. current fluctuation amplitude at the sheath entrances, normalized to the on-axis peak value of $j_{\text{sat}} = q_i n c_s \approx 1300 \text{ A m}^{-2}$ ('constant normalization') and to the local value of j_{sat} ('local normalization'). The large relative current fluctuation amplitudes permitted by conducting-sheath boundary conditions would not be present in a simulation that used insulating-sheath boundary conditions.

Figure 4.13 shows the r.m.s. current fluctuation level as a function of radius, measured at the sheath entrances. The current fluctuation amplitude is normalized to both the on-axis peak value of $j_{\text{sat}} = q_i n c_s \approx 1300 \text{ A m}^{-2}$ and to the local value of j_{sat} . Not shown is the mean total current at the sheath entrance, which has a peak value of approximately 100 A m^{-2} . The observed behavior is significantly different from the $j_{\parallel} = 0$ condition that would be imposed by insulating-sheath (logical-sheath) boundary conditions, and future work can investigate the impact of $j_{\parallel} = 0$ vs. $j_{\parallel} \neq 0$ boundary conditions. Thakur *et al.* (2013) investigated the use of both conducting and insulating end plates on the controlled shear de-correlation experiment (CSDX), observing several changes in the turbulence characteristics. Kelvin–Helmholtz modes driven by sheared azimuthal flows appear to be absent in drift-reduced Braginskii fluid simulations using insulating-sheath boundary conditions (Vaezi *et al.*, 2017; Leddy & Dudson, 2017).

4.4 Limiter-Biasing Simulations

Without having to write additional C++ code, we can trivially modify these simulations of LAPD to include a model of a biasable limiter. In previous experiments on LAPD (Schaffner *et al.*, 2012, 2013; Schaffner, 2013), an annular, aluminum limiter was installed that intersected the magnetic field lines in the edge region, modifying the parallel boundary conditions for $r > r_s$ while leaving the parallel boundary con-

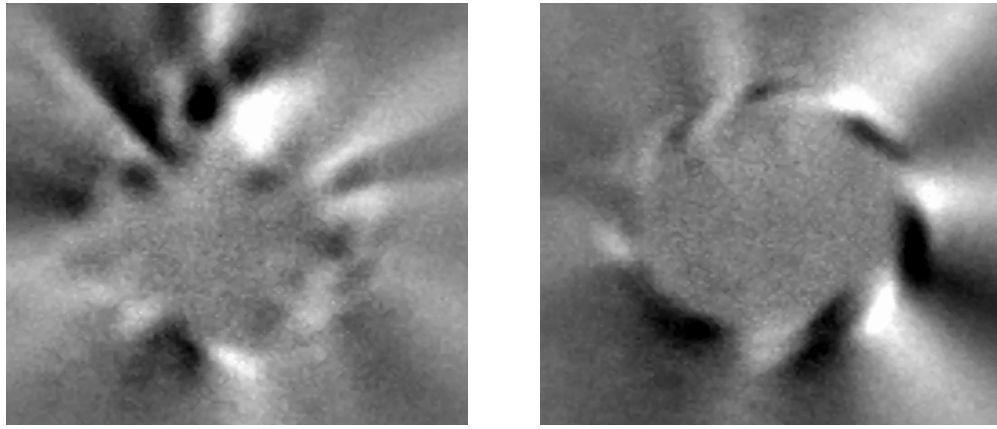


Figure 4.14: Passive-imaging measurements of visible light from a LAPD discharge at 0.05 T (left) before limiter biasing is turned on and (right) after limiter biasing is turned on. The measured light is due to emission from neutral Helium in the device. Qualitative changes in the turbulence are observed after limiter biasing is turned on, including a reversal of the plasma rotation direction for large positive bias voltages (relative to the source anode) and the development of a coherent mode in strongly biased cases. Note that the fast-framing camera, located at the end of the device downstream from the source, records light from the entire \sim 18 m-long plasma column. These images are used with permission from T. Carter.

ditions in the core region ($r < r_s$) unaffected. This limiter can be biased positive and negative relative to the anode of the plasma source, which modifies the plasma potential in the edge region and consequently results in a $\partial_r\phi = -E_r$ profile that drives a poloidal $E \times B$ rotation near the limiter edge. By using the biasable limiter to drive strong azimuthal flows and flow shear near the limiter edge, Schaffner *et al.* (2012, 2013); Schaffner (2013) found that turbulent transport was suppressed. Figure 4.14 shows visible light images of the LAPD plasma column before and after (positive) limiter biasing in one of these experiments. These experiments are related to tokamak experiments in the late 1980s in which electrically biased limiters (Phillips *et al.*, 1987) and electrodes (Taylor *et al.*, 1989) were used to modify radial electric fields, driving poloidal flows that consequently resulted in improvements to energy and particle confinement.

Flow shear in fusion plasmas is typically associated with a reduction in turbulence levels. One popular theory to explain this observation is that a shear flow stretches and distorts a turbulent eddy, shortening the eddy lifetime (eddy turnover time) by causing the eddy to reach the eddy coherence length faster than in the no-shear-flow case (Terry, 2000). This enhanced eddy decorrelation rate results in lower turbulence intensity levels. In a fusion device, a localized region of flow shear that suppress cross-field turbulent transport is referred to as a *transport barrier*. An edge-region transport barrier is believed to responsible for the attractive confinement properties of the H-mode (high-confinement mode) in tokamaks (Wagner *et al.*, 1982; Wagner, 2007), and advanced operational regimes for ITER rely on the formation and control of

transport barriers (Gormezano *et al.*, 2007). A better understanding of how externally driven and spontaneously generated sheared flows interact with turbulence in different parameter regimes is important to improving plasma confinement.

As discussed in the previous section, spontaneous azimuthal rotation of the LAPD plasma in the ion-diamagnetic-drift (IDD) direction is observed in both simulations (Shi *et al.*, 2017; Fisher *et al.*, 2015) and experiments (Schaffner *et al.*, 2012, 2013; Schaffner, 2013) when the limiter is unbiased, which is equivalent to setting the limiter model described in this section to $\phi_{\text{bias}} = 0$ V. This edge flow rotation is strongest just outside the limiter edge. By biasing the limiter positive (relative to the anode), Schaffner *et al.* (2012, 2013); Schaffner (2013) observed that the plasma rotation slows down and eventually reverses direction. Plasma rotation in the IDD direction was enhanced for negative limiter bias. A zero-shear-flow state with increased turbulent transport was also found at an intermediate positive limiter bias, and large flow shear in either direction was associated with reduced levels of turbulent transport. Schaffner *et al.* (2013); Schaffner (2013) later compared the experimental measurements to some shear-suppression models by using power-law fits and found limited agreement. Only very recently were the first Braginskii fluid simulations of limiter biasing in LAPD performed (Fisher & Rogers, 2017).

In these simulations, we model limiter biasing by modifying the parallel boundary condition on each end of the simulation domain in the same way for simplicity and symmetry, and so we deviate from the LAPD experiment in this regard. The actual LAPD experiment only has a single biasable limiter at one end of the device, which is located 2.1 m from the cathode 1.8 m from the anode. An electrically floating conducting end mesh is located at the other end of the device in the experiment (Schaffner *et al.*, 2012; Gekelman *et al.*, 2016). The ability to bias only one end plate while leaving the other end plate grounded is already supported, but we have not yet investigated this case. Fisher & Rogers (2017) explored both limiter-biasing configurations using the GBS code and observed flow reversal in the electron-diamagnetic-drift (EDD) direction for large negative bias only when both end plates were biased, which is a key feature observed in the experiments.

As discussed in Section 2.5, the sheath potential drop at a point located on the parallel boundaries is

$$\Delta\phi(x, y) = \phi_{sh}(x, y) - \phi_w(x, y), \quad (4.13)$$

where ϕ_{sh} is the potential at the sheath entrance and ϕ_w is the wall potential, which was set to 0 for the simulation reported in the previous section to model grounded end plates. We model the effect of the limiter through the use of a non-zero $\phi_w(x, y)$ field that has the form

$$\phi_w(x, y) = \begin{cases} 0 & \text{if } \sqrt{x^2 + y^2} < r_s, \\ V_{\text{bias}} & \text{else.} \end{cases} \quad (4.14)$$

Here, we investigate the use of bias voltages $V_{\text{bias}} = -10$ V and $V_{\text{bias}} = +15$ V, and we compare these results to the unbiased simulation with $V_{\text{bias}} = 0$ V. These two bias voltages were chosen because they resulted in large-amplitude sheared flows in the

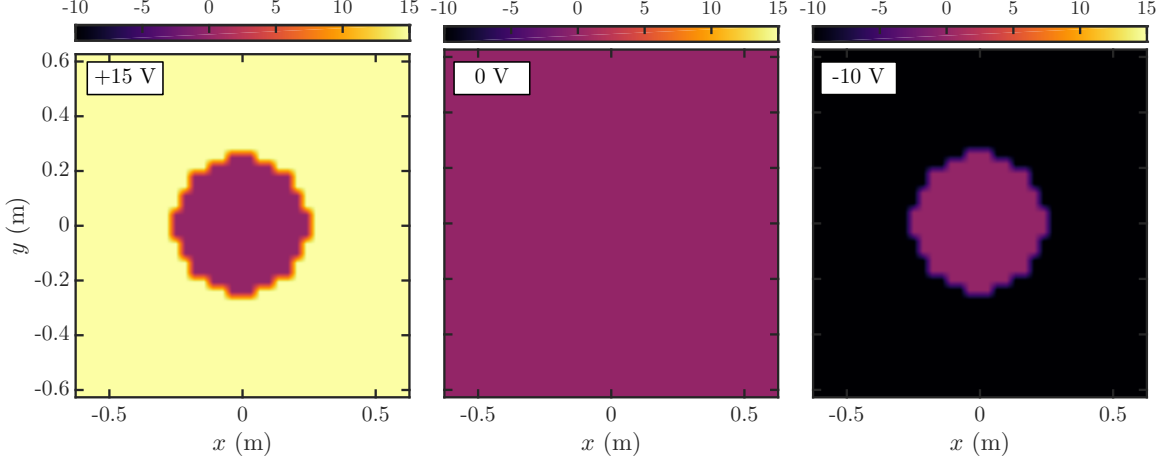


Figure 4.15: The $\phi_w(x, y)$ fields used in the sheath-model boundary conditions to model limiters biased with $V_{\text{bias}} = +15$ V, 0 V, and -10 V. These fields modify the sheath potential drop in the boundary conditions applied at each end of the simulation domain in the parallel direction. We assume that the limiter has an aperture of radius $r_s = 0.25$ m, so ϕ_w is zero for $r < r_s$ because these innermost field lines always terminate on a grounded end plate and not on the limiter. The jagged nature of the boundary between the $\phi_w = 0$ and $\phi_w = V_{\text{bias}}$ regions is due to the use of a Cartesian grid.

experiment ([Schaffner et al., 2012, 2013; Schaffner, 2013](#)). The corresponding $\phi_w(x, y)$ fields are shown in figure 4.15. By applying a bias voltage to the limiter, we cause the electrostatic potential in the edge region (where the plasma is on magnetic field lines that terminate on the limiter plates) to increase or decrease relative to the values in the unbiased case, and large $E \times B$ flows can be induced for large enough V_{bias} . Figure 4.16 shows the locations where the limiter plates modify the sheath-model boundary conditions in an $x-z$ cut of the simulation domain. As in figure 4.3, the plasma source, side-wall boundary conditions, and magnetic field direction are also indicated.

To save computational time in these simulations, we take initial conditions from the steady state of the unbiased LAPD simulation described in Section 4.3. Therefore, we must use the same parameters as in the unbiased LAPD simulations described in table 4.2.. The experiments performed by [Schaffner et al. \(2012, 2013\); Schaffner \(2013\)](#) have a higher peak electron temperature (8 eV), stronger magnetic field (0.1 T), and lower plasma density ($2 \times 10^{18} \text{ m}^{-3}$). For each of the three limiter bias voltages, we run a simulation for at least 1.5 ms and use data from the last 1 ms of the simulation in our analysis. The limiter biasing is applied instantaneously from $t = 0$ s, so we do not ramp up V_{bias} from 0 V to the desired value over some specified duration to model the circuit response in the real experiment. In the actual limiter-biasing experiments ([Schaffner et al., 2012, 2013; Schaffner, 2013](#)), the limiter was biased for ≈ 5 ms during the ≈ 15 ms discharge

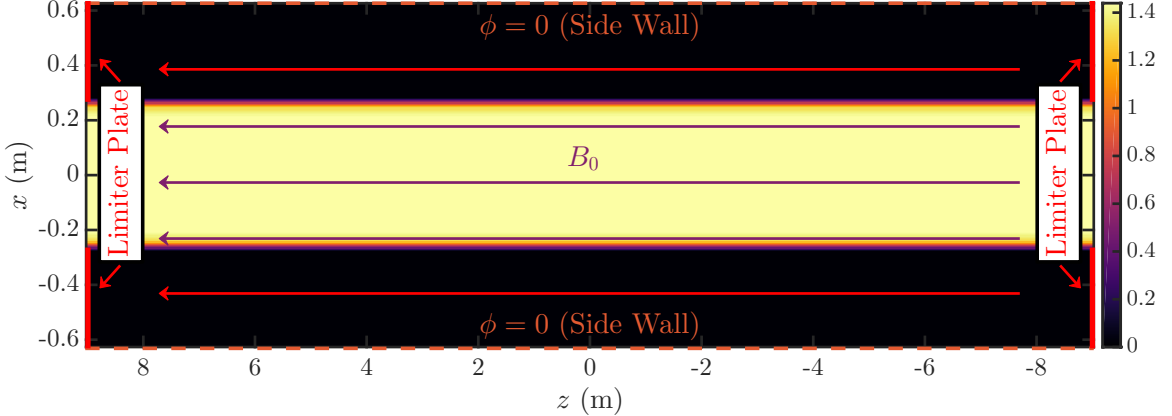


Figure 4.16: LAPD-simulation density source rate (in $10^{21} \text{ m}^{-3} \text{ s}^{-1}$) in the x - z plane at $y = 0$ m with additional annotations to indicate biasable-limiter locations. Sheath-model boundary conditions are still applied at the entire upper and lower boundaries in z . The field lines in red are in contact with the biasable limiter, while the field lines in purple terminate on grounded end plates.

Due to the rapid parallel response of the electrons, we see that the plasma potential adjusts to the limiter biasing on a time scale on the order of the electron transit time, which is $\approx 84 \mu\text{s}$ for electrons in the colder edge region ($T_e = 1.2 \text{ eV}$). Figure 4.17 shows the parallel structure of the electrostatic potential $100 \mu\text{s}$ from the start of the limiter biasing simulations. We see that the value of the potential in the core region ($r < r_s$) is nearly the same regardless of V_{bias} , but the potential in the edge region self-consistently adjusts to stay a few T_e above V_{bias} to keep the electron and ion fluxes to the end plates approximately in balance.

Figure 4.18 shows the time evolution of the electron density viewed in the x - y plane at $z = 0$ m for the simulation with $V_{\text{bias}} = +15 \text{ V}$. The plasma immediately reverses rotation and a strong sheared flow in the EDD direction is observed while the density in the core rises due to a decrease in radial particle transport. At $t = 0.6 \text{ ms}$, we see the emergence of a coherent mode of mode number localized to the limiter edge with mode number $m = 5$. At much later times, we see that this coherent mode persists, while the radial transport of density to regions not in the immediate vicinity of the limiter edge is extremely small. In the simulation with $V_{\text{bias}} = -10 \text{ V}$, the rotation in the IDD direction is enhanced and a coherent mode with $m = 6$ develops. Coherent modes were observed in cases with high shearing rates on LAPD, although the mode number values were not described in Schaffner *et al.* (2012) or in Schaffner *et al.* (2013). In drift-reduced Braginskii fluid simulations, $m = 6 \pm 1$ was reported for the $V_{\text{bias}} = +18 \text{ V}$ case investigated by Fisher & Rogers (2017). Schaffner *et al.* (2012); Schaffner (2013) proposed that this mode is caused by the Kelvin–Helmholtz instability or the rotational-interchange instability.

Figure 4.19(a) shows a reduction in the time-averaged radial $E \times B$ particle flux in the simulations with applied limiter biasing. The peak radial particle flux is reduced by approximately 50% in the biased simulations, and the radial region over which

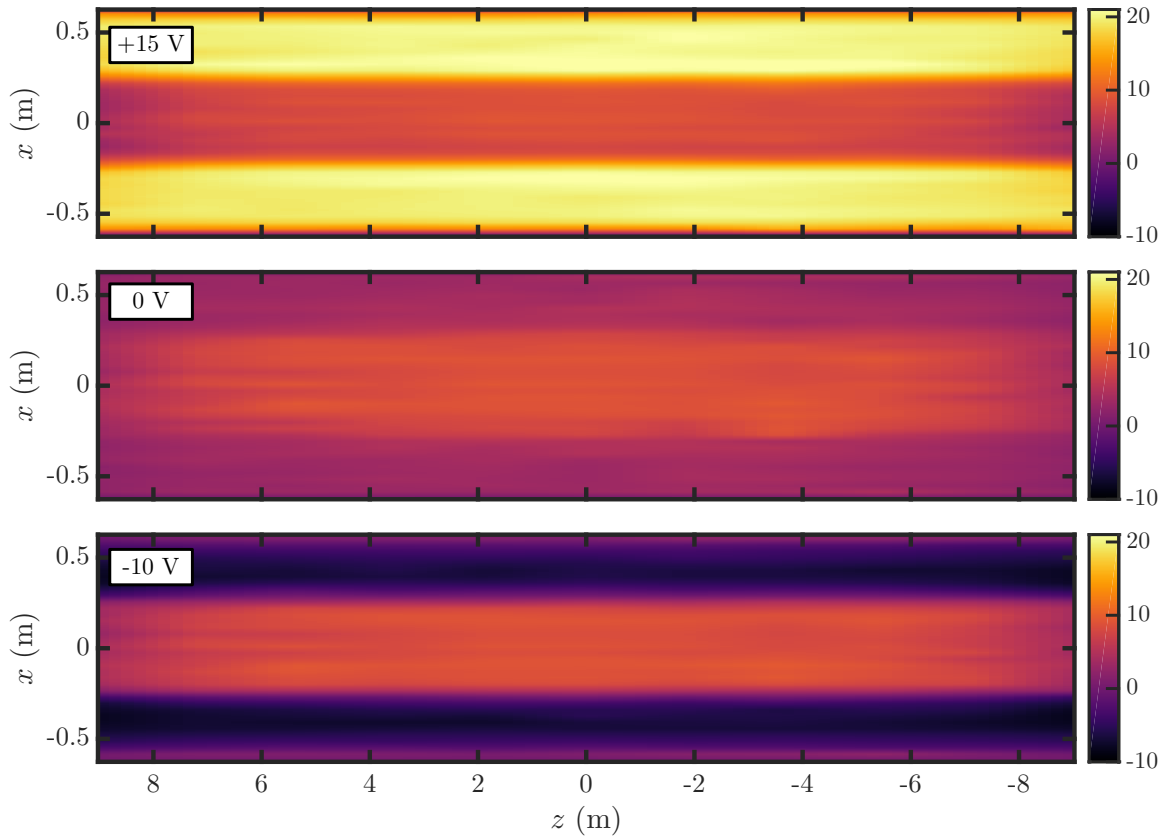


Figure 4.17: Snapshots of the electrostatic potential (in V) in three LAPD simulations, which have +15 V limiter biasing, 0 V limiter biasing (grounded limiter), and -10 V limiter biasing. Limiter biasing modifies the potential in the edge region while leaving the potential in the core region relatively unchanged, which results in a poloidal $E \times B$ rotation near the limiter edge at $r_s = 20\rho_{s0} = 0.25$ m. All three simulations start from the same initial condition taken from an unbiased LAPD simulation that has reached a quasi-steady state, and the snapshots are taken at $t = 100$ μ s. The plots are made in the x - z plane at $y = 0$ m.

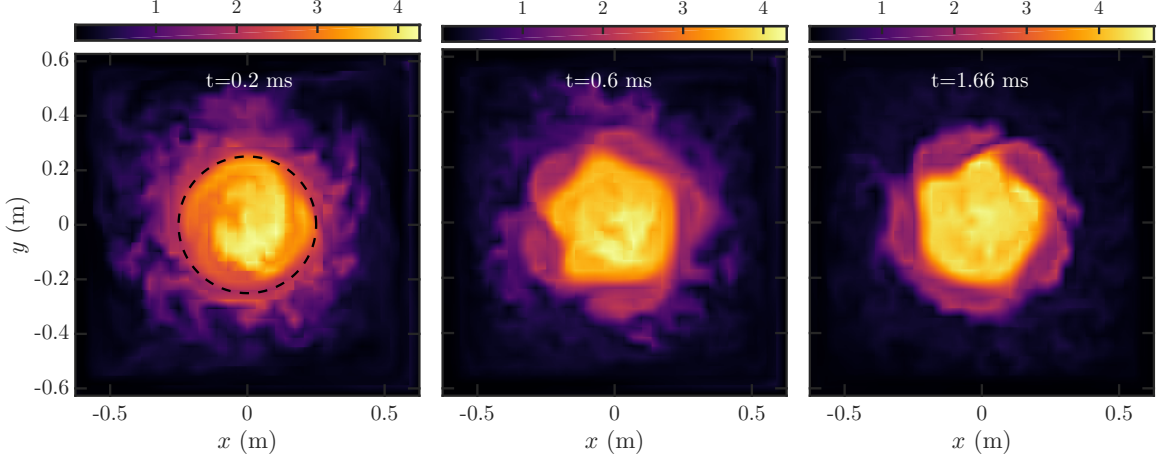


Figure 4.18: Snapshots of the electron density in the x - y plane at $z = 0$ m for a simulation with +15 V limiter biasing at $t = 0.2$ ms, $t = 0.6$ ms, and $t = 1.66$ ms. The plasma immediately reverses its rotation direction and radial particle transport is suppressed. Eventually, a coherent mode localized to the limiter edge develops and persists for the rest of the simulation. The limiter edge, which is the boundary between the core and edge regions, is indicated by the dashed line in the $t = 0.2$ ms plot. Note that each plot uses a different color scale to better show the features.

there is significant radial particle flux is also much narrower in the biased simulations. Figure 4.19(b) shows that the time-averaged total outward parallel particle fluxes in the simulations with +15 V and -10 V limiter biasing are enhanced in the core, which is consistent with the decreased radial particle transport in the biased simulations. These trends are also observed in LAPD experiments (see Schaffner *et al.*, 2013, figure 3(c)). The reduction in the cross-field turbulent fluxes result in somewhat steeper density profiles.

Figure 4.20 shows radial profiles of the mean potential, mean density, and r.m.s. electron-density fluctuation level (normalized to the peak on-axis density for the 0 V case) for the three simulations with different values of the limiter bias voltage. These plots are made using data in the same $-4 \text{ m} < z < 4 \text{ m}$ region that was used for the radial profile plots in Section 4.3. In the plot of the mean potential (figure 4.20(a)), we see that the potential in the core region is nearly identical for the three cases except near the limiter edge, where steep radial gradients in the potential develop in the +15 V and -10 V cases. In the edge region, the gradients in the potential are small away from the limiter edge. From this plot, we see that the large, sheared azimuthal flows that are observed in the +15 V and -10 V cases is due to $E \times B$ motion of the plasma. Consistent with a reduction in radial particle transport, we see that mean electron density in the core region slightly increases, while the density at large r decreases when comparing the two biased cases with the unbiased case. The electron-density fluctuation level is also lower for the +15 V and -10 V cases, although the fluctuation level for all three cases peaks at the limiter edge location, which is likely due to the coherent mode for the biased cases. The reduction of

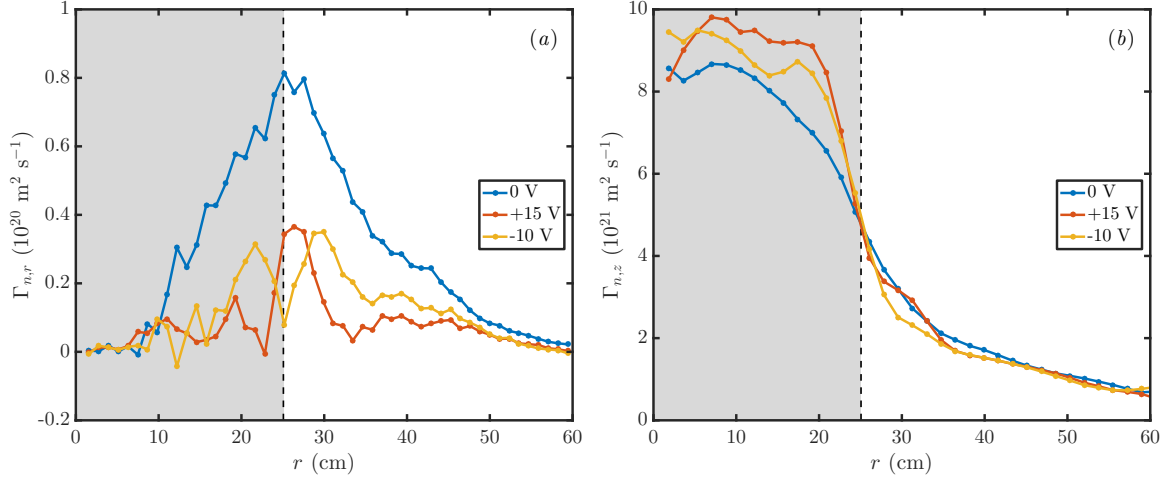


Figure 4.19: Comparison of the (a) time-averaged radial particle fluxes $\Gamma_{n,r}$ due to $E \times B$ fluctuations and (b) the time-averaged total outward parallel particle fluxes $\Gamma_{n,z}$ for simulations with different values of limiter biasing. The shaded region illustrates the core region inside the limiter edge at $r = r_s$.

low-frequency density fluctuation amplitudes in the biased cases are believed to be the primary factor in the reduction of turbulent radial particle flux in the limiter biasing experiments on LAPD (Schaffner *et al.*, 2012).

We now consider the radial-particle-flux reduction observed in the biased simulations in more detail. The time-averaged radial $E \times B$ particle flux $\langle \Gamma_{n,r} \rangle$ can be spectrally decomposed into the amplitudes, cross phase, and cross coherency of density and potential fluctuations (Powers, 1974; Carter & Maggs, 2009). We define the Fourier-transform pair

$$f(t) = \frac{1}{\sqrt{2\pi}} \int_{-\infty}^{\infty} d\omega \hat{f}(\omega) e^{-i\omega t}, \quad (4.15)$$

$$\hat{f}(\omega) = \frac{1}{\sqrt{2\pi}} \int_{-\infty}^{\infty} dt f(t) e^{i\omega t}, \quad (4.16)$$

and the complex-valued cross-power spectrum

$$P_{1,2}(\omega) = \hat{f}_1^*(\omega) \hat{f}_2(\omega) = |P_{1,2}(\omega)| e^{i\alpha_{1,2}(\omega)}. \quad (4.17)$$

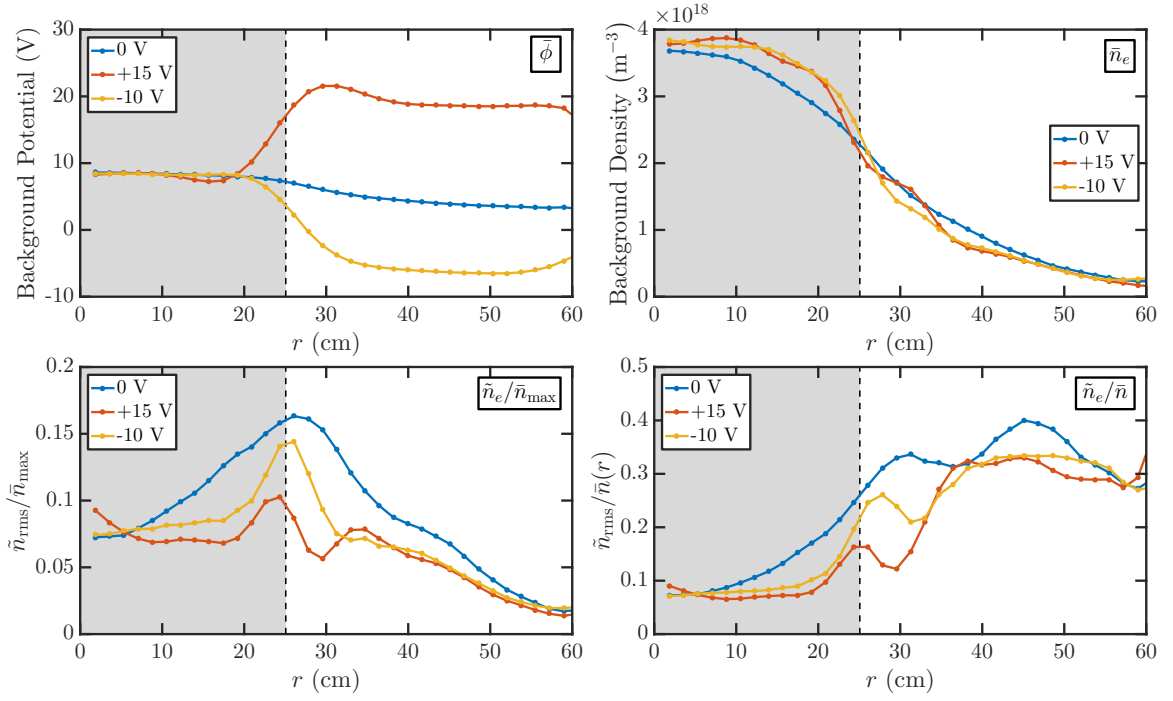


Figure 4.20: Comparison of the radial profiles of the background electrostatic potential, background electron density, and r.m.s. electron-density fluctuation levels (normalized to both the peak background electron density and to the local background electron density) for three LAPD simulations, which have 0 V, +15 V and -10 V limiter biasing. The core region whose field lines always terminate on a grounded end plate is shaded in gray, while the field lines in the unshaded edge region terminate on a biasable limiter. The background potential is significantly modified in the biased cases, which results in strong $E \times B$ azimuthal flows near the limiter edge. This sheared flow suppress radial particle transport, which results in an elevated density in the core region and a reduced density in the edge region. The density fluctuation levels are also lower in the vicinity of the limiter edge in the biased cases.

Noting that $\mathbf{v}_E \cdot \hat{\mathbf{r}} = E_\theta/B$, we have

$$\int_{-\infty}^{\infty} dt \tilde{n} \tilde{v}_E = \frac{1}{B} \int_{-\infty}^{\infty} dt \tilde{n} \tilde{E}_\theta \quad (4.18)$$

$$= \frac{1}{B} \int_{-\infty}^{\infty} dt \left[\frac{1}{\sqrt{2\pi}} \int_{-\infty}^{\infty} d\omega \hat{n}(\omega) e^{-i\omega t} \right] \left[\frac{1}{\sqrt{2\pi}} \int_{-\infty}^{\infty} d\omega' \hat{E}_\theta(\omega') e^{-i\omega' t} \right] \quad (4.19)$$

$$= \frac{1}{2\pi B} \int_{-\infty}^{\infty} d\omega \hat{n}(\omega) \int_{-\infty}^{\infty} d\omega' \hat{E}_\theta(\omega') \int_{-\infty}^{\infty} dt e^{-i(\omega+\omega')t} \quad (4.20)$$

$$= \frac{1}{B} \int_{-\infty}^{\infty} d\omega \hat{n}(\omega) \int_{-\infty}^{\infty} d\omega' \hat{E}_\theta(\omega') \delta(\omega + \omega') \quad (4.21)$$

$$= \frac{1}{B} \int_{-\infty}^{\infty} d\omega' \hat{n}(-\omega') \hat{E}_\theta(\omega') \quad (4.22)$$

$$= \frac{1}{B} \int_{-\infty}^{\infty} d\omega' \hat{n}^*(\omega') \hat{E}_\theta(\omega'), \quad (4.23)$$

where the last equality holds because \tilde{n} is real. Furthermore, we can write

$$\int_{-\infty}^{\infty} dt \tilde{n} \tilde{v}_E = \frac{1}{B} \int_0^{\infty} d\omega' \left(\hat{n}^*(\omega') \hat{E}_\theta(\omega') + \hat{n}^*(-\omega') \hat{E}_\theta(-\omega') \right) \quad (4.24)$$

$$= \frac{1}{B} \int_0^{\infty} d\omega' \left(\hat{n}^*(\omega') \hat{E}_\theta(\omega') + \hat{n}(\omega') \hat{E}_\theta^*(\omega') \right) \quad (4.25)$$

$$= \frac{2}{B} \int_0^{\infty} d\omega' \operatorname{Re} \left(\hat{n}^*(\omega') \hat{E}_\theta(\omega') \right) \quad (4.26)$$

$$= \frac{2}{B} \int_0^{\infty} d\omega \operatorname{Re} (P_{n,E}) \quad (4.27)$$

$$= \frac{2}{B} \int_0^{\infty} d\omega |P_{n,E}(\omega)| \cos(\alpha_{nE}(\omega)) \quad (4.28)$$

$$= \frac{2}{B} \int_0^{\infty} d\omega \left| \hat{E}_\theta(\omega) \right| |\hat{n}(\omega)| |\gamma_{n,E}(\omega)| \cos(\alpha_{nE}(\omega)) \quad (4.29)$$

We expanded the integrand in (4.28) into four terms in (4.29): the amplitude spectral densities of the electric-field and density fluctuations $|\hat{E}_\theta(\omega)|$ and $|\hat{n}(\omega)|$, the *coherence spectrum* $|\gamma_{n,E}(\omega)|$, and the cosine of the *cross phase* $\cos(\alpha_{n,E}(\omega))$.

The cross-power spectrum $P_{n,E}(\omega)$ is first computed at each node as:

$$P_{n,E}(\omega) = \hat{n}_e^* \hat{E}_\theta, \quad (4.30)$$

where $\hat{n}_e(\mathbf{R}, \omega)$ and $\hat{E}_\theta(\mathbf{R}, \omega)$ are the Fourier transforms of the time series of $\tilde{n}_e(\mathbf{R}, t)$ and $\tilde{E}_\theta(\mathbf{R}, t)$. The cross-power spectrum is then spatially averaged, and the cross phase is computed as

$$\alpha_{n,E}(\omega) = \operatorname{Im} \log (\langle P_{n,E}(\omega) \rangle), \quad (4.31)$$

where $\langle \dots \rangle$ denotes a spatial average in the region $20 \text{ cm} < r < 30 \text{ cm}$ and $-4 \text{ m} < z < 4 \text{ m}$. The coherence spectrum is defined as (Powers, 1974)

$$|\gamma_{n,E}(\omega)| = \frac{|\langle P_{n,E}(\omega) \rangle|}{\langle P_{n,n}(\omega) \rangle^{1/2} \langle P_{E,E}(\omega) \rangle^{1/2}}, \quad (4.32)$$

where $P_{n,n} = |\hat{n}(\omega)|^2$ and $P_{E,E} = |\hat{E}_\theta(\omega)|^2$ are the real-valued power spectra of \tilde{n}_e and \tilde{E}_θ , respectively.

Figure 4.21 shows plots of the total radial-particle-flux integrand (4.28), cosine of the cross phase, and the coherence spectrum for the unbiased and biased simulations. In figure 4.21(a), we see that frequencies higher than $\sim 10 \text{ kHz}$ do not contribute to the integral for both unbiased and biased cases, which is due to the exponential decay at high frequencies in the cross-power amplitude spectrum. We see in figure 4.21(b) that the cross phase in the biased cases is less favorable for outward radial transport when compared to the cross phase in the unbiased case, while figure 4.21(c) shows that the coherence in the biased cases is more favorable for outward radial transport. The net effect, however, appears to be a reduction in the outward radial particle flux in the biased cases.

The results for the unbiased simulation is similar to the spectra measured in LAPD (see Carter & Maggs, 2009, figure 10) at frequencies below 10 kHz, where the fluctuation levels are the strongest as shown in the power spectrum (see figure 4.11(c)). At these low frequencies, Carter & Maggs (2009) report a cross phase that is ≈ 0 and a cross coherency that is $\approx 0.2\text{--}0.6$ for the unbiased case. We note that there is a questionable feature in the low-frequency ($< 10 \text{ kHz}$) components of the cross phase and coherence of the unbiased simulation in figures 4.21(b) and (c). In a frequency window where the coherence is relatively low (< 0.5), the cross phase is not well defined, so we expect the corresponding cross phase in the same frequency window to be unstable. Instead, we see in figure 4.21(b) that the low-frequency cross phase is relatively flat for the unbiased case. Similar results are obtained by using a 3 times larger time-sampling window for the spectral decomposition. We note that figure 10 in Carter & Maggs (2009) also shows a similar trend. This feature could be due to errors in calculating E_θ , both in the simulation and in the experiment.

The power spectral densities of E_θ and n_e fluctuations are shown in figure 4.22. In the biased simulations, we see a peaking in the fluctuation power spectra at $\approx 5.8 \text{ kHz}$ for $+15 \text{ V}$ and $\approx 7.8 \text{ kHz}$ for -10 V , which are believed to be Kelvin–Helmholtz modes in the experiments (Schaffner *et al.*, 2012; Schaffner, 2013). Biasing experiments on LAPD show a peak at $\approx 12 \text{ kHz}$ in the power spectral density of density fluctuations for a case in which the limiter was biased at 13.1 V (see Schaffner, 2013, figure 6.9(b)).

4.5 Conclusions

We have presented results from the first 3D2V gyrokinetic continuum simulations of turbulence in an open-field-line plasma. The simulations were performed using a version of the Gkeyll code that employs an energy-conserving discontinuous Galerkin

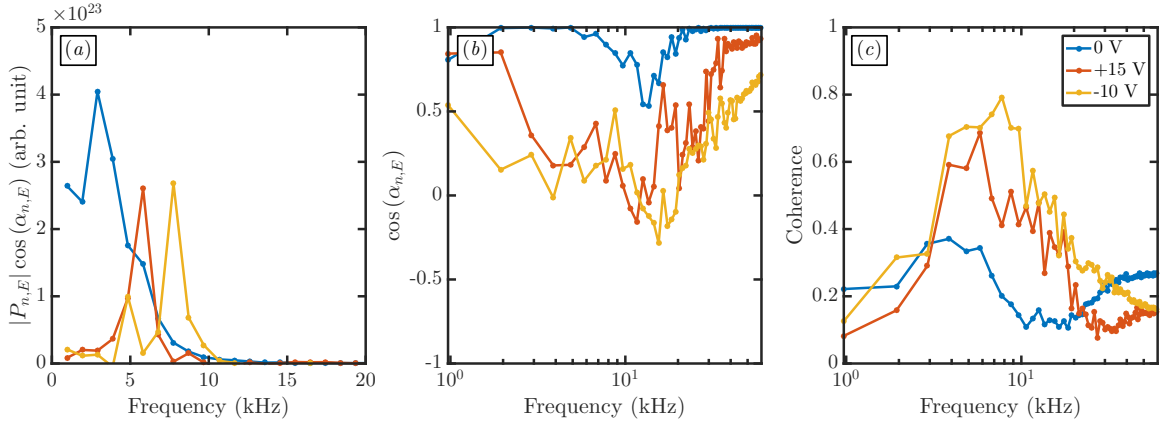


Figure 4.21: Comparison of the (a) total radial-particle-flux integrands (4.28), (b) cosine of cross phases, and (c) coherence spectra (4.32) for three LAPD simulations, with different values of limiter biasing. The primary cause of the reduction of radial particle flux in this region ($20 \text{ cm} < r < 30 \text{ cm}$) in the biased simulations (see figure 4.19) appears to be a reduction in n_e and E_θ fluctuation amplitudes at low frequencies (see figure 4.22), as opposed to large changes in the cross phase or coherence.

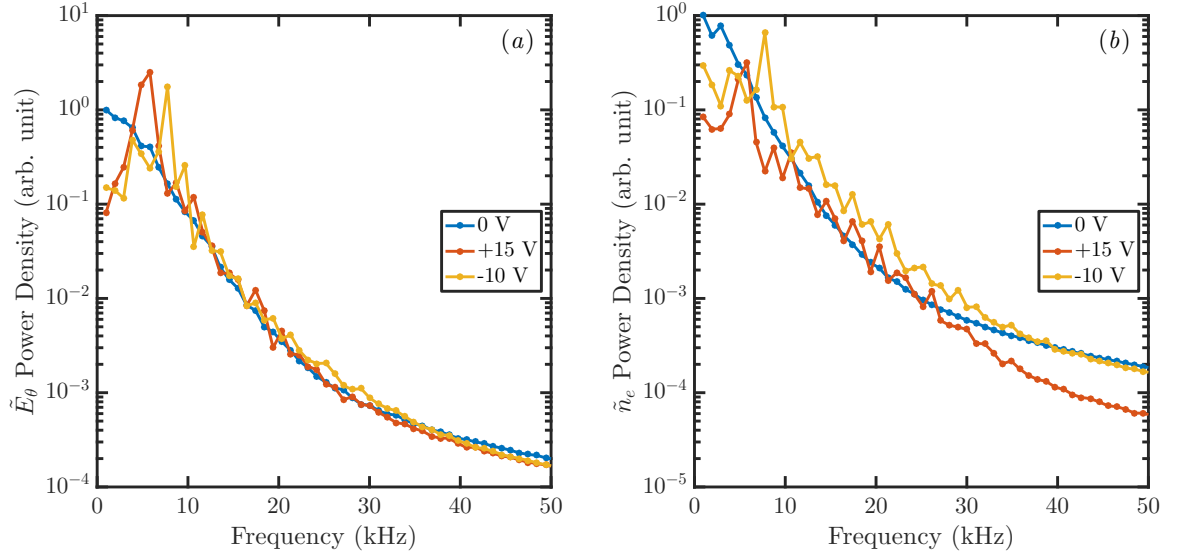


Figure 4.22: Comparison of the (a) electric-field-fluctuation power spectral densities and (b) the density-fluctuation power spectral densities for three LAPD simulations with different values of limiter biasing. In both plots, a peak from the coherent mode is observed in the spectra of the biased simulations (at $\approx 5.8 \text{ kHz}$ for $+15 \text{ V}$ and $\approx 7.8 \text{ kHz}$ for -10 V).

algorithm. We found it important to include self-species collisions in the electrons to avoid driving high-frequency instabilities in our simulations. Our gyrokinetic simulations are generally in good qualitative agreement with previous Braginskii fluid simulations of LAPD and with previously published experimental data.

We use sheath-model boundary conditions for electrons that are a kinetic extension of the sheath model used in past fluid simulations, which allows self-consistent currents to flow into and out of the end plates. In this approach, the sheath potential is determined from the gyrokinetic Poisson equation (analogous to how the vorticity equation is used in the fluid approach of [Rogers & Ricci \(2010\)](#)). The ion boundary conditions used at present are the same as for the logical-sheath model, in which ions flow out at whatever velocity they have been accelerated to at the sheath edge. This boundary condition appears to work well for the time period of this LAPD simulation. As discussed in Section 2.5, future work is planned to consider improved models of a kinetic sheath, including the role of rarefaction dynamics near the sheath that may modify the outflowing distribution function and the effective outflow Mach number.

We demonstrated in Section 4.4 that a biasable limiters could be modeled through a simple modification to the sheath-model boundary conditions. By biasing the limiter positive or negative relative to the grounded end plates, a sheared flow in the azimuthal direction could be driven at the limiter edge. Consistent with the experiments ([Schaffner et al., 2012, 2013; Schaffner, 2013](#)), we see that radial turbulent particle transport is suppressed in the strongly biased simulations relative to the unbiased simulation. Future work can explore more values for the limiter biasing and identify the bias voltage that results in a zero-flow-shear state, in which the outward radial particle transport is maximized.

A number of possible modifications to the simulations could allow closer quantitative modeling of the LAPD experiment to enable gyrokinetic simulation as a tool for planning LAPD experiments, especially in the lower-collisionality regime $T_i \sim T_e \sim 10$ eV accessible in the upgraded device ([Gekelman et al., 2016](#)). In the real LAPD experiment, a cathode–anode discharge emits an energetic 40–60 eV electron beam that ionizes the background gas along the length of the device ([Leneman et al., 2006; Gekelman et al., 2016; Carter & Maggs, 2009](#)), creating the plasma source that we have directly modeled in our simulations. At present, we are ignoring the current from these energetic electrons and modeling the anode as a regular conducting end plate. Because the anode in the actual device is a semi-transparent mesh, there is finite pressure on the other side of the anode from the main plasma that can act to slow down ion outflows and thus relax the Bohm sheath criterion.

Since our simulations are kinetic, future work could include the non-Maxwellian high-energy electrons and a model of the ionization process instead of using explicit source terms. Future work could also investigate the primary mechanism driving the cross-field transport observed in our simulations (such as linear drift-wave, nonlinear, or Kelvin–Helmholtz instabilities) by analyzing the energy dynamics of the system ([Friedman et al., 2012, 2013](#)) and through the use of presence/absence tests ([Rogers & Ricci, 2010; Fisher et al., 2015](#)). Additionally, the applicability of the current set of parallel boundary conditions should be investigated more carefully. It is possible that the assumption that all magnetic field lines terminate on grounded end plates or

a biasable limiter is not sufficiently accurate for modeling the LAPD experiment, and a more realistic set of parallel boundary conditions that also allows some field lines to terminate on the cathode or anode structures could lead to qualitatively different results. We also note in passing that the capability we have developed could also eventually find use in simulating certain plasma-mass-filter concepts (Ochs *et al.*, 2017; Gueroult *et al.*, 2016; Gueroult & Fisch, 2014; Fetterman & Fisch, 2011), which direct ~ 10 eV ions to be preferentially lost along open magnetic field lines (some of which terminate on a concentric set of biasable electrodes to drive plasma rotation) at different ion-mass-dependent locations.

We plan several improvements to our numerical algorithms. The time step restriction in our LAPD simulations is currently set by the electron-electron collision frequency. A super-time-stepping method, such as the Runge-Kutta-Legendre method (Meyer *et al.*, 2014), or an implicit method could significantly alleviate this restriction. The use of non-polynomial basis functions (Yuan & Shu, 2006) for efficient velocity-space discretization is expected to reduce the computational cost of these simulations (by allowing for a coarser velocity-space grid) and to preserve the positivity of the distribution function. Future studies will also implement the full nonlinear ion polarization density in gyrokinetic Poisson equation (2.4), which is related to removing the Boussinesq approximation in fluid models (Dudson *et al.*, 2015; Halpern *et al.*, 2016). This modification requires replacing n_{i0}^g in (2.4) with the full $n_i^g(\mathbf{R}, t)$ and retaining a corresponding second-order contribution to the Hamiltonian (2.3) necessary for energy conservation (Krommes, 2012, 2013; Scott & Smirnov, 2010)

Chapter 5

Simulations of a Helical Scrape-Off-Layer Model

The work presented in this chapter builds on our previous work with flux-driven simulations of open-magnetic-field-line turbulence in the Large Plasma Device (Gekelman *et al.*, 2016) using the gyrokinetic continuum capabilities of the Gkeyll code (Chapter 4). In those LAPD simulations, the magnetic field was straight and uniform, and the plasma was highly collisional, which necessitated the use of an artificial electron-to-ion mass ratio ($m_i/m_e = 400$) and reduced electron collision frequencies to make the simulations tractable. Nevertheless, we found that our numerical approach based on discontinuous Galerkin methods and sheath-model boundary conditions was stable and produced qualitatively reasonable results, which led to the first demonstration of open-field-line turbulence with a gyrokinetic continuum code. These restrictions are relaxed for the simulations presented in this chapter, which now include a slightly more complex magnetic geometry.

We have added magnetic curvature and $\nabla\mathbf{B}$ drifts to the code and can simulate a helical magnetic geometry approximating that in simple magnetized tori (SMTs), such as TORPEX (Fasoli *et al.*, 2006) and Helimak (Gentle & He, 2008). In tokamaks, probe and imaging diagnostics have revealed the existence of intermittent coherent structures in the SOL referred to as *plasma filaments* or *blobs*, which convectively transport particles, heat, momentum, and current across magnetic field lines (D’Ippolito *et al.*, 2011). Blob are characterized by densities that are much higher than local background levels, a structure that is highly elongated along the magnetic field (much larger than the plasma radius), and much smaller scales perpendicular to the magnetic field $\sim 10\rho_i$, where ρ_i is the ion gyroradius (D’Ippolito *et al.*, 2011; Zweben *et al.*, 2007).

The curvature and $\nabla\mathbf{B}$ forces are believed to set up a charge-separated dipole potential structure across the blob cross-section that results in its outward radial propagation via convective $E \times B$ transport (Krasheninnikov, 2001; D’Ippolito *et al.*, 2011). Finite-temperature effects of the blob can also cause spin motion if the blob is sheath-connected, which can reduce this radial motion (Myra *et al.*, 2004). Numerically, blob dynamics have been studied using seeded-blob fluid simulations (Angus *et al.*, 2012; Riva *et al.*, 2016; Walkden *et al.*, 2015; Shanahan & Dudson, 2016), al-

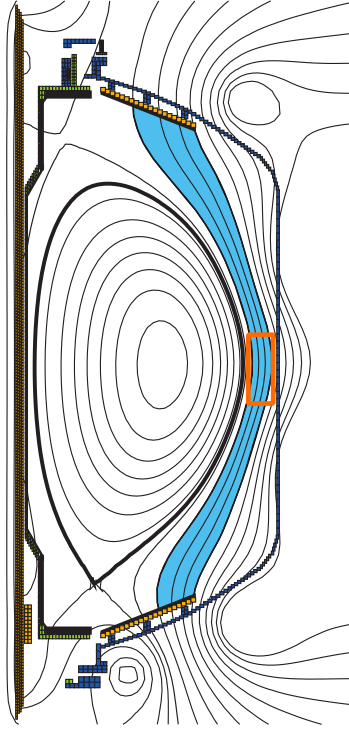


Figure 5.1: Illustration of the basic tokamak region approximated by the helical-SOL simulation domain (highlighted in blue). The SOL is modeled as a region of helical magnetic field lines that terminate on grounded end plates at each end, with their parallel length determined by the magnetic-field-line incidence angle. The orange box roughly indicates the projection of a flux-tube cross section onto this poloidal plane. This figure was adapted from figure 1.1 of [Stoltzfus-Dueck \(2009\)](#).

though recent turbulence simulations observe self-consistent blob formation ([Churchill et al., 2017; Ricci & Rogers, 2013](#)). In contrast to previous work on the simulation of turbulence in SMTs based on the cold-ion drift-reduced Braginskii equations ([Ricci et al., 2008; Ricci & Rogers, 2009; Li et al., 2011](#)), we employ a gyrokinetic approach that allows us to investigate plasmas with $T_i \gtrsim T_e$, which is commonly observed in the scrape-off layer (SOL) ([Boedo et al., 2009; Kočan et al., 2011, 2012](#)).

Although our simulations do yet not simultaneously contain open and closed-field-line regions ([Ribeiro & Scott, 2008; Zweber et al., 2009; Halpern et al., 2016; Dudson & Leddy, 2017; Zhu et al., 2017; Li et al., 2017](#)), we believe that many basic properties of SOL turbulence and transport are reproduced in this open-field-line model. Additionally, the turbulence in this helical open-field-line geometry with parameters appropriate for a tokamak SOL has not been previously studied using a gyrokinetic PIC approach, either. We do acknowledge, however, that gyrokinetic PIC codes that have the necessary capabilities for the problem described in this chapter have already been developed ([Churchill et al., 2017; Korpilo et al., 2016](#)).

5.1 Simulation Parameters

In the non-orthogonal field-aligned geometry used in the simulation (Beer *et al.*, 1995; Hammett *et al.*, 1993), z measures distances along field lines, x is the radial coordinate, and y is constant along a field line and measures distances perpendicular to field lines. The simulation geometry is a flux tube on the outboard side that wraps around the torus a number of times, terminating on material surfaces at each end in z . We use parameters roughly approximating a singly ionized H-mode deuterium plasma in the NSTX SOL (Zweben *et al.*, 2015, 2016): $n_0 = 7 \times 10^{18} \text{ cm}^{-3}$, $T_e \sim 30 \text{ eV}$, $T_i \sim 60 \text{ eV}$, $B_{\text{axis}} = 0.5 \text{ T}$, $R_0 = 0.85 \text{ m}$, and $a_0 = 0.5 \text{ m}$. Although we use parameters for an H-mode plasma, we do not attempt or claim to capture H-mode physics (e.g. an edge transport barrier) in our simulations.

The simulation box has dimensions $L_x = 50\rho_{s0} \approx 14.6 \text{ cm}$, $L_y = 100\rho_{s0} \approx 29.1 \text{ cm}$, $L_z = L_p / \sin \theta$, where $L_p = 2.4 \text{ m}$, $\rho_{s0} = c_{s0}/\Omega_i \approx 2.9 \text{ mm}$, and θ is the magnetic-field-line incidence angle. For the results presented in this chapter, we used $\sin \theta = B_v/B_z = (0.2, 0.3, 0.6)$, which corresponds to $L_z = (12, 8, 4) \text{ m}$. The magnetic field is taken to be comprised primarily of a toroidal component with a smaller vertical component (referred to as B_v), resulting in a helical-field-line geometry that roughly approximates the tokamak SOL, as shown in figure 5.1. In this study, the magnetic-field-line incidence angle is not accounted for in the sheath boundary conditions (no Chodura sheath (Chodura, 1982)). The phase-space-grid parameters are summarized in table 5.2. With these parameters, $T_{e,\min} \approx 12.1 \text{ eV}$, $T_{\parallel e,\min} = 4.3 \text{ eV}$, and $T_{\perp e,\min} = 16 \text{ eV}$. The simulation parameters and some time and length scales of interest are listed in table 5.1.

In these equations, we neglect geometrical factors arising from a cylindrical coordinate system everywhere except in $\mathbf{B}^* = \mathbf{B} + (Bv_{\parallel}/\Omega_s)\nabla \times \mathbf{b}$, where we make the approximation that perpendicular gradients are much stronger than parallel gradients:

$$\begin{aligned} (\nabla \times \mathbf{b}) \cdot \nabla f(x, y, z) &= [(\nabla \times \mathbf{b}) \cdot \nabla y] \frac{\partial f(x, y, z)}{\partial y} + [(\nabla \times \mathbf{b}) \cdot \nabla z] \frac{\partial f(x, y, z)}{\partial z} \\ &\approx [(\nabla \times \mathbf{b}) \cdot \mathbf{e}^y] \frac{\partial f(x, y, z)}{\partial y}. \end{aligned} \quad (5.1)$$

Here, we assume that $(\nabla \times \mathbf{b}) \cdot \mathbf{e}^y = -1/x$, where $\mathbf{e}^y = \nabla y$ is a ‘co-basis’ direction. This type of approximation has also been employed in some fluid simulations of SMTs (Ricci & Rogers, 2009, 2010). We assume that $\mathbf{B} = B_{\text{axis}}(R_0/x)\mathbf{e}_z$. For the helical-SOL simulations, the 5D gyrokinetic system we solve (see (2.1) and (2.43)) has the following form for $\mathcal{J}\Pi$:

$$\mathcal{J}\Pi = \begin{pmatrix} 0 & -1/q_s & 0 & 0 & 0 \\ 1/q_s & 0 & 0 & B_y^*/m_s & 0 \\ 0 & 0 & 0 & B/m_s & 0 \\ 0 & -B_y^*/m_s & -B/m_s & 0 & 0 \\ 0 & 0 & 0 & 0 & 0 \end{pmatrix}, \quad (5.2)$$

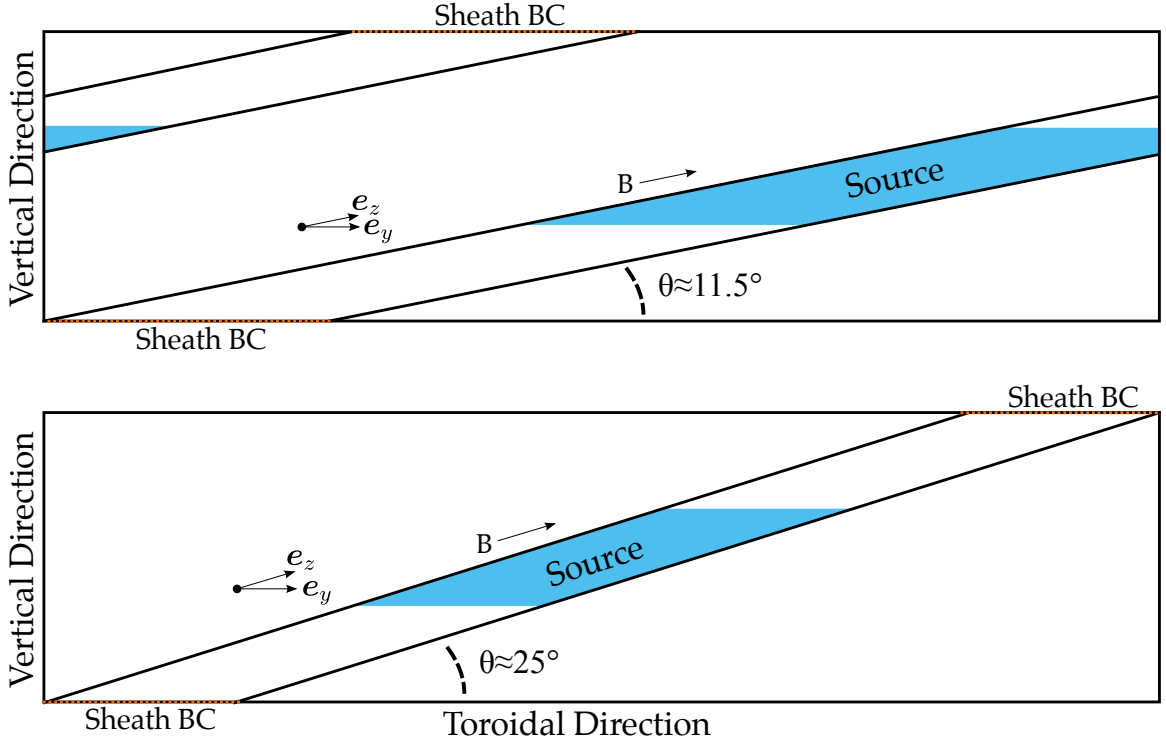


Figure 5.2: Illustrations of 2D simulation flux surfaces for a case with a magnetic-field-line incidence angle $\theta \approx 11.5^\circ$ and a case with a slightly steeper $\theta \approx 25^\circ$. The coordinate y is constant along a field line and measures distances perpendicular to field lines, while the coordinate z measures distances along field lines. Note that this coordinate system is non-orthogonal. The basis vectors are $e_y = \partial_y \mathbf{R}$ and $e_z = \partial_z \mathbf{R}$, where \mathbf{R} is the Cartesian coordinate in space. Sheath-model boundary conditions are applied at each end of the flux tube in e_z , and e_y is a periodic direction. In the steeper θ case, the flux tube covers a smaller fraction of the entire tokamak volume, and so the total source is scaled appropriately to maintain a fixed volumetric source rate. For additional details about the non-orthogonal coordinate system, the reader is referred to [Beer et al. \(1995\)](#); [Scott \(1998\)](#); [Hammett et al. \(1993\)](#).

Table 5.1: Summary of simulation parameters for helical-SOL simulations. These parameters are based on data for H-mode NSTX plasmas ([Zweben et al., 2015, 2016](#)). The ion mass is expressed in terms of the proton mass m_p . Also included are some time and length scales of interest, assuming $T_e = 25$ eV and $T_i = 40$ eV (typical values at the LCFS in the simulation).

Symbol	Value	Description
R_0	0.85 m	Device major radius
a_0	0.5 m	Device minor radius
$T_{e,\text{src}}$	74 eV	Electron source temperature
$T_{i,\text{src}}$	74 eV	Ion source temperature
n_0	$7 \times 10^{18} \text{ cm}^{-3}$	Density normalization
m_i	$2.014m_p$	Mass of ion species
B_{axis}	0.5 T	On-axis magnetic field strength
B_0	0.315 T	Magnetic field in middle of simulation domain
ρ_{s0}	2.9 mm	Ion sound radius normalization
L_p	2.4 m	Poloidal distance from midplane to end plates
L_y	29.1 cm	Width of simulation domain in y
L_x	14.6 cm	Width of simulation domain in x
L_z	4, 8, 12 m	Parallel length of simulation domain
B_v/B_z	0.6, 0.3, 0.2	Magnetic-field-line pitch
P_{source}	270, 540, 810 kW	Total source power
$S_{n,\text{vol}}$	$1.14 \times 10^{23} \text{ m}^{-3} \text{ s}^{-1}$	Volumetric source particle rate
θ	$64.4^\circ, 30.47^\circ, 20.14^\circ$	Magnetic-field-line incidence angle
Ω_i	$1.50 \times 10^7 \text{ rad/sec}$	Ion gyrofrequency
τ_{ii}	$79 \mu\text{s}$	Typical ion–ion collision time
τ_{ee}	$0.46 \mu\text{s}$	Typical electron–electron collision time
λ_{ii}	3.5 m	Typical ion–ion mean free path
λ_{ee}	0.96 m	Typical electron–electron mean free path
ρ_i	2.9 mm	Typical ion gyroradius
ρ_e	0.048 mm	Typical electron gyroradius

Table 5.2: Parameters for the phase-space grid used in the helical-SOL simulations. The parameters appearing in the velocity-space extents are $T_{i,\text{grid}} = T_{e,\text{grid}} = 40$ eV and $B_0 = B_{\text{axis}}R_0/(R_0 + a_0)$. Piecewise-linear basis functions are used, resulting in 32 degrees of freedom per cell

Coordinate	Number of Cells	Minimum	Maximum
x	18	$R_0 + a_0 - L_x/2$	$R_0 + a_0 + L_x/2$
y	36	$-50\rho_{s0}$	$50\rho_{s0}$
z	10	$-L_p/(2 \sin \theta)$	$L_p/(2 \sin \theta)$
v_{\parallel}	10	$-4\sqrt{T_{s,\text{grid}}/m_s}$	$4\sqrt{T_{s,\text{grid}}/m_s}$
μ	5	0	$0.75m_s v_{\parallel,\text{max}}^2/(2B_0)$

where $B_y^* = -m_s v_{\parallel} / (q_s x)$.

Periodic boundary conditions are applied to both f (the distribution function) and ϕ (the electrostatic potential) in y , the Dirichlet boundary condition $\phi = 0$ is applied in x , which prevents gyrocenters from crossing the surfaces in x . Sheath-model boundary conditions are applied to f in z , which partially reflect gyrocenters of one species and fully absorb gyrocenters of the other species into the wall depending on the sign of the sheath potential. Typically, the sheath will accelerate all incident ions into the wall and reflect the low-energy electrons back into the plasma. As described in Section 2.5.2, we obtain the sheath potential by solving the gyrokinetic Poisson equation (2.4) and evaluating ϕ at the sheath entrances (the surfaces of the simulation box in z).

The plasma density source has the following form:

$$S(x, z) = \begin{cases} S_0 \max \left(\exp \left(\frac{-(x-x_s)^2}{2\lambda_s^2} \right), 0.1 \right) & |z| < L_z/4, \\ 0 & \text{else,} \end{cases} \quad (5.3)$$

where $x_s = -0.05$ m + $R_0 + a_0$, $\lambda_s = 5 \times 10^{-3}$ m, and S_0 is chosen so that the source has total (electron plus ion) power $P_{\text{source}} = 0.27L_z/L_{z0}$ MW, where $L_{z0} = 4$ m. The expression for the source power comes from multiplying $P_{\text{SOL}} = 5.4$ MW, the total power into the SOL, by the fraction of the total device volume covered by the simulation box. A floor of $0.1S_0$ is used in the $|z| < L_z/4$ region to prevent regions of $n \ll n_0$ from developing at large x , which can result in distribution-function positivity issues. The distribution function of the sources are non-drifting Maxwellians with a temperature profile $T_{e,\text{src}} = T_{i,\text{src}} = 74$ eV for $x < x_s + 3\lambda_s$ and $T_{e,\text{src}} = T_{i,\text{src}} = 33$ eV for $x \geq x_s + 3\lambda_s$. These choices result in an integrated source particle rate of $\approx 9.6 \times 10^{21}$ s⁻¹ for the $L_z = L_{z0}$ ($B_v/B_z = 0.6$) case. Plots of the density source rate and the source temperature of electrons and ions in the x - y plane at $z = 0$ m are shown in figure 5.3. Figure 5.4 shows the parallel variation of the density source rate in the x - z plane. The density source rate shown in these two figures are for the $B_v/B_z = 0.6$ simulation.

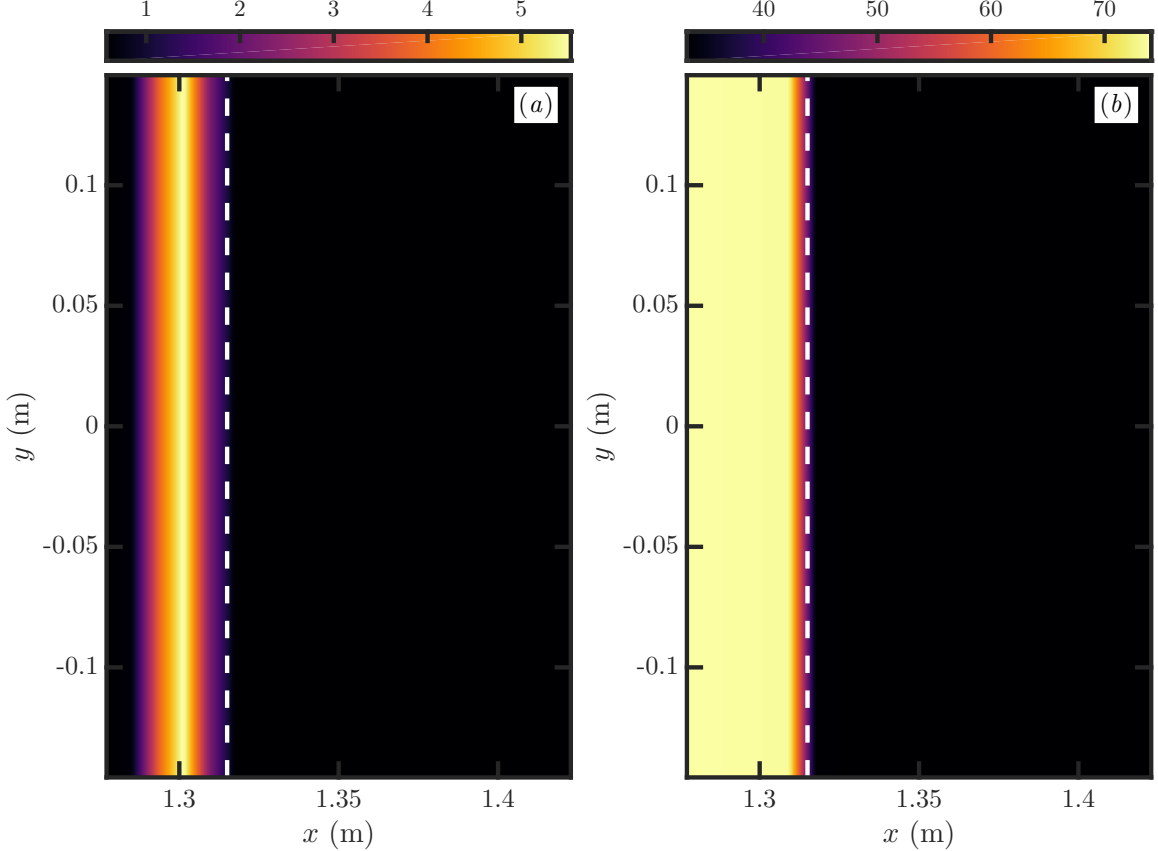


Figure 5.3: Helical-SOL-simulation (a) source density rate (in $10^{23} \text{ m}^{-3} \text{ s}^{-1}$) and (b) source temperature of electrons and ions (in eV) in the x - y plane at $z = 0 \text{ m}$. The source shown here is used for the $B_v/B_z = 0.6$ simulation. For other values of B_v/B_z , the source fueling rate is scaled to keep the volumetric source rate fixed. The dashed white line in each plot indicates the edge of the source region for comparison with other figures in this chapter.

We cannot yet include a closed-field-line region in our simulations, so we only simulate a SOL. The $x < x_s + 3\lambda_s$ region will be referred to as the source region in this chapter, while the $x \geq x_s + 3\lambda_s$ region will be referred to as the SOL region. We treat the $x = x_s + 3\lambda_s$ location as the last closed flux surface. For these reasons, we will only comment on the dynamics in the SOL region of our simulations and neglect the plasma behavior in the source region, which is believed to be strongly influenced by the source presence and the inner-wall radial boundary condition.

While larger time steps can be taken in these simulations, we note that the use of a spatially varying magnetic field also increases the computational cost for two reasons. First, the number of Gaussian quadrature points required for the exact evaluation of integrals is increased from 2 to 3 (at present, Gaussian quadrature rules for multiple dimensions are constructed from a tensor product of the 1D Gaussian quadrature rule). To give an example, consider the $-B_y^*/m_s$ entry in $\mathcal{J}\Pi$ (5.2). This term results in the following integral to solve the gyrokinetic equation after multiplying

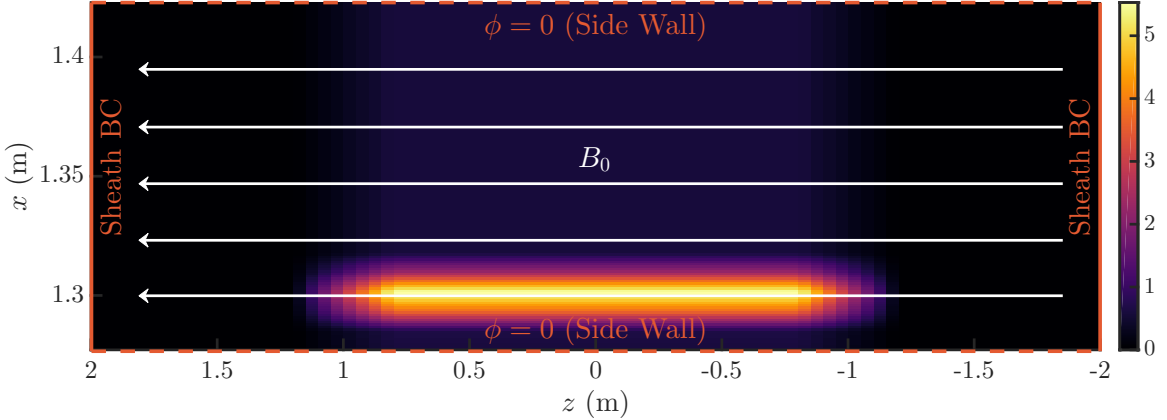


Figure 5.4: Helical-SOL-simulation plasma density source rate (in $10^{23} \text{ m}^{-3} \text{ s}^{-1}$) in the x - z plane for the $B_v/B_z = 0.6$ case. Annotations indicate the direction of the magnetic field, side-wall boundary conditions, and sheath-model boundary condition locations. The source is uniform in the periodic y direction.

(2.1) by an arbitrary test function ψ_k , integrating over all space $\int d\Lambda = \int d^3x \int d^3v$, and performing an integration by parts to move a partial derivative onto ψ_k :

$$-\int d\Lambda \frac{\partial \psi_k}{\partial v_{\parallel}} \frac{B_y^*}{m_s} \frac{\partial H_s}{\partial y} f_s.$$

The integrand is generally of order $4p$ in x , with each term contributing one power of p . Since we use $p = 1$ (piecewise-linear basis functions) in these simulations, the Gaussian quadrature rule must be able to integrate fourth-order polynomials in x exactly, which requires 3 quadrature nodes in x . For the LAPD simulations, this integral was zero because $B_y^* = 0$ for the straight-magnetic-field-line system, so only 2 quadrature nodes in x were required.

Secondly, more matrix-multiplication operations are required to solve the gyrokinetic equation (2.1) because the Jacobian $\mathcal{J} = B_{\parallel}^* = B$ can have spatial variation. In the LAPD simulations, the Jacobian-weighted mass matrices \mathbb{M} (see (2.22)) were the same in every cell, so every computing zone could compute and store one set of matrices at the beginning of the computation that would be used to solve the gyrokinetic equation at each time step. By allowing for a spatially varying \mathcal{J} , it becomes memory intensive to store all the Jacobian-weighted basis-function matrices, since a set of matrices would need to be stored for every variation of the Jacobian in a zone. A separate version of the gyrokinetic equation solver was written that evaluates certain matrix products involving the inverse of the Jacobian-weighted mass matrices on every time step, rather than storing the matrix products, which are independent of time, in memory.

From our prior experience in simulating LAPD (Chapter 4), we observed that uniform, zero-velocity initial conditions can take a significant time $\sim \tau_i = (L_z/2)/v_{ti}$ to reach a quasi-steady state. To reduce the computational cost, we decided to initialize our helical-SOL simulations from profiles calculated using a 1D single-fluid

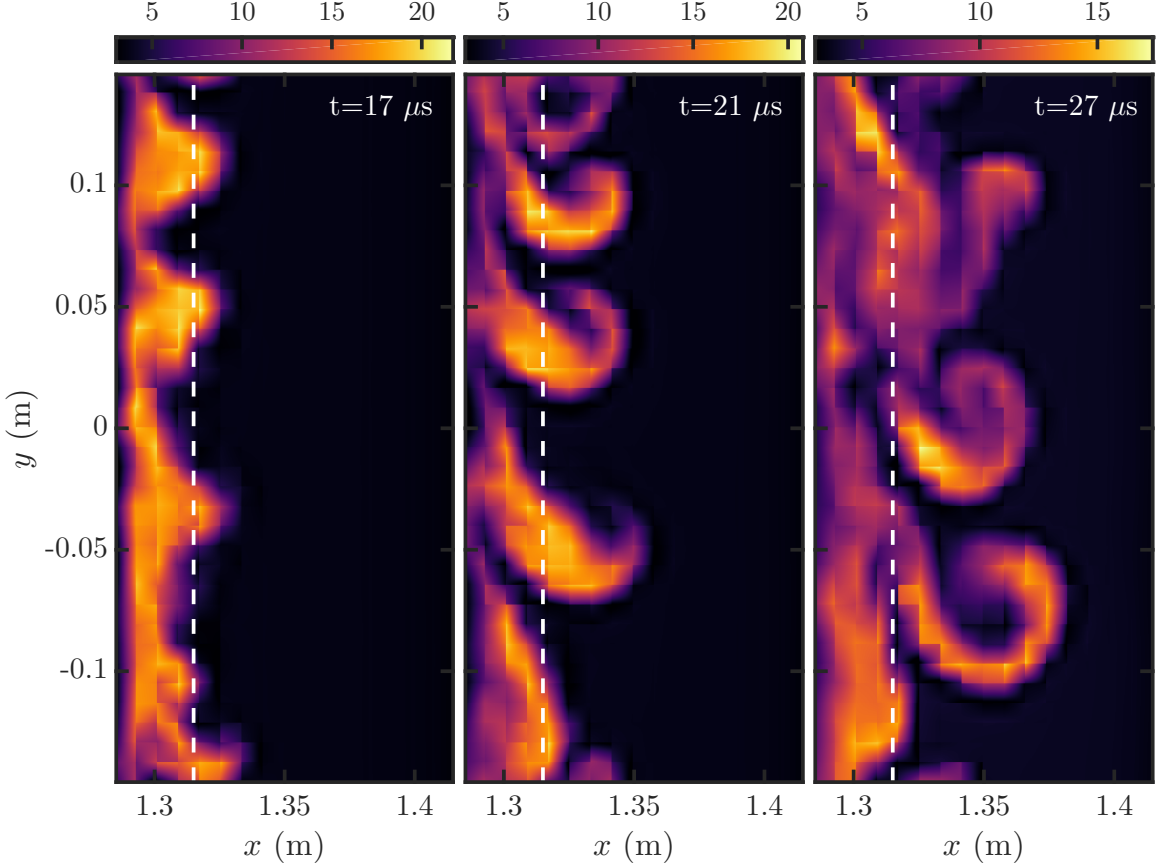


Figure 5.5: Snapshots of the electron density (in 10^{18} m^{-3}) at various times ($t = 17 \mu\text{s}$, $21 \mu\text{s}$, and $27 \mu\text{s}$) near the beginning of a simulation in the perpendicular x - y plane at $z = 0 \text{ m}$. This simulation has $B_v/B_z = 0.3$. The dashed line indicates the region in which the source is concentrated. Note that each plot uses a different color scale to better show the features.

analysis that neglects electric fields and thermal conduction. These initial conditions are derived and specified in Appendix D.

5.2 Simulation Results

Starting from an initial condition estimated by the steady-state solution of 1D fluid equations, the sources steepen the plasma profiles, quickly triggering curvature-driven modes that grow on a time scale comparable to $\gamma \sim c_s/\sqrt{R\lambda_p}$ (see Appendix E for details). We emphasize that our system does not contain ballooning modes since there are no ‘good-curvature’ regions. As shown in figure 5.5, radially elongated structures extending far from the source region are generated and subsequently broken up by sheared flows in the y direction in the source region, leaving radially propagating blobs. Using the time-averaged profiles from the same $B_v/B_z = 0.3$ ($L_z = 8 \text{ m}$) simulation, we estimate $\gamma \sim 1.9 \times 10^5 \text{ s}^{-1}$ using $\lambda_p \approx 2.9 \text{ cm}$, $T_e \approx 30 \text{ eV}$, and $R = x_s = 1.3 \text{ m}$. On a time scale long compared to γ^{-1} and $\tau_i = (L_z/2)/v_{ti}$, a quasi-

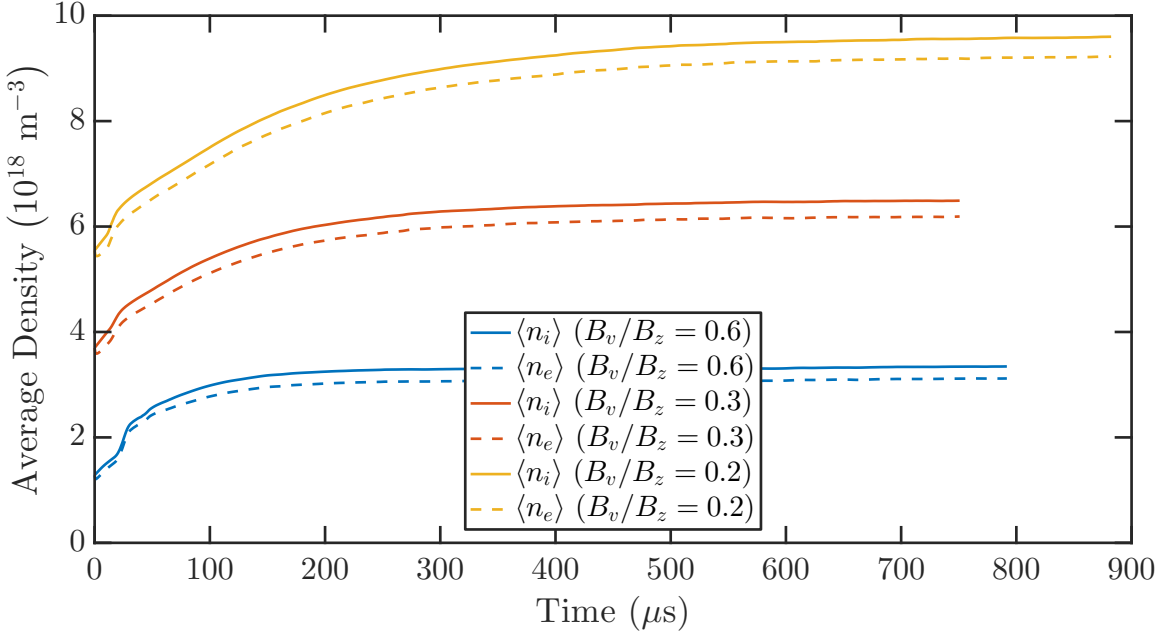


Figure 5.6: Average density of ions (solid lines) and electrons (dashed lines) vs. time for three simulations with different magnetic-field-line pitches. Starting from an initial condition, the simulations reach a quasi-steady state in which the particle losses to the end plates are balanced by the plasma sources.

steady state is reached in which the particle losses to the end plates are balanced by the plasma sources. Time traces of the average density in the simulation domain are shown in figure 5.6. Snapshots of the electron density, electron temperature, and electrostatic potential from the quasi-steady state ($t = 625 \mu\text{s}$) for the $B_v/B_z = 0.3$ case are shown in figure 5.7.

For the steepest magnetic-field-line-pitch case ($B_v/B_z = 0.6$), we performed a second simulation with magnetic-curvature effects removed and keeping all other parameters the same. The resulting magnetic geometry consists only of straight magnetic field lines, as in the LAPD simulations of Chapter 4, so coherent structures of elevated plasma density cannot become polarized by curvature forces. As shown in the electron density snapshot comparison in figure 5.8, the presence of magnetic curvature appears to have an important role in the turbulent dynamics of the system. When magnetic-curvature effects are removed, the radial propagation of coherent structures appears to be significantly weakened or absent, and most of the density is localized to the source region.

Figure 5.9 compares radial profiles of the background electron-densities, normalized electron-density fluctuation levels, and radial $E \times B$ particle fluxes $\Gamma_{n,r}$ between these two simulations. The radial particle flux due to electrostatic turbulence is estimated as $\Gamma_{n,r} = \langle \tilde{n}_e \tilde{v}_r \rangle$ (Zweben *et al.*, 2007), where $v_r = E_y/B$ and the brackets $\langle \dots \rangle_t$ indicate an average in time over a period that is long compared to the fluctuation time scale. The fluctuation of a time-varying quantity A is denoted as \tilde{A} , which is related to the total A as $\tilde{A} = A - \langle A \rangle_t$. Notable differences between these two

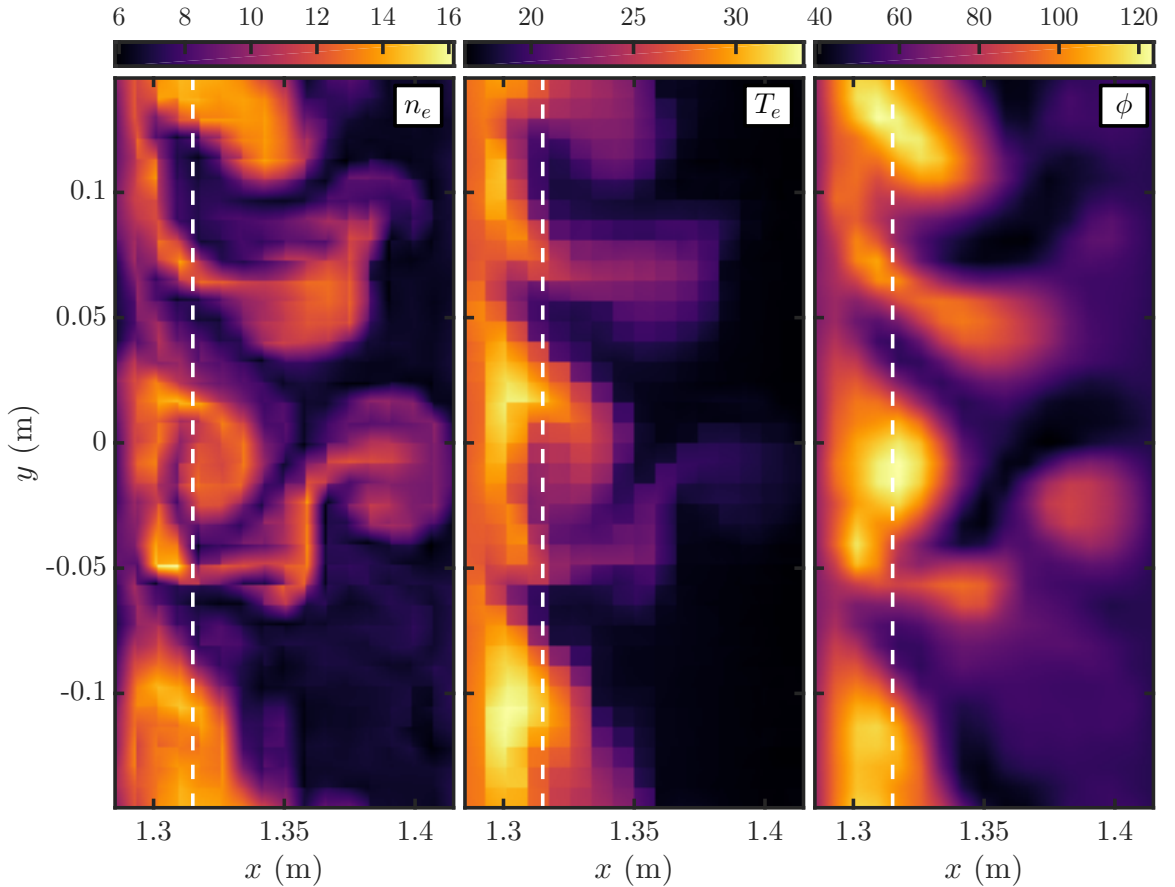


Figure 5.7: Snapshots of the electron density (in 10^{18} m^{-3}), electron temperature (in eV), and electrostatic potential (in V) in the plane perpendicular to the magnetic field at $z = 0$ m. This plot is made at $t = 625 \mu\text{s}$, which is after several ion transit times ($\tau_i \approx 46 \mu\text{s}$). This simulation has $B_v/B_z = 0.3$. The dashed line indicates the region in which the source is concentrated. A mushroom structure in the blob density is observed at large x . For additional details about how this plot and ones like it were created, see Appendix A.

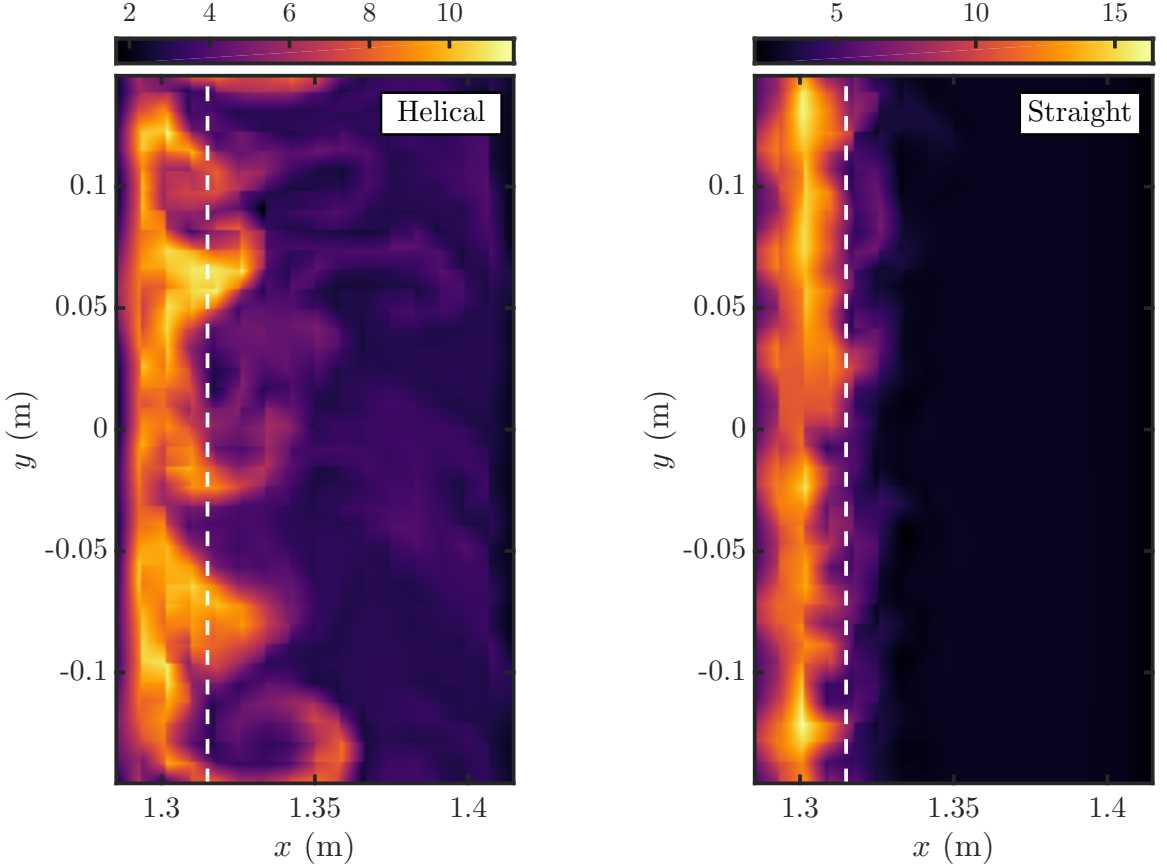


Figure 5.8: Comparison of an electron density snapshot (in 10^{18} m^{-3}) between (a) a simulation in a helical-magnetic-field-line geometry and (b) a simulation in a straight-magnetic-field-line geometry with $B = B_{\text{axis}}$. The formation of blobs in the helical-SOL simulation results in the transport of density to large x and a broad density profile. Coherent structures of elevated plasma density do not appear to convect to large x straight-magnetic-field-line case, and so density is mostly localized to the source region. The plots are made in the perpendicular x - y plane at $z = 0$ m and $t = 681 \mu\text{s}$. The dashed line indicates the region in which the source is concentrated. Note that each plot uses a different color scale to better show the features.

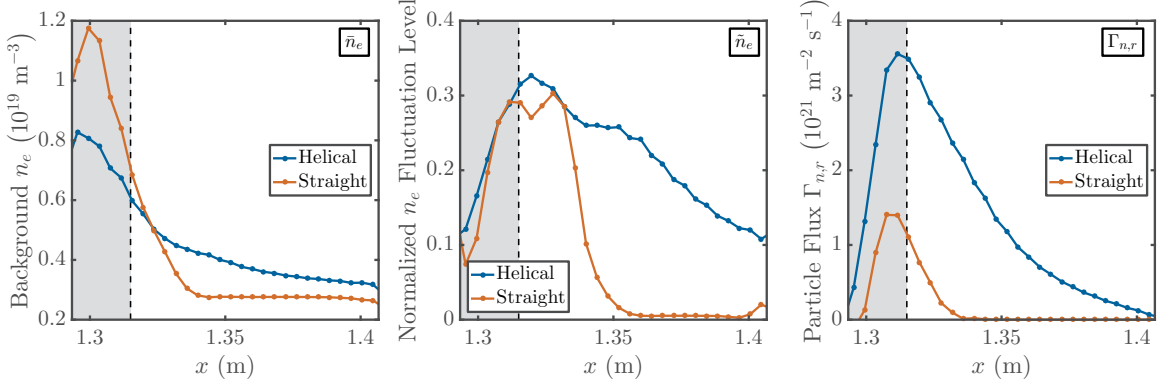


Figure 5.9: Radial profiles of the background electron densities (in 10^{19} m^{-3}), normalized-electron-density fluctuation levels, and radial $E \times B$ particle fluxes $\Gamma_{n,r}$ (in $10^{21} \text{ m}^{-2} \text{ s}^{-1}$) for a helical SOL simulation and a straight-field-line simulation with $B = B_{\text{axis}}$. These plots are computed using data near the midplane in the region $-0.5 \text{ m} < z < 0.5 \text{ m}$ and sampled at $0.25 \mu\text{s}$ intervals over a $\sim 400 \mu\text{s}$ period. The shaded area indicates the region in which the source is concentrated. The background density profile in the straight-field-line simulation does not decay to 0 at large x due to the presence of a constant low-amplitude source in that region to help mitigate positivity issues with the distribution function.

simulations are found in all three quantities plotted. Compared to the helical-SOL simulation, the straight-field-line simulation has a background density profile that decays more rapidly, fluctuation levels that quickly drop to $\approx 0\%$ outside $x \approx 1.35 \text{ m}$, and a ≈ 2.5 times smaller $\Gamma_{n,r}$ that also drops to ≈ 0 outside $x \approx 1.34 \text{ m}$.

We have also performed a scan of the mass ratio m_i/m_e from the actual ratio of 3698 down to 100 (by increasing the electron mass), and we observed no significant quantitative or qualitative changes in the turbulence. The electron-density profile and fluctuation statistics are shown for a mass ratio scan in figure 5.10. The mass ratio might play an important role in a different parameter regime, however.

Effects connected to $B_v \sim B_p \sim I_{\text{plasma}}$ are explored by since $\sin \theta = B_v/B_z$. We have performed simulations at three values of magnetic-field-line pitches $B_v/B_z = (0.2, 0.3, 0.6)$, which correspond to $L_z = (12, 8, 4) \text{ m}$ and $\theta = (20.14^\circ, 30.47^\circ, 64.4^\circ)$. In the various simulations, we scale the source appropriately to maintain a fixed volumetric source rate. In all these simulations, the source is localized to the $z \in [-L_z/4, L_z/4]$ region to model a source with a fixed poloidal extent. As θ is decreased, the plasma profiles are observed to become less peaked, implying that turbulence transport in the x -direction increased with decreasing θ .

We calculate the steady-state parallel heat flux $q = \sum_s \int d^3v H_s v_{\parallel} f_s$ at the sheath entrance and average q in the y -direction to obtain a radial profile of the steady-state parallel heat flux for each case. To compare the heat fluxes on an equal footing, we plot the component of the parallel heat flux normal to the divertor plate $q_{\perp} = q \sin \theta$ in figure 5.11. Compared to the $B_v/B_z = 0.6$ case, the heat-flux profiles for the cases with a shallower pitch are much broader. This behavior is consistent with the

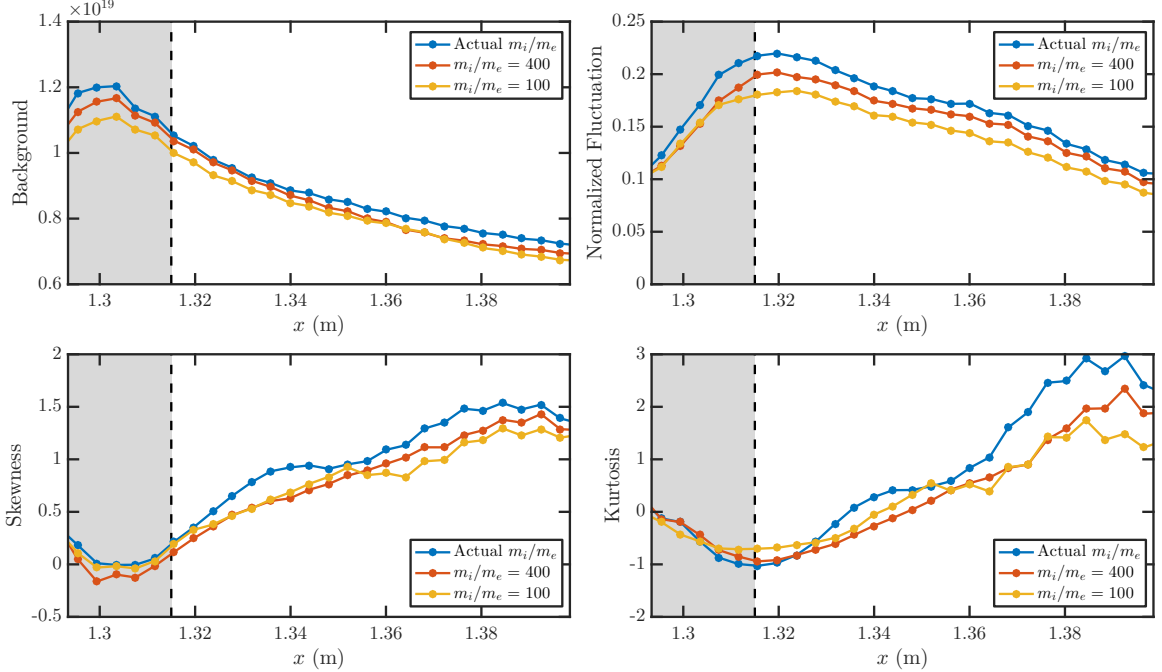


Figure 5.10: Comparison of electron-density profiles and fluctuation statistics for three cases with varying electron mass. As the mass ratio is reduced from the actual value $m_i/m_e \approx 3698$ to an artificially low value $m_i/m_e = 100$, the qualitative trends are unchanged, and the quantitative differences are small. The shaded area indicates the region in which the source is concentrated.

observation in tokamaks that the SOL heat-flux width is inversely proportional to the poloidal magnetic field (analogous to B_v in this model) and the plasma current (Eich *et al.*, 2013; Makowski *et al.*, 2012), although the physics reasons behind the scaling in our model and in a tokamak SOL may be quite different. We note that a significant amount of plasma in the smallest θ case reaches the outer radial wall, where it is quickly lost in the parallel direction since there is no E_{\parallel} to constrain the plasma flows on the outer radial boundary. Simulations with a larger domain extent in the x coordinate might exhibit more of a exponential fall off in the radial profiles than observed at these present box sizes.

The broad heat flux profiles in figure 5.11 can be connected to the increased outward radial turbulent transport as B_v/B_z becomes shallower. We compute the steady state radial particle flux $\Gamma_{n,r}$ near the midplane in the region $-0.5 \text{ m} < z < 0.5 \text{ m}$ for each value of B_v/B_z and plot the y -averaged fluxes in figure 5.12 (solid lines). Since the simulation box occupies a larger fraction the device volume as B_v/B_z is decreased, but the source occupies the same fraction of the simulation box and has a fixed volumetric source rate (see figure 5.2), the background density levels increase as B_v/B_z decreases. Therefore, the magnitude of the $\Gamma_{n,r}$ profiles in figure 5.12 should not be taken alone as a measure of turbulence levels. The $\Gamma_{n,r}$ profiles can be compared with the radial particle fluxes that result from assuming Bohm diffusion, i.e. $\Gamma_B = D_B \partial_x n_e$, where the diffusion coefficient $D_B = \frac{1}{16} \frac{k_B T_e}{eB}$. In the $x > 1.36 \text{ m}$ region,

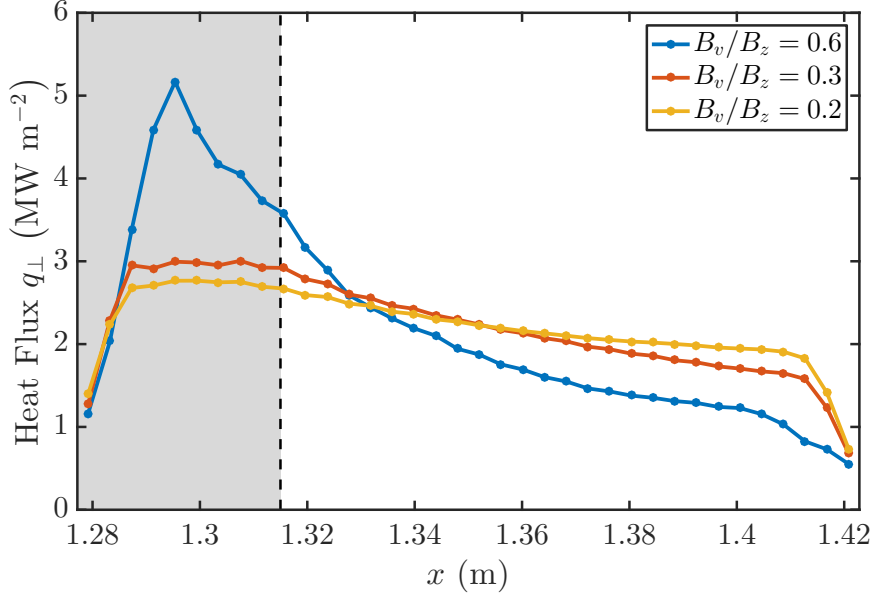


Figure 5.11: Comparison of the steady-state parallel heat flux normal to the divertor plate for three cases with different magnetic-field-line pitches. The shaded area indicates the region in which the source is concentrated. The heat-flux profile is observed to broaden as B_v/B_z is decreased. Since a large amount of plasma reaches the outer radial boundary, where parallel losses are enhanced due to the side-wall boundary conditions, the profiles in the shallower-pitch cases may exhibit more of an exponential fall off by increasing the box size in the radial direction.

$\Gamma_{n,r}/\Gamma_B \approx 16$ for the $B_v/B_z = 0.2$ case, while $\Gamma_{n,r}/\Gamma_B \approx 8$ for the $B_v/B_z = 0.6$ case. One might expect the maximum level of turbulent transport to be around the levels set by D_B , but it is important to remember that D_B is a *diffusive* transport estimate. The *convective* transport of blobs in these simulations appears to be responsible for the much-higher turbulent fluxes. Experimental data from tokamaks also suggest that the higher-than-Bohm particle transport in the SOL is due to the non-diffusive transport of blobs ([Krasheninnikov et al., 2008](#); [Zweben et al., 2007](#)).

Density fluctuation statistics are often of interest in the SOL to characterize the turbulence. Considering again a time-varying quantity A , we define the skewness of A as $E[\tilde{A}^3]/\sigma^3$ and the excess kurtosis of A as $E[\tilde{A}^4]/\sigma^4 - 3$, where σ is the standard deviation of A and $E[\dots]$ denotes the expected value. Figure 5.13 shows the radial profiles of the normalized fluctuation level, skewness, and excess kurtosis for electron-density fluctuations and electrostatic-potential fluctuations computed near the $z = 0$ m plane. Unlike in Chapter 4, where we sometimes normalize density fluctuations by a global value, we normalize density and potential fluctuations to their local background values in this chapter. The positive skewness and excess kurtosis values are signatures of intermittency, which indicates an enhancement of large-amplitude positive-density-fluctuation events and is connected to the transport of blobs ([Zweben et al., 2007](#)).

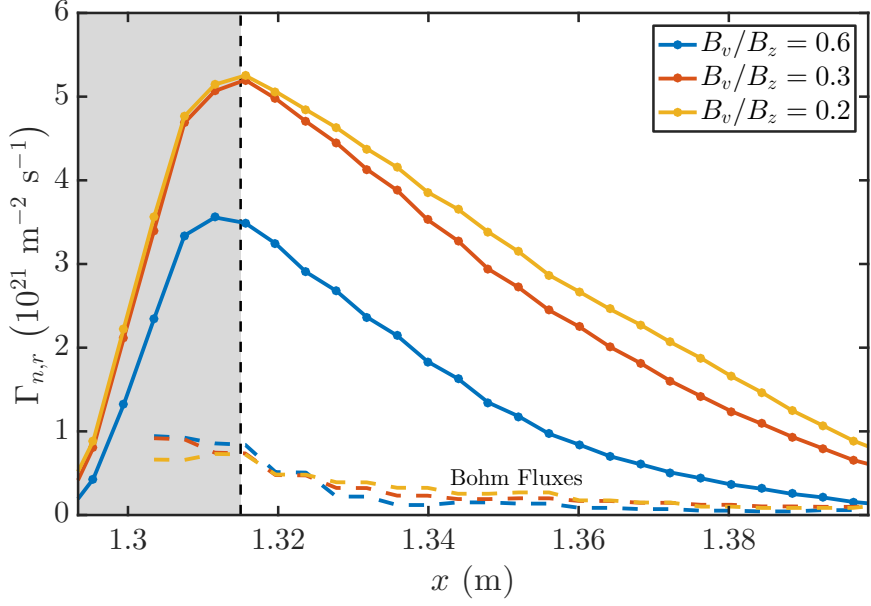


Figure 5.12: Comparison of the radial $E \times B$ particle flux evaluated near the midplane for three cases with different magnetic-field-line pitches. The shaded area indicates the region in which the source is concentrated. The dashed lines are Bohm flux estimates for comparison.

A somewhat counter-intuitive result is the reduction of density fluctuation levels as B_v/B_z is decreased, given that figures 5.11 and 5.12 indicate that turbulent spreading is increased as B_v/B_z is decreased. The skewness and excess kurtosis plots in figure 5.13 indicate that the density fluctuations become closer to a normal distribution as B_v/B_z is decreased. These trends in the density fluctuation statistics can be understood by noting that the background density profile becomes less peaked and more uniform in the x -direction as B_v/B_z is decreased, so a blob that is formed in the source region propagating in the SOL has a density that is closer to the background level, which results in lower relative fluctuation, skewness, and excess kurtosis values when compared to the large B_v/B_z case. Additionally, the density flux is constrained by the use of a fixed volumetric source rate, so as the background density increases with decreasing B_v/B_z , the relative density fluctuation levels tend to decrease. We also observe that the potential fluctuations are much less intermittent than the density fluctuations at the same B_v/B_z . This observation could be a real, physical effect, but we note that the fact that the temperature at large x runs into the grid resolution (the lowest temperature that can be represented on the velocity grid) could be influencing the potential fluctuation statistics in this region. Unlike the density fluctuations, the normalized potential fluctuation levels tend to increase with decreasing B_v/B_z .

Figure 5.14 shows radial profiles of the steady-state ion and electron temperatures and ion-to-electron temperature ratios near the midplane for different B_v/B_z . Similar to the heat-flux profiles shown in figure 5.11, the profiles are steepest for the case with $B_v/B_z = 0.6$ and decay more gradually in the lower- B_v/B_z cases. SOL measurements

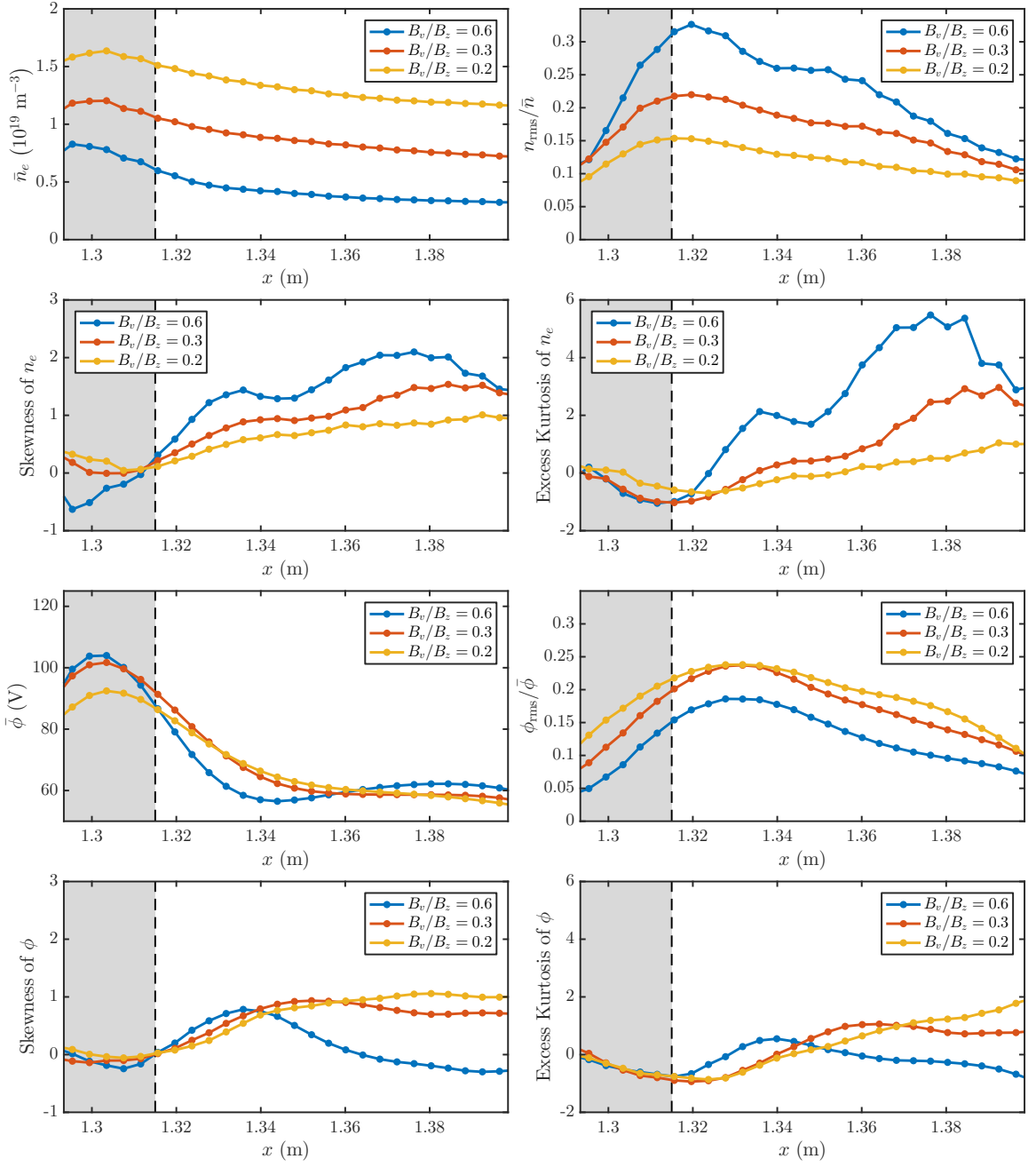


Figure 5.13: Comparison of the electron-density fluctuation statistics (first two rows) and electrostatic-potential fluctuation statistics (bottom two rows) computed near the $z = 0$ m plane for three cases with different magnetic-field-line pitches. The potential fluctuations are notably less intermittent than the density fluctuations. The shaded area indicates the region in which the source is concentrated.

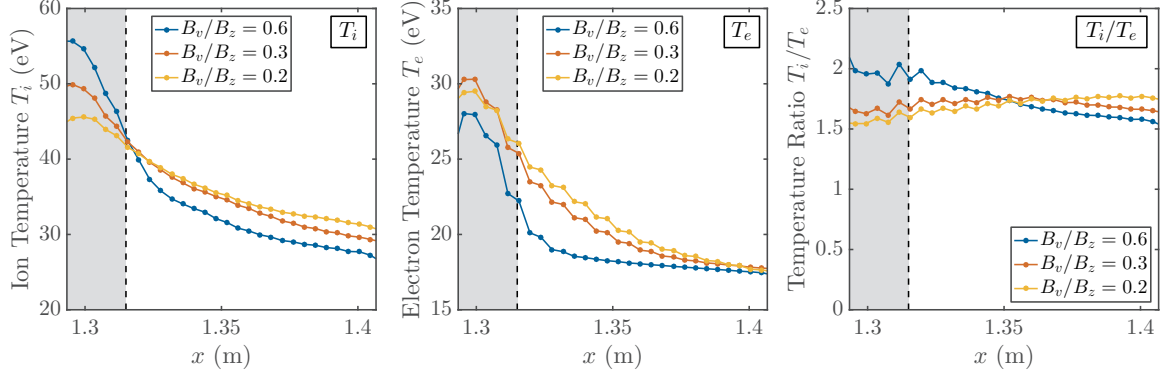


Figure 5.14: Radial profiles of the steady-state ion and electron temperatures near the midplane and ion-to-electron temperature ratios for cases with different magnetic-field-line pitches. Although both electrons and ions are sourced at the same temperature, the sheath allows high-energy electrons to be rapidly lost from the system, resulting in lower electron temperatures in the SOL if collisions are not rapid enough to equilibrate the two species (Strangeby & McCracken, 1990; Kočan *et al.*, 2011).

typically show that the ratio T_i/T_e increases with radius (Kočan *et al.*, 2011). We see this trend in figure 5.14 for $B_v/B_z = 0.3$ and 0.2 , but not for $B_v/B_z = 0.6$. This reversed trend for $B_v/B_z = 0.6$ is likely connected to the relatively flat T_e at large x . In the $B_v/B_z = 0.6$ case, the low-amplitude source of ~ 33 eV electrons at large x (see the form of the plasma source (5.3)) could be setting T_e in this region. The flat T_e at large x could also be an artifact from the electron's running into a floor in the temperature at large x (although we note that $T_{\perp e, \min} = 16$ eV, which is still a few eV lower than the T_e seen in this region). For all three simulations, T_i/T_e falls in the range 1.5–2, which is within the range of 1–10 that is observed a few centimeters outside the LCFS in tokamaks (Kočan *et al.*, 2011).

The normalized root-mean-square (r.m.s.) electron-density fluctuation level in the x – z plane is shown in figure 5.15. For all three values of B_v/B_z , the density fluctuation levels are the strongest in the source region $|z| < L_z/4$. The normalized density fluctuation levels in the $B_v/B_z = 0.6$ case are fairly uniform along the field lines, while they tend to fall off by about a factor of 2–3 towards the sheaths in the smaller B_v/B_z cases. This effect is likely a result of the stronger influence of the sheath on the potential as the distance from the source to the sheath is decreased. The instantaneous snapshots of \tilde{n}_e (not shown) indicate a strong $k_{\parallel} = 0$ component for the largest B_v/B_z cases, while more parallel structure is apparent in the smaller B_v/B_z cases.

The fluctuation statistics can also give information about the strength of the electron adiabatic response for each simulation. By assuming that the electrons are

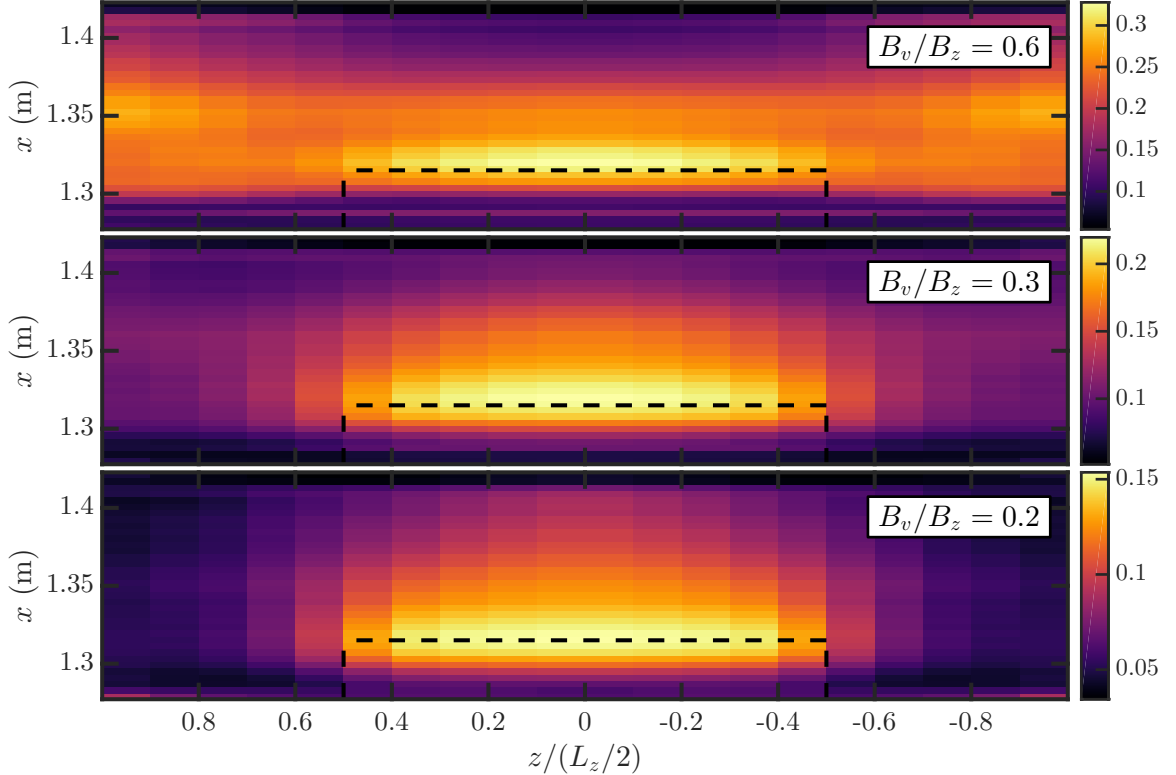


Figure 5.15: Comparison of the parallel structure of the normalized r.m.s. electron-density fluctuation amplitude for three cases with different magnetic-field-line pitches. While the density fluctuations are primarily $k_{\parallel} = 0$ in the $B_v/B_z = 0.6$ case, more parallel structure is observed in the lower- B_v/B_z cases. The source region is indicated by the dashed black lines.

isothermal along field lines, parallel force balance satisfies

$$\nabla_{\parallel} (n_e e E_{\parallel} + P_e) = 0 \quad (5.4)$$

$$-n_e e E_{\parallel} = T_e \nabla_{\parallel} n_e \quad (5.5)$$

$$\frac{e \nabla_{\parallel} \phi}{T_e} = \nabla_{\parallel} \ln n_e \quad (5.6)$$

$$\frac{e \phi_{\text{mid}}}{T_e} = \frac{e \phi_{sh}}{T_e} + \ln \left(\frac{n_{\text{min}}}{n_{sh}} \right), \quad (5.7)$$

where ϕ_{sh} and n_{sh} are the electrostatic potential and electron density evaluated at the sheath entrances and ϕ_{mid} and n_{mid} are the same quantities, but evaluated at the mid-plane ($z = 0$ m). To compute the cross-coherence diagnostic (Scott, 2005a; Ribeiro & Scott, 2005; Mosetto *et al.*, 2013), ordered pairs $(e\phi_{\text{mid}}/T_e, e\phi_{sh}/T_e + \ln(n_{\text{mid}}/n_{sh}))$ falling in the region $1.318 \text{ m} \leq x \leq 1.326 \text{ m}$ (approximately where the maximum density and potential fluctuations are) are sampled at $1 \mu\text{s}$ intervals over a $\sim 1 \text{ ms}$ period for each simulation. Figure 5.16 shows the resulting plots (normalized bivariate histograms), which all indicate a strong correlation between the two sides of (5.7),

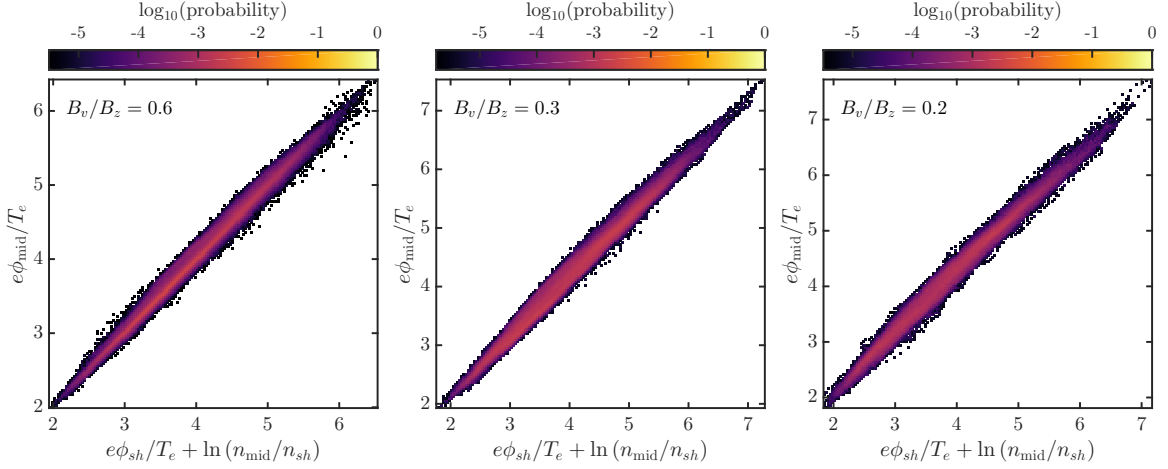


Figure 5.16: Comparison of the cross-coherence between the midplane potential $e\phi_{mid}/T_e$ and $e\phi_{sh}/T_e + \ln(n_{mid}/n_{sh})$ for three cases with different magnetic-field-line pitches θ . Here, ϕ_{sh} is the sheath potential, n_{mid} is the midplane electron density, and n_{sh} is the sheath electron density. These plots are created by binning ordered pairs of the two quantities sampled every $0.25 \mu\text{s}$ over a $\sim 1 \text{ ms}$ time interval at solution nodes falling in the region $1.318 \text{ m} \leq x \leq 1.326 \text{ m}$. In all three cases, the two quantities are highly correlated, which indicates that the electrons are strongly adiabatic (near parallel force balance).

and so the electrons are strongly adiabatic, meaning that the electron distribution function along a field line closely follows a Boltzmann distribution ([Stoltzfus-Dueck, 2009](#)). This result indicates that it might be possible to obtain similar results using an axisymmetric model (with sheath-model boundary conditions) for the parameters considered here.

Figure 5.17(a) shows the radial profile of the autocorrelation time τ_{ac} (computed from time traces of the density fluctuations). In the SOL of the simulation, τ_{ac} tends to increase with radius, which is a trend observed in measurements on NSTX (see [Zweben et al., 2015](#), figure 12). The autocorrelation time for the $B_v/B_z = 0.2$ and $B_v/B_z = 0.3$ cases is found to vary between $\sim 5 \mu\text{s}$ and $\sim 9 \mu\text{s}$, while the autocorrelation time for the $B_v/B_z = 0.6$ case exhibits a larger variation in the SOL, with $\tau_{ac} \approx 4 \mu\text{s}$ for $x < 1.34 \text{ m}$ and increasing to $\approx 12 \mu\text{s}$ at the outer radial boundary. The autocorrelation times we observe in our simulations are lower than the $\tau_{ac} \sim 10\text{--}40 \mu\text{s}$ reported by [Zweben et al. \(2015\)](#) for the NSTX edge and SOL, but are well within the $\tau_{ac} \sim 2\text{--}20 \mu\text{s}$ range that is typical for edge and SOL turbulence in other tokamaks ([Boedo et al., 2009](#); [Zweben et al., 2007](#)).

Figure 5.17(b) shows the poloidal and radial correlation lengths (L_{pol} and L_{rad} respectively) using the electron-density fluctuations near the $z = 0 \text{ m}$ plane. The correlation length at a radial location is obtained by averaging the correlation length computed at several points in y . At an individual point, the correlation length is determined from the correlation function, which is constructed by computing the equal-time two-point autocorrelation function for density fluctuations separated by

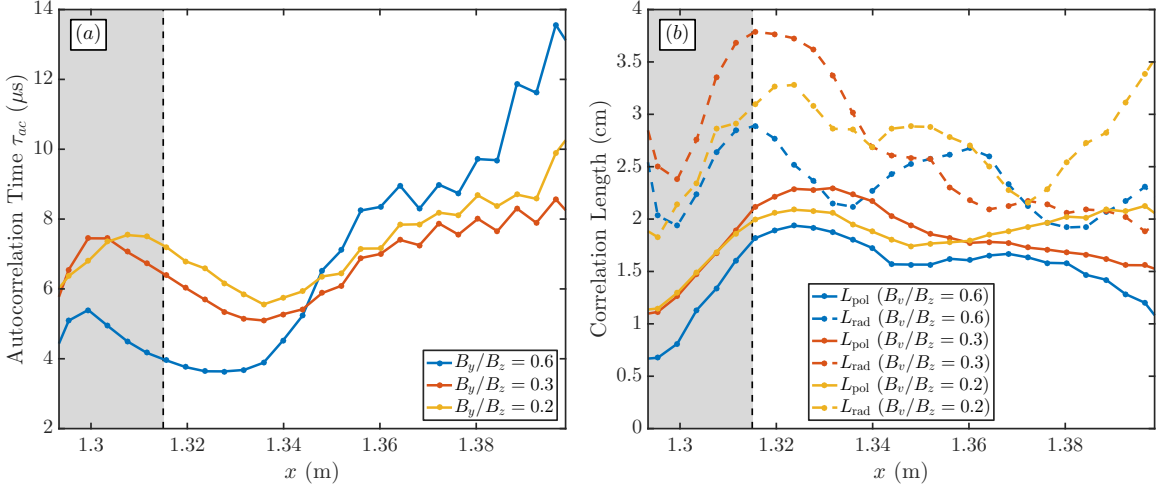


Figure 5.17: Radial profiles of the (a) autocorrelation time and (b) poloidal (dashed lines) and radial (solid lines) correlation lengths computed at the $z = 0$ m plane for three cases with different magnetic-field-line pitches. The shaded area indicates the region in which the source is concentrated. $L_{\text{pol}}/L_{\text{rad}} \sim 1.2\text{--}1.6$ is observed across the radial domain.

some distance Δy for L_{pol} or Δx for L_{rad} . Having observed a significant wave feature in the poloidal correlation function, we determined L_{pol} by fitting the poloidal correlation function to $e^{-|\Delta y|/L_{\text{pol}}} \cos(k_{\text{wave}}\Delta y)$. The radial correlation function, which does not have a wave feature, is computed using the full width at half maximum (FWHM) as $L_{\text{rad}} = \text{FWHM}/(2 \ln 2)$.

For all three values of B_v/B_z , we observe that the ratio $L_{\text{pol}}/L_{\text{rad}}$ is between 1.2 and 1.6 for most of the radial domain, which is similar to the $L_{\text{pol}}/L_{\text{rad}} \sim 1\text{--}2$ that is typically observed in tokamaks and stellarators (Zweben *et al.*, 2007; Boedo *et al.*, 2009). An average $L_{\text{pol}}/L_{\text{rad}} = 1.5 \pm 0.1$ was reported for representative Ohmic NSTX discharges (Zweben *et al.*, 2016), although larger ratios $L_{\text{pol}}/L_{\text{rad}} \sim 3\text{--}4$ have been observed in some experiments (Huber *et al.*, 2005) and simulations (Churchill *et al.*, 2017).

As discussed in Section 2.5, there are two kinds of sheath-model boundary conditions that are commonly used in fluid and gyrokinetic codes. Logical-sheath boundary conditions enforce $j_{\parallel} = 0$ at the sheath entrances, while current fluctuations into the sheath are permitted in conducting-sheath boundary conditions. Figure 5.18 shows the radial profiles of the steady-state parallel current into the sheath for the three cases under consideration. The currents have been normalized to peak steady-state ion saturation current $j_{\text{sat}} = q_i n_i c_s$, where $c_s = \sqrt{(T_e + \gamma T_i)/m_i}$ and $\gamma = 3$ is used because the collisionless layer in front of the sheaths should be resolved in all three cases. All three cases are quite quantitatively similar, and the outward sheath currents are found to be highly symmetric in the z , which is consistent with the strong adiabatic response shown in figure 5.16. A large excess electron outflow (negative current) is seen in the source region, which is compensated by a large excess ion outflow (positive current) just outside the source region. The peak values are approximately 20% of

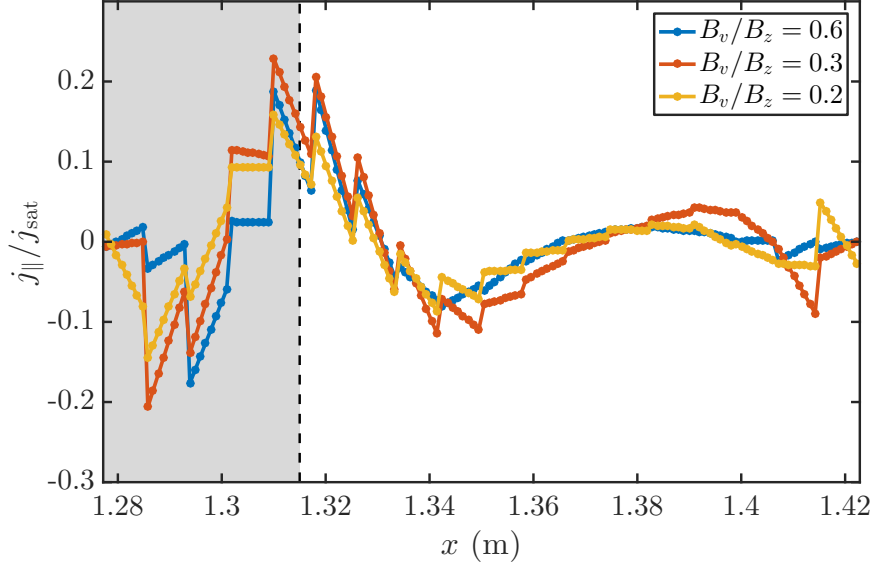


Figure 5.18: Radial profiles of the steady-state parallel currents into the sheaths for cases with different magnetic-field-line pitches. The current is normalized to the peak value of the steady-state ion saturation current $j_{\text{sat}} = q_i n_i c_s$ for each simulation. All three cases are quite quantitatively similar, featuring a large excess electron outflow in the source region that is balanced by a large excess ion outflow just outside of the source region.

the ion saturation current, which motivates future studies regarding the use of how various sheath-model boundary conditions affect turbulence in these simulations. In more realistic models of the SOL, the plasma source is in a region of closed magnetic field lines, so there cannot be large electron sheath currents in the source region in these models. It will be interesting to explore how these profiles change when this capability is added to the code.

5.3 Conclusions

We have developed a model to investigate interchange-driven SOL turbulence in a simplified helical-magnetic-field geometry and performed numerical simulations of the system using an electrostatic gyrokinetic continuum code. The blobs in our simulations appear to originate as radially elongated structures that extend from the source region into the SOL and get broken up by sheared poloidal flows. The blobs appear to efficiently transport plasma across the magnetic field, leading to radial particle fluxes that are much higher than Bohm-flux estimates. Such large-amplitude and large-scale blobs were not observed in a set of simulations we performed without magnetic-curvature effects. We note, however, that coherent structures with high plasma density have been observed in linear devices with negligible magnetic curvature ([Antar et al., 2001](#); [Carter, 2006](#)). The mechanism that polarizes such

Table 5.3: Summary of helical-SOL simulation results with comparison to experimental values for an H-mode NSTX SOL reported in Zweben *et al.* (2015). The values of $\Gamma_{n,r}$, T_e , and n_e refer to values near the LCFS (whose location is not precisely known in the experiments (Zweben *et al.*, 2004)). Since GPI cannot be used to obtain particle fluxes, the value of $\Gamma_{n,r}$ for the NSTX case is taken from Boedo *et al.* (2014). The ‘ \sim ’ symbol is used here to indicate that there can be large variations in such quantities between discharges with different parameters. Ion temperature measurements in the plasma boundary of NSTX were not available, so the value of 1–2 (seen on AUG and MAST (Kočan *et al.*, 2011)) is assumed.

Quantity	Simulation Range	NSTX SOL
τ_{ac} (μs)	4–14	15–40
L_{pol} (cm)	2–4	3–5
L_{rad} (cm)	1–2.5	2–3
$\tilde{n}_{\text{rms}}/\bar{n}$ (%)	10–30	20–100
$\Gamma_{n,r}$ ($10^{21} \text{ m}^{-2} \text{ s}^{-1}$)	3.5–5.1	~ 4
n_e (10^{19} cm^{-3})	0.5–1.5	~ 1
T_e (eV)	26–29	~ 29
T_i/T_e	1.5–2	1–2

coherent structures in linear devices and leads to outward radial propagation could be due to neutral wind (Krasheninnikov & Smolyakov, 2003).

We characterized the turbulence using a variety of diagnostics and found that various quantities of interest are within the range expected for SOL turbulence in tokamaks, such as fluctuation levels, autocorrelation times, and correlation lengths. A summary of some quantities from our simulations is given in table 5.3, which also includes experimental values from the NSTX SOL (Zweben *et al.*, 2015; Boedo *et al.*, 2014). We varied the magnetic-field-line pitch in a set of simulations, which indicated an increasing level of radial turbulent particle transport with decreasing pitch. A cross-coherence diagnostic comparing potential fluctuations at the sheaths with those at the midplane indicated that all three simulations appeared to fall into a similar turbulent regime with strongly adiabatic electrons. The application of this model to investigate turbulence in the Helimak device (Gentle & He, 2008) is currently underway, which will also allow for comparisons with a previous GBS Braginskii fluid simulation (Li *et al.*, 2011).

The helical-SOL model can be extended by the addition of a closed-magnetic-field-line region (with periodic boundary conditions in the parallel direction). While the Gkeyll code can already perform simulations with periodicity in the parallel direction, additional work is required to simultaneously include both open and closed-magnetic-field-line regions in the same simulation. The addition of good-magnetic-curvature regions and electromagnetic effects are also important extensions that will make this model more applicable to tokamaks. Since our model is relatively simple compared

to a realistic tokamak SOL, the helical-SOL model could also eventually serve as a test case for the cross verification of gyrokinetic boundary-plasma codes. This test case might be useful for revealing major discrepancies due to different numerical approaches, sheath-model boundary conditions, and collision operators implemented in various codes relatively early on in the development cycle before more significant investments are made.

Chapter 6

Conservative Exponentially Weighted Basis Functions

This chapter discusses work on a conservative discontinuous Galerkin (DG) method that employs non-polynomial approximation spaces to represent the distribution function. As discussed in Chapter 2, the solution domain in DG methods is divided into a number of non-overlapping elements (cells) and the numerical solution itself is represented as a linear combination of local basis functions in each element. One must choose a finite-element space in which the local solution is represented, and even a different representation can be used in every element (related to p-adaptivity). This flexibility in the mesh comes from the lack of inter-element-continuity enforcement in the DG method. Typically, the local approximation space is chosen to be the space of polynomials up to a particular degree, resulting in the use of piecewise polynomial basis functions. Piecewise polynomials may not always provide the best approximation to the solution, however. For example, distribution functions often have Maxwellian tails that behave as $\propto \exp(-v^2)$ as $v \rightarrow \pm\infty$, where v is a velocity coordinate. Therefore, it is of interest to examine alternative finite-element spaces for kinetic problems to improve solution accuracy and reduce computational cost.

[Yuan & Shu \(2006\)](#) studied DG methods using non-polynomial (trigonometric and exponential) approximation spaces and explored methods to adjust the approximation spaces as the solution changes over time. They proved that non-polynomial finite element spaces satisfying certain conditions have approximation rates similar to those of polynomial finite element spaces of the same dimension. Their 1D and 2D numerical results demonstrated that DG approximations based on suitably selected non-polynomial functions could be much more accurate than using standard piecewise polynomials. The authors did, however, acknowledge the challenge in efficiently identifying appropriate approximation spaces for practical problems of interest. Additionally, the authors did not investigate the conservation properties of the algorithm, which we will show to be a serious issue later in this chapter.

Gyrokinetic simulations of plasma microturbulence are often computationally intensive, requiring the calculation of distribution function in a 3D2V (three spatial dimensions and two velocity dimensions) phase space. It is important to pursue efficient numerical methods for 5D gyrokinetic turbulence codes because algorithmic

choices have a big impact on what problems can be simulated on current supercomputers. Some strategies to reduce the computational cost of gyrokinetic simulations include the use of multigrid methods, implicit-time-stepping methods, and sparse-grid methods. For codes using grid-based (continuum) algorithms, one must be careful not to waste grid points in regions where fine resolution of the distribution function is not necessary. Additionally, it can be challenging to represent disparate temperatures of the same particle species on the same phase-space grid because the velocity-space resolution must be fine enough to resolve the colder particles, and the velocity-space extents must be large enough so that the warmer particles are still far from the velocity-space boundaries.

[Landreman & Ernst \(2013\)](#) explored various collocation strategies for efficient velocity-space discretization in the context of pseudospectral methods using the speed coordinate v defined on the semi-infinite domain $[0, \infty)$. They found that calculations employing a little-known family of non-classical polynomials orthogonal with respect to $v^\nu e^{-v^2}$ ($\nu > -1$) on the interval $v \in [0, \infty)$ ([Shizgal, 1979, 1981](#); [Ball, 2002](#)) often yielded superior performance at both differentiating and integrating distribution functions when compared to more commonly used collocation schemes. These non-classical polynomials have been recently applied to the time-dependent problem of relaxation to a Maxwellian via Fokker-Planck collisions ([Wilkening et al., 2015](#)). While the results in [Wilkening et al. \(2015\)](#) were promising, the authors recognized the additional complication arising from calculations on a dense stiffness matrix.

In this chapter, we explore the use of exponentially weighted polynomials to represent the velocity dependence of a distribution function in problems with Fokker–Planck collisions. We focus on the application of these ideas in the DG framework, which results in calculations with smaller matrices due to the high degree of locality inherent to such methods. We discuss representations of the distribution function using exponentially weighted polynomials in Section 6.1 and show how conservation issues arise from the use of non-polynomial representations in the standard DG method, a consequence that has not been previously discussed in the literature. We propose a modification that allows one to use certain non-polynomial-weighted basis functions in DG methods while respecting the conservation properties of the original equations. Using our proposed numerical scheme, we study the 1D relaxation to a Maxwellian distribution in Section 6.2 and the calculation of the parallel heat flux in a simplified Spitzer–Härm test problem ([Spitzer & Härm, 1953](#)) in Section 6.3.

We note that the algorithms discussed in this chapter have not yet been implemented in the Gkeyll code. It is possible that the exponentially weighted basis functions as they are described here might introduce too much overhead to the calculations to be competitive with standard polynomial basis functions. Nevertheless, we provide some evidence in this chapter that the use of non-polynomial basis functions is an idea worth pursuing in future versions of the code because of the potentially significant savings that it could enable.

6.1 The General Algorithm

We first briefly review how the standard Runge–Kutta discontinuous Galerkin (RKDG) method is applied to solving nonlinear conservation laws of the form

$$\frac{\partial f}{\partial t} + \frac{\partial g(f)}{\partial v} = 0. \quad (6.1)$$

This method uses an explicit Runge–Kutta time discretization and a discontinuous-Galerkin space discretization. For more information about the RKDG method, we refer the reader to Section 2.2 and the references therein.

We approximate the solution in each interval $I_j = [v_{j-\frac{1}{2}}, v_{j+\frac{1}{2}}]$ by expanding in terms of N local, predetermined basis functions as

$$f_h(v, t) = \sum_{k=1}^N f_j^k(t) \psi_j^k(v), \quad v \in I_j. \quad (6.2)$$

Typically, the basis functions span the space of polynomials up to a certain degree. In a modal discontinuous Galerkin approach, the standard choice is to take $\psi_j^k(v)$ to be the Legendre polynomials $P_k(v)$ defined on I_j . The standard piecewise-polynomial approximation space of degree k is denoted in this chapter as

$$V^k = \{w : w|_{I_j} \in \text{span}\{1, (v - v_j), \dots, (v - v_j)^k\}, v \in I_j\}. \quad (6.3)$$

Starting from an initial condition, the solution for $t > 0$ is determined by applying a Galerkin method to solve for $\partial f_h / \partial t$. The weak formulation is obtained by multiplying (6.1) by a test function $w(v)$ and integrating over I_j :

$$\int_{I_j} dv w(v) \left(\frac{\partial f_h}{\partial t} + \frac{\partial g(f_h)}{\partial v} \right) = 0. \quad (6.4)$$

In the DG method, $w(v)$ is chosen to span the same space as the basis functions, so (6.4) leads to a system of N equations for N unknowns $\partial f_j^k / \partial t$ in each interval I_j . As noted in Section 2.2, (6.4) with $w(v)$ chosen to be the basis functions also arises from a minimization of the squared- L^2 -norm error with respect to $\partial f_h / \partial t$. Integration by parts is used to move the spatial derivative from the nonlinear term g onto $w(v)$:

$$\begin{aligned} \int_{I_j} dv w(v) \frac{\partial f_h}{\partial t} &= \int_{I_j} dv \frac{\partial w}{\partial v} g(f_h) + -\hat{g} \left(f_h \left(v_{j+\frac{1}{2}}, t \right) \right) w \left(v_{j+\frac{1}{2}}^- \right) \\ &\quad + \hat{g} \left(f_h \left(v_{j-\frac{1}{2}}, t \right) \right) w \left(v_{j-\frac{1}{2}}^+ \right), \end{aligned} \quad (6.5)$$

where we have replaced the flux g evaluated at the boundaries by the numerical flux \hat{g} . The numerical flux is a single-valued function of the left and right limits of the discontinuous solution at the boundary, i.e. $\hat{g} \left(f_h \left(v_{j+\frac{1}{2}}, t \right) \right) =$

$\hat{g} \left(f_h \left(v_{j+\frac{1}{2}}^-, t \right), f_h \left(v_{j+\frac{1}{2}}^+, t \right) \right)$. Depending on the problem, common choices are to use a centered flux or an upwind flux. The value of the test function evaluated on the boundaries is taken from within the interval I_j .

If we represent f using the standard piecewise-polynomial approximation space, the numerical scheme locally conserves particle number. The numerical scheme satisfies (6.5) with $w = 1$ because piecewise constants are in the approximation space V^k :

$$\int_{I_j} dv \frac{\partial f_h}{\partial t} = -\hat{g} \left(f_h \left(v_{j+\frac{1}{2}}, t \right) \right) + \hat{g} \left(f_h \left(v_{j-\frac{1}{2}}, t \right) \right). \quad (6.6)$$

The quantity on the left-hand side is simply the rate of change in the particle number in the interval I_j , while the right-hand side is comprised of the fluxes across each boundary of cell j .

In this work, we are interested in approximating f on each interval I_j for Fokker-Planck equations using the following two non-polynomial expansions:

$$f_h(v_{\parallel}, t) = \sum_{k=1}^N f_j^k(t) \psi_j^k(v_{\parallel}) = \sum_{k=1}^N f_j^k(t) \beta_{0,j} \exp \left(-\beta_{1,j} \frac{(v_{\parallel} - \beta_{2,j})^2}{2} \right) P_k(v_{\parallel}), \quad (6.7)$$

$$f_h(\mu, t) = \sum_{k=1}^N f_j^k(t) \psi_j^k(\mu) = \sum_{k=1}^N f_j^k(t) \alpha_{0,j} \exp(-\alpha_{1,j} \mu) P_k(\mu), \quad (6.8)$$

where the variables $\beta_{0,j}$, $\beta_{1,j}$, $\beta_{2,j}$, $\alpha_{0,j}$, and $\alpha_{1,j}$ are free parameters of the basis functions that may also vary in time as well as in each cell. One can recognize these forms as the standard piecewise polynomials weighted by an exponential factor in v_{\parallel} (the parallel velocity) or μ (the magnetic moment), so we refer to these specific non-polynomial basis functions will be referred to as *exponentially weighted polynomials*. For the exponentially weighted basis functions to be an attractive (and hopefully superior) alternative to polynomial basis functions, it is important to be able to dynamically adjust the exponential weighting factor as the solution changes in time-dependent problems. Although our initial tests use predetermined values for the parameters of the exponential weighting factor, we propose a method to automatically choose these parameters in Section 6.4.

Figure 6.1 shows a comparison of standard polynomial basis functions with the exponentially weighted basis functions in (6.7). Besides the advantage of potentially being a better approximation than piecewise polynomials, these approximation spaces also permit the use of the complete velocity space domain $[0, \infty)$ in μ and $(-\infty, \infty)$ in v_{\parallel} instead of requiring truncation of the velocity domain at a finite and arbitrary value, which is typically chosen to be a few thermal velocities.

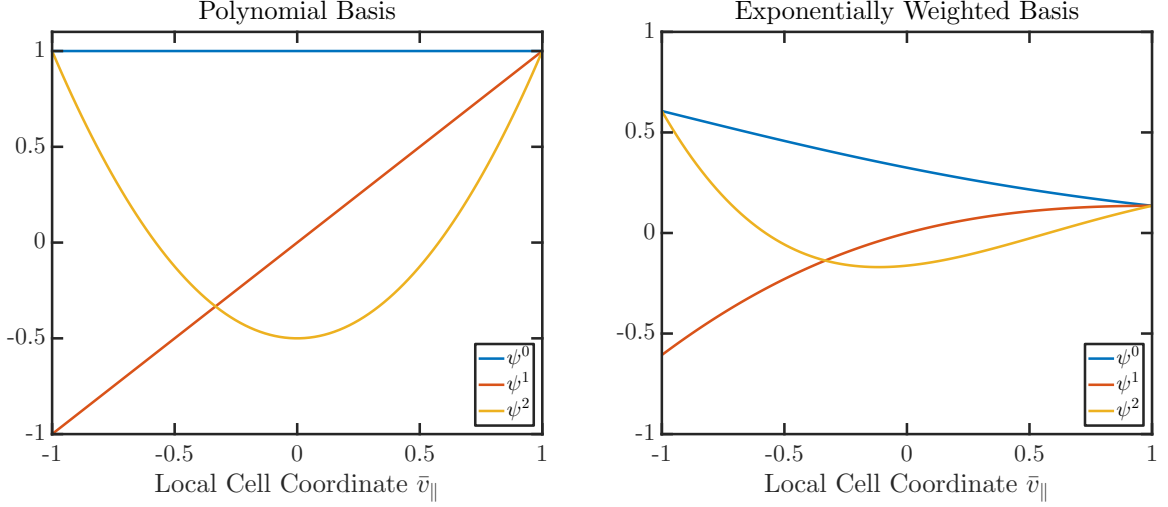


Figure 6.1: Comparison of standard polynomial basis functions (Legendre polynomials) with a set of exponentially weighted basis functions (6.7). For the exponentially weighted basis, we use the parameters $\beta_{0,j} = 1$, $\beta_{1,j} = 1/4$, and $\beta_{2,j} = 1$ and plot the basis functions for the cell with centroid located at $v_j = 4$. While the polynomial basis functions are the same in every cell, the exponentially weighted basis functions can vary cell-to-cell due to the weighting factor.

The approximation spaces corresponding to the representations in (6.7) and (6.8) are

$$\bar{M}^k(\beta) = \left\{ w : w|_{I_j} \in \text{span} \left\{ \beta_0 e^{-\beta_1(v-v_j-\beta_2)^2/2}, \beta_0 e^{-\beta_1(v-v_j-\beta_2)^2/2}(v-v_j), \dots, \right. \right. \\ \left. \left. \beta_0 e^{-\beta_1(v-v_j-\beta_2)^2/2}(v-v_j)^k \right\}, v \in I_j \right\}, \quad (6.9)$$

$$M^k(\alpha) = \left\{ w : w|_{I_j} \in \text{span} \left\{ \alpha_{0,j} e^{-\alpha_{1,j}(\mu-\mu_j)}, \alpha_{0,j} e^{-\alpha_{1,j}(\mu-\mu_j)}(\mu-\mu_j), \dots, \right. \right. \\ \left. \left. \alpha_{0,j} e^{-\alpha_{1,j}(\mu-\mu_j)}(\mu-\mu_j)^k \right\}, v \in I_j \right\}, \quad (6.10)$$

where v_j and μ_j are the coordinates in v_\parallel and μ of the centroid of cell j .

If one represents f using (6.7) or (6.8) and uses the standard RKDG algorithm (6.5) to solve the hyperbolic equation (6.1), the resulting numerical schemes no longer conserve particle number. We can no longer substitute $w = 1$ into (6.5) because piecewise constants are no longer contained in the approximation spaces M^k and \bar{M}^k used to represent f , and (6.6) is not satisfied. This numerical scheme will be referred to as the *non-conservative exponentially weighted DG method* in the rest of this chapter. Similarly, there are issues with the conservation of other polynomial moments of the distribution function that were conserved prior to discretization (such as energy or momentum). The lack of number and energy conservation is numerically demonstrated for an example problem in Section 6.2. These conservation issues are not simply of academic concern; in plasma physics, small errors in number conservation

can lead to large errors in the electric field, and small errors in energy can lead to significant errors when integrating for long time scales.

One way to recover the conservation properties of the physical equation is to introduce a weighting function $1/W$ into the definition of the error that is minimized by the DG scheme such that the weighting function cancels out the exponential weighting of the basis functions. For w in the same approximation space as f_h , the residual in the interval I_j is now chosen to satisfy

$$\int_{I_j} dv \frac{w}{W} \left(\frac{\partial f_h}{\partial t} + \frac{\partial g(f_h)}{\partial v} \right) = 0. \quad (6.11)$$

To be pedantic, the resulting system of equations is

$$\begin{aligned} \int_{I_j} dv \frac{w}{W} \frac{\partial f_h}{\partial t} &= \int_{I_j} dv \frac{\partial}{\partial v} \left(\frac{w}{W} \right) g(f_h) - \hat{g} \left(f_h \left(v_{j+\frac{1}{2}}, t \right) \right) \frac{w(v_{j+\frac{1}{2}}^-)}{W(v_{j+\frac{1}{2}}^-)} \\ &\quad + \hat{g} \left(f_h \left(v_{j-\frac{1}{2}}, t \right) \right) \frac{w(v_{j-\frac{1}{2}}^+)}{W(v_{j-\frac{1}{2}}^+)}. \end{aligned} \quad (6.12)$$

Equation (6.12) will be referred to in this chapter as the *conservative exponentially weighted DG method*.

When approximating f using the forms in (6.7) or (6.8), the weighting functions to restore the conservation properties are respectively

$$W_\mu = \alpha_0 \exp(-\alpha_1 \mu), \quad (6.13)$$

$$W_{v_\parallel} = \beta_0 \exp \left(-\beta_1 \frac{(v_\parallel - \beta_2)^2}{2} \right). \quad (6.14)$$

The resulting numerical scheme is considered a Petrov-Galerkin scheme, in which the test function w is not in the same approximation space as the solution f_h , by interpreting w/W to be the test function.

More generally, this procedure can be used to design conservative numerical schemes that represent the solution using polynomials weighted by some non-polynomial function (e.g., a power law) $W_j(v)$ in cell j as:

$$f_h(v, t) = \sum_{k=1}^N f_j^k(t) \psi_j^k(v) = \sum_{k=1}^N f_k(t) W_j(v) P_k(v) \quad (6.15)$$

If one or both velocity space extents are to be located at $\pm\infty$, then $W(v)$ has the additional constraint that $W_j(v)P_k(v) \rightarrow 0$ as $v \rightarrow \pm\infty$ for all k in the boundary cells.

For certain conservation properties to be satisfied when using a non-polynomial approximation space, we modified the definition of the error norm minimized by the

DG method by introducing the non-polynomial weighting factor $1/W(v)$. This means that solutions of the conservative, non-polynomial DG method will have a higher (non-weighted) squared- L^2 -norm error than those of the non-conservative, non-polynomial DG method. In our numerical tests, however, we do not find this difference to be significant.

6.2 1D Collision Operator Tests

In this section, we study the evolution of a 1D distribution function represented using the exponentially weighted basis (6.8) in the presence of collisions only:

$$\frac{\partial f}{\partial t} = C[f]. \quad (6.16)$$

We choose to model collisions using the same-species Lenard–Bernstein collision operator (Lenard & Bernstein, 1958), which has the general nonlinear form

$$C[f] = \nu \frac{\partial}{\partial \mathbf{v}} \cdot \left[(\mathbf{v} - \mathbf{u}) f + v_t^2 \frac{\partial f}{\partial \mathbf{v}} \right], \quad (6.17)$$

where ν is a collision frequency and the variables $\mathbf{u} = \mathbf{u}(f)$ and $v_t^2(f)$ are chosen to ensure that the collision operator conserves momentum and energy. In addition to conserving number, momentum, and energy, this collision operator relaxes distributions to a Maxwellian. For simplicity, we have taken the transport coefficients that appear in the collision operator to be constants and neglected the velocity-dependence in the collision frequency in our tests. A complete treatment would involve the calculation of Rosenbluth potentials (Rosenbluth *et al.*, 1957). As an approximation to the Landau collision operator, the Lenard–Bernstein collision operator is better suited than the Krook model to model collisions in a plasma due to its Fokker–Planck form, which represents the dominance of small-angle scattering in plasmas.

We first investigate self-species collisions in the perpendicular velocity coordinate μ , the magnetic moment, which is equal to $mv_\perp^2/2B$ when the magnetic field is static and uniform and is commonly used as a velocity-space coordinate in gyrokinetics. Here, the collision operator has the form

$$C[f] = \nu \frac{\partial}{\partial \mu} \left[2\mu f + \mu_t \left(2\mu \frac{\partial f}{\partial \mu} \right) \right], \quad (6.18)$$

where ν is taken to be a constant and $\mu_t = \int d\mu \mu f / \int d\mu f = \langle \mu \rangle$. Number and energy are conserved in this system. Total energy conservation in the exact system

is obtained as

$$\begin{aligned}
\frac{d}{dt} n \langle \mu \rangle &= \frac{d}{dt} \int_0^\infty f \mu \, d\mu \\
&= \int_0^\infty \frac{\partial f}{\partial t} \mu \, d\mu \\
&= -2\nu n (\langle \mu \rangle - \mu_t) \\
&= 0,
\end{aligned} \tag{6.19}$$

where $n = \int d\mu f$. We have also made use of the assumption that $f \rightarrow 0$ as $\mu \rightarrow \infty$ to eliminate boundary terms. Numerically, the drag term is calculated using an upwind flux and the diffusive term is calculated using the recovery-based DG method of [van Leer & Nomura \(2005\)](#), in which the solution and its derivatives evaluated on a boundary are found through the recovery of a smooth solution that spans the two neighboring cells (see Section 2.3). We compare the performance of linear ($k = 1$) polynomial basis functions with exponentially weighted linear polynomial basis functions, both of which have two degrees of freedom per cell.

Time stepping is performed using the third-order SSP Runge–Kutta method (2.32)–(2.34). Zero-flux boundary conditions are applied at $\mu = 0$ and $\mu = \mu_{\max}$ for a piecewise-polynomial representation and at $\mu = 0$ for a exponentially weighted-polynomial representation. In the grid for exponentially weighted basis, there is a cell that extends to infinity, so no boundary conditions are required there. The velocity-space domain used for the polynomial case is $\mu \in [0, 18\mu_t]$ and the grid used for the exponentially weighted cases is $\mu \in [0, \infty)$, with the last cell covering the interval $[18\mu_t - \Delta\mu, \infty)$. We use normalized values of $\mu_t = 1$ and $\nu = 1$. The exponential weighting factors were fixed to be $\alpha_{0,j} = 1$ and $\alpha_{1,j} = 1$ in every cell.

We set the initial condition to the projection of $f(\mu, t = 0) = H(\mu - \mu_0)$ onto the respective basis functions, where $H(\mu)$ is the Heaviside step function, and we evolve the solution to a steady state. One can quickly verify that the exact steady-state solution to (6.18) is $f \propto e^{-\mu/\mu_t}$. Figure 6.2 compares the steady-state distribution function (plotted at $t = 2$) for various DG algorithms with the exact solution, using the same grid resolution and amount of data ($N_\mu = 8$ and two degrees of freedom per cell) to represent the numerical solution in each case. It is apparent that the exponentially weighted polynomials in the form of (6.8) result in a more accurate representation of the solution than standard polynomials when compared to the exact solution. The polynomial solution also exhibits negative overshoots at cell edges, which can cause numerical difficulties and violates the realizability of the distribution function. We note that despite using numerical methods that minimize different error norms, the conservative and non-conservative exponentially weighted solutions are quite visually similar.

There are, however, serious conservation issues using the exponentially weighted representation of (6.8) with the standard DG algorithm (6.5). These conservation issues are shown in figure 6.3, which plots the relative error in number and in energy vs. time for the three numerical methods considered. We see that the exponentially weighted representation paired with the standard DG algorithm does not conserve

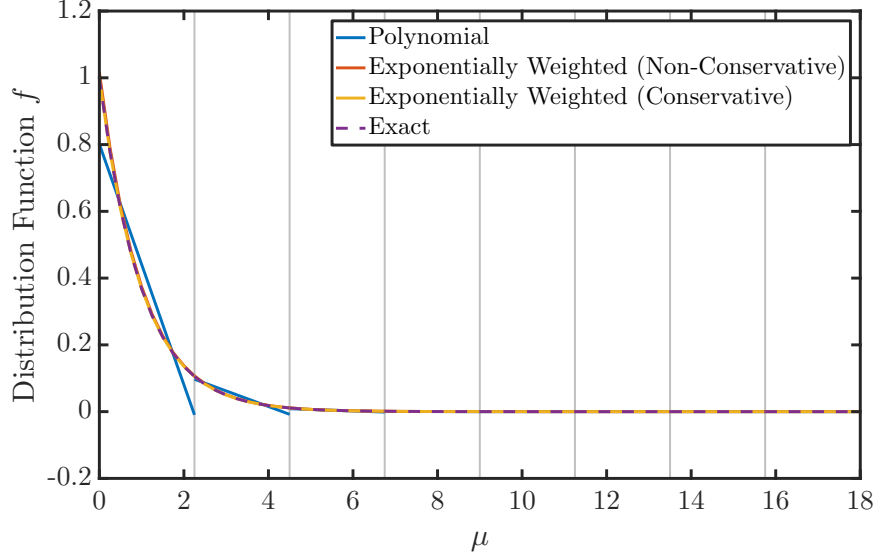


Figure 6.2: Comparison of the steady-state solutions to a collision operator test in μ using three DG methods. The methods used are standard DG with polynomial basis functions ($k = 1$), standard DG with exponentially weighted basis functions, and conservative DG with exponentially weighted basis functions. The exact steady-state solution $f = e^{-\mu}$ is indicated in the dashed purple line. The initial condition is a top-hat distribution, and the solution to (6.16) at $t = 10$ is plotted. The exponentially weighted solutions and the exact steady-state solution all lie on top of each other in the plot, while the equivalent linear-polynomial solution exhibits some negative overshoots at cell edges (indicated by vertical lines).

number or energy, and the degree of non-conservation is quite severe. The piecewise-polynomial representation is able to conserve number and energy to relative errors of order $\mathcal{O}(10^{-14})$, but the exponentially weighted representation only conserves number and energy to relative errors of order $\mathcal{O}(10^{-2})$. While one might think that conservation errors of $\mathcal{O}(10^{-2})$ are tolerable, small errors in charge conservation lead to large errors in the electric field in plasmas.

We verify in this numerical example that introducing a $1/W$ weighting from (6.13) allows one to recover the same machine-precision level of number and energy conservation as using the standard piecewise-polynomial representation of the distribution function. Additionally, the conservative exponentially weighted representation is a much more accurate representation of the exact steady-state solution than the polynomial representation when compared to the exact steady-state solution.

For collisions in v_{\parallel} , the collision operator is

$$C[f] = \nu \frac{\partial}{\partial v_{\parallel}} \left((v_{\parallel} - u_{\parallel}) f + v_t^2 \frac{\partial f}{\partial v_{\parallel}} \right). \quad (6.20)$$

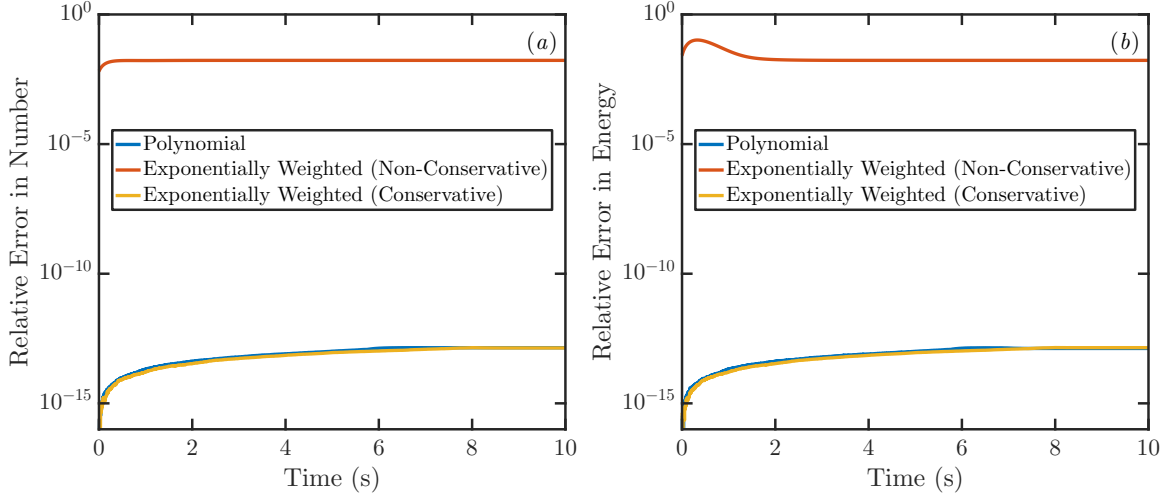


Figure 6.3: Comparison of the (a) number and (b) energy-conservation properties of various DG methods using polynomial and exponentially weighted basis functions for a collision-operator test in μ . The relative error is plotted for each quantity as a function of time. The use of exponentially weighted basis functions in the standard DG approach leads to unacceptable levels of error in total number and total energy, while a conservative DG method that uses exponentially weighted basis functions is obtained with use of an appropriate weighting function as in (6.12).

The initial condition used in these tests is the projection of

$$f(v_{\parallel}, t = 0) = \frac{H(v_{\parallel} + \sqrt{3}v_t) - H(v_{\parallel} - \sqrt{3}v_t)}{2\sqrt{3}v_t} \quad (6.21)$$

onto the respective basis functions. The grid has $N_{v_{\parallel}} = 8$ cells and $v_{\parallel} \in [-6v_t, 6v_t]$ for the polynomial case and $v_{\parallel} \in (-\infty, \infty)$ for the exponentially weighted case, with the boundary cells on the intervals $(-\infty, -6v_t + \Delta v_{\parallel}]$ and $[6v_t - \Delta v_{\parallel}, \infty)$. We also set $v_t = 1$ and $\alpha = 1$ for these simulations. We do not plot the results for the non-conservative DG method with exponentially weighted basis functions for simplicity. Figure 6.4 shows the steady-state solutions of the standard DG method with quadratic polynomials and the conservative DG method with exponentially weighted quadratic polynomials. The number, momentum, and energy-conservation properties of the two DG methods are shown in figure 6.5. As expected, both DG methods have similar machine-level conservation errors.

6.3 A Classical-Heat-Transport Problem

Next, we benchmark the performance of exponentially weighted basis functions using a 1D test problem in v_{\parallel} motivated by the classical Braginskii procedure for calculating heat conduction in a plasma (analogous to the Hilbert–Chapman–Enskog procedure in a gas). We solve an equation in the high-collision-frequency regime, so the use of

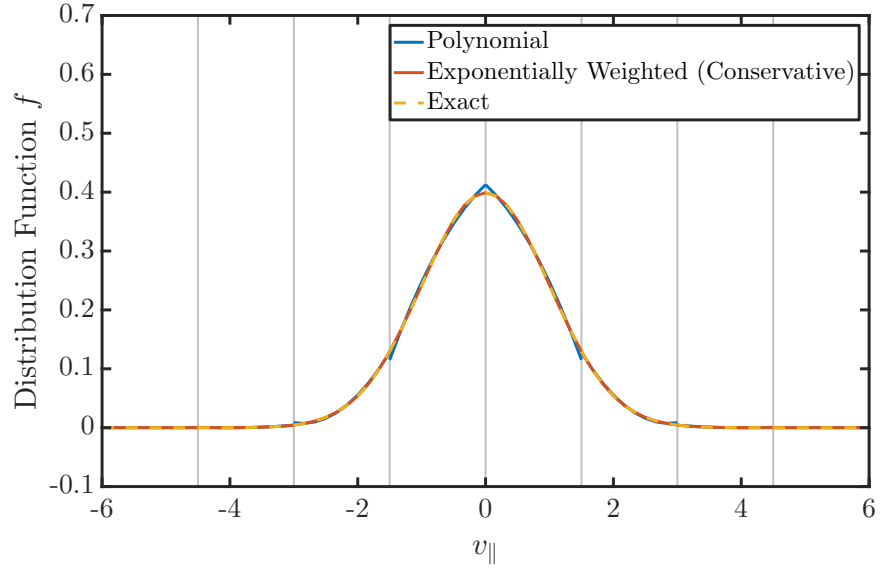


Figure 6.4: Comparison of the steady-state solutions to a collision operator problem in v_{\parallel} using two DG methods. The two methods used are standard DG with quadratic polynomial basis functions and conservative DG with exponentially weighted basis functions. The exact steady-state solution $f = e^{-v_{\parallel}^2/2}/\sqrt{2\pi}$ is indicated in the dashed yellow line. The initial condition is a top-hat distribution function, and the solution to (6.16) at $t = 10$ is plotted.

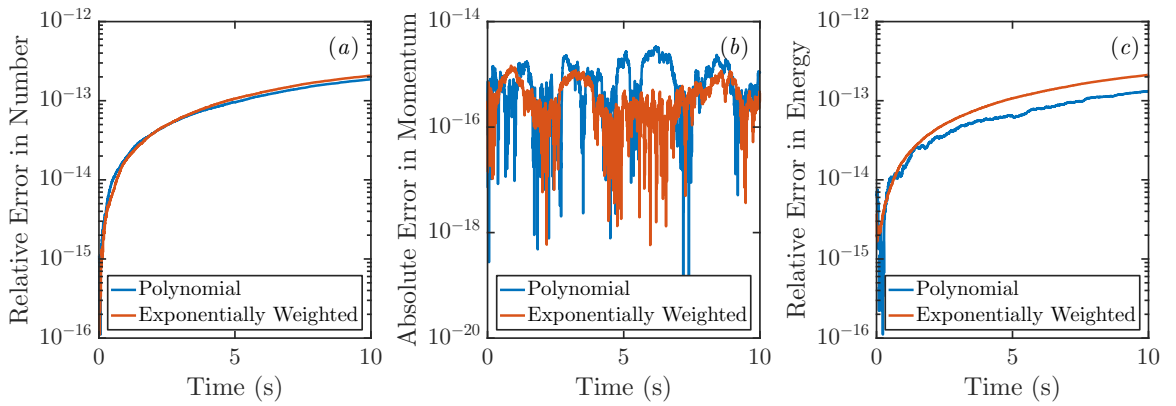


Figure 6.5: Comparison of the number, momentum, and energy-conservation properties of conservative DG methods using quadratic-polynomial and exponentially weighted basis functions for a collision-operator test in v_{\parallel} . (a) shows the relative error in number, (b) shows the absolute error in momentum, and (c) shows the relative error in energy. As expected, the analytically conserved quantities are also conserved by these numerical methods.

the exponentially weighted basis functions is appropriate. A source term is added to the equation to drive the solution to a non-Maxwellian.

Our starting point is the following kinetic equation for the distribution function $f(z, v_{\parallel}, t)$ in a 2D phase space:

$$\frac{\partial f}{\partial t} + v_{\parallel} \frac{\partial f}{\partial z} = C[f] \quad (6.22)$$

We have neglected electric and magnetic fields, but retained the behavior of small-angle collisions that occur in a plasma through the use of a Lenard–Bernstein collision operator. If we were modeling a gas, where large-angle scattering events are dominant, the use of a Krook-type collision operator would be more appropriate.

The standard Chapman–Enskog-type procedure assumes that the collision frequency is large $\nu \sim 1/\epsilon$, so the collision operator is the largest term, and expands $f = f_0 + f_1 + \dots$. To lowest order, $C[f_0] = 0$, so f_0 is a local Maxwellian of the form

$$f_0(z, v_{\parallel}) = f_M(z, v_{\parallel}) = \frac{n(z)}{\sqrt{2\pi v_t^2(z)}} \exp\left(-\frac{(v_{\parallel} - u_{\parallel})^2}{2v_t^2(z)}\right). \quad (6.23)$$

The temperature $T(z)$ is related to $v_t^2(z)$ as $v_t^2(z) = T(z)/m$, where m is the particle mass.

To next order, one gets

$$\frac{\partial f_0}{\partial t} + v_{\parallel} \frac{\partial f_0}{\partial z} = C[f_1]. \quad (6.24)$$

We assume that there are background temperature and density gradients in f_0 and that these two parameters can be related by invoking local pressure balance $\partial p / \partial z = \partial(nT) / \partial z = 0$. We can then rewrite the kinetic equation as

$$\frac{\partial f_0}{\partial t} + \frac{v_{\parallel}}{L_T} \left(\frac{v_{\parallel}^2}{2v_t^2} - \frac{3}{2} \right) f_0 = C[f_1], \quad (6.25)$$

where $L_T = T / (\partial T / \partial z)$ is the strength of the local background-temperature gradient.

For simplicity, we turn this 2D equation into a 1D equation at a single value of z with a specified input value of L_T . Since the collision operator vanishes on f_0 , we can write the right-hand side of (6.25) as $C[f_1] \rightarrow C[f]$, where $f = f_0 + f_1$. In the high-collision-frequency, short-mean-free-path limit, $f_1 \ll f_0$, we can replace f_0 on the left-hand side of (6.25) with f . The 1D model can then be written as

$$\frac{\partial f}{\partial t} = C[f] - \frac{v_{\parallel}}{L_T} \left(\frac{v_{\parallel}^2}{2v_t^2} - \frac{3}{2} c_1 \right) f. \quad (6.26)$$

The time-dependent coefficient $c_1 = 1$ for an exact Maxwellian and must be adjusted in the simulations to ensure that the second term on the right-hand side of (6.26) injects no momentum, as the numerical f_0 can have deviations from the exact

Maxwellian:

$$\int_{-\infty}^{\infty} \frac{v_{\parallel}^2}{L_T} \left(\frac{v_{\parallel}^2}{2v_t^2} - \frac{3}{2} c_1 \right) f \, dv_{\parallel} = 0. \quad (6.27)$$

In practice, $c_1 \approx 1$. Since the initial condition for f is chosen to have zero momentum and there is no momentum source in the system, we set $u_{\parallel} = 0$ in the collision operator (6.20). As in the previous section, we set $v_t = 1, m = 1, n = 1$, and $\nu = 1$, but one should make ν depend on velocity in future work for a more realistic model of plasma collisions. The initial condition $f(v_{\parallel}, t = 0)$ is the projection of $f_0(v_{\parallel})$ onto the respective polynomial or exponentially weighted basis functions. We also choose $T/L_T = 10^{-5}$.

The goal of this test problem is to solve (6.26) to a steady state and calculate the heat flux $q = \int dv_{\parallel} mv_{\parallel}^3 f / 2$, which can then be compared with the analytical solution. A prediction for the heat-flux profile $q(t)$ in the high-collision-frequency, small- f_1 limit can be obtained by multiplying (6.26) by $mv_{\parallel}^3/2$ (taking $c_1 = 1$) and integrating over v_{\parallel} . The result is

$$q(t) = \frac{nv_t^2}{2\nu} \frac{T}{L_T} (e^{-3\nu t} - 1). \quad (6.28)$$

Figure 6.6 shows a comparison of the heat flux $q(t)$ evolution for simulations using linear polynomials and exponentially weighted linear polynomials to represent the distribution function. Here, the grid extents are kept fixed at $[-8v_t, 8v_t]$ for polynomials and $(-\infty, \infty)$ for exponentially weighted polynomials, and the number of cells are varied. All three of the exponentially weighted solutions plotted in figure 6.6 are extremely close to the exact solution, while the polynomial simulation needs to use 32 cells in velocity space to achieve similar levels of accuracy. Additionally, the heat flux has an incorrect sign and magnitude for the lowest-resolution (8 cells) case that uses polynomials.

Figure 6.7 shows a comparison of the relative error in the quantity $q(t = 10)$ using three numerical methods versus effective grid size. The three numerical methods considered are standard DG with linear polynomials, conservative DG with exponentially weighted linear polynomials, and a standard second-order finite volume method. Since the DG methods in figure 6.7 store two pieces of data per cell while the finite-volume method stores only one, the relative error is plotted versus $\Delta v_{\text{avg}} = \Delta v_{\text{cell}}/N_{\text{nodes}}$ to compare the numerical methods on a common footing. The velocity-space domain is $v_{\parallel} \in [-8v_t, 8v_t]$ for the standard DG and finite volume methods. Since the outermost cells of the velocity space domain extend to $\pm\infty$, the effective cell width for the conservative exponentially weighted DG method is computed using only the interior cells. The leftmost cell has domain $v_{\parallel} \in [-\infty, -8v_t + \Delta v_{\parallel}]$ and the rightmost cell has domain $v_{\parallel} \in [8v_t - \Delta v_{\parallel}, \infty]$. For both DG methods, the total number of cells range from 4 to 72 cells.

Figure 6.7 demonstrates that exponentially weighted polynomials are $\sim 10^2$ times more accurate than polynomials at the same resolution in calculating the heat flux.

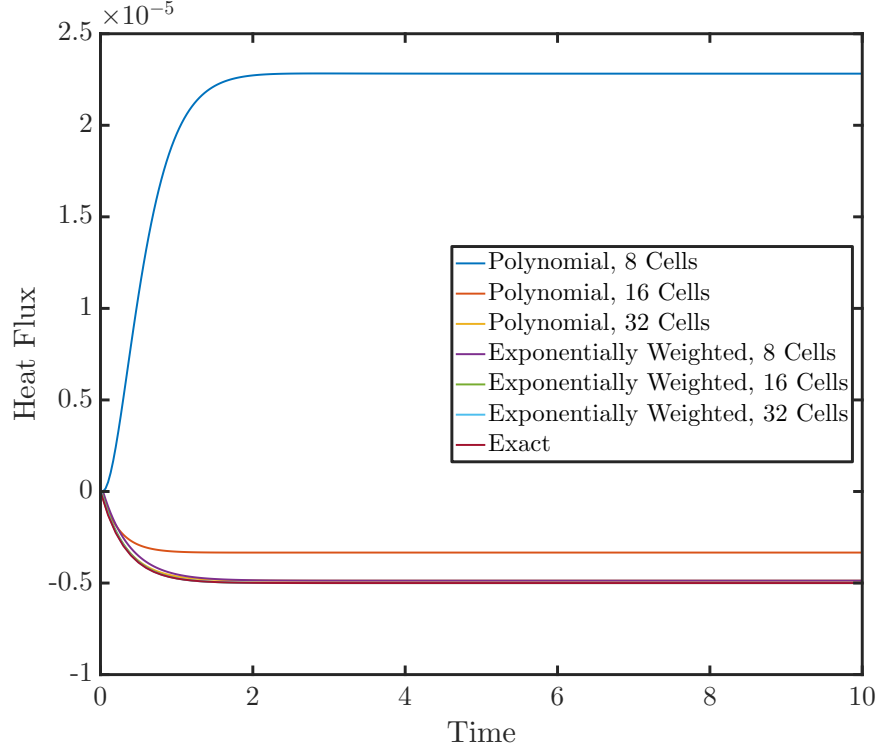


Figure 6.6: Time evolution of the heat flux in simulations using polynomial and exponentially weighted polynomials at various grid resolutions. The exact solution is given in (6.28). While all the simulations using exponentially weighted polynomials have a $q(t)$ trace that is close to the exact solution, 32 cells are required for the simulation using polynomials to achieve a similar level of accuracy. Additionally, the heat flux has the wrong magnitude and sign for one of the polynomial cases performed on a coarse grid.

For the same level of error, one can use ~ 8 times fewer cells in v_{\parallel} using exponentially weighted polynomials instead of standard piecewise polynomials. For problems in (v_{\parallel}, μ) coordinates used in gyrokinetics, one could potentially see a factor of 10 speedup using exponentially weighted basis functions, accounting some for the additional complexity of using these exponentially weighted basis functions.

We attribute the large difference between the exponentially weighted and polynomial methods in the heat flux calculation to the need to represent the tails of the distribution accurately, as the heat-flux integrand scales as $v_{\parallel}^6 f_M$ for a velocity-independent collision frequency. Figure 6.8 shows that the dominant contribution to the heat-flux integral comes from the tail of the distribution function rather than the bulk. The need to resolve the tail accurately is even greater in three velocity dimensions, in which case the heat-flux integrand scales as $v^{11} f_M$ when the collision frequency scales as v^{-3} . If one is restricted to representing the distribution function using piecewise polynomials, a fine resolution in the tails and a large v_{\max} are both needed for the accurate evaluation of these heat-flux integrals.

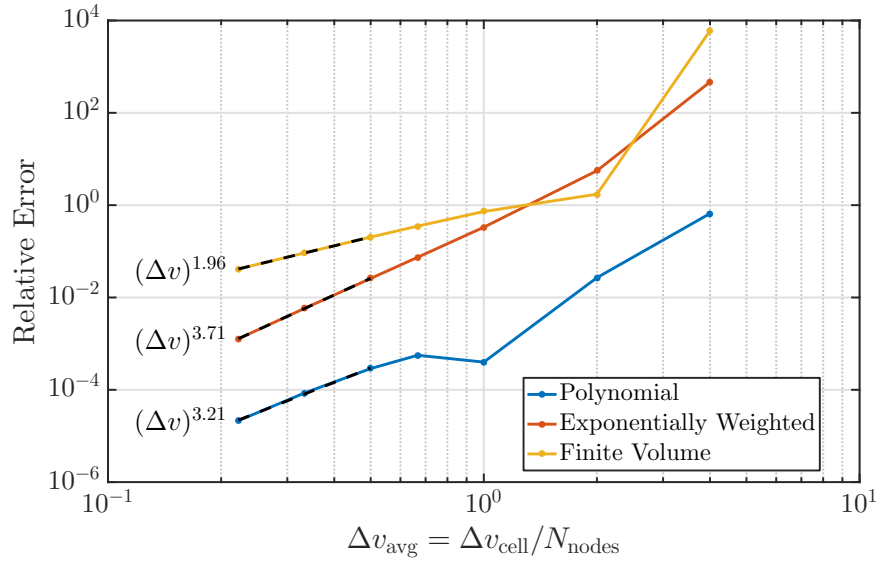


Figure 6.7: Relative error in the steady-state heat flux (computed at $t = 10$) versus effective cell size for various numerical methods. Here, $v_{\max}=8v_t$ for the polynomial and finite volume methods. The numerical methods plotted are standard DG with linear polynomials, conservative DG with exponentially weighted linear polynomials, and a standard second-order finite-volume method.

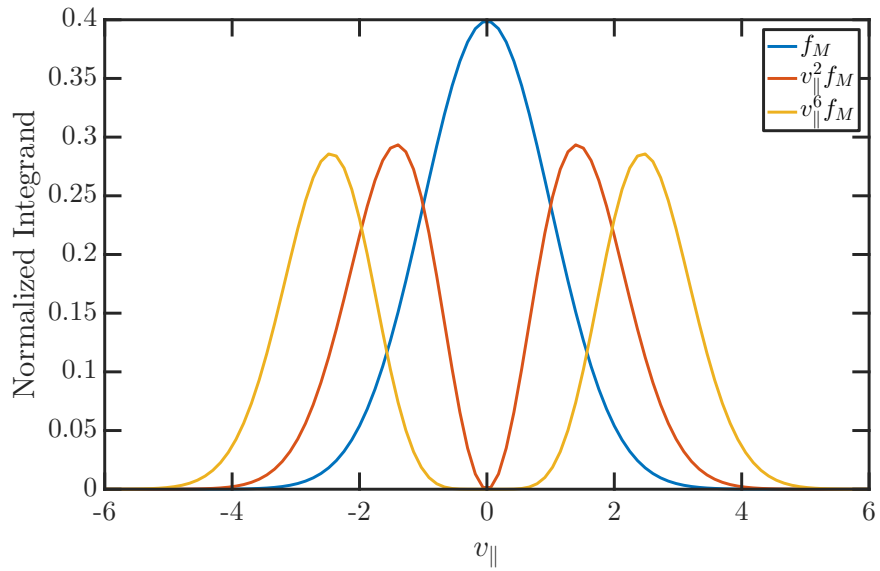


Figure 6.8: Illustration of the normalized integrands for the calculation of a few moments of a Maxwellian distribution. For an accurate evaluation of the heat flux, which has an integrand that scales as $v_{\parallel}^6 f_M$ in the test problem considered in this section, good resolution in the tails of the distribution function is required. Exponentially weighted polynomials appear to be able to use fewer pieces of data to resolve the distribution function tails to a certain level of accuracy when compared to standard polynomials.

6.4 Adjustment of the Exponential Weighting Factor

In our tests, we selected the free parameters (the exponential weighting factor) of our basis functions based on knowledge of the analytical solution and required that every cell use the same values for these parameters. In practice, these constraints would make the use of exponentially weighted basis functions impractical for many problems of interest in which the background temperature changes over time or the solution develops non-Maxwellian features. As the solution in each cell changes in time, it is also important for the exponential weighting factor in each cell to adjust so that the basis functions can continue to accurately represent the solution.

We propose a method to adjust the free parameters that determine the approximation space defined on the interval I_j based on the numerical solution in the same interval. Essentially, we determine the new parameters such that all of the polynomial variation in a cell is put into the exponential weighting factor. Equivalently, we find a Maxwellian in a cell that has the same number momentum, and energy (or just number and energy in μ coordinates) as the solution-to-be-projected. This procedure can be used to determine the initial values of the basis function parameters and also to change from one approximation space to another at the end of each time step. To reduce the computational expense of this procedure, the adjustment of the exponential weighting factor can be performed at regular intervals consisting of several time steps.

One advantage of this procedure is that the solution in the new approximation space is already known once the new basis function parameters have been determined. The methods proposed in [Yuan & Shu \(2006\)](#) require a stage to solve for the new parameters and another stage to project the solution from the old approximation space to the new one. Additionally, the 1D approximation spaces considered by ([Yuan & Shu, 2006](#)) only had one free parameter per cell, and the adjustment procedure proposed by the authors does not easily generalize to multiple free parameters.

If one represents the solution using (6.7), the parameters $\beta_{0,j}$, $\beta_{1,j}$, and $\beta_{2,j}$ can be found by solving the nonlinear system using common root-finding methods:

$$\int_{I_j} dv_{\parallel} \beta_{0,j} \exp\left(-\beta_{1,j} \frac{(v_{\parallel} - \beta_{2,j})^2}{2}\right) = \int_{I_j} dv_{\parallel} f \quad (6.29)$$

$$\int_{I_j} dv_{\parallel} \beta_{0,j} \exp\left(-\beta_{1,j} \frac{(v_{\parallel} - \beta_{2,j})^2}{2}\right) v_{\parallel} = \int_{I_j} dv_{\parallel} f v_{\parallel} \quad (6.30)$$

$$\int_{I_j} dv_{\parallel} \beta_{0,j} \exp\left(-\beta_{1,j} \frac{(v_{\parallel} - \beta_{2,j})^2}{2}\right) v_{\parallel}^2 = \int_{I_j} dv_{\parallel} f v_{\parallel}^2. \quad (6.31)$$

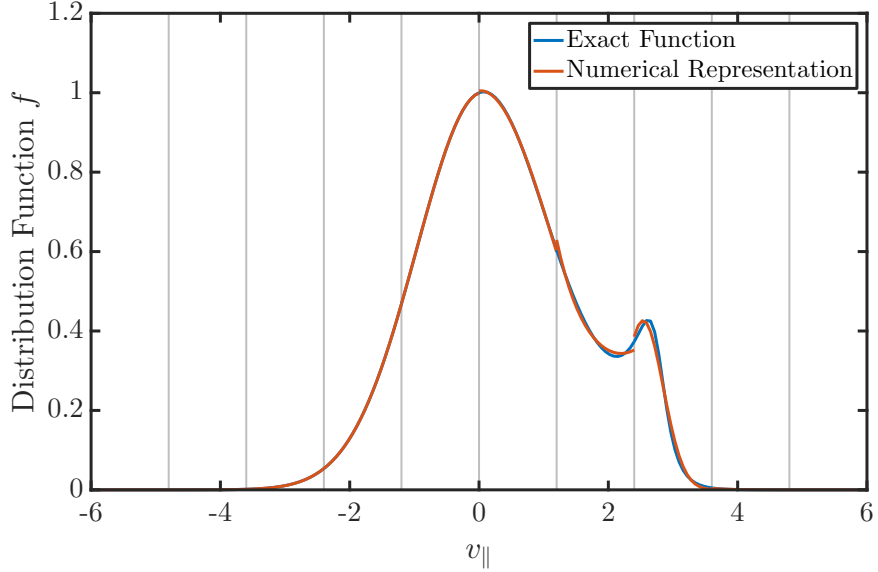


Figure 6.9: Calculation of an exponentially weighted approximation space from a specified initial condition. The red curve is the result of a nonlinear solve in each cell to determine the local approximation space such that the local solution can be represented solely as a Maxwellian (specified by three parameters). The blue curve is the initial condition for the calculation, given as (6.32). This procedure can also be employed to automatically adjust the exponentially weighted basis functions in a time-dependent calculation so that the basis functions can continue to provide an accurate representation of the solution.

Figure 6.9 presents an example of applying this procedure to calculate the initial approximation space given the analytical initial condition

$$f(v_{\parallel}) = \exp\left(-\frac{v_{\parallel}^2}{2}\right) \left(1 + \frac{0.5v_{\parallel}}{(2.75 - v_{\parallel})^2 + 0.3^2}\right). \quad (6.32)$$

This test demonstrates both the ability of exponentially weighted polynomials to represent strongly non-Maxwellian features and the feasibility of a procedure to determine the exponential weighting factor automatically.

The procedure for an algorithm that uses conservative exponentially weighted polynomials for time-dependent problems can be summarized as:

1. Calculate the initial parameters from the initial condition. This procedure determines both the initial approximation space M_h^0 and the initial numerical solution $f(t_0) \in M_h^0$.
2. With the solution $f(t_n) \in M_h^n$ known at time t_n , calculate the preliminary numerical solution $f(t_{n+1}) \in M_h^n$ (such as by using a standard multi-stage Runge–Kutta method).

3. Find the approximation space M_h^{n+1} to better represent the solution using the same procedure that determined the initial basis function parameters. By construction, $f(t_{n+1}) \in M_h^{n+1}$ is also found at the same time. To save computational time, the adjustment procedure can be performed after regular intervals consisting of several time steps.
4. Repeat Steps 2 and 3 above until the final time.

We recognize that some or even all of the savings in computation time from being able to use a coarser grid are lost due to the additional complexity of using time-dependent, exponentially weighted basis functions. Gaussian quadrature points and weights must be recomputed every time the free parameters are adjusted, which requires evaluations of the $\text{erf}(x)$ function. Additionally, one must be mindful to compute the correct quadrature rule. When using piecewise polynomials, one typically uses Gauss-Legendre quadrature for the calculation of integrals:

$$\int_{-1}^1 f(x) dx \approx \sum_{i=1}^n w_i f(x_i), \quad (6.33)$$

where n is the number of quadrature points, which is generally equal to the number of local basis functions. The quadrature rule is exact when $f(x)$ is a polynomial of degree $2n - 1$ or fewer. For conservative exponentially weighted DG, the quadrature rule must now satisfy

$$\int_{-1}^1 W(x)f(x) dx \approx \sum_{i=1}^n w'_i f(x'_i), \quad (6.34)$$

where $W(x)$ is the local exponentially weighted weighting function. The quadrature rules for the weights in (6.13) and (6.14) are straightforward to derive (Press *et al.*, 2007) and can be worked out as a function of the basis function parameters in advance, since n in a DG method is a small, $\mathcal{O}(1)$ number in practice.

6.5 Conclusions

We have developed a conservative discontinuous Galerkin method that uses an approximation space consisting of exponentially weighted polynomials for the efficient representation of distribution functions in the presence of collisions. While the velocity-space domain must be truncated when using standard polynomials, the velocity-space domain can be extended to $\pm\infty$ in the exponentially weighted polynomial approach. The lack of number and energy conservation when one uses exponentially weighted basis functions in the approach of Yuan & Shu (2006) was demonstrated in a test problem with a collision operator with a Fokker-Planck form. We fixed this issue through the addition of a corresponding exponential weighting factor in the error norm used for the DG method and showed numerically that the desired conservation properties are preserved.

We studied a Spitzer–Härm problem involving the accurate calculation of heat fluxes in 1D with an additional source term to drive the solution non-Maxwellian. We demonstrated that conservative, exponentially weighted polynomials produced results that were $\sim 10^2$ times more accurate than standard piecewise polynomials at the same grid resolution. Conservative, exponentially weighted polynomials achieved the same level of relative error as polynomials on a ~ 8 times coarser grid. We attributed these results to the ability of the exponentially weighted representation to better capture the variation in the distribution function tails when compared to a piecewise-polynomial representation. Lastly, we outlined a local procedure to determine the exponentially weighted approximation space in each element, which adds to the computational cost of this method but makes it much more robust and applicable to practical problems in which an accurate exponential weighting factor cannot be determined in advance.

While we have focused on exponentially weighted polynomials in this work, we recognize that our procedure can more generally be used with other types of non-polynomial-weighted basis functions for applications in which exact conservation is needed or velocity-space truncation is not desired. For example, it might be more useful to use polynomials weighted by a power law x^{-a} for cosmic-ray problems or radio-frequency-heating problems in fusion with a quasilinear operator. We have also limited our analyses to cases in which the solution in every velocity-space element was expanded in a similar conservative, exponentially weighted basis. It may be advantageous to use a mixed representation consisting of standard polynomials in the bulk of the distribution ($|v| < v_c$) and conservative exponentially weighted polynomials in the tails ($|v| > v_c$). Future work could also explore efficient ways to employ a non-uniform velocity grid spacing, as we have restricted our attention to velocity space cells of uniform width in this work. For application to 5D gyrokinetic simulations, it is also important to generalize the use of these 1D basis functions to higher dimensions, such as $(x, y, z, v_{\parallel}, \mu)$.

For finite-volume or finite-difference codes, one could consider somewhat related exponential interpolation methods instead of simple linear interpolation as is usually done. This would be different than the Chang–Cooper algorithm (Chang & Cooper, 1970), which looks at the ratio of the drag and diffusion coefficients to set the degree of upwind differencing in order to get the correct equilibrium solution. This procedure will not give exact conservation of higher moments like energy (for which one might add small correction terms similar to the recent work of Taitano *et al.* (2015)), but it could help improve the accuracy of the results, allowing coarser grids for the same level of accuracy.

Chapter 7

Summary and Future Directions

7.1 Summary

This thesis presented several advances towards a gyrokinetic-continuum-simulation capability for the boundary plasma. The main contribution was the development of the first gyrokinetic continuum simulations of turbulence in straight (Chapter 4) and helical (Chapter 5) open-field-line plasmas. Prior efforts to include this capability in a gyrokinetic continuum code appeared to have run into difficulties with number conservation, energy conservation, or sheath-boundary-condition stability. The simulations in this thesis solved gyrokinetic equations in an electrostatic long-wavelength (drift-kinetic) limit, which will be replaced with more general gyrokinetic equations in the future. To address potential conservation issues, we needed to evaluate, generalize, and extend existing discontinuous Galerkin (DG) algorithms for application to the gyrokinetic system (Chapter 2). This work also appears to be the first application of DG methods to numerically solve a gyrokinetic system, and we hope that the documentation of the issues that we ran into will be useful in the development of other codes for various applications, including gyrokinetic continuum and particle-in-cell (PIC) codes for edge and scrape-off-layer (SOL) simulations. A key algorithm in our numerical approach is an extension of a DG algorithm for 2D incompressible flow ([Liu & Shu, 2000](#)) to general Hamiltonian systems, which we showed conserves number and energy. To model the mediating effects of the plasma sheath that cannot be resolved in gyrokinetics, we developed a kinetic analog of the conducting-wall boundary conditions used in some fluid and gyrofluid plasma simulations that allow fluctuations in the current to the wall, which we refer to as conducting-sheath boundary conditions.

We first implemented and evaluated DG algorithms for 1D1V (1 dimension in position space, 1 dimension in velocity space) simulations of the parallel propagation of an edge-localized-mode (ELM) heat pulse in the SOL using logical-sheath boundary conditions. We showed that our simulations could recover similar results to those obtained using a 1D1V Vlasov–Poisson code ([Havlíčková et al., 2012](#)) at a fraction of the computational cost (taking minutes to run instead of fifteen hours). Most of the savings in our simulations came from not having to resolve the restrictive time and length scales required in fully kinetic simulations. We later extended these simulations

to 1D2V with self-species collisions modeled by a Lenard–Bernstein collision operator, which improved the quantitative agreement with the 1D3V PIC simulations (with collisions) of Pitts *et al.* (2007); Havlíčková *et al.* (2012).

Having developed 1D1V and 1D2V models of the ELM heat-pulse problem, we then extended our kinetic equation solver to 2D2V, which we used to perform simulations of electron-temperature-gradient-driven (ETG) turbulence (not discussed in this thesis). For those simulations, we verified using parameter scans of the background temperature gradient in a periodic slab geometry that the correct linear growth rates were recovered and that nonlinearly saturated turbulent states were reached. Some initial 5D (3D2V) simulations of ETG turbulence were also performed to investigate basic code stability.

After we developed a 5D gyrokinetic solver (and A. Hakim parallelized his gyrokinetic-Poisson-equation solver), we generalized the logical-sheath boundary conditions that were implemented in our 1D1V and 1D2V simulations to 3D2V. We encountered stability issues with these boundary conditions in our simulations of the Large Plasma Device (LAPD), which could be thoroughly documented in a future paper. We found better success by generalizing a set of conducting-wall boundary conditions used in some prior fluid and gyrofluid simulations of open-field-line plasmas, which became the present set of sheath-model boundary conditions used in our model. The final barrier in the LAPD simulations was a way to deal with issues concerning the positivity of the distribution function, since this property was not automatically guaranteed in our algorithms. Our current solution to maintain the positivity was discussed in Section 2.4, which is not a fully satisfactory solution but appears to work well for current applications. The resulting simulations of LAPD turbulence appear qualitatively reasonable when compared to experimental data from the device and drift-reduced Braginskii fluid simulations from the Global Braginskii Solver (GBS) code (Chapter 4). While our LAPD simulations were intended as a way to gain confidence in our model and algorithms in a simplified, well-diagnosed open-field-line geometry, the gyrokinetic-simulation capability we have developed can eventually lead to improved modeling of LAPD experiments with the future addition of more accurate treatments of the plasma source and boundary conditions.

We later developed simulations of a helical SOL in an all-bad-curvature slab (Chapter 5) using parameters for a National Spherical Torus Experiment (NSTX) SOL, which is much less collisional than the plasmas in LAPD. Because of the additional interchange-instability mechanism, the radial turbulent transport in these simulations is much stronger and the overall turbulence character is qualitatively distinct when compared to our simulations of turbulence in LAPD. Initial analysis suggests that these simulations are in a sheath-connected regime, and so some qualitative features of these simulations might be well reproduced in isothermal 2D models. The helical SOL simulations are currently being applied to simulate turbulence in the Helimak device. This model will be used as a starting point for additional levels of sophistication on the path towards realistic boundary-plasma simulations spanning the SOL and the confined edge.

Finally, we developed a conservative DG method that employs exponentially weighted basis functions to discretize the velocity-space dependence of the distri-

bution function (Chapter 6). DG methods can be extended to use non-polynomial basis functions in a straightforward manner (Yuan & Shu, 2006), although such basis functions are rarely used in practice. We found that Yuan & Shu (2006) did not recognize potential conservation issues in using non-polynomial basis functions in a standard DG method, and we developed a Petrov-Galerkin approach that allows the use of discontinuous exponentially weighted basis functions and also conserves number, momentum, and energy. In a simple but non-trivial heat-flux benchmark, we demonstrated the potential savings of our conservative exponentially weighted DG method in reducing velocity-space resolution requirements when compared to the standard DG approach that uses polynomials to represent the solution. Generalization of this method to higher dimensions is left to future work.

7.2 Future Directions

We have made a number of simplifications to the simulations presented in this thesis, and it is important to increase the sophistication of the models and improve the design and implementation of the numerical methods used so that the code can eventually be applied to study relevant physics issues on present-day and future tokamaks. Of course, high priority should be placed in adding finite-Larmor-radius effects (e.g. gyroaveraging in the gyrokinetic Poisson equation and in the gyrokinetic equation). It will be interesting to explore how the turbulence in the helical-SOL model changes with the inclusion of finite-Larmor-radius effects when compared to our existing simulations for the long-wavelength (drift-kinetic) gyrokinetic system. Here, we discuss in more detail some other less-obvious priorities for near-term future work.

Distribution-function positivity. Since the numerical algorithm we use to solve the gyrokinetic equation does not automatically preserve the positivity of the distribution functions (either in a cell-average sense or everywhere within a cell), we currently apply a positivity-adjustment procedure (Section 2.4) at the end of every intermediate Runge–Kutta substage to remove the negative-valued portions of the distribution functions. This procedure usually results in a non-negligible source of particles and energy (approximately 10–20% of the fixed plasma sources). While the simulations discussed in this thesis appear to produce qualitatively reasonable results, it is highly desirable to modify the algorithms used in the code so that the extra source of particles and energy is greatly reduced or even eliminated. The current correction procedure is overly conservative because it prevents a piecewise-linear representation $f(x) = f_0 + f_1(x - x_j)$ from going negative anywhere within a cell, which restricts $|f_1|/f_0 < 1$, while there are physically realizable positive functions that have the same moments even if $|f_1|/f_0$ is somewhat larger than this. We are pursuing ideas to relax this constraint, which are related to the exponentially weighted basis-function approach explored in Chapter 6. These ideas are also related to positivity-preserving limiters and positivity-preserving fluxes used to preserve the positivity of cell-averaged quantities (Zhang, 2017; Zhang & Shu, 2010, 2011). Additional correction steps will be needed if the distribution function is required be positive everywhere within a cell, which is stricter than requiring

that cell averages are non-negative. We also note that there exists a large body of literature on positivity-preserving algorithms for finite-volume and DG methods (for example, see [Rossmannith & Seal, 2011](#)).

Code optimization. Although the simulations presented in this thesis were all performed using a reasonable amount of computational resources, it is important to honestly compare the computational cost of similar gyrokinetic simulations using different numerical methods. Specifically, a collaborative effort should be made among existing gyrokinetic codes under development for boundary plasma simulation to benchmark code performance on an agreed-upon test case. While we acknowledge that timing comparisons can be a sensitive topic, a major reason why this project was originally undertaken was to explore the potential of advanced continuum methods to provide cheaper gyrokinetic simulations of edge and SOL turbulence. Additionally, it is in the interests of the fusion-research community to know if one code requires orders of magnitude more resources to produce the same result as other codes to identify areas in need of algorithmic improvements. At present, the underlying DG algorithm is neither fully modal nor fully nodal in its implementation (see [Durran, 2010](#), Section 6.6), and consequently is unable to realize the full computational advantages of either approach. For example, the DG solution is represented using nodal basis functions, but the solution nodes are different from the Gauss–Legendre quadrature nodes. Therefore, interpolation matrices are required to evaluate the solution at quadrature nodes whenever numerical evaluation of integrals over the volume or a surface of an element is required. Future versions of the code should commit to implementing algorithms consistently in a nodal or modal sense. It is also crucial for future version of the code to exploit the well-known adaptive h (element size) and p (basis function degree) grid refinement and coarsening features of the DG method ([Remacle et al., 2003](#)) to dynamically adjust the grid so that memory can be used efficiently. The current approach uses a uniformly spaced grid with the same number of basis functions in each cell, which almost certainly wastes some data by using many pieces of information to resolve the distribution function in locations where such resolution is unneeded.

Open and closed-magnetic-field-line regions. As a first step towards increasing the complexity of the magnetic geometry, one should add to the code the ability to include a confined edge region consisting of closed magnetic field lines and a SOL region consisting of open magnetic field lines in the same simulation ([Ribeiro & Scott, 2008](#); [Halpern et al., 2016](#); [Dudson & Leddy, 2017](#)). The two regions are presumably distinguished only by the parallel boundary conditions on the distribution functions and potential. Periodic boundary conditions must be applied to the distribution function and potential on closed field lines and sheath-model boundary conditions are applied to the distribution function on open field lines. As in the purely open-field-line simulations, no parallel boundary conditions are required for the potential in the open-field-line region. This capability could enable studies concerning the effects of ion drift orbit excursions from the edge into the SOL on edge rotation ([Stoltzfus-Dueck, 2012](#)), radial-electric-field profiles, and SOL profiles.

Electromagnetic effects. One of the potential advantages of continuum methods over PIC methods discussed in Section 1.2.2 is the relative ease with which numerical problems in the implementation of electromagnetic effects can be handled (specifically, magnetic perturbations arising from the parallel magnetic potential A_{\parallel}). Electromagnetic simulations can still be challenging in some regimes for physics reasons regardless of the numerical approach taken. The root of this advantage appears to be the lack of sampling noise in continuum methods, which avoids the well-known Ampère’s law cancellation problem (Hatzky *et al.*, 2007) as long as the numerical integrations for the solution of the parallel magnetic potential are performed consistently¹ (Dannert & Jenko, 2004). While the direct cross-field transport of particles and heat due to magnetic fluctuations is generally negligible when compared to the cross-field transport due to the $E \times B$ drift (see references in Zweben *et al.*, 2007), magnetic induction slows the electron parallel dynamics, weakening the adiabatic electron response. A discussion of the dimensionless parameters to characterize the relative importance of collisional, inertial, and inductive processes in strengthening the non-adiabatic electron response can be found in Scott (2003, 2007a); Ribeiro & Scott (2008). For typical edge-plasma parameters, electromagnetic effects lead to stronger turbulence in simulations (Scott, 2007a, 1997, 2003; Scott *et al.*, 2010). In addition to the physics studies it would enable, a demonstration that electromagnetic effects can be handled in a stable and efficient (i.e., without increasing the computational cost by an order of magnitude or larger) manner for open-field-line gyrokinetic-turbulence simulations would be a significant achievement.

Sheath-model boundary conditions. As discussed in Section 2.5, the only boundary conditions that are applied to the ions at the sheath entrance are zero-inflow boundary conditions. Otherwise, ions freely flow out of the domain, and there is no mechanism in the ion boundary conditions to ensure that the Bohm sheath criterion is satisfied. While there might not be much difference between ion outflow at thermal velocities instead of at the ion sound speed for typical SOL parameters because T_i is typically a few times larger than T_e , this issue might be more of an issue in achieving quantitatively correct simulations of basic-plasma-physics experiments. In XGCa gyrokinetic simulations of a DIII-D SOL (Churchill *et al.*, 2016), the authors observed subsonic ion flows at the sheath entrance with a Mach number typically 0.4–0.7, but argued that the standard Bohm-sheath-criterion result was inapplicable. Future work should develop a set of sheath-model boundary conditions for ions that includes the effects of the rarefaction fan (Munz, 1994) that accelerates ions to sonic outflow speeds if the Bohm sheath criterion is not satisfied. Such an improvement would benefit both continuum and PIC codes that use sheath-model boundary conditions.

Other important additions to the code that are only mentioned in passing here include a Rosenbluth–Fokker–Planck (Rosenbluth *et al.*, 1957; Taitano *et al.*, 2015)

¹This solution was first presented by G. Hammett and F. Jenko in presentations at the Plasma Microturbulence Project meeting at General Atomics on July 25, 2001 (see Chen & Parker, 2003, footnote 13).

or Fokker–Planck–Landau collision operator, realistic magnetic geometry (including the X-point), neutral and impurity-species modeling, and atomic-physics modeling. As discussed in Chapter 1, the fusion-energy community has recognized a need for a first-principles gyrokinetic-simulation capability for the boundary plasma (Ricci, 2015; Boedo *et al.*, 2009; Cohen & Xu, 2008). We hope that our contributions will accelerate the development of predictive gyrokinetic continuum codes for modeling the boundary plasma of and improving the performance of future devices.

Appendix A

Plot Creation

Several 1D and 2D plots are presented in this thesis to illustrate simulation results. No data interpolation (estimation) is used, such as when plotting DG solutions versus position. This is because DG methods expand the solution in terms of predetermined basis functions, a topic which is covered in Chapter 2. With the degrees of freedom known in a cell, the solution can be evaluated exactly at an arbitrary number of points within the same cell. For plotting scalar data versus two position coordinates. e.g. the electron density in the x - y plane, we generally evaluate the solution on an 8×8 grid of equally spaced points in each cell.

Figure A.1 illustrates the procedure through which a 2D plot of a DG solution is created for visualization in post processing. We start with the full DG solution in figure A.1(a), where the full solution in two cells sharing a common boundary are shown. Our goal is to create a matrix from this data that can be used to create an image, in which the value of row i and column j in the matrix specifies the color of the pixel at row i and column j in the image.

Having decided on the resolution of the image we want to generate, we divide up each cell into a number of subcells, which is shown in figure A.1(b). In this example, we divide up each cell into a finer grid of 8×8 cells. Each subcell will each correspond to a single pixel in the final image. The value of the DG solution in the center of each subcell is evaluated without approximation using knowledge of the basis functions and stored into a matrix. Each value of this matrix is then assigned a particular color to each pixel according to a color map. With the image matrix filled out, we can use standard plotting packages to generate an image from this data. In Matlab, we use the `imagesc` function to create the image. The end result of the plotting procedure is shown in figure A.1(c).

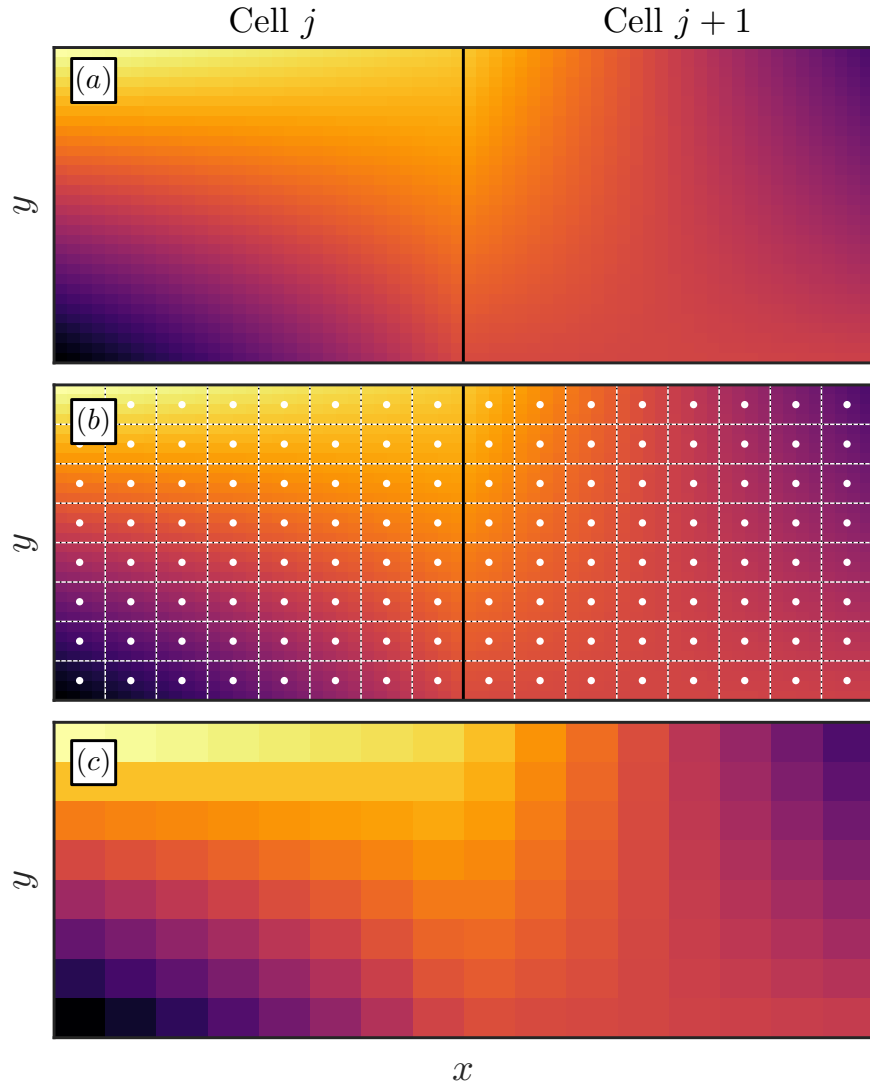


Figure A.1: Illustration of the image-creation procedure for a DG solution. (a) The complete DG solution in two neighboring cells is shown. (b) According to the desired resolution for the image that will be created, each cell is divided up into a number of subcells such that each subcell corresponds to a single pixel in the final image. The value of each pixel is determined by evaluating the DG solution at the center of each subcell (white markers) and mapped to a color according to a color map. (c) The final image is created from the subcell-gridded data using standard plotting routines.

Appendix B

Additional Comparisons Between ELM-Heat-Pulse Simulations

In Section 3.5, we noted that the time-integrated total heat flux for the 1D2V ELM-heat-pulse simulation with collisions is $\approx 9.9\%$ larger (over a 1.5 ms integration window), as shown in figure B.1. Here, we explore the reason for this discrepancy of approximately 0.34 MJ m^{-2} .

We investigate the energy balance of the system to explain the differences in the time-integrated parallel heat fluxes between the cases with and without collisions. In

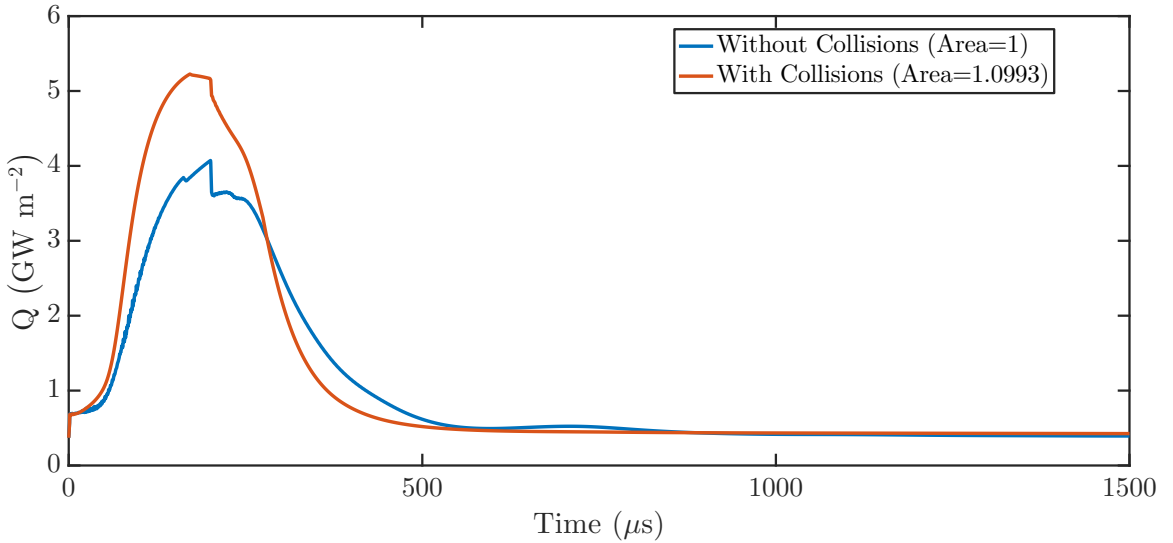


Figure B.1: Comparison of the total parallel heat flux at the divertor plate versus time for 1D2V ELM-heat-pulse simulations with and without same-species Lenard–Bernstein collisions. By integrating the area under each curve and normalizing the area to the smaller value, we find that the time-integrated total heat flux for the case with collisions is $\approx 9.9\%$ larger.

the collisionless case, our system is described by the system

$$\frac{\partial f_e}{\partial t} + v_{\parallel} \frac{\partial f_e}{\partial z} + \frac{q_e}{m_e} E_{\parallel} \frac{\partial f_e}{\partial v_{\parallel}} = S_e(z, \mathbf{v}, t), \quad (\text{B.1})$$

$$\frac{\partial f_i}{\partial t} + v_{\parallel} \frac{\partial f_i}{\partial z} + \frac{q_i}{m_i} E_{\parallel} \frac{\partial f_i}{\partial v_{\parallel}} - \frac{e^2 k_{\perp 0}^2 \rho_{s0}^2}{m_i T_{e0}} \delta\phi E_{\parallel} \frac{\partial f_i}{\partial v_{\parallel}} = S_i(z, \mathbf{v}, t), \quad (\text{B.2})$$

$$n_i (k_{\perp 0} \rho_{s0})^2 \frac{e^2 \delta\phi}{T_{e0}} = \sum_s q_s n_s. \quad (\text{B.3})$$

We consider the time evolution of the total energy:

$$\frac{dW_{\text{tot}}}{dt} = \int d\Lambda \sum_s \left(f_s \frac{\partial H_s}{\partial t} + \frac{\partial f_s}{\partial t} H_s \right), \quad (\text{B.4})$$

where $\int d\Lambda = \int dz \int d^3 \mathbf{v}$. The electron and ion Hamiltonians are

$$H_e = \frac{1}{2} m_e v_{\parallel}^2 + \mu B - e\delta\phi, \quad (\text{B.5})$$

$$H_i = \frac{1}{2} m_i v_{\parallel}^2 + \mu B + e\delta\phi - \frac{1}{2} \frac{e^2}{T_{e0}} (k_{\perp 0} \rho_{s0})^2 \delta\phi^2, \quad (\text{B.6})$$

where $k_{\perp 0} \rho_{s0} = 0.2$ and the second-order Hamiltonian in the electrons has been neglected since electrons are much less massive than the ions. Recall that the second-order term in the Hamiltonian was constructed so that $\int d\Lambda \sum_s f_s \partial_t H_s = 0$ in Section 3.2.1. Therefore, we need to calculate $\int d\Lambda \sum_s H_s \partial_t f_s$, which is not going to be zero when we include the sheath losses:

$$\int d\Lambda H_s \frac{\partial f_s}{\partial t} = - \int d\Lambda H_s v_{\parallel} \frac{\partial f_s}{\partial z} + \int d\Lambda H_s \frac{1}{m_s} \frac{\partial H_s}{\partial z} \frac{\partial f_s}{\partial v_{\parallel}} + \int d\Lambda H_s S_s. \quad (\text{B.7})$$

The second term on the right-hand side of (B.7) can be integrated by parts to get

$$\int d\Lambda H_s \frac{1}{m_s} \frac{\partial H_s}{\partial z} \frac{\partial f_s}{\partial v_{\parallel}} = \int dz \int d^2 v_{\perp} \frac{1}{m_s} H_s \frac{\partial H_s}{\partial z} f_s \Big|_{-v_{\parallel,\max}}^{v_{\parallel,\max}} - \int d\Lambda \frac{\partial H_s}{\partial v_{\parallel}} \frac{1}{m_s} \frac{\partial H_s}{\partial z} f_s \quad (\text{B.8})$$

$$= - \int d\Lambda \frac{\partial H_s}{\partial z} v_{\parallel} f_s, \quad (\text{B.9})$$

where we have used the zero-flux boundary condition in v_{\parallel} . This term then combines with the first term on the right-hand side of (B.7) as $\int d\Lambda v_{\parallel} \partial_z (H_s f_s)$. Therefore, the energy-evolution equation is

$$\frac{dW_{\text{tot}}}{dt} = - \int d^3 \mathbf{v} \sum_s v_{\parallel} H_s f_s \Big|_{z=-L_{\parallel}}^{z=L_{\parallel}} + \int d\Lambda \sum_s H_s S_s. \quad (\text{B.10})$$

We can simplify this result further by noting that the source terms have the property $\int d^3\mathbf{v} S_i = \int d^3\mathbf{v} S_e$ and using the logical sheath boundary conditions:

$$\frac{dW_{\text{tot}}}{dt} = - \int d^3\mathbf{v} \sum_s v_{\parallel} H_{s,0} f_s \Big|_{z=-L_{\parallel}}^{z=L_{\parallel}} + \int d^3\mathbf{v} v_{\parallel} H_{i,2} f_i \Big|_{z=-L_{\parallel}}^{z=L_{\parallel}} + \int d\Lambda \sum_s H_{s,0} S_s + \int d\Lambda H_{i,2} S_i, \quad (\text{B.11})$$

where $H_{s,0} = \frac{1}{2} m_s v_{\parallel}^2 + \mu B$ and $H_{i,2} = e^2 (k_{\perp 0} \rho_{s0})^2 \delta \phi^2 / (2 T_{e0})$. The first term on the right-hand side of (B.11) is the total parallel heat flux, which we already have plotted in figure 3.7. The second term on the right-hand side of (B.11) is proportional to the outgoing ion particle flux Γ_i , so we must compute a diagnostic for

$$H_{i,2}(t) = \frac{1}{2} \frac{e^2}{T_{e0}} (k_{\perp 0} \rho_{s0})^2 \delta \phi^2 \Gamma_i(z) \Big|_{z=-L_{\parallel}}^{z=L_{\parallel}}. \quad (\text{B.12})$$

The third term on the right-hand side of (B.11) will be the same for the simulations with and without collisions, as it is time independent. We must also keep a record of the fourth term on the right-hand side of (B.11) and $W_{\text{measured}}(t) = \sum_s \int d\Lambda H_s f_s$ to quantify the error in energy conservation in the simulation. In this case, we define the energy error as $|\Delta W_{\text{measured}} - \Delta W_{\text{predicted}}| / \Delta W_{\text{predicted}}$, where

$$\Delta W_{\text{predicted}} = \int_0^{t_{\text{end}}} dt \frac{dW_{\text{tot}}}{dt}, \quad (\text{B.13})$$

and use (B.11) to calculate the integrand at the end of each time step. We use a trapezoid rule to evaluate the integral in time for $\Delta W_{\text{predicted}}$ and take $t_{\text{end}} = 2$ ms in our tests.

By comparing the energy diagnostics from the two simulations, we find that the difference in the time-integrated heat flux is explained by difference in $W_{\text{measured}}(t)$. Figure B.2 shows the time traces of the total energy $W_{\text{measured}}(t)$ measured in the two simulations, as well as the individual contributions from electrons and ions to $W_{\text{measured}}(t)$. The 1D2V ELM-heat-pulse simulation without collisions simply has a larger system energy W_{measured} at any given instant than the simulation with collisions, which results in a lower time-integrated heat flux for the collisionless simulation. The two simulations both start with $W_{\text{measured}} \approx 0.39$ MJ/m², but the collisionless simulation has $W_{\text{measured}(t_{\text{end}})} \approx 0.55$ MJ m⁻² and the simulation with collisions has $W_{\text{measured}(t_{\text{end}})} \approx 0.21$ MJ m⁻². Additionally, the energy error was found to be 0.04% for the two simulations, so energy is well conserved.

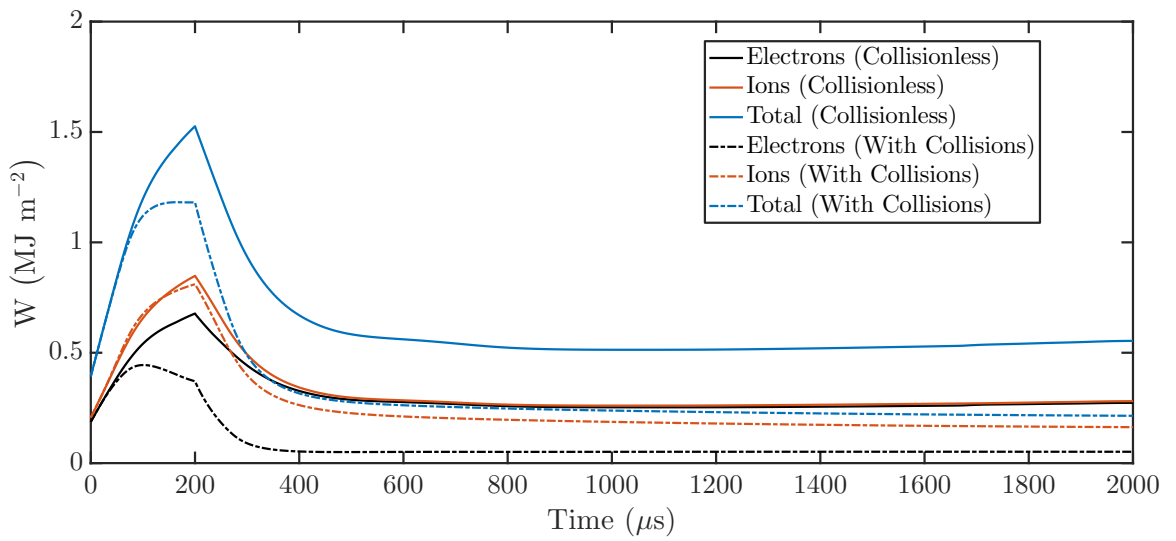


Figure B.2: Comparison of the total energy and electron and ion contributions between 1D2V ELM-heat-pulse simulations with and without same-species Lenard–Bernstein collisions. Starting from the same initial condition, the collisionless simulation has more than twice the total energy of the simulation with collisions at $t = 2$ ms. This plot helps explain the difference in the total heat flux in figures 3.7 and B.1, where the time-integrated total heat flux is observed to be larger in the simulation with collisions.

Appendix C

Numerical Energy Conservation in LAPD Simulations

Here, we investigate the energy-conservation properties of our LAPD simulations discussed in Chapter 4. As discussed in Section 2.2, the space discretization exactly conserves energy, but the SSP-RK3 time integrator introduces energy conservation errors. Therefore, it is interesting to quantify the energy non-conservation that results from the time discretization. The evolution of total energy $W = W_k + W_\phi$ (with perfect spatial and temporal energy conservation) can be obtained by adding together (4.6) and (4.9):

$$\frac{\partial W}{\partial t} = -P_{\text{loss}} + P_{\text{source}}, \quad (\text{C.1})$$

$$P_{\text{loss}} = - \int dx dy \sum_s \int d^3v H_s v_{\parallel} f_s \Big|_{z_{\text{lower}}}^{z_{\text{upper}}}, \quad (\text{C.2})$$

$$P_{\text{source}} = \int d^3x \sum_s \int d^3v H_s S_s = \int d^3x \sum_s \int d^3v H_0 S_s, \quad (\text{C.3})$$

where we have assumed a charge-neutral source for the second equality in (C.3). Although we also have a non-negligible source of energy from the positivity-adjustment procedure, this source of energy can also be measured and accounted for using diagnostics, i.e. by computing the total energy before and after the positivity-adjustment procedure, which is applied to the distribution functions at the end of each intermediate Runge–Kutta stage. By taking into account the details of the multi-stage SSP-RK3 time integrator, we can derive a simple expression for the expected change in the total energy of the system after a total time step of size Δt that involves a combination of power loss and source terms from each substage.

For clarity, the SSP-RK3 algorithm to advance an equation of the form $\partial_t f = \xi(f, \phi)$ from $f(t^n) = f^n$ to $f(t^{n+1})$, where $t^{n+1} = t^n + \Delta t$, is written as (Gottlieb

et al., 2001; Peterson & Hammett, 2013)

$$f^* = f^n + \Delta t \xi(f^n, \phi^n), \quad (\text{C.4})$$

$$f' = \frac{3}{4} f^n + \frac{1}{4} [f^* + \Delta t \xi(f^*, \phi^*)], \quad (\text{C.5})$$

$$f^{n+1} = \frac{1}{3} f^n + \frac{2}{3} [f' + \Delta t \xi(f', \phi')]. \quad (\text{C.6})$$

The positivity-adjustment procedure is applied to f^* , f' , and f^{n+1} before it is used in the $\xi(f, \phi)$ operator of the subsequent stage, so we denote the extra energy added to the electrons and ions at the end of each substage as W_{pos}^* , W_{pos}' , and W_{pos}^{n+1} . The SSP-RK3 algorithm (C.4)–(C.6) can be combined as

$$f^{n+1} = f^n + \Delta t \left(\frac{1}{6} \xi(f^n, \phi^n) + \frac{1}{6} \xi(f', \phi') + \frac{2}{3} \xi(f^*, \phi^*) \right) \quad (\text{C.7})$$

Using (C.1), we notice that the energy change associated with a term like $\xi(f^n, \phi^n)$ is

$$\int d^3x \sum_s \int d^3v H_s^n \xi(f_s^n, \phi^n) = -P_{\text{loss}}^n + P_{\text{source}}^n, \quad (\text{C.8})$$

where the superscript n on P_{loss} and P_{source} indicates that (C.2) and (C.3) are to be evaluated with H^n and f^n . By multiplying (C.7) by H^{n+1} , integrating over phase space, and summing over both species, the energy change in the system after the total time step can be written as

$$\begin{aligned} P_{\text{total}} &= \frac{W^{n+1} - W^n}{\Delta t} = \left(\frac{1}{6} P_{\text{loss}}^n + \frac{1}{6} P_{\text{loss}}^* + \frac{2}{3} P_{\text{loss}}' \right) \\ &\quad + \left(\frac{1}{6} P_{\text{source}}^n + \frac{1}{6} P_{\text{source}}^* + \frac{2}{3} P_{\text{source}}' \right) \\ &\quad + \frac{1}{\Delta t} \left(\frac{1}{6} W_{\text{pos}}^* + \frac{2}{3} W_{\text{pos}}' + W_{\text{pos}}^{n+1} \right) + P_{\text{err}}, \end{aligned} \quad (\text{C.9})$$

$$W^n = \int d^3x \int d^3v \left(H^n - \frac{1}{2} q_s \phi^n \right) f^n, \quad (\text{C.10})$$

$$W^{n+1} = \int d^3x \int d^3v \left(H^{n+1} - \frac{1}{2} q_s \phi^{n+1} \right) f^{n+1}, \quad (\text{C.11})$$

where P_{err} is a measure of the energy conservation error $\propto (\partial_t W)^4 (\Delta t)^3$ resulting from the time discretization scheme. While it has a complicated expression, it can be tracked in the code by measuring all the other terms in (C.9) using diagnostics.

Figure C.1 shows the time traces of the terms appearing in the power balance (C.9) over a 0.1 ms period of the simulation in a quasi-steady turbulent state, or approximately 2×10^4 time steps. Also plotted in figure C.1 is P_{err} , which is found to vary in magnitude between 1–6 W ($\sim 10^{-4}$ relative error), so the energy conservation error introduced by the time discretization is extremely low.

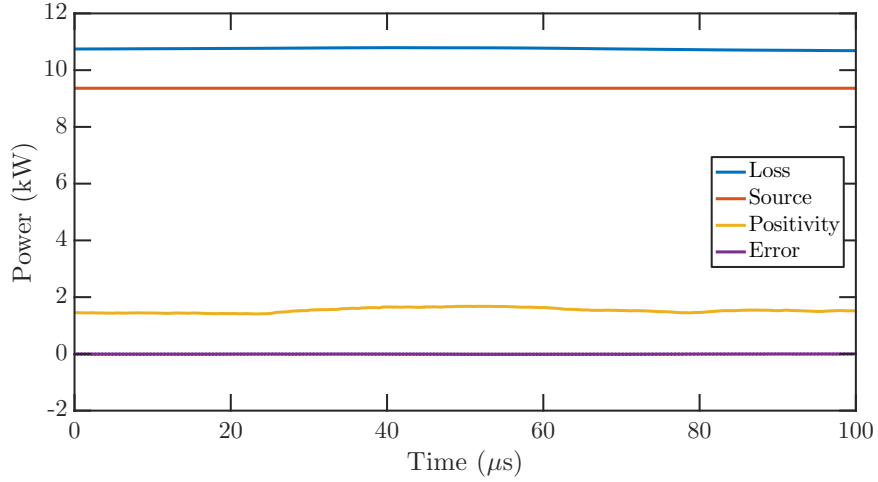


Figure C.1: Time traces of diagnostics tracking power sources, power sinks, and power error over a 0.1 ms period in a LAPD simulation. The power error, which is defined in (C.9) and arises from the time discretization, fluctuates in amplitude between 1 and 6 W ($\sim 10^{-4}$ relative error). This plot indicates that the energy conservation error introduced by the time discretization is extremely low.

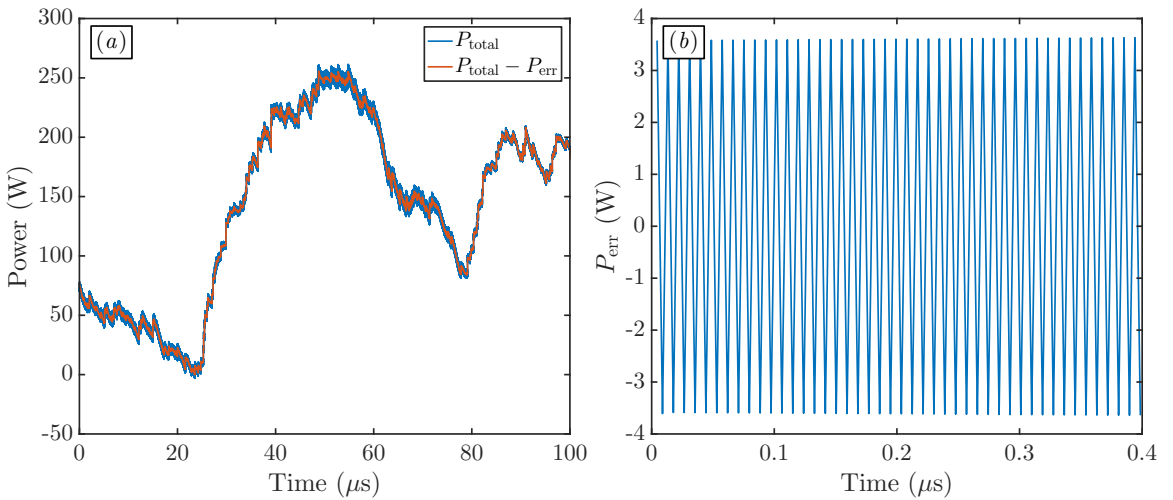


Figure C.2: Time traces power-error diagnostics in a LAPD simulation. (a) P_{err} is computed by taking the difference between the sum of power sources and sinks in the system ($P_{\text{total}} - P_{\text{err}}$ in (C.9)) is compared with numerical net power P_{total} , which is computed by taking the difference in the total system energy before and after a time step. (b) From the two curves in (a), we can quantify the error in power that arises from the time discretization. Note that the time interval has been reduced to show the oscillations in P_{err} . Over a larger 0.1 ms time interval, P_{err} fluctuates in amplitude between 1 and 6 W.

Appendix D

Initial Conditions for Helical-SOL Simulations

Here, we derived the initial conditions used in the helical-SOL simulations of Chapter 5. The results can also be used to provide initial conditions for the LAPD simulations of Chapter 4. The calculation presented here is based on notes by G. Hammett.

We consider a problem in which a uniform mass source S_ρ and energy source S_E is continuously active in the region $|z| < L_s/2$. This fluid flows out to perfectly absorbing boundaries at $|z| = L_z/2$. We treat the plasma as a single fluid with mass density $\rho \approx n_e m_i$ and energy density $(3/2)n_e(T_e + T_i)$, so $S_\rho = m_i S_n$ and $S_E = (3/2)T_{\text{src}}S_n$, where S_n is the electron and ion particle source rate and $T_{\text{src}} = T_{e,\text{src}} + T_{i,\text{src}}$ is the effective single-fluid source temperature. This system is described by the steady-state fluid equations

$$0 = -\frac{\partial}{\partial z}(\rho u) + S_\rho, \quad (\text{D.1})$$

$$0 = -\frac{\partial}{\partial z}(\rho u^2 + p), \quad (\text{D.2})$$

$$0 = -\frac{\partial}{\partial z}\left(\frac{1}{2}\rho u^3 + \frac{5}{2}pu\right) + S_E, \quad (\text{D.3})$$

where u is the fluid velocity, ρ is the mass density, and p is the pressure. We treat the source as having no mean flow in the z direction.

We integrate these equations from $z = 0$ to an arbitrary position $z < L_s/2$ and use the boundary condition $u(z = 0) = 0$ to get

$$\rho u = S_\rho, \quad (\text{D.4})$$

$$\rho u^2 + p = p_0, \quad (\text{D.5})$$

$$\frac{1}{2}\rho u^3 + \frac{5}{2}pu = zS_E, \quad (\text{D.6})$$

where $p_0 \equiv p(z = 0)$. The first two equations can be solved for ρ and p respectively, and we obtain a quadratic equation for $u(z)$ by substituting these expressions into

the last equation. The solution to this system is

$$p(z) = \frac{3p_0 \mp \sqrt{25p_0^2 - 32z^2S_\rho S_E}}{8}, \quad (\text{D.7})$$

$$u(z) = \frac{5p_0 \pm \sqrt{25p_0^2 - 32z^2S_\rho S_E}}{8S_\rho z}, \quad (\text{D.8})$$

$$\rho(z) = \frac{zS_p}{u}. \quad (\text{D.9})$$

Since the pressure cannot be negative, the only physical solution for small z is the negative branch for $u(z)$ and the positive branch for $p(z)$. The central pressure p_0 is determined by the boundary conditions at $|z| = L_s/2$. A steady-state solution at a perfectly absorbing wall requires $\mathcal{M} \geq 1$ at the wall (Munz, 1994), where the Mach number $\mathcal{M}(z) \equiv u(z)/c_s(z) = u(z)/\sqrt{(5/3)p(z)/\rho(z)}$. We see that

$$\mathcal{M}(z)^2 = \frac{\rho(z)u(z)^2}{(5/3)p(z)^2} = \frac{3}{5} \frac{p_0 - p}{p}. \quad (\text{D.10})$$

The maximum value of $\mathcal{M}(z)$ occurs at the z that minimizes $p(z)$. This value z_{\max} turns out to be the z that makes the radicand in (D.7) zero, so we find that

$$z_{\max}^2 = \frac{25}{32} \frac{p_0^2}{S_p S_E}, \quad (\text{D.11})$$

$$p(z_{\max}) = \frac{3}{8} p_0, \quad (\text{D.12})$$

$$\mathcal{M}(z_{\max}) = 1. \quad (\text{D.13})$$

This result means that the outflow requirement must be $\mathcal{M} = 1$ and provides a constraint on the value of p_0 such that $z_{\max} = L_s/2$:

$$p_0 = \frac{L_s}{2} \sqrt{\frac{32}{25} S_p S_E}. \quad (\text{D.14})$$

Using this expression for p_0 , we have the following profiles in the source region $0 < |z| < L_s/2$:

$$p(z) = p_0 \left(\frac{3 + 5\sqrt{1 - z^2/(L_s/2)^2}}{8} \right), \quad (\text{D.15})$$

$$u(z) = \frac{\sqrt{3}}{2} \sqrt{\frac{T_{\text{src}}}{m_i}} \left(\frac{1 - \sqrt{1 - z^2/(L_s/2)^2}}{z/(L_s/2)} \right), \quad (\text{D.16})$$

$$\rho(z) = \frac{16S_p^2}{5p_0} \left(\frac{L_s}{2} \right)^2 \left(\frac{1 + \sqrt{1 - z^2/(L_s/2)^2}}{2} \right). \quad (\text{D.17})$$

In order to use these profiles to initialize a Maxwellian initial condition for a kinetic simulation, we note that these profiles correspond to density ($n = \rho/m_i$) and temperature ($T = m_i p/\rho$) profiles in the source region given by

$$T(z) = \frac{3}{5} T_{\text{src}} \left(\frac{3 + 5\sqrt{1 - z^2/(L_s/2)^2}}{4 + 4\sqrt{1 - z^2/(L_s/2)^2}} \right), \quad (\text{D.18})$$

$$n(z) = \frac{4\sqrt{5}}{3} \frac{(L_s/2)S_n}{c_{\text{ss}}} \left(\frac{1 + \sqrt{1 - z^2/(L_s/2)^2}}{2} \right), \quad (\text{D.19})$$

where $c_{\text{ss}} = \sqrt{(5/3)T_{\text{src}}/m_i}$. In the source-free regions $z > L_s/2$ or $z < -L_s/2$, $n(z)$, $T(z)$, and $u(z)$ are all constant and equal to the value that their respective profiles evaluated at the corresponding edge of the source region at $z = L_s/2$ or $z = -L_s/2$. The 1D equilibrium profiles (D.16), (D.18), and (D.19), the density source in the helical-SOL simulations (5.3), and the temperature profiles of the electron and ion sources are used to generate spatially varying initial conditions in (x, y, z) .

One could go further by calculating the ion guiding-center density profile that gives the desired equilibrium potential $\phi(x, y, z)$ when the gyrokinetic Poisson equation is solved. For now, we simply set $n_i^g(x, y, z) = n_e(x, y, z)$ and initialize with $\phi = 0$, as we did in the LAPD simulations.

Appendix E

Estimates of Interchange Instability

Here, we estimate the frequencies and growth rates of interchange-like instabilities that may be relevant for the helical SOL simulations discussed in Chapter 5. The notes here are based on discussions with T. Stoltzfus-Dueck. For simplicity, we look for modes with $k_{\parallel} = 0$, take ions to be cold ($T_i = 0$) and singly charged, and take electrons to be isothermal.

E.1 Basic Interchange Instability

We start with the system of equations in 2D describing the electron density, ion gyrocenter density, and electrostatic potential:

$$\frac{\partial \tilde{n}_e}{\partial t} + \frac{1}{B_0} \{ \phi, \tilde{n}_e + n_{e0} \} + \frac{1}{e} \mathcal{K} (\tilde{n}_e T_{e0} - n_{e0} e \phi) = 0, \quad (\text{E.1})$$

$$\frac{\partial \tilde{n}_i}{\partial t} + \frac{1}{B_0} \{ \phi, \tilde{n}_i + n_{i0} \} - \frac{1}{e} \mathcal{K} (n_{i0} e \phi) = 0, \quad (\text{E.2})$$

$$-n_{i0} m_i \frac{1}{B^2} \nabla_{\perp}^2 \phi = e (\tilde{n}_i - \tilde{n}_e), \quad (\text{E.3})$$

where the densities have been split into background n_{s0} and fluctuating \tilde{n}_s components and the Poisson bracket for $E \times B$ advection is $\{f, g\} = (\partial_x f)(\partial_y g) - (\partial_y f)(\partial_x g)$. The curvature operator is $\mathcal{K} = \mathcal{K}^x \partial_x + \mathcal{K}^y \partial_y$, where $\mathcal{K}^x = -(2/B) \mathbf{b} \times \nabla \ln B \cdot \nabla x$ and $\mathcal{K}^y = -(2/B) \mathbf{b} \times \nabla \ln B \cdot \nabla y$. The term $\mathcal{K}(\tilde{n}_e T_{e0})/e$ represents the advection of density by the electron curvature drift. Since we have assumed that the ions are singly charged, $n_{i0} = n_{e0} = n_0$.

First, we take a time derivative of the quasineutrality equation (E.3) and substitute (E.1) and (E.2):

$$-n_0 m_i \frac{1}{B^2} \nabla_{\perp}^2 \frac{\partial \phi}{\partial t} = e \left(-\frac{1}{B_0} \{ \phi, \tilde{n}_i + n_0 \} + \frac{1}{e} \mathcal{K}(n_0 e \phi) \right) - e \left(-\frac{1}{B_0} \{ \phi, \tilde{n}_e + n_0 \} - \frac{1}{e} \mathcal{K}(\tilde{n}_e T_{e0} - n_0 e \phi) \right) \quad (\text{E.4})$$

$$n_0 m_i \frac{1}{B^2} \nabla_{\perp}^2 \frac{\partial \phi}{\partial t} = \frac{e}{B_0} \{ \phi, (\tilde{n}_i + n_0) - (\tilde{n}_e + n_0) \} + \mathcal{K}(-n_0 e \phi - \tilde{n}_e T_{e0} + n_0 e \phi) \quad (\text{E.5})$$

$$n_0 m_i \frac{1}{B^2} \nabla_{\perp}^2 \frac{\partial \phi}{\partial t} = -n_0 m_i \frac{1}{B_0 B^2} \{ \phi, \nabla_{\perp}^2 \phi \} - \mathcal{K}(\tilde{n}_e T_{e0}) \quad (\text{E.6})$$

Next, we linearize the equations by taking $\tilde{n}_e/n_0 \ll 1$ and $e\phi/T_{e0} \ll 1$. Additionally, we assume that $\nabla n_0 = -n_0 \hat{x}/L_n$ to write

$$\frac{\partial \tilde{n}_e}{\partial t} + \frac{1}{B_0} \frac{\partial \phi}{\partial y} \frac{n_0}{L_n} + \frac{1}{e} \mathcal{K}^x \frac{\partial}{\partial x} (\tilde{n}_e T_{e0} - n_0 e \phi) + \frac{1}{e} \mathcal{K}^y \frac{\partial}{\partial y} (\tilde{n}_e T_{e0} - n_0 e \phi) = 0, \quad (\text{E.7})$$

$$n_0 m_i \frac{1}{B^2} \nabla_{\perp}^2 \frac{\partial \phi}{\partial t} = -\mathcal{K}^x \frac{\partial}{\partial x} (\tilde{n}_e T_{e0}) - \mathcal{K}^y \frac{\partial}{\partial y} (\tilde{n}_e T_{e0}). \quad (\text{E.8})$$

For the helical-SOL geometry, we set $\mathcal{K}^x = 0$ because we assume that $\nabla x \parallel \nabla B$ and $\mathcal{K}^y \sim 2/(BR)$. Next, we look at a single Fourier component of the fluctuations by taking $\tilde{n}_e = \hat{n}_e \exp(ik_y y - i\omega t)$ and $\tilde{\phi} = \hat{\phi} \exp(ik_y y - i\omega t)$ to solve for ω as a function of k_y :

$$\omega \hat{n}_e - \frac{k_y}{B_0} \hat{\phi} \frac{n_0}{L_n} - \frac{k_y}{e} \mathcal{K}^y (\hat{n}_e T_{e0} - n_0 e \hat{\phi}) = 0, \quad (\text{E.9})$$

$$-\omega n_0 m_i \frac{1}{B^2} k_{\perp}^2 \hat{\phi} = k_y \mathcal{K}^y \hat{n}_e T_{e0}. \quad (\text{E.10})$$

These equations can be rearranged as

$$\left(\omega - k_y \frac{T_{e0} \mathcal{K}^y}{e} \right) \frac{\hat{n}_e}{n_0} = \left(k_y \frac{T_{e0}}{e B_0 L_n} - k_y \frac{T_{e0} \mathcal{K}^y}{e} \right) \frac{e \hat{\phi}}{T_{e0}}, \quad (\text{E.11})$$

$$\frac{e \hat{\phi}}{T_{e0}} = -\frac{k_y}{\omega k_{\perp}^2} \frac{T_{e0} \mathcal{K}^y}{e} \frac{e^2 B^2}{m_i T_{e0}} \frac{\hat{n}_e}{n_0}. \quad (\text{E.12})$$

To simplify the notation, we define the velocities

$$v_{de} \equiv \frac{T_{e0} \mathcal{K}^y}{e} \sim 2 \frac{\rho_s}{R_0} c_s \quad (\text{E.13})$$

$$v_{*e} \equiv \frac{T_{e0}}{e B_0 L_n} = \frac{\rho_s}{L_n} c_s, \quad (\text{E.14})$$

where $c_s^2 = T_{e0}/m_i$ and $\rho_s^2 = c_s^2/\Omega_{ci}^2 = m_i T_{e0}/(e^2 B^2)$. Using these definitions and substituting (E.12) into (E.11), we get

$$(\omega - k_y v_{de}) = -k_y^2 (v_{*e} - v_{de}) \frac{v_{de}}{\omega k_\perp^2 \rho_s^2} \quad (\text{E.15})$$

We make the additional assumption that $v_{de}/v_{*e} \sim L_n/R_0 \ll 1$, so $v_{*e} - v_{de} \approx v_{*e}$. The mode frequency ω then satisfies the quadratic equation

$$\omega^2 - k_y v_{de} \omega + \frac{k_y^2 v_{de} v_{*e}}{k_\perp^2 \rho_s^2} = 0. \quad (\text{E.16})$$

By assuming that $k_\perp \rho_s \lesssim 1$, we see that the term linear in ω is small compared to at least one of the other terms, since

$$\frac{k_y v_{de} \omega}{\omega^2} \frac{k_y v_{de} \omega}{\frac{k_y^2 v_{de} v_{*e}}{k_\perp^2 \rho_s^2}} = k_\perp^2 \rho_s^2 \frac{v_{de}}{v_{*e}} \ll 1. \quad (\text{E.17})$$

Therefore, we neglect this term and obtain the following result for ω :

$$\omega \approx \pm i \frac{|k_y|}{k_\perp} \frac{\sqrt{v_{*e} v_{de}}}{\rho_s} \sim \pm i \frac{|k_y|}{k_\perp} \frac{\sqrt{2} c_s}{\sqrt{R_0 L_n}}. \quad (\text{E.18})$$

The growth rate is maximized for $k_x \rightarrow 0$, in which case we get the standard interchange estimate that the mode grows with a rate $\sim c_s / \sqrt{R_0 L_n}$.

E.2 Addition of Sheath Effects

Next, we attempt to incorporate sheath effects to refine our estimate for the interchange-mode growth rate. We assume that the electron temperature is constant along a field line and that the ions are cold. The sheath boundary conditions used in the helical-SOL simulations permit fluctuations in the parallel current at the sheath entrance, while the steady-state parallel current is assumed to be zero. Taking f_e to be a Maxwellian, the total parallel electron current into the sheath is

$$j_{\parallel e} = -e \int_{v_c}^{\infty} dv_{\parallel} v_{\parallel} \frac{n_e}{\sqrt{2\pi v_{te}^2}} e^{-v_{\parallel}^2/2v_{te}^2} = -\frac{n_e e}{\sqrt{2\pi v_{te}^2}} \int_{v_c}^{\infty} dv_{\parallel} \frac{\partial}{\partial v_{\parallel}} \left(-v_{te}^2 e^{-v_{\parallel}^2/2v_{te}^2} \right) \quad (\text{E.19})$$

$$= -\frac{n_e e v_{te}}{\sqrt{2\pi}} e^{-v_c^2/2v_{te}^2}, \quad (\text{E.20})$$

where $v_c^2 = 2e\phi/m_e$.

In the cold-ion limit, we assume that the ions are accelerated to c_s at the sheath entrance (as required by the Bohm sheath criterion $u_{\parallel i} \geq c_s$), so the parallel ion current into the sheath is simply taken to be $n_i e c_s$. The zeroth-order potential comes

from solving $j_{\parallel i} + j_{\parallel e} = 0$:

$$\frac{n_e e v_{te}}{\sqrt{2\pi}} e^{-e\phi_0/T_{e0}} = n_i e c_s \quad (\text{E.21})$$

$$\phi_0 = \frac{T_{e0}}{e} \ln \left(\frac{n_e v_{te}}{\sqrt{2\pi} n_i c_s} \right) \quad (\text{E.22})$$

The individual fluctuating parallel currents at the sheath entrance are

$$\tilde{j}_{\parallel e} = -\frac{n_{e0} e v_{te}}{\sqrt{2\pi}} e^{-e\phi_0/T_{e0}} \left(\frac{\tilde{n}_e}{n_{e0}} + \frac{1}{2} \frac{\tilde{T}_e}{T_{e0}} - \frac{e\tilde{\phi}}{T_{e0}} + \frac{e\phi_0}{T_{e0}} \frac{\tilde{T}_e}{T_{e0}} \right), \quad (\text{E.23})$$

$$\tilde{j}_{\parallel i} = n_{i0} e c_s \frac{\tilde{n}_i}{n_{i0}}. \quad (\text{E.24})$$

The total fluctuating parallel current can be written as

$$\tilde{j}_{\parallel} = \tilde{j}_{\parallel i} + \tilde{j}_{\parallel e} \quad (\text{E.25})$$

$$= n_{e0} e c_s \left(\frac{\tilde{n}_i - \tilde{n}_e}{n_{i0}} + \frac{e\tilde{\phi}}{T_{e0}} - \frac{1}{2} \frac{\tilde{T}_e}{T_{e0}} - \frac{e\phi_0}{T_{e0}} \frac{\tilde{T}_e}{T_{e0}} \right) \quad (\text{E.26})$$

$$= n_{e0} e c_s \left(-m_i n_{i0} \frac{1}{e B^2} \nabla_{\perp}^2 \tilde{\phi} + \frac{e\tilde{\phi}}{T_{e0}} - \left(\frac{1}{2} + \frac{e\phi_0}{T_{e0}} \right) \frac{\tilde{T}_e}{T_{e0}} \right) \quad (\text{E.27})$$

$$= n_{e0} e c_s \left(\left(1 - \rho_s^2 \nabla_{\perp}^2 \right) \frac{e\tilde{\phi}}{T_{e0}} - \left[\frac{1}{2} + \ln \left(\frac{n_e v_{te}}{\sqrt{2\pi} n_i c_s} \right) \right] \frac{\tilde{T}_e}{T_{e0}} \right), \quad (\text{E.28})$$

where the quasineutrality condition (E.3) was used to write $\tilde{n}_i - \tilde{n}_e$ in terms of the fluctuating potential $\tilde{\phi}$. In (E.28), the $\rho_s^2 \nabla_{\perp}^2 e\tilde{\phi}/T_{e0}$ correction should be discarded, as it arises from the neglect of parallel ion-polarization-density flow.

Going back to the equation describing the evolution of the electron density, we restore the $\nabla_{\parallel} (n_e u_{\parallel e})$ term in (E.1) that was originally neglected through the assumption of $k_{\parallel} = 0$:

$$\frac{\partial \tilde{n}_e}{\partial t} + \frac{1}{B_0} \{ \phi, \tilde{n}_e + n_{e0} \} + \frac{1}{e} \mathcal{K} (\tilde{n}_e T_{e0} - n_{e0} e \phi) = -\nabla_{\parallel} (n_e u_{\parallel e}). \quad (\text{E.29})$$

After linearization, we have

$$\frac{\partial \tilde{n}_e}{\partial t} + \frac{1}{B_0} \frac{\partial \phi}{\partial y} \frac{n_0}{L_n} + \frac{1}{e} \mathcal{K}^x \frac{\partial}{\partial x} (\tilde{n}_e T_{e0} - n_0 e \phi) + \frac{1}{e} \mathcal{K}^y \frac{\partial}{\partial y} (\tilde{n}_e T_{e0} - n_0 e \phi) = -\nabla_{\parallel} (n_0 \tilde{u}_{\parallel e}). \quad (\text{E.30})$$

We can relate $\nabla_{\parallel} (n_0 \tilde{u}_{\parallel e})$ to fluctuations in the current outflow at the sheaths (located at $\pm L_z/2$) by assuming that \tilde{j}_{\parallel} is linear in z

$$-\nabla_{\parallel} (n_0 \tilde{u}_{\parallel e}) \approx \frac{1}{e} \frac{2}{L_z} \tilde{j}_{\parallel} \Big|_{sh} \quad (\text{E.31})$$

We make the additional approximation $\tilde{j}_{\parallel} \approx \tilde{j}_{\parallel e}$ by assuming that the parallel response of the ions is too slow to contribute to the current fluctuations at typical instability timescales. As a first step, we also neglect electron temperature fluctuations, so we set $\tilde{T}_e = 0$ in (E.23) and get

$$\tilde{j}_{\parallel} \Big|_{sh} = -n_0 e c_s \frac{e \hat{\phi}}{T_{e0}}. \quad (\text{E.32})$$

Keeping the equation for the ion gyrocenter density (E.2) unchanged, the linearized system that includes sheath effects is

$$\frac{\partial \tilde{n}_e}{\partial t} + \frac{1}{B_0} \frac{\partial \phi}{\partial y} \frac{n_0}{L_n} + \frac{1}{e} \mathcal{K}^y \frac{\partial}{\partial y} (\tilde{n}_e T_{e0} - n_0 e \phi) = \frac{1}{e} \frac{2}{L_z} \tilde{j}_{\parallel} \Big|_{sh}, \quad (\text{E.33})$$

$$n_0 m_i \frac{1}{B^2} \nabla_{\perp}^2 \frac{\partial \phi}{\partial t} = -\mathcal{K}^y \frac{\partial}{\partial y} (\tilde{n}_e T_{e0}) + \frac{2}{L_z} \tilde{j}_{\parallel} \Big|_{sh}. \quad (\text{E.34})$$

As before, we look at a single Fourier component $\tilde{n}_e = \hat{n}_e \exp(ik_y y - i\omega t)$ and $\tilde{\phi} = \hat{\phi} \exp(ik_y y - i\omega t)$:

$$\left(\omega - k_y \frac{T_{e0} \mathcal{K}^y}{e} \right) \frac{\hat{n}_e}{n_0} = \left[k_y \left(\frac{T_{e0}}{e B_0 L_n} - \frac{T_{e0} \mathcal{K}^y}{e} \right) + i \frac{2}{L_z} c_s \right] \frac{e \hat{\phi}}{T_{e0}}, \quad (\text{E.35})$$

$$i\omega k_{\perp}^2 n_0 m_i \frac{1}{B^2} \hat{\phi} = -\mathcal{K}^y i k_y \hat{n}_e T_{e0} + \frac{2}{L_z} n_0 e c_s \frac{e \hat{\phi}}{T_{e0}}. \quad (\text{E.36})$$

Using the definitions for v_{de} (E.13) and v_{*e} (E.14) and defining a new frequency $\omega_t = 2c_s/L_z$, the system becomes

$$(\omega - k_y v_{de}) \frac{\hat{n}_e}{n_0} = [k_y (v_{*e} - v_{de}) + i\omega_t] \frac{e \hat{\phi}}{T_{e0}}, \quad (\text{E.37})$$

$$(\omega k_{\perp}^2 \rho_s^2 + i\omega_t) \frac{e \hat{\phi}}{T_{e0}} = -k_y v_{de} \frac{\hat{n}_e}{n_0}. \quad (\text{E.38})$$

These equations are again combined to give a quadratic equation for ω :

$$\omega^2 + \left(i \frac{\omega_t}{k_{\perp}^2 \rho_s^2} - k_y v_{de} \right) \omega + \frac{k_y^2 v_{de} v_{*e}}{k_{\perp}^2 \rho_s^2} \approx 0, \quad (\text{E.39})$$

where we have again taken $v_{de}/v_{*e} \sim L_n/R_0 \ll 1$. As before, we can neglect the $k_y v_{de} \omega$ term because it is small compared to one or both of the constant and quadratic terms. We similarly compare the new sheath-contribution term to the other two terms:

$$\frac{\left(\omega \frac{\omega_t}{k_{\perp}^2 \rho_s^2} \right)^2}{\omega^2 \frac{k_y^2 v_{de} v_{*e}}{k_{\perp}^2 \rho_s^2}} = \frac{\omega_t^2}{k_{\perp}^2 \rho_s^2 k_y^2 v_{de} v_{*e}} \sim \frac{4c_s^2}{L_z^2} \frac{1}{k_{\perp}^2 \rho_s^2 k_y^2} \frac{R_0 L_n}{2 \rho_s^2 c_s^2} = \frac{2}{k_y^2 k_{\perp}^2 \rho_s^4} \frac{L_n}{L_z} \frac{R_0}{L_z} \equiv \epsilon_t. \quad (\text{E.40})$$

Here, $L_n/L_z \ll 1$, $R_0/L_z \sim \mathcal{O}(1)$, and $k_y^2 k_{\perp}^2 \rho_s^4$ is typically small, so ϵ_t can be big or small compared to 1.

The solution to the quadratic equation (E.39) is

$$\omega = -i \frac{\omega_t}{2k_{\perp}^2 \rho_s^2} \pm i \frac{1}{2} \sqrt{\frac{\omega_t^2}{k_{\perp}^4 \rho_s^4} + \frac{4k_y^2 v_{de} v_{*e}}{k_{\perp}^2 \rho_s^2}}, \quad (\text{E.41})$$

so the sheath current has a stabilizing effect on the growth rate when compared to the result of the previous section. In the weak-sheath-current limit ($\epsilon_t \ll 1$),

$$\omega = -i \frac{\omega_t}{2k_{\perp}^2 \rho_s^2} \pm i \frac{|k_y|}{k_{\perp} \rho_s} \sqrt{v_{de} v_{*e}} \sqrt{1 + \frac{\epsilon_t}{4}} \approx \pm i \frac{|k_y|}{k_{\perp}} \frac{\sqrt{2} c_s}{\sqrt{R_0 L_n}} - i \frac{\omega_t}{2k_{\perp}^2 \rho_s^2}, \quad (\text{E.42})$$

so the growth rate of the mode has been slightly reduced. In the strong-sheath-current limit ($\epsilon_t \gg 1$),

$$\omega = -i \frac{\omega_t}{2k_{\perp}^2 \rho_s^2} \pm i \frac{\omega_t}{2k_{\perp}^2 \rho_s^2} \sqrt{1 + \frac{4}{\epsilon_t}}. \quad (\text{E.43})$$

Choosing the upper branch, the solution is

$$\omega \approx i \frac{k_y^2 v_{de} v_{*e}}{\omega_t} = i \frac{1}{\sqrt{\epsilon_t}} \frac{|k_y|}{k_{\perp}} \frac{\sqrt{2} c_s}{\sqrt{R_0 L_n}}, \quad (\text{E.44})$$

so the growth rate can be reduced by a large factor if $\epsilon_t \gg 1$ (e.g. at low k_{\perp}).

Bibliography

- Ahn, J.-W., Canik, J., Soukhanovskii, V., Maingi, R. & Battaglia, D. 2010 Modification of divertor heat and particle flux profiles with applied 3D fields in NSTX H-mode plasmas. *Nucl. Fusion* **50** (4), 045010.
- Angus, J. R. & Umansky, M. V. 2014 Modeling of large amplitude plasma blobs in three-dimensions. *Phys. Plasmas* **21** (1), 012514.
- Angus, J. R., Umansky, M. V. & Krasheninnikov, S. I. 2012 Effect of drift waves on plasma blob dynamics. *Phys. Rev. Lett.* **108** (21), 215002.
- Antar, G. Y., Krasheninnikov, S. I., Devynck, P., Doerner, R. P., Hollmann, E. M., Boedo, J. A., Luckhardt, S. C. & Conn, R. W. 2001 Experimental evidence of intermittent convection in the edge of magnetic confinement devices. *Phys. Rev. Lett.* **87** (6), 065001.
- Archer, B. & Weisstein, E. W. 2005 Lagrange interpolating polynomial. From MathWorld—A Wolfram Web Resource. <http://mathworld.wolfram.com/LagrangeInterpolatingPolynomial.html>.
- Arnold, D. N. & Awanou, G. 2011 The serendipity family of finite elements. *Found. Comput. Math.* **11** (3), 337–344.
- Ball, J. S. 2002 Half-range generalized Hermite polynomials and the related Gaussian quadratures. *SIAM J. Numer. Anal.* **40** (6), 2311–2317.
- Barnes, M. 2008 Trinity: A unified treatment of turbulence, transport, and heating in magnetized plasmas. PhD thesis, University of Maryland, College Park.
- Batishchev, O. V., Krasheninnikov, S. I., Catto, P. J., Batishcheva, A. A., Sigmar, D. J., Xu, X. Q., Byers, J. A., Rognlien, T. D., Cohen, R. H., Shoucri, M. M. & Shkarofskii, I. P. 1997 Kinetic effects in tokamak scrape-off layer plasmas. *Phys. Plasmas* **4** (5), 1672–1680.
- Beer, M. A., Cowley, S. C. & Hammett, G. W. 1995 Fieldaligned coordinates for nonlinear simulations of tokamak turbulence. *Phys. Plasmas* **2** (7), 2687–2700.
- Belli, E. A. & Hammett, G. W. 2005 A numerical instability in an ADI algorithm for gyrokinetics. *Comput. Phys. Commun.* **172** (2), 119–132.

- Beyer, P., de Solminihac, F., Leconte, M., Garbet, X., Waelbroeck, F. L., Smolyakov, A. I. & Benkadda, S. 2011 Turbulence simulations of barrier relaxations and transport in the presence of magnetic islands at the tokamak edge. *Plasma Phys. Controlled Fusion* **53** (5), 054003.
- Birdsall, C. & Langdon, A. 2004 *Plasma Physics via Computer Simulation*. Taylor & Francis.
- Bisai, N., Das, A., Deshpande, S., Jha, R., Kaw, P., Sen, A. & Singh, R. 2005 Edge and scrape-off layer tokamak plasma turbulence simulation using two-field fluid model. *Phys. Plasmas* **12** (7), 072520.
- Boedo, J. 2009 Edge turbulence and SOL transport in tokamaks. *J. Nucl. Mater.* **390**, 29–37.
- Boedo, J., Rudakov, D., Colchin, R., Moyer, R., Krasheninnikov, S., Whyte, D., McKee, G., Porter, G., Schaffer, M., Stangeby, P., West, W., Allen, S. & Leonard, A. 2003 Intermittent convection in the boundary of DIII-D. *J. Nucl. Mater.* **313**, 813–819.
- Boedo, J. A., Crocker, N., Chousal, L., Hernandez, R., Chalfant, J., Kugel, H., Roney, P. & Wertenbaker, J. 2009 Fast scanning probe for the NSTX spherical tokamak. *Rev. Sci. Instrum.* **80** (12), 123506.
- Boedo, J. A., Myra, J. R., Zweben, S., Maingi, R., Maqueda, R. J., Soukhanovskii, V. A., Ahn, J. W., Canik, J., Crocker, N., D’Ippolito, D. A., Bell, R., Kugel, H., Leblanc, B., Roquemore, L. A. & Rudakov, D. L. 2014 Edge transport studies in the edge and scrape-off layer of the National Spherical Torus Experiment with Langmuir probes. *Phys. Plasmas* **21** (4), 042309.
- Borland, D. & Taylor II, R. M. 2007 Rainbow color map (still) considered harmful. *IEEE Comput. Graph. Appl. Mag.* **27** (2), 14–17.
- Bottino, A., Peeters, A. G., Hatzky, R., Jolliet, S., McMillan, B. F., Tran, T. M. & Villard, L. 2007 Nonlinear low noise particle-in-cell simulations of electron temperature gradient driven turbulence. *Phys. Plasmas* **14** (1), 010701.
- Bottino, A. & Sonnendrücker, E. 2015 Monte Carlo particle-in-cell methods for the simulation of the Vlasov–Maxwell gyrokinetic equations. *J. Plasma Phys.* **81** (5), 435810501.
- Brandt, C., Grulke, O., Klinger, T., Negrete, J., Bousselin, G., Brochard, F., Bonhomme, G. & Oldenbürger, S. 2011 Spatiotemporal mode structure of nonlinearly coupled drift wave modes. *Phys. Rev. E* **84** (5), 056405.
- Brizard, A. J. 2000a New variational principle for the Vlasov–Maxwell equations. *Phys. Rev. Lett.* **84** (25), 5768–5771.

- Brizard, A. J. 2000b Variational principle for nonlinear gyrokinetic Vlasov–Maxwell equations. *Phys. Plasmas* **7**, 4816–4822.
- Brizard, A. J. & Hahm, T. S. 2007 Foundations of nonlinear gyrokinetic theory. *Rev. Mod. Phys.* **79** (2), 421–468.
- Burin, M. J., Tynan, G. R., Antar, G. Y., Crocker, N. A. & Holland, C. 2005 On the transition to drift turbulence in a magnetized plasma column. *Phys. Plasmas* **12** (5), 052320.
- Cagas, P., Hakim, A., Juno, J. & Srinivasan, B. 2017 Continuum kinetic and multi-fluid simulations of classical sheaths. *Phys. Plasmas* **24** (2), 022118.
- Candy, J., Holland, C., Waltz, R. E., Fahey, M. R. & Belli, E. 2009 Tokamak profile prediction using direct gyrokinetic and neoclassical simulation. *Phys. Plasmas* **16** (6), 060704.
- Candy, J. & Waltz, R. 2003a An Eulerian gyrokinetic-Maxwell solver. *J. Comput. Phys.* **186** (2), 545–581.
- Candy, J. & Waltz, R. E. 2003b Anomalous transport scaling in the DIII-D tokamak matched by supercomputer simulation. *Phys. Rev. Lett.* **91** (4), 045001.
- Candy, J. & Waltz, R. E. 2006 Velocity-space resolution, entropy production, and upwind dissipation in Eulerian gyrokinetic simulations. *Phys. Plasmas* **13** (3), 032310.
- Carter, T. A. 2006 Intermittent turbulence and turbulent structures in a linear magnetized plasma. *Phys. Plasmas* **13** (1), 010701.
- Carter, T. A. & Maggs, J. E. 2009 Modifications of turbulence and turbulent transport associated with a bias-induced confinement transition in the Large Plasma Device. *Phys. Plasmas* **16** (1), 012304.
- Chang, C., Ku, S., Loarte, A., Parail, V., Kchl, F., Romanelli, M., Maingi, R., Ahn, J.-W., Gray, T., Hughes, J., LaBombard, B., Leonard, T., Makowski, M. & Terry, J. 2017 Gyrokinetic projection of the divertor heat-flux width from present tokamaks to ITER. *Nucl. Fusion* **57** (11), 116023.
- Chang, C. S., Ku, S., Diamond, P. H., Lin, Z., Parker, S., Hahm, T. S. & Samatova, N. 2009 Compressed ion temperature gradient turbulence in diverted tokamak edge. *Phys. Plasmas* **16** (5), 056108.
- Chang, J. & Cooper, G. 1970 A practical difference scheme for Fokker–Planck equations. *J. Comput. Phys.* **6** (1), 1–16.
- Chen, F. F. 1984 *Introduction to Plasma Physics and Controlled Fusion*. Springer US.
- Chen, Y. & Parker, S. 2001 Gyrokinetic turbulence simulations with kinetic electrons. *Phys. Plasmas* **8** (5), 2095–2100.

- Chen, Y. & Parker, S. E. 2003 A δf particle method for gyrokinetic simulations with kinetic electrons and electromagnetic perturbations. *J. Comput. Phys.* **189** (2), 463–475.
- Chodura, R. 1982 Plasma–wall transition in an oblique magnetic field. *Phys. Fluids* **25** (9), 1628–1633.
- Churchill, R., Canik, J., Chang, C., Hager, R., Leonard, A., Maingi, R., Nazikian, R. & Stotler, D. 2016 Kinetic simulations of scrape-off layer physics in the DIII-D tokamak. *Nucl. Mater. Energy* **0**, 1–6.
- Churchill, R., Chang, C. & Ku, S. 2017 Pedestal and edge turbulence characteristics from an XGC1 gyrokinetic simulation , arXiv: 1703.03015.
- Cockburn, B., Karniadakis, G. E. & Shu, C.-W., ed. 2000 *Discontinuous Galerkin Methods, Lecture Notes in Computational Science and Engineering*, vol. 11. Springer-Verlag Berlin Heidelberg.
- Cockburn, B. & Shu, C.-W. 1998a The local discontinuous Galerkin method for time-dependent convection-diffusion systems. *SIAM J. Numer. Anal.* **35** (6), 2440–2463.
- Cockburn, B. & Shu, C.-W. 1998b The Runge–Kutta discontinuous Galerkin method for conservation laws V. *J. Comput. Phys.* **141** (2), 199–224.
- Cockburn, B. & Shu, C.-W. 2001 Runge–Kutta discontinuous Galerkin methods for convection-dominated problems. *J. Sci. Comput.* **16** (3), 173–261.
- Cohen, B. I., Umansky, M. V., Nevins, W. M., Makowski, M. A., Boedo, J. A., Rudakov, D. L., McKee, G. R., Yan, Z. & Groebner, R. J. 2013 Simulations of drift resistive ballooning L-mode turbulence in the edge plasma of the DIII-D tokamak. *Phys. Plasmas* **20** (5), 055906.
- Cohen, R. H. & Xu, X. Q. 2008 Progress in kinetic simulation of edge plasmas. *Contrib. Plasma Phys.* **48** (1-3), 212–223.
- Colella, P., Dorr, M., Hittinger, J. & Martin, D. 2011 High-order, finite-volume methods in mapped coordinates. *J. Comput. Phys.* **230** (8), 2952–2976.
- Connor, J. W. & Wilson, H. R. 2000 A review of theories of the L–H transition. *Plasma Phys. Controlled Fusion* **42** (1), R1–R74.
- Dannert, T. & Jenko, F. 2004 Vlasov simulation of kinetic shear Alfvén waves. *Comput. Phys. Commun.* **163** (2), 67–78.
- Dekeyser, W., Baelmans, M., Voskoboynikov, S., Rozhansky, V., Reiter, D., Wiesen, S., Kotov, V. & Börner, P. 2011 B2–B2.5 code benchmarking. *Tech. Rep.* Jülich-4337. Jülich.
- Dimits, A. M. 2012 Gyrokinetic equations for strong-gradient regions. *Phys. Plasmas* **19** (2), 022504.

- Dimits, A. M., Bateman, G., Beer, M. A., Cohen, B. I., Dorland, W., Hammett, G. W., Kim, C., Kinsey, J. E., Kotschenreuther, M., Kritz, A. H., Lao, L. L., Mandrekas, J., Nevins, W. M., Parker, S. E., Redd, A. J., Shumaker, D. E., Sydora, R. & Weiland, J. 2000 Comparisons and physics basis of tokamak transport models and turbulence simulations. *Phys. Plasmas* **7** (3), 969–983.
- D'Ippolito, D. A., Myra, J. R. & Zweben, S. J. 2011 Convective transport by intermittent blob-filaments: Comparison of theory and experiment. *Phys. Plasmas* **18** (6), 060501.
- Dorf, M. A., Cohen, R. H., Compton, J. C., Dorr, M., Rognlien, T. D., Angus, J., Krasheninnikov, S., Colella, P., Martin, D. & McCorquodale, P. 2012 Progress with the COGENT edge kinetic code: Collision operator options. *Contrib. Plasma Phys.* **52** (5-6), 518–522.
- Dorf, M. A., Cohen, R. H., Dorr, M., Rognlien, T., Hittinger, J., Compton, J., Colella, P., Martin, D. & McCorquodale, P. 2013 Simulation of neoclassical transport with the continuum gyrokinetic code COGENT. *Phys. Plasmas* **20** (1), 012513.
- Dorf, M. A., Dorr, M. R., Hittinger, J. A., Cohen, R. H. & Rognlien, T. D. 2016 Continuum kinetic modeling of the tokamak plasma edge. *Phys. Plasmas* **23** (5), 056102.
- Dorland, W. & Hammett, G. W. 1993 Gyrofluid turbulence models with kinetic effects. *Phys. Fluids B* **5** (3), 812–835.
- Dorland, W., Jenko, F., Kotschenreuther, M. & Rogers, B. N. 2000 Electron temperature gradient turbulence. *Phys. Rev. Lett.* **85** (26), 5579–5582.
- Doyle, E., Houlberg, W., Kamada, Y., Mukhovatov, V., Osborne, T., Polevoi, A., Bateman, G., Connor, J., Cordey, J., Fujita, T., Garbet, X., Hahm, T., Horton, L., Hubbard, A., Imbeaux, F., Jenko, F., Kinsey, J., Kishimoto, Y., Li, J., Luce, T., Martin, Y., Ossipenko, M., Parail, V., Peeters, A., Rhodes, T., Rice, J., Roach, C., Rozhansky, V., Ryter, F., Saibene, G., Sartori, R., Sips, A., Snipes, J., Sugihara, M., Synakowski, E., Takenaga, H., Takizuka, T., Thomsen, K., Wade, M., Wilson, H., Transport Physics Topical Group, I., Confinement Database, I., Modelling Topical Group, Pedestal, I. & Edge Topical Group 2007 Chapter 2: Plasma confinement and transport. *Nucl. Fusion* **47** (6), S18–S127.
- Dudson, B. D., Allen, A., Breyiannis, G., Brugger, E., Buchanan, J., Easy, L., Farley, S., Joseph, I., Kim, M., McGann, A. D., Omotani, J. T., Umansky, M. V., Walkden, N. R., Xia, T. & Xu, X. Q. 2015 BOUT++: Recent and current developments. *J. Plasma Phys.* **81** (1), 365810104.
- Dudson, B. D. & Leddy, J. 2017 Hermes: global plasma edge fluid turbulence simulations. *Plasma Phys. Controlled Fusion* **59** (5), 054010.

- Dudson, B. D., Umansky, M. V., Xu, X. Q., Snyder, P. B. & Wilson, H. R. 2009 BOUT++: A framework for parallel plasma fluid simulations. *Comput. Phys. Commun.* **180** (9), 1467–1480.
- Durran, D. R. 2010 *Numerical Methods for Fluid Dynamics With Applications to Geophysics, Texts in Applied Mathematics*, vol. 32. Springer-Verlag New York.
- Eddins, S. L. 2014 Rainbow color map critiques: An overview and annotated bibliography. <https://mathworks.com/company/newsletters/articles/rainbow-color-map-critiques-an-overview-and-annotated-bibliography.html>.
- Eich, T., Leonard, A., Pitts, R., Fundamenski, W., Goldston, R., Gray, T., Herrmann, A., Kirk, A., Kallenbach, A., Kardaun, O., Kukushkin, A., LaBombard, B., Maingi, R., Makowski, M., Scarabosio, A., Sieglin, B., Terry, J., Thornton, A., ASDEX Upgrade Team & JET EFDA Contributors 2013 Scaling of the tokamak near the scrape-off layer H-mode power width and implications for ITER. *Nucl. Fusion* **53** (9), 093031.
- Eich, T., Sieglin, B., Scarabosio, A., Fundamenski, W., Goldston, R. J. & Herrmann, A. 2011 Inter-ELM power decay length for JET and ASDEX Upgrade: Measurement and comparison with Heuristic Drift-based model. *Phys. Rev. Lett.* **107** (21), 215001.
- Evans, T. E., Roeder, R. K. W., Carter, J. A., Rapoport, B. I., Fenstermacher, M. E. & Lasnier, C. J. 2005 Experimental signatures of homoclinic tangles in poloidally diverted tokamaks. *J. Phys. Conf. Ser.* **7** (1), 174–190.
- Fasoli, A., Labit, B., McGrath, M., Müller, S. H., Plyushchev, G., Podestà, M. & Poli, F. M. 2006 Electrostatic turbulence and transport in a simple magnetized plasma. *Phys. Plasmas* **13** (5), 055902.
- Fetterman, A. J. & Fisch, N. J. 2011 The magnetic centrifugal mass filter. *Phys. Plasmas* **18** (9), 094503.
- Fisher, D. M. & Rogers, B. N. 2017 Two-fluid biasing simulations of the large plasma device. *Phys. Plasmas* **24** (2), 022303.
- Fisher, D. M., Rogers, B. N., Rossi, G. D., Guice, D. S. & Carter, T. A. 2015 Three-dimensional two-fluid Braginskii simulations of the large plasma device. *Phys. Plasmas* **22** (9), 092121.
- Fitzpatrick, R. 2011 Braginskii equations. <http://farside.ph.utexas.edu/teaching/plasma/Plasmahtml/node35.html>.
- Franck, C. M., Grulke, O. & Klinger, T. 2002 Transition from unbounded to bounded plasma whistler wave dispersion. *Phys. Plasmas* **9** (8), 3254–3258.

- Friedman, B., Carter, T. A., Umansky, M. V., Schaffner, D. & Dudson, B. 2012 Energy dynamics in a simulation of LAPD turbulence. *Phys. Plasmas* **19** (10), 102307.
- Friedman, B., Carter, T. A., Umansky, M. V., Schaffner, D. & Joseph, I. 2013 Non-linear instability in simulations of Large Plasma Device turbulence. *Phys. Plasmas* **20** (5), 055704.
- Garbet, X., Idomura, Y., Villard, L. & Watanabe, T. 2010 Gyrokinetic simulations of turbulent transport. *Nucl. Fusion* **50** (4), 043002.
- Garcia, O. E., Naulin, V., Nielsen, A. H. & Rasmussen, J. J. 2006 Turbulence simulations of blob formation and radial propagation in toroidally magnetized plasmas. *Phys. Scripta* **2006** (T122), 89.
- Gekelman, W., Pfister, H., Lucky, Z., Bamber, J., Leneman, D. & Maggs, J. 1991 Design, construction, and properties of the large plasma research device—The LAPD at UCLA. *Rev. Sci. Instrum.* **62** (12), 2875–2883.
- Gekelman, W., Pribyl, P., Lucky, Z., Drandell, M., Leneman, D., Maggs, J., Vincena, S., Compernolle, B. V., Tripathi, S. K. P., Morales, G., Carter, T. A., Wang, Y. & DeHaas, T. 2016 The upgraded Large Plasma Device, a machine for studying frontier basic plasma physics. *Rev. Sci. Instrum.* **87** (2), 025105.
- Gentle, K. W. & He, H. 2008 Texas Helimak. *Plasma Sci. Tech.* **10** (3), 284–289.
- Gentle, K. W., Liao, K., Lee, K. & Rowan, W. L. 2010 Comparison of velocity shear with turbulence reduction driven by biasing in a simple cylindrical slab plasma. *Plasma Sci. Tech.* **12** (4), 391–396.
- Geraldini, A., Parra, F. I. & Militello, F. 2017 Gyrokinetic treatment of a grazing angle magnetic presheath. *Plasma Phys. Controlled Fusion* **59** (2), 025015.
- Gilmore, M., Lynn, A. G., Desjardins, T. R., Zhang, Y., Watts, C., Hsu, S. C., Betts, S., Kelly, R. & Schamiloglu, E. 2015 The HelCat basic plasma science device. *J. Plasma Phys.* **81** (1).
- Goldston, R. 2012 Heuristic drift-based model of the power scrape-off width in low-gas-puff H-mode tokamaks. *Nucl. Fusion* **52** (1), 013009.
- Goldston, R. 2015 Theoretical aspects and practical implications of the heuristic drift SOL model. *J. Nucl. Mater.* **463**, 397–400.
- Görler, T., White, A. E., Told, D., Jenko, F., Holland, C. & Rhodes, T. L. 2014 A flux-matched gyrokinetic analysis of DIII-D L-mode turbulence. *Phys. Plasmas* **21** (12), 122307.

- Gormezano, C., Sips, A., Luce, T., Ide, S., Becoulet, A., Litaudon, X., Isayama, A., Hobirk, J., Wade, M., Oikawa, T., Prater, R., Zvonkov, A., Lloyd, B., Suzuki, T., Barbato, E., Bonoli, P., Phillips, C., Vdovin, V., Joffrin, E., Casper, T., Ferron, J., Mazon, D., Moreau, D., Bundy, R., Kessel, C., Fukuyama, A., Hayashi, N., Imbeaux, F., Murakami, M., Polevoi, A. & John, H. S. 2007 Chapter 6: Steady state operation. *Nucl. Fusion* **47** (6), S285–S336.
- Gottlieb, S., Shu, C.-W. & Tadmor, E. 2001 Strong stability-preserving high-order time discretization methods. *SIAM Rev.* **43** (1), 89–112.
- Grandgirard, V., Brunetti, M., Bertrand, P., Besse, N., Garbet, X., Ghendrih, P., Manfredi, G., Sarazin, Y., Sauter, O., Sonnendrücker, E., Vaclavik, J. & Villard, L. 2006 A drift-kinetic Semi-Lagrangian 4D code for ion turbulence simulation. *J. Comput. Phys.* **217** (2), 395–423.
- Grandgirard, V., Sarazin, Y., Angelino, P., Bottino, A., Crouseilles, N., Darmet, G., Dif-Pradalier, G., Garbet, X., Ghendrih, P., Jolliet, S., Latu, G., Sonnendrücker, E. & Villard, L. 2007 Global full- f gyrokinetic simulations of plasma turbulence. *Plasma Phys. Controlled Fusion* **49** (12B), B173–B182.
- Grulke, O., Terry, J. L., LaBombard, B. & Zweben, S. J. 2006 Radially propagating fluctuation structures in the scrape-off layer of Alcator C-Mod. *Phys. Plasmas* **13** (1), 012306.
- Gueroult, R., Evans, E. S., Zweben, S. J., Fisch, N. J. & Levinton, F. 2016 Initial experimental test of a helicon plasma based mass filter. *Plasma Sources Sci. Technol.* **25** (3), 035024.
- Gueroult, R. & Fisch, N. J. 2014 Plasma mass filtering for separation of actinides from lanthanides. *Plasma Sources Sci. Technol.* **23** (3), 035002.
- Hahm, T. S., Wang, L. & Madsen, J. 2009 Fully electromagnetic nonlinear gyrokinetic equations for tokamak edge turbulence. *Phys. Plasmas* **16** (2), 022305.
- Halpern, F., Ricci, P., Jolliet, S., Loizu, J., Morales, J., Mosetto, A., Musil, F., Riva, F., Tran, T. & Wersal, C. 2016 The GBS code for tokamak scrape-off layer simulations. *J. Comput. Phys.* **315**, 388–408.
- Halpern, F. D., LaBombard, B., Terry, J. L. & Zweben, S. J. 2017 Outer midplane scrape-off layer profiles and turbulence in simulations of Alcator C-Mod inner-wall limited discharges. *Phys. Plasmas* **24** (7), 072502.
- Halpern, F. D., Terry, J. L., Zweben, S. J., LaBombard, B., Podesta, M. & Ricci, P. 2015 Comparison of 3D flux-driven scrape-off layer turbulence simulations with gas-puff imaging of Alcator C-Mod inner-wall limited discharges. *Plasma Phys. Controlled Fusion* **57** (5), 054005.

- Hammett, G. W., Beer, M. A., Dorland, W., Cowley, S. C. & Smith, S. A. 1993 Developments in the gyrofluid approach to tokamak turbulence simulations. *Plasma Phys. Controlled Fusion* **35** (8), 973–985.
- Hatzky, R., Knies, A. & Mishchenko, A. 2007 Electromagnetic gyrokinetic PIC simulation with an adjustable control variates method. *J. Comput. Phys.* **225** (1), 568–590.
- Havlíčková, E., Fundamenski, W., Tskhakaya, D., Manfredi, G. & Moulton, D. 2012 Comparison of fluid and kinetic models of target energy fluxes during edge localized modes. *Plasma Phys. Controlled Fusion* **54** (4), 045002.
- Heikkinen, J., Janhunen, S., Kiviniemi, T. & Ogando, F. 2008 Full f gyrokinetic method for particle simulation of tokamak transport. *J. Comput. Phys.* **227** (11), 5582–5609.
- Hesthaven, J. & Warburton, T. 2008 *Nodal Discontinuous Galerkin Methods: Algorithms, Analysis, and Applications. Texts in Applied Mathematics*. Springer New York.
- Hu, G. & Krommes, J. A. 1994 Generalized weighting scheme for δf particle-simulation method. *Phys. Plasmas* **1** (4), 863–874.
- Huba, J. D. 2013 *NRL Plasma Formulary*. Washington, DC: Naval Research Laboratory.
- Huber, A., Samm, U., Schweer, B. & Mertens, P. 2005 Results from a double Li-beam technique for measurement of both radial and poloidal components of electron density fluctuations using two thermal beams. *Plasma Phys. Controlled Fusion* **47** (3), 409–440.
- Idomura, Y. 2012 Accuracy of momentum transport calculations in full- f gyrokinetic simulations. *Comput. Sci. Discov.* **5** (1), 014018.
- Idomura, Y. 2014 Full- f gyrokinetic simulation over a confinement time. *Phys. Plasmas* **21** (2), 022517.
- Idomura, Y., Urano, H., Aiba, N. & Tokuda, S. 2009 Study of ion turbulent transport and profile formations using global gyrokinetic full- f vlasov simulation. *Nucl. Fusion* **49** (6), 065029.
- Ierusalimschy, R., de Figueiredo, L. H. & Filho, W. C. 1996 Lua—an extensible extension language. *Softw. Pract. Exper.* **26** (6), 635–652.
- Jakubowski, M., Evans, T., Fenstermacher, M., Groth, M., Lasnier, C., Leonard, A., Schmitz, O., Watkins, J., Eich, T., Fundamenski, W., Moyer, R., Wolf, R., Baylor, L., Boedo, J., Burrell, K., Frerichs, H., deGrassie, J., Gohil, P., Joseph, I., Mordijk, S., Lehnert, M., Petty, C., Pinsker, R., Reiter, D., Rhodes, T., Samm, U., Schaffer, M., Snyder, P., Stoschus, H., Osborne, T., Unterberg, B., Unterberg, E.

- & West, W. 2009 Overview of the results on divertor heat loads in RMP controlled H-mode plasmas on DIII-D. *Nucl. Fusion* **49** (9), 095013.
- Jenko, F. 2000 Massively parallel Vlasov simulation of electromagnetic drift-wave turbulence. *Comput. Phys. Commun.* **125** (1), 196–209.
- Jenko, F. & Dorland, W. 2001 Nonlinear electromagnetic gyrokinetic simulations of tokamak plasmas. *Plasma Phys. Controlled Fusion* **43** (12A), A141–A150.
- Juno, J., Hakim, A., TenBarge, J., Shi, E. & Dorland, W. 2017 Discontinuous Galerkin algorithms for fully kinetic plasmas , arXiv: 1705.05407.
- Kardaun, O., Thomsen, K. & Chudnovskiy, A. 2008 Corrections to a sequence of papers in Nuclear Fusion. *Nucl. Fusion* **48** (9), 099801.
- Kaw, P. & Bandyopadhyay, I. 2012 The case for fusion. In *Fusion Physics* (ed. M. Kikuchi, K. Lackner & M. Q. Tran), pp. 1–58. International Atomic Energy Agency.
- Kawai, C., Idomura, Y., Maeyama, S. & Ogawa, Y. 2017 Impact of plasma parameter on self-organization of electron temperature gradient driven turbulence. *Phys. Plasmas* **24** (4), 042303.
- Kendl, A., Scott, B. D. & Ribeiro, T. T. 2010 Nonlinear gyrofluid computation of edge localized ideal ballooning modes. *Phys. Plasmas* **17** (7), 072302.
- Kinsey, J., Staebler, G., Candy, J., Waltz, R. & Budny, R. 2011 ITER predictions using the GYRO verified and experimentally validated trapped gyro-Landau fluid transport model. *Nucl. Fusion* **51** (8), 083001.
- Kleiber, R., Hatzky, R., Könies, A., Mishchenko, A. & Sonnendrücker, E. 2016 An explicit large time step particle-in-cell scheme for nonlinear gyrokinetic simulations in the electromagnetic regime. *Phys. Plasmas* **23** (3), 032501.
- Korpilo, T., Gurevich, A., Gusakov, E., Heikkilä, J., Janhunen, S., Kiviniemi, T., Leerink, S., Niskala, P. & Perevalov, A. 2016 Gyrokinetic full-torus simulations of ohmic tokamak plasmas in circular limiter configuration. *Comput. Phys. Commun.* **203**, 128–137.
- Kotschenreuther, M., Dorland, W., Beer, M. A. & Hammett, G. W. 1995 Quantitative predictions of tokamak energy confinement from first-principles simulations with kinetic effects. *Phys. Plasmas* **2** (6), 2381–2389.
- Kotschenreuther, M., Mahajan, S., Valanju, P. M., Covele, B., Waelbroeck, F. L., Canik, J. M. & LaBombard, B. 2016 Taming the heat flux problem: Advanced divertors towards fusion power. *J. Fusion Energ.* **35** (1), 27–30.
- Kočan, M., Gennrich, F. P., Kendl, A., Müller, H. W. & the ASDEX Upgrade Team 2012 Ion temperature fluctuations in the ASDEX upgrade scrape-off layer. *Plasma Phys. Controlled Fusion* **54** (8), 085009.

- Kočan, M., Gunn, J., Carpentier-Chouchana, S., Herrmann, A., Kirk, A., Komm, M., Müller, H., Pascal, J.-Y., Pitts, R., Rohde, V. & Tamain, P. 2011 Measurements of ion energies in the tokamak plasma boundary. *J. Nucl. Mater.* **415** (1, Supplement), S1133–S1138.
- Kramer, D. 2016 ITER costs are pinned down, with caveats. *Phys. Today* .
- Krasheninnikov, S. 2001 On scrape off layer plasma transport. *Phys. Lett. A* **283** (5), 368–370.
- Krasheninnikov, S. 2016 On the origin of plasma density blobs. *Phys. Lett. A* **380** (46), 3905 – 3907.
- Krasheninnikov, S. I., D’Ippolito, D. A. & Myra, J. R. 2008 Recent theoretical progress in understanding coherent structures in edge and SOL turbulence. *J. Plasma Phys.* **74** (5), 679–717.
- Krasheninnikov, S. I. & Smolyakov, A. I. 2003 On neutral wind and blob motion in linear devices. *Phys. Plasmas* **10** (7), 3020–3021.
- Krommes, J. A. 2007 Nonequilibrium gyrokinetic fluctuation theory and sampling noise in gyrokinetic particle-in-cell simulations. *Phys. Plasmas* **14** (9), 090501.
- Krommes, J. A. 2010 Nonlinear gyrokinetics: a powerful tool for the description of microturbulence in magnetized plasmas. *Phys. Scripta* **2010** (T142), 014035.
- Krommes, J. A. 2012 The gyrokinetic description of microturbulence in magnetized plasmas. *Annu. Rev. Fluid Mech.* **44**, 175–201.
- Krommes, J. A. 2013 The physics of the second-order gyrokinetic magnetohydrodynamic Hamiltonian: μ conservation, galilean invariance, and ponderomotive potential. *Phys. Plasmas* **20** (12), 124501.
- Krommes, J. A. & Hu, G. 1994 The role of dissipation in the theory and simulations of homogeneous plasma turbulence, and resolution of the entropy paradox. *Phys. Plasmas* **1** (10), 3211–3238.
- Ku, S., Hager, R., Chang, C., Kwon, J. & Parker, S. 2016 A new hybrid-Lagrangian numerical scheme for gyrokinetic simulation of tokamak edge plasma. *J. Comput. Phys.* **315**, 467–475.
- Kukushkin, A., Pacher, H., Pacher, G., Kotov, V., Pitts, R. & Reiter, D. 2013 Consequences of a reduction of the upstream power SOL width in ITER. *J. Nucl. Mater.* **438**, S203–S207.
- Lackner, K., Günter, S., Lauber, P., Pautasso, G. & Scott, B. D. 2012 Equilibrium and macroscopic stability of tokamaks. In *Fusion Physics* (ed. M. Kikuchi, K. Lackner & M. Q. Tran), pp. 225–359. International Atomic Energy Agency.

- Landreman, M. & Ernst, D. R. 2013 New velocity-space discretization for continuum kinetic calculations and Fokker-Planck collisions. *J. Comput. Phys.* **243**, 130–150.
- Lapillonne, X., McMillan, B. F., Görler, T., Brunner, S., Dannert, T., Jenko, F., Merz, F. & Villard, L. 2010 Nonlinear quasisteady state benchmark of global gyrokinetic codes. *Phys. Plasmas* **17** (11), 112321.
- Leddy, J. & Dudson, B. 2017 Intrinsic suppression of turbulence in linear plasma devices , arXiv: 1706.04550.
- Lee, W. W. 1983 Gyrokinetic approach in particle simulation. *Phys. Fluids* **26** (2), 556–562.
- Lee, W. W. 1987 Gyrokinetic particle simulation model. *J. Comput. Phys.* **72** (1), 243–269.
- van Leer, B., Lo, M. & van Raalte, M. 2007 A discontinuous Galerkin method for diffusion based on recovery. In *18th AIAA computational fluid dynamics conference*. American Institute of Aeronautics and Astronautics.
- van Leer, B. & Nomura, S. 2005 *Discontinuous Galerkin for Diffusion*. American Institute of Aeronautics and Astronautics.
- Lenard, A. & Bernstein, I. B. 1958 Plasma oscillations with diffusion in velocity space. *Phys. Rev.* **112** (5), 1456–1459.
- Leneman, D., Gekelman, W. & Maggs, J. 2006 The plasma source of the Large Plasma Device at University of California, Los Angeles. *Rev. Sci. Instrum.* **77** (1), 015108.
- Leonard, A. W. 2014 Edge-localized-modes in tokamaks. *Phys. Plasmas* **21** (9), 090501.
- LeVeque, R. J. 2002 *Finite volume methods for hyperbolic problems. Cambridge texts in applied mathematics* . Cambridge, New York: Cambridge University Press.
- Li, B., Rogers, B. N., Ricci, P., Gentle, K. W. & Bhattacharjee, A. 2011 Turbulence and bias-induced flows in simple magnetized toroidal plasmas. *Phys. Rev. E* **83** (5), 056406.
- Li, B., Wang, X. Y., Sun, C. K., Meng, C., Zhou, A. & Liu, D. 2017 Edge transport bifurcation in plasma resistive interchange turbulence. *Phys. Plasmas* **24** (5), 055905.
- Li, B., Wang, X. Y., Sun, C. K., Zhou, A., Liu, D., Ma, C. H. & Wang, X. G. 2016 Bifurcation and hysteresis of plasma edge transport in a flux-driven system. *Phys. Rev. E* **94** (4), 043201.
- Li, J., Guo, H. Y., McCracken, G. M. & Chen, J. L. 2012 Plasma–wall interactions. In *Fusion Physics* (ed. M. Kikuchi, K. Lackner & M. Q. Tran), pp. 756–846. International Atomic Energy Agency.

- Lipschultz, B., Coenen, J., Barnard, H., Howard, N., Reinke, M., Whyte, D. & Wright, G. 2012 Divertor tungsten tile melting and its effect on core plasma performance. *Nucl. Fusion* **52** (12), 123002.
- Liu, J.-G. & Shu, C.-W. 2000 A high-order discontinuous Galerkin method for 2D incompressible flows. *J. Comput. Phys.* **160** (2), 577–596.
- Loarte, A., Lipschultz, B., Kukushkin, A., Matthews, G., Stangeby, P., Asakura, N., Counsell, G., Federici, G., Kallenbach, A., Krieger, K., Mahdavi, A., Philipps, V., Reiter, D., Roth, J., Strachan, J., Whyte, D., Doerner, R., Eich, T., Fundamenski, W., Herrmann, A., Fenstermacher, M., Ghendrih, P., Groth, M., Kirschner, A., Konoshima, S., LaBombard, B., Lang, P., Leonard, A., Monier-Garbet, P., Neu, R., Pacher, H., Pegourie, B., Pitts, R., Takamura, S., Terry, J., Tsitrone, E. & the ITPA Scrape-off Layer and Divertor Physics Topical Group 2007 Chapter 4: Power and particle control. *Nucl. Fusion* **47** (6), S203–S263.
- Loizu, J., Ricci, P., Halpern, F. D. & Jolliet, S. 2012 Boundary conditions for plasma fluid models at the magnetic presheath entrance. *Phys. Plasmas* **19** (12), 122307.
- Lysak, R. L. & Lotko, W. 1996 On the kinetic dispersion relation for shear Alfvén waves. *J. Geophys. Res. Space Phys.* **101** (A3), 5085–5094.
- Maggs, J. E., Carter, T. A. & Taylor, R. J. 2007 Transition from Bohm to classical diffusion due to edge rotation of a cylindrical plasma. *Phys. Plasmas* **14** (5), 052507.
- Makowski, M. A., Elder, D., Gray, T. K., LaBombard, B., Lasnier, C. J., Leonard, A. W., Maingi, R., Osborne, T. H., Stangeby, P. C., Terry, J. L. & Watkins, J. 2012 Analysis of a multi-machine database on divertor heat fluxes. *Phys. Plasmas* **19** (5), 056122.
- Manfredi, G., Hirstoaga, S. & Devaux, S. 2011 Vlasov modelling of parallel transport in a tokamak scrape-off layer. *Plasma Phys. Control. Fusion* **53** (1), 015012.
- McMillan, B. F., Lapillonne, X., Brunner, S., Villard, L., Jolliet, S., Bottino, A., Görler, T. & Jenko, F. 2010 System size effects on gyrokinetic turbulence. *Phys. Rev. Lett.* **105** (15), 155001.
- McMillan, B. F. & Sharma, A. 2016 A very general electromagnetic gyrokinetic formalism. *Phys. Plasmas* **23** (9), 092504.
- Meyer, C. D., Balsara, D. S. & Aslam, T. D. 2014 A stabilized Runge–Kutta–Legendre method for explicit super-time-stepping of parabolic and mixed equations. *J. Comput. Phys.* **257**, Part A, 594–626.
- Mishchenko, A., Hatzky, R. & Knies, A. 2004 Conventional δf -particle simulations of electromagnetic perturbations with finite elements. *Phys. Plasmas* **11** (12), 5480–5486.

- Mishchenko, A., Knies, A., Kleiber, R. & Cole, M. 2014 Pullback transformation in gyrokinetic electromagnetic simulations. *Phys. Plasmas* **21** (9), 092110.
- Mitchell, D. A., Berovic, M. & Krieger, N. 2000 Biochemical engineering aspects of solid state bioprocessing. In *New Products and New Areas of Bioprocess Engineering* (ed. T. Scheper), pp. 61–138. Springer Berlin Heidelberg.
- Mosetto, A. 2014 Turbulent regimes in the tokamak scrape-off layer. PhD thesis, École Polytechnique Fédérale de Lausanne.
- Mosetto, A., Halpern, F. D., Jollet, S., Loizu, J. & Ricci, P. 2013 Turbulent regimes in the tokamak scrape-off layer. *Phys. Plasmas* **20** (9), 092308.
- Munz, C.-D. 1994 A tracking method for gas flow into vacuum based on the vacuum riemann problem. *Math Methods Appl. Sci.* **17** (8), 597–612.
- Myra, J. R., D'Ippolito, D. A., Krasheninnikov, S. I. & Yu, G. Q. 2004 Convective transport in the scrape-off-layer by nonthermalized spinning blobs. *Phys. Plasmas* **11** (9), 4267–4274.
- Naulin, V. 2007 Turbulent transport and the plasma edge. *J. Nucl. Mater.* **363**, 24–31.
- Naulin, V., Windisch, T. & Grulke, O. 2008 Three-dimensional global fluid simulations of cylindrical magnetized plasmas. *Phys. Plasmas* **15** (1), 012307.
- Nevins, W. M., Hammett, G. W., Dimits, A. M., Dorland, W. & Shumaker, D. E. 2005 Discrete particle noise in particle-in-cell simulations of plasma microturbulence. *Phys. Plasmas* **12** (12), 122305.
- Ng, J., Huang, Y.-M., Hakim, A., Bhattacharjee, A., Stanier, A., Daughton, W., Wang, L. & Germaschewski, K. 2015 The island coalescence problem: Scaling of reconnection in extended fluid models including higher-order moments. *Phys. Plasmas* **22** (11), 112104.
- Numata, R., Howes, G. G., Tatsuno, T., Barnes, M. & Dorland, W. 2010 AstroGK: Astrophysical gyrokinetics code. *J. Comput. Phys.* **229** (24), 9347–9372.
- Ochs, I. E., Gueroult, R., Fisch, N. J. & Zweben, S. J. 2017 Collisional considerations in axial-collection plasma mass filters. *Phys. Plasmas* **24** (4), 043503.
- Omotani, J. & Dudson, B. 2013 Non-local approach to kinetic effects on parallel transport in fluid models of the scrape-off layer. *Plasma Phys. Control. Fusion* **55** (5), 055009.
- Pan, Q., Told, D. & Jenko, F. 2016 Fully nonlinear δf gyrokinetics for scrape-off layer parallel transport. *Phys. Plasmas* **23** (10), 102302.
- Park, G. Y., Kim, S. S., Jhang, H., Diamond, P. H., Rhee, T. & Xu, X. Q. 2015 Flux-driven simulations of turbulence collapse. *Phys. Plasmas* **22** (3), 032505.

- Parker, S. E., Procassini, R. J., Birdsall, C. K. & Cohen, B. I. 1993 A suitable boundary condition for bounded plasma simulation without sheath resolution. *J. Comput. Phys.* **104** (1), 41–49.
- Parra, F. I. & Calvo, I. 2011 Phase-space Lagrangian derivation of electrostatic gyrokinetics in general geometry. *Plasma Phys. Controlled Fusion* **53** (4), 045001.
- Parra, F. I., Calvo, I., Burby, J. W., Squire, J. & Qin, H. 2014 Equivalence of two independent calculations of the higher order guiding center Lagrangian. *Phys. Plasmas* **21** (10), 104506.
- Peterson, J. L. & Hammett, G. W. 2013 Positivity preservation and advection algorithms with applications to edge plasma turbulence. *SIAM J. Sci. Comput.* **35** (3), B576–B605.
- Phillips, P., Wootton, A., Rowan, W., Ritz, C., Rhodes, T., Bengtson, R., Hodge, W., Durst, R., McCool, S., Richards, B., Gentle, K., Brower, D., Peebles, W., Luhmann, N., Schoch, P., Forster, J., Hickok, R. & Evans, T. 1987 Biased limiter experiments on TEXT. *J. Nucl. Mater.* **145–147**, 807–811.
- Pierre, T., Leclert, G. & Braun, F. 1987 Magnetized double-plasma device for wave studies. *Rev. Sci. Instrum.* **58** (1), 6–11.
- Pitts, R., Andrew, P., Arnoux, G., Eich, T., Fundamenski, W., Huber, A., Silva, C., Tskhakaya, D. & JET EFDA Contributors 2007 ELM transport in the JET scrape-off layer. *Nucl. Fusion* **47** (11), 1437–1448.
- Pitts, R. A., Coad, J. P., Coster, D. P., Federici, G., Fundamenski, W., Horacek, J., Krieger, K., Kukushkin, A., Likonen, J., Matthews, G. F., Rubel, M., Strachan, J. D. & JET EFDA Contributors 2005 Material erosion and migration in tokamaks. *Plasma Phys. Control. Fusion* **47** (12B), B303–B322.
- Popovich, P., Umansky, M. V., Carter, T. A. & Friedman, B. 2010a Analysis of plasma instabilities and verification of the BOUT code for the Large Plasma Device. *Phys. Plasmas* **17** (10), 102107.
- Popovich, P., Umansky, M. V., Carter, T. A. & Friedman, B. 2010b Modeling of plasma turbulence and transport in the Large Plasma Device. *Phys. Plasmas* **17** (12), 122312.
- Powers, E. 1974 Spectral techniques for experimental investigation of plasma diffusion due to polychromatic fluctuations. *Nucl. Fusion* **14** (5), 749–752.
- Press, W. H., Teukolsky, S. A., Vetterling, W. T. & Flannery, B. P. 2007 *Numerical Recipes 3rd Edition: The Art of Scientific Computing*, 3rd edn. New York, NY, USA: Cambridge University Press.
- Reiter, D., Baelmans, M. & Brner, P. 2005 The EIRENE and B2-EIRENE codes. *Fusion Sci. Technol.* **47** (2), 172–186.

- Remacle, J.-F., Flaherty, J. E. & Shephard, M. S. 2003 An adaptive discontinuous Galerkin technique with an orthogonal basis applied to compressible flow problems. *SIAM Rev.* **45** (1), 53–72.
- Rewoldt, G., Lin, Z. & Idomura, Y. 2007 Linear comparison of gyrokinetic codes with trapped electrons. *Comput. Phys. Commun.* **177** (10), 775–780.
- Ribeiro, T. T. & Scott, B. 2005 Tokamak turbulence computations on closed and open magnetic flux surfaces. *Plasma Phys. Controlled Fusion* **47** (10), 1657–1679.
- Ribeiro, T. T. & Scott, B. 2008 Gyrofluid turbulence studies of the effect of the poloidal position of an axisymmetric Debye sheath. *Plasma Phys. Controlled Fusion* **50** (5), 055007.
- Ricci, P. 2015 Simulation of the scrape-off layer region of tokamak devices. *J. Plasma Phys.* **81** (2).
- Ricci, P., Riva, F., Theiler, C., Fasoli, A., Furno, I., Halpern, F. D. & Loizu, J. 2015 Approaching the investigation of plasma turbulence through a rigorous verification and validation procedure: A practical example. *Phys. Plasmas* **22** (5), 055704.
- Ricci, P. & Rogers, B. N. 2009 Three-dimensional fluid simulations of a simple magnetized toroidal plasma. *Phys. Plasmas* **16** (9), 092307.
- Ricci, P. & Rogers, B. N. 2010 Turbulence phase space in simple magnetized toroidal plasmas. *Phys. Rev. Lett.* **104** (14), 145001.
- Ricci, P. & Rogers, B. N. 2013 Plasma turbulence in the scrape-off layer of tokamak devices. *Phys. Plasmas* **20** (1), 010702.
- Ricci, P., Rogers, B. N. & Brunner, S. 2008 High- and low-confinement modes in simple magnetized toroidal plasmas. *Phys. Rev. Lett.* **100** (22), 225002.
- Ricci, P., Theiler, C., Fasoli, A., Furno, I., Gustafson, K., Iraji, D. & Loizu, J. 2011 Methodology for turbulence code validation: Quantification of simulation-experiment agreement and application to the TORPEX experiment. *Phys. Plasmas* **18** (3), 032109.
- Ricci, P., Theiler, C., Fasoli, A., Furno, I., Labit, B., M'uller, S. H., Podestá, M. & Poli, F. M. 2009 Langmuir probe-based observables for plasma-turbulence code validation and application to the TORPEX basic plasma physics experiments). *Phys. Plasmas* **16** (5), 055703.
- Riva, F., Colin, C., Denis, J., Easy, L., Furno, I., Madsen, J., Militello, F., Naulin, V., Nielsen, A. H., Olsen, J. M. B., Omotani, J. T., Rasmussen, J. J., Ricci, P., Serre, E., Tamain, P. & Theiler, C. 2016 Blob dynamics in the TORPEX experiment: a multi-code validation. *Plasma Phys. Controlled Fusion* **58** (4), 044005.

- Rogers, B. N. & Ricci, P. 2010 Low-frequency turbulence in a linear magnetized plasma. *Phys. Rev. Lett.* **104** (22), 225002.
- Rognlien, T. D., Brown, P. N., Campbell, R. B., Kaiser, T. B., Knoll, D. A., McHugh, P. R., Porter, G. D., Rensink, M. E. & Smith, G. R. 1994 2-D fluid transport simulations of gaseous/radiative divertors. *Contrib. Plasma Phys.* **34** (2-3), 362–367.
- Rognlien, T. D., Ryutov, D. D., Mattor, N. & Porter, G. D. 1999 Two-dimensional electric fields and drifts near the magnetic separatrix in divertor tokamaks. *Phys. Plasmas* **6** (5), 1851–1857.
- Rognlien, T. D., Umansky, M. V., Xu, X. Q. & Cohen, R. H. 2004 Self-consistent simulation of turbulence and transport in tokamak edge plasmas. *Contrib. Plasma Phys.* **44** (1-3), 188–193.
- Rogowitz, B. E. & Treinish, L. A. 1998 Data visualization: the end of the rainbow. *IEEE Spectr.* **35** (12), 52–59.
- Rood, R. B. 1987 Numerical advection algorithms and their role in atmospheric transport and chemistry models. *Rev. Geophys.* **25** (1), 71–100.
- Rosenbluth, M. N., MacDonald, W. M. & Judd, D. L. 1957 Fokker–Planck equation for an inverse-square force. *Phys. Rev.* **107** (1), 1–6.
- Rossmannith, J. A. & Seal, D. C. 2011 A positivity-preserving high-order semi-Lagrangian discontinuous Galerkin scheme for the Vlasov–Poisson equations. *J. Comput. Phys.* **230** (16), 6203–6232.
- Rozhansky, V., Kaveeva, E., Molchanov, P., Veselova, I., Voskoboynikov, S., Coster, D., Counsell, G., Kirk, A., Lisgo, S., the ASDEX-Upgrade Team & the MAST Team 2009 New B2SOLPS5.2 transport code for H-mode regimes in tokamaks. *Nucl. Fusion* **49** (2), 025007.
- Rudakov, D., Boedo, J., Moyer, R., Stangeby, P., Watkins, J., Whyte, D., Zeng, L., Brooks, N., Doerner, R., Evans, T., Fenstermacher, M., Groth, M., Hollmann, E., Krasheninnikov, S., Lasnier, C., Leonard, A., Mahdavi, M., McKee, G., McLean, A., Pigarov, A., Wampler, W., Wang, G., West, W. & Wong, C. 2005 Far SOL transport and main wall plasma interaction in DIII-D. *Nucl. Fusion* **45** (12), 1589–1599.
- Ryutov, D. D., Cohen, R. H., Rognlien, T. D. & Umansky, M. V. 2008 The magnetic field structure of a snowflake divertor. *Phys. Plasmas* **15** (9), 092501.
- Schaffner, D. A. 2013 Study of flow, turbulence and transport on the Large Plasma Device. PhD thesis, Princeton University.

- Schaffner, D. A., Carter, T. A., Rossi, G. D., Guice, D. S., Maggs, J. E., Vincena, S. & Friedman, B. 2012 Modification of turbulent transport with continuous variation of flow shear in the Large Plasma Device. *Phys. Rev. Lett.* **109** (13), 135002.
- Schaffner, D. A., Carter, T. A., Rossi, G. D., Guice, D. S., Maggs, J. E., Vincena, S. & Friedman, B. 2013 Turbulence and transport suppression scaling with flow shear on the Large Plasma Device. *Phys. Plasmas* **20** (5), 055907.
- Schekochihin, A. A., Cowley, S. C., Dorland, W., Hammett, G. W., Howes, G. G., Quataert, E. & Tatsuno, T. 2009 Astrophysical gyrokinetics: Kinetic and fluid turbulent cascades in magnetized weakly collisional plasmas. *Astrophys. J. Suppl. S.* **182** (1), 310–377.
- Schneider, R., Bonnin, X., Borrass, K., Coster, D. P., Kastelawicz, H., Reiter, D., Rozhansky, V. A. & Braams, B. J. 2006 Plasma edge physics with B2-Eirene. *Contrib. Plasma Phys.* **46** (1-2), 3–191.
- Schneider, R., Reiter, D., Zehrfeld, H., Braams, B., Baelmans, M., Geiger, J., Kastelawicz, H., Neuhauser, J. & Wunderlich, R. 1992 B2-EIRENE simulation of ASDEX and ASDEX-Upgrade scrape-off layer plasmas. *J. Nucl. Mater.* **196**, 810–815.
- Schneider, R. & Runov, A. 2007 Challenges in plasma edge fluid modelling. *Plasma Phys. Controlled Fusion* **49** (7), S87–S95.
- Scott, B. 1997 Three-dimensional computation of drift Alfvén turbulence. *Plasma Phys. Controlled Fusion* **39** (10), 1635.
- Scott, B. 1998 Global consistency for thin flux tube treatments of toroidal geometry. *Phys. Plasmas* **5** (6), 2334–2339.
- Scott, B. 2006a Gyrokinetic study of the edge shear layer. *Plasma Phys. Controlled Fusion* **48** (5A), A387–A392.
- Scott, B., Kendl, A. & Ribeiro, T. 2010 Nonlinear dynamics in the tokamak edge. *Contrib. Plasma Phys.* **50** (3-5), 228–241.
- Scott, B. & Smirnov, J. 2010 Energetic consistency and momentum conservation in the gyrokinetic description of tokamak plasmas. *Phys. Plasmas* **17** (11), 112302.
- Scott, B. D. 2003 Computation of electromagnetic turbulence and anomalous transport mechanisms in tokamak plasmas. *Plasma Phys. Controlled Fusion* **45** (12A), A385.
- Scott, B. D. 2005a Drift wave versus interchange turbulence in tokamak geometry: Linear versus nonlinear mode structure. *Phys. Plasmas* **12** (6), 062314.
- Scott, B. D. 2005b Energetics of the interaction between electromagnetic ExB turbulence and zonal flows. *New J. Phys.* **7** (1), 92.

- Scott, B. D. 2006*b* Edge turbulence and its interaction with the equilibrium. *Contrib. Plasma Phys.* **46** (7-9), 714–725.
- Scott, B. D. 2007*a* Nonlinear polarization and dissipative correspondence between low-frequency fluid and gyrofluid equations. *Phys. Plasmas* **14** (10), 102318.
- Scott, B. D. 2007*b* Tokamak edge turbulence: background theory and computation. *Plasma Phys. Controlled Fusion* **49** (7), S25–S41.
- Shanahan, B. W. & Dudson, B. D. 2016 Blob dynamics in TORPEX poloidal null configurations. *Plasma Phys. Controlled Fusion* **58** (12), 125003.
- Shi, E. L., Hakim, A. H. & Hammett, G. W. 2015 A gyrokinetic one-dimensional scrape-off layer model of an edge-localized mode heat pulse. *Phys. Plasmas* **22** (2), 022504.
- Shi, E. L., Hammett, G. W., Stoltzfus-Dueck, T. & Hakim, A. 2017 Gyrokinetic continuum simulation of turbulence in a straight open-field-line plasma. *J. Plasma Phys.* **83** (3), 905830304.
- Shizgal, B. 1979 Eigenvalues of the Lorentz Fokker–Planck equation. *J. Chem. Phys.* **70** (4), 1948–1951.
- Shizgal, B. 1981 A Gaussian quadrature procedure for use in the solution of the Boltzmann equation and related problems. *J. Comput. Phys.* **41** (2), 309–328.
- Shu, C.-W. 2009 Discontinuous Galerkin methods: General approach and stability. In *Numerical Solutions of Partial Differential Equations* (ed. S. Bertoluzza, S. Falletta, G. Russo & C.-W. Shu), pp. 149–195. Birkhäuser Basel.
- Shurygin, R. V. 2001 Numerical modeling of L–H transitions in the presence of a radial current at the edge of a tokamak plasma. *Plasma Phys. Rep.* **27** (1), 18–29.
- Simakov, A. N. & Catto, P. J. 2003 Drift-ordered fluid equations for field-aligned modes in low- β collisional plasma with equilibrium pressure pedestals. *Phys. Plasmas* **10** (12), 4744–4757.
- Simonini, R., Corrigan, G., Radford, G., Spence, J. & Taroni, A. 1994 Models and numerics in the multi-fluid 2-D edge plasma code EDGE2D/U. *Contrib. Plasma Phys.* **34** (2-3), 368–373.
- Smith, N. & van der Walt, S. 2016 Matplotlib colormaps. <https://bids.github.io/colormap/>.
- Smith, S. A. 1997 Dissipative closures for statistical moments, fluid moments, and subgrid scales in plasma turbulence. PhD thesis, Princeton University.
- Snyder, P. B., Hammett, G. W. & Dorland, W. 1997 Landau fluid models of collisionless magnetohydrodynamics. *Phys. Plasmas* **4** (11), 3974–3985.

- Soukhanovskii, V. A. 2017 A review of radiative detachment studies in tokamak advanced magnetic divertor configurations. *Plasma Phys. Controlled Fusion* **59** (6), 064005.
- Spitzer, L. & Härm, R. 1953 Transport phenomena in a completely ionized gas. *Phys. Rev.* **89** (5), 977–981.
- Staebler, G. M., Kinsey, J. E. & Waltz, R. E. 2007 A theory-based transport model with comprehensive physics. *Phys. Plasmas* **14** (5), 055909.
- Strangeby, P. & McCracken, G. 1990 Plasma boundary phenomena in tokamaks. *Nucl. Fusion* **30** (7), 1225–1379.
- Strangeby, P. C. 2000 *The plasma boundary of magnetic fusion devices. Plasma Physics Series*. Bristol ; Philadelphia: Institute of Physics Publishing.
- Stoltzfus-Dueck, T. 2009 Tokamak edge turbulence and the approach to adiabatic response. PhD thesis, Princeton University.
- Stoltzfus-Dueck, T. 2012 Tokamak-edge toroidal rotation due to inhomogeneous transport and geodesic curvature. *Phys. Plasmas* **19** (5), 055908.
- Stoltzfus-Dueck, T. 2016 Parallel electron force balance and the L-H transition. *Phys. Plasmas* **23** (5), 054505.
- Su, C. H. & Oberman, C. 1968 Collisional damping of a plasma echo. *Phys. Rev. Lett.* **20** (9), 427–429.
- Sugama, H. 2000 Gyrokinetic field theory. *Phys. Plasmas* **7** (2), 466–480.
- Taitano, W., Chacón, L., Simakov, A. & Molvig, K. 2015 A mass, momentum, and energy conserving, fully implicit, scalable algorithm for the multi-dimensional, multi-species Rosenbluth–Fokker–Planck equation. *J. Comput. Phys.* **297**, 357–380.
- Takizuka, T. 2017 Kinetic effects in edge plasma: kinetic modeling for edge plasma and detached divertor. *Plasma Phys. Controlled Fusion* **59** (3), 034008.
- Tamain, P., Ghendrih, P., Tsitrone, E., Grandgirard, V., Garbet, X., Sarazin, Y., Serre, E., Ciraolo, G. & Chiavassa, G. 2010 TOKAM-3D: A 3D fluid code for transport and turbulence in the edge plasma of tokamaks. *J. Comput. Phys.* **229** (2), 361–378.
- Taylor, R. J., Brown, M. L., Fried, B. D., Grote, H., Liberati, J. R., Morales, G. J., Pribyl, P., Darrow, D. & Ono, M. 1989 H-mode behavior induced by cross-field currents in a tokamak. *Phys. Rev. Lett.* **63** (21), 2365–2368.
- Terry, J. L., LaBombard, B., Lipschultz, B., Greenwald, M. J., Rice, J. E. & Zweben, S. J. 2007 The scrape-off layer in Alcator C-Mod: Transport, turbulence, and flows. *Fusion Sci. Technol.* **51** (3), 342–356.

- Terry, J. L., Zweben, S. J., Hallatschek, K., LaBombard, B., Maqueda, R. J., Bai, B., Boswell, C. J., Greenwald, M., Kopon, D., Nevins, W. M., Pitcher, C. S., Rogers, B. N., Stotler, D. P. & Xu, X. Q. 2003 Observations of the turbulence in the scrape-off-layer of Alcator C-Mod and comparisons with simulation. *Phys. Plasmas* **10** (5), 1739–1747.
- Terry, P. W. 2000 Suppression of turbulence and transport by sheared flow. *Rev. Mod. Phys.* **72** (1), 109–165.
- Thakur, S. C., Brandt, C., Cui, L., Gosselin, J. J., Light, A. D. & Tynan, G. R. 2014 Multi-instability plasma dynamics during the route to fully developed turbulence in a helicon plasma. *Plasma Sources Sci. and Technol.* **23** (4), 044006.
- Thakur, S. C., Xu, M., Manz, P., Fedorczak, N., Holland, C. & Tynan, G. R. 2013 Suppression of drift wave turbulence and zonal flow formation by changing axial boundary conditions in a cylindrical magnetized plasma device. *Phys. Plasmas* **20** (1), 012304.
- Togo, S., Takizuka, T., Nakamura, M., Hoshino, K., Ibano, K., Lang, T. L. & Ogawa, Y. 2016 Self-consistent treatment of the sheath boundary conditions by introducing anisotropic ion temperatures and virtual divertor model. *J. Comput. Phys.* **310**, 109–126.
- Tronko, N., Bottino, A., Görler, T., Sonnendrücker, E., Told, D. & Villard, L. 2017 Verification of gyrokinetic codes: Theoretical background and applications. *Phys. Plasmas* **24** (5), 056115.
- Tronko, N., Bottino, A. & Sonnendrücker, E. 2016 Second order gyrokinetic theory for particle-in-cell codes. *Phys. Plasmas* **23** (8), 082505.
- Tskhakaya, D., Matyash, K., Schneider, R. & Taccogna, F. 2007 The particle-in-cell method. *Contrib. Plasma Phys.* **47** (8-9), 563–594.
- Tynan, G. R., Fujisawa, A. & McKee, G. 2009 A review of experimental drift turbulence studies. *Plasma Phys. Controlled Fusion* **51** (11), 113001.
- Umansky, M. V., Krasheninnikov, S. I., LaBombard, B. & Terry, J. L. 1998 Comments on particle and energy balance in the edge plasma of Alcator C-Mod. *Phys. Plasmas* **5** (9), 3373–3376.
- Umansky, M. V., Popovich, P., Carter, T. A., Friedman, B. & Nevins, W. M. 2011 Numerical simulation and analysis of plasma turbulence the Large Plasma Device. *Phys. Plasmas* **18** (5), 055709.
- Vaezi, P., Holland, C., Thakur, S. C. & Tynan, G. R. 2017 Understanding the impact of insulating and conducting endplate boundary conditions on turbulence in CSDX through nonlocal simulations. *Phys. Plasmas* **24** (4), 042306.

- Valanju, P. M., Kotschenreuther, M., Mahajan, S. M. & Canik, J. 2009 Super-X divertors and high power density fusion devices. *Phys. Plasmas* **16** (5), 056110.
- Vincena, S., Gekelman, W. & Maggs, J. 2004 Shear Alfvén wave perpendicular propagation from the kinetic to the inertial regime. *Phys. Rev. Lett.* **93** (10), 105003.
- Wagner, F. 2007 A quarter-century of H-mode studies. *Plasma Phys. Controlled Fusion* **49** (12B), B1–B33.
- Wagner, F., Becker, G., Behringer, K., Campbell, D., Eberhagen, A., Engelhardt, W., Fussmann, G., Gehre, O., Gernhardt, J., Gierke, G. v., Haas, G., Huang, M., Karger, F., Keilhacker, M., Klüber, O., Kornherr, M., Lackner, K., Lisitano, G., Lister, G. G., Mayer, H. M., Meisel, D., Müller, E. R., Murmann, H., Niedermeyer, H., Poschenrieder, W., Rapp, H., Röhr, H., Schneider, F., Siller, G., Speth, E., Stäbler, A., Steuer, K. H., Venus, G., Vollmer, O. & Yü, Z. 1982 Regime of improved confinement and high beta in neutral-beam-heated divertor discharges of the ASDEX tokamak. *Phys. Rev. Lett.* **49** (19), 1408–1412.
- Walkden, N., Dudson, B., Easy, L., Fishpool, G. & Omotani, J. 2015 Numerical investigation of isolated filament motion in a realistic tokamak geometry. *Nucl. Fusion* **55** (11), 113022.
- Wang, L., Hakim, A. H., Bhattacharjee, A. & Germaschewski, K. 2015 Comparison of multi-fluid moment models with particle-in-cell simulations of collisionless magnetic reconnection. *Phys. Plasmas* **22** (1), 012108.
- Ware, C. 1988 Color sequences for univariate maps: theory, experiments and principles. *IEEE Comput. Graph. Appl. Mag.* **8** (5), 41–49.
- Wersal, C. & Ricci, P. 2015 A first-principles self-consistent model of plasma turbulence and kinetic neutral dynamics in the tokamak scrape-off layer. *Nucl. Fusion* **55** (12), 123014.
- Wiesen, S., Reiter, D., Kotov, V., Baelmans, M., Dekeyser, W., Kukushkin, A., Lisgo, S., Pitts, R., Rozhansky, V., Saibene, G., Veselova, I. & Voskoboinikov, S. 2015 The new SOLPS-ITER code package. *J. Nucl. Mater.* **463**, 480–484.
- Wilkening, J., Cerfon, A. J. & Landreman, M. 2015 Accurate spectral numerical schemes for kinetic equations with energy diffusion. *J. Comput. Phys.* **294**, 58–77.
- Wilkie, G. J. & Dorland, W. 2016 Fundamental form of the electrostatic δf -pic algorithm and discovery of a converged numerical instability. *Phys. Plasmas* **23** (5), 052111.
- Windisch, T., Grulke, O., Naulin, V. & Klinger, T. 2011 Intermittent transport events in a cylindrical plasma device: experiment and simulation. *Plasma Phys. Controlled Fusion* **53** (8), 085001.

- Xu, X., Bodi, K., Cohen, R., Krasheninnikov, S. & Rognlien, T. 2010 TEMPEST simulations of the plasma transport in a single-null tokamak geometry. *Nucl. Fusion* **50** (6), 064003.
- Xu, X., Cohen, R., Porter, G., Rognlien, T., Ryutov, D., Myra, J., D'Ippolito, D., Moyer, R. & Groebner, R. 2000 Turbulence studies in tokamak boundary plasmas with realistic divertor geometry. *Nucl. Fusion* **40** (3Y), 731–736.
- Xu, X., Umansky, M., Dudson, B. & Snyder, P. 2008 Boundary plasma turbulence simulations for tokamaks. *Tech. Rep. LLNL-JRNL-404082*. United States.
- Xu, X., Xiong, Z., Dorr, M., Hittinger, J., Bodi, K., Candy, J., Cohen, B., Cohen, R., Colella, P., Kerbel, G., Krasheninnikov, S., Nevins, W., Qin, H., Rognlien, T., Snyder, P. & Umansky, M. 2007 Edge gyrokinetic theory and continuum simulations. *Nucl. Fusion* **47** (8), 809–816.
- Xu, X. Q. & Cohen, R. H. 1998 Scrape-off layer turbulence theory and simulations. *Contrib. Plasma Phys.* **38** (1-2), 158–170.
- Xu, X. Q., Xi, P. W., Dimits, A., Joseph, I., Umansky, M. V., Xia, T. Y., Gui, B., Kim, S. S., Park, G. Y., Rhee, T., Jhang, H., Diamond, P. H., Dudson, B. & Snyder, P. B. 2013 Gyro-fluid and two-fluid theory and simulations of edge-localized-modes. *Phys. Plasmas* **20** (5), 056113.
- Yuan, L. & Shu, C.-W. 2006 Discontinuous Galerkin method based on non-polynomial approximation spaces. *J. Comput. Phys.* **218** (1), 295–323.
- Zeiler, A., Drake, J. F. & Rogers, B. 1997 Nonlinear reduced Braginskii equations with ion thermal dynamics in toroidal plasma. *Phys. Plasmas* **4** (6), 2134–2138.
- Zhang, X. 2017 On positivity-preserving high order discontinuous Galerkin schemes for compressible Navier–Stokes equations. *J. Comput. Phys.* **328**, 301–343.
- Zhang, X. & Shu, C.-W. 2010 On positivity-preserving high order discontinuous Galerkin schemes for compressible Euler equations on rectangular meshes. *J. Comput. Phys.* **229** (23), 8918–8934.
- Zhang, X. & Shu, C.-W. 2011 Maximum-principle-satisfying and positivity-preserving high-order schemes for conservation laws: survey and new developments. *Proc. Math. Phys. Eng. Sci.* **467** (2134), 2752–2776.
- Zhu, B., Francisquez, M. & Rogers, B. N. 2017 Global 3D two-fluid simulations of the tokamak edge region: Turbulence, transport, profile evolution, and spontaneous eb rotation. *Phys. Plasmas* **24** (5), 055903.
- Zweben, S., Davis, W., Kaye, S., Myra, J., Bell, R., LeBlanc, B., Maqueda, R., Munsat, T., Sabbagh, S., Sechrest, Y., Stotler, D. & the NSTX Team 2015 Edge and SOL turbulence and blob variations over a large database in NSTX. *Nucl. Fusion* **55** (9), 093035.

- Zweben, S. & Gould, R. 1985 Structure of edge-plasma turbulence in the Caltech tokamak. *Nucl. Fusion* **25** (2), 171–183.
- Zweben, S., Maqueda, R., Stotler, D., Keesee, A., Boedo, J., Bush, C., Kaye, S., LeBlanc, B., Lowrance, J., Mastrocola, V., Maingi, R., Nishino, N., Renda, G., Swain, D., Wilgen, J. & the NSTX Team 2004 High-speed imaging of edge turbulence in NSTX. *Nucl. Fusion* **44** (1), 134–153.
- Zweben, S. J. 1985 Search for coherent structure within tokamak plasma turbulence. *Phys. Fluids* **28** (3), 974–982.
- Zweben, S. J., Boedo, J. A., Grulke, O., Hidalgo, C., LaBombard, B., Maqueda, R. J., Scarin, P. & Terry, J. L. 2007 Edge turbulence measurements in toroidal fusion devices. *Plasma Phys. Controlled Fusion* **49** (7), S1–S23.
- Zweben, S. J., Maqueda, R. J., Terry, J. L., Munsat, T., Myra, J. R., D'Ippolito, D., Russell, D. A., Krommes, J. A., LeBlanc, B., Stoltzfus-Dueck, T., Stotler, D. P., Williams, K. M., Bush, C. E., Maingi, R., Grulke, O., Sabbagh, S. A. & White, A. E. 2006 Structure and motion of edge turbulence in the National Spherical Torus Experiment and Alcator C-Mod. *Phys. Plasmas* **13** (5), 056114.
- Zweben, S. J., Myra, J. R., Davis, W. M., D'Ippolito, D. A., Gray, T. K., Kaye, S. M., LeBlanc, B. P., Maqueda, R. J., Russell, D. A., Stotler, D. P. & the NSTX-U Team 2016 Blob structure and motion in the edge and SOL of NSTX. *Plasma Phys. Controlled Fusion* **58** (4), 044007.
- Zweben, S. J., Scott, B. D., Terry, J. L., LaBombard, B., Hughes, J. W. & Stotler, D. P. 2009 Comparison of scrape-off layer turbulence in Alcator C-Mod with three dimensional gyrofluid computations. *Phys. Plasmas* **16** (8), 082505.
- Zweben, S. J., Terry, J. L., Stotler, D. P. & Maqueda, R. J. 2017 Invited Review Article: Gas puff imaging diagnostics of edge plasma turbulence in magnetic fusion devices. *Rev. Sci. Instrum.* **88** (4), 041101.